INTERNATIONAL ATOMIC ENERGY AGENCY
UNITED NATIONS EDUCATIONAL, SCIENTIFIC AND CULTURAL ORGANIZATION
INTERNATIONAL CENTRE FOR THEORETICAL PHYSICS
I.C.T.P., P.O. BOX 586, 34100 TRIESTE, ITALY, CABLE: CENTRATOM TRIESTE
UNITED NATIONS INDUSTRIAL DEVELOPMENT ORGANIZATION
INTERNATIONAL CENTRE FOR SCIENCE AND HIGH TECHNOLOGY

SMR: 630/8

MINIWORKSHOP ON NONLINEARITY:
Dynamics of Surfaces in Nonlinear Physics

(13 - 24 July 1992)

"Along a Road to Developed Turbulence:
Free Thermal Convection in Low Temperature Helium Gas"

presented by:

A. Libchaber
NEC Research Institute
4 Independence Way
Princeton, NJ 08540
U.S.A..

THE UNIVERSITY OF CHICA O

ALONG A ROAD TO DEVELOPED TURBULENCE: FREE THERMAL CONVECTION IN LOW TEMPERATURE HELIUM GAS

A DISSERTATION SUBMITTED TO
THE FACULTY OF THE DIVISION OF THE PHYSICAL SCIENCES
IN CANDIDACY FOR THE DEGREE OF
DOCTOR OF PHILOSOPHY

DEPARTMENT OF PHYSICS

BY
XIAO ZHONG WU

CHICAGO, ILLINOIS
JUNE, 1991

ACKNOWLEDGEMENTS

I would like to thank my advisor Prof. A. Libchaber for his excellent guidance, sustained encouragement and sincere care. Patiently, he has taught me, a naive student having no research experience when joining him, from basic writing skills to experimental techniques, from scientific thinking to the attitude in pursuing research... It may even be improper to express my gratitude to him in this thesis, since it has been almost written by him and me together. Those daily discussions and chats, and the late night drinks after each big success as well as failure, will remain precious memories.

A special thanks goes to Prof. L. Kadanoff, for his readiness to discuss with me and show me the way of thinking. All the progress has been made with his guidance and participation.

The ground of this thesis work has been laid by Dr. F. Heslot and Prof. B. Castaing. Their marks remain in all aspects of this experiment, long after they left. I wish to thank them for their valuable suggestions and advice, especially Prof. B. Castaing for leading me into this experiment. I have enjoyed more than one year of collaboration with Dr. M. Sano. This collaboration has produced not only the main experimental results of this thesis work, but a lot of interesting discussions on science and culture as well. I am fortunate to have J. Bechhoefer, G. Zocchi, A. Simon, E. Moses, E. Braun, J. -M. Flesselles and the others as my colleagues in Libchaber's group–a friendly and stimulating international family. I thank J. -M. Flesselles for helping me in preparing this manuscript with his favorite LaTeX.

I acknowledge Prof. R. Hildebrand for presenting us the bolometers, which are essential to this experiment, and Mr. Jezewski for working on them.

I benefit enormously from discussions with E. Ching, I. Procaccia, E. Siggia, S. Thomae, L. Wu, V. Yakhot and S. Zaleski.

I thank Prof. A. Libchaber, Prof. L. Kadanoff, Prof. Y. Nambu and Prof. R. Rosner to serve in my Ph. D committee.

When I left home for the US six years ago, I had absolutely no idea of what kind of life it was going to be. There is an old Chinese saying "Count on parents when at home, Count on friends when abroad". Counting on my fellow Chinese friends, I have made it, joyfully, even though the life sometimes was as hard as it could be. I thank them all for their friendship. I also appreciate those American friends and professors who have patiently shown me the ways, particularly Prof. S. Krasner, Ms. N. McNeill and my hostess Ms. B. Ro.

At the time of completing my Ph. D degree, I can not forget to acknowledge the two most influential teachers of my early age, Mr. S. M. Chen and Ms. Z. Z. Hu.

Finally, I would like to thank my parents and sister for their love and encouragement. The achievement of this thesis, I hope, is a satisfaction to their expectation. For the last three years, especially the year of our marriage, the love from my wife, Wenjie Deng, has been my strongest spiritual support. To her, I am deeply indebted.

TABLE OF CONTENTS

LIST OF TABLES

LIST OF FIGURES

CHAPTER 1

INTRODUCTION

Turbulence, a common natural phenomenon, is associated with both spatial and temporal random flow motions. Because of its random nature, and the non-linearity of the Navier-Stokes equation which describes the flow motion, turbulence remains as an essentially unsolved problem, and may even not be a well posed one. The most far reaching theory of turbulence was proposed by Kolmogorov 50 years ago (Kolmogorov 1941). In that theory, boundaries are assumed to be at infinity and the flow isotropic and homogeneous. For a large Reynolds number ($Re \gg 1$), the energy cascades from large to small scales without dissipation, until a viscous cut-off length η is reached (η is deduced from the relation that the Reynolds number Re based on it is about 1, $Re_\eta \approx 1$). From this model, the energy at each length scale, or wave number k, follows a power law $k^{-5/3}$. This model is regarded as a good description of fully developed turbulence. However, in natural systems, boundaries are always part of the whole turbulence problem, it is never clear if they can be ignored. Also, in all experiments, coherent structures are observed, with characteristic length and time scales. It is thus surprising that those scales disappear from the problem, as suggested from the preceding theory, where the only scale is a dissipative one.

In a theory proposed by Landau (1944), the number of modes in turbulence increases with the Reynolds number (Re). From the recent development of

dynamical system (see Eckmann 1981; Cvitanovic 1984) it appears clearly that temporal chaos simply evolves from a few modes. This understanding raised the hope of being able to study how the flow develops from laminar to turbulent, study how many modes are relevant, and whether there exist turbulent states different from the Kolmogorov one.

Our aim, in this thesis, was to find and study an experimental system with well defined boundary conditions, and where the flow could be changed from a laminar state to a turbulent one in a control way. A wind tunnel is the most common turbulence generator (see Champagne 1978; Anselmet *et al.* 1984). Because of its large size and fast speed, the *Re* is large. Most of the turbulence studies come from the velocity measurements in wind tunnels. However, it is not the candidate for our experimental system, because it does not have a well defined boundary condition at the input and output of the flow, and the *Re* has a limited range of variation.

Free thermal convection seems to meet our demands. Experimentally, it is just an horizontal fluid layer heated from below. The boundary conditions are simple and experimentally easy to impose: fix the top of the fluid layer at one temperature and the bottom at a higher one. The lateral boundary can be made of thermal insulators. By varying the size of the cell, or the temperature drop across the cell, or the fluid properties, one is able to study in such a closed box, how a flow evolves from laminar to turbulent. As a matter of fact, turbulence observed in nature, like in the atmosphere, is generated by convection.

Thermal convection was studied first experimentally by Benard (1901), and theoretically by Rayleigh (1916). A thermal convection state is characterized by a Rayleigh number (*Ra*), which is approximately proportional to the square of *Re*. By now a large number of scientific and engineering studies on this

subject exists, the main review papers being : Rossby (1969), Spiegel (1971), Normand *et al.* (1977), Busse (1978), Behringer (1985). In most of these experiments, *Ra* is increased by changing the temperature difference, at most two decades, and the cell size, which is rather inconvenient. Threlfall (1974, 1975) was the first one to use low temperature helium gas, and change the densities to span a large range of *Ra*. *Ra* is inversely proportional to the product of the kinematic viscosity and thermal diffusivity, which are small for low temperature helium gas, and can be further decreased by increasing the gas densities. Thus Threlfall was able to cover 8 decades of *Ra* by changing the temperature by only one decade, but the gas density by three decades. He showed that convection with low temperature helium gas is an ideal system to study the development of different flow states. But he only studied the global heat transfer. Experiments, using local detectors in the fluid, were mainly initiated by us, in the case of thermal convection.

Convection systems have also shortcomings compared with other turbulence system, for example wind tunnels. First, the energy is input in the form of heating. From the second law of thermodynamics, we know that it is inefficient as a flow generator. *Re* in a laboratory convection system is small when compared to a moderate room temperature wind tunnel, unless we use high density low temperature helium gas. The second shortcoming, or may be a merit, is the introduction of one more variable, temperature. This new variable increases the richness of the subject, gives us one more observable to study, but on the other hand, increases the complexity of this already difficult problem.

We thus chose to study thermal convection, using low temperature helium gas, and in three cylindrical cells of diameters 8.7, 20 and 20 cm, heights 8.7, 40 and 3 cm, thus of aspect ratio (diameter over height) 1, 0.5, and 6.7 corre-

spondingly. The maximum Ra achieved are 10^{12}, 10^{15} and 10^{11}, respectively. The main results are summarized in table 1.

The first quantity we studied is the Nusselt number (Nu). It is a measure of the heat transport efficiency, and thus reflects the changes of turbulent states as well. On the other hand, it is closely related to the thermal boundary layers, as we shall see latter. Assuming the thermal boundary layers to be marginally stable, Malkus (1954) and Howard (1966) predicted that Nu changes as $Ra^{1/3}$. Some experiments supported this 1/3 theory (Townsend 1959; Goldstein & Tokuda 1980), while many others did not (Goldstein & Chu 1969; Threlfall 1974; Tanaka & Miyata 1980). Our experimental results for the three cells show clearly that the exponent of the power law is smaller than 1/3, for large Ra. Thus a new selection mechanism for the boundary layers, and consequently a new length scale, are needed (Castaing *et al.* 1989). By breaking the symmetry between the colder and hotter boundary layers(Non-Boussinesq effects), we have verified the new selection mechanism for the boundary layers (Wu & Libchaber 1991).

In thermal convection, the velocity, pressure and temperature field are the three variables. They have their own characters, but they are all coupled together and all must bear the signature of the turbulent states as a whole. However, the velocity field is hard to measure in this experiment. The most common velocity measurement techniques are the hot wire and the laser Doppler velocimeter. The hot wire technique can not be used here because there is no large mean velocity and the temperature field fluctuations may affect the measurement. The Doppler shift anemometer is hard to use because optical methods are difficult to implement under cryogenic conditions. Also seeding with particles, needed for laser anemometry, is highly non-trival at low temperature. Visualizing the thermal convection flow has been carried out in

water (Chu & Goldstein 1973; Gross *et al.* 1988; Solomon & Gollub 1990), but a serious technical effort is needed before we can adapt it to the low temperature helium gas. Pressure measurements may be possible, and are currently being tested with piezoelectric transducers. In contrast, temperature is relatively easy to measure using semiconductor sensors. The only problem is the size of the sensor. It has to be small in order to have good spatial resolution, fast time response, and avoid perturbing the flow in any significant way.

In our experiment, we have measured the local temperature fluctuations with bolometers of size 200 μm. The time response of these bolometers is of the order of ms, while our turbulence signals extend up to 200 Hz beyond which electronic noise becomes dominant. Large scale velocity has been measured, via the correlation of two adjacent bolometers (Sano *et al.* 1989). Typical values are about 10 cm/sec. Therefore the frequency corresponding to the size of the bolometer, 200 μm, is about 500Hz. So the bolometer response is fast enough, and do not a priory perturb in the frequency range we measure.

The local temperature signals reveal a lot : The relation between the rms value of the fluctuations and Ra changes around 10^8. The probability distribution functions of the local temperature fluctuations are invariant for each cell and non-Gaussian for $Ra > 10^8$. The turbulent state for $Ra > 10^8$ is called "hard turbulence", and below "soft turbulence"(Heslot *et al.* 1987; Castaing *et al.* 1989).

The power spectrum of the local temperature signals does not show any power law in the soft turbulence regime, but only an exponential cut-off tail. It seems that there are only a few large scale modes in the flow motion, and no cascade from the large scale to the small ones. As the Ra increased above 10^8, a power law $f^{-1.4}$ develops. Hard turbulence seems similar to the cascade

model described by Kolmogorov, or more specifically by Obukhov(1959) and Bolgiano(1959) in a temperature field version.

However, as Ra gets beyond 10^{11}, the power spectrum can no longer be described as a power law with an exponential cut-off (Wu *et al.* 1990), it changes shape. It seems that a second power law of exponent -2.4 develops between the first power law and the exponential cut-off. The changing process has been described phenomenologically as a multi-fractal like transformation. Physical models underlying this process have been proposed, but none could give a satisfactory explanation (Castaing 1990; Frisch & Vergassola 1991; Procaccia *et al.* 1991).

A summary of our main results being given above, let us now describe the organization of the thesis. Chapter 2 introduces the fluid physical properties, describes the experimental set up, the techniques and procedures in general. Chapter 3 includes the experimental results of the three cells. In this chapter, all the results are provided objectively, with the minimum of analysis and interpretation, and wher possible, presented in exhaustive tables. In chapter 4 existing models are presented and compared with experimental data. In Appendix A, a publishe paper on non-Boussinesq effects is included.

CHAPTER 2

THE EXPERIMENTAL ENVIRONMENT

Three cells have been studied, their diameters (D) are 8.7 cm, 20 cm and 20 cm, their heights (L) 8.7 cm, 40 cm and 3 cm, thus their aspect ratio (D/L), 1.0, 0.5 and 6.7, respectively. Two different cryogenic set-up have been used, one for the 8.7 cm cell and another one for the others. Nonetheless, the basic principles are the same. Since the cell of aspect ratio 1.0 was the first to be studied, I shall use it as an example to detail the experiment set-up and experimental procedures. As for the other system, I shall only mention the differences.

2.1 Helium gas

The control parameters of the convection experiment are the Prandtl number Pr

$$Pr = \frac{\nu}{\kappa} \tag{2.1}$$

and the Rayleigh number Ra,

$$Ra = \frac{g\alpha\Delta L^3}{\nu\kappa} \ , \tag{2.2}$$

where g is the gravitational acceleration, α is the thermal expansion coefficient, Δ is the temperature drop across the cell, L is the height of the cell, ν is the kinematic viscosity and κ the thermal diffusivity.

We would like to have as large a range of Ra as possible. Most of the previous experiments achieved it by changing the height of the cell. Since the cross section of the cell cannot be changed unless a new system is built, most experiments use different heights, thus different aspect ratios. For a fixed Pr and Ra, Deardorff & Willis (1965) and Threlfall (1975) show that the Nusselt number Nu is not even a monotonic function of the aspect ratio, this is confirmed by our experiment (table 2). Therefore there is a need to cover a large Ra range with a fixed aspect ratio.

This can be achieved by changing the physical constants of the fluid. For ideal gas, the thermal expansion coefficient α is equal to $1/T$, so it increases as the temperature T decreases. However, as the temperature of the system decreases, the range of the temperature difference Δ is correspondingly restricted. So we cannot gain much from the product $\alpha\Delta$ by lowering the temperature. However, let's look at the kinematic viscosity ν and the thermal diffusivity κ. Both of them have a dimension of $[L^2T^{-1}]$, or the product of length by velocity. For an ideal gas, a good description of low density gas, the only length scale involved is the mean free path $1/(n\sigma)$, and the only velocity is the thermal velocity $\sqrt{kT/m}$, here σ, m and n are the helium atom cross section, mass, gas number density respectively. So

$$\nu, \kappa \approx \frac{1}{n\sigma}\sqrt{\frac{kT}{m}} \quad . \tag{2.3}$$

Then Ra can be written as

$$Ra = gL^3(\alpha\Delta)\frac{(n\sigma)^2 m}{kT} \quad . \tag{2.4}$$

According to this estimation, the Ra will increase by a factor of 60 as the temperature T decreases from 300 K to 5 K, provided everything else is unchanged; it will also cover 6 decades if the gas density changes from 1×10^{-5} to 1×10^{-2}g/cm^3 (the liquid helium density is about 0.1 g/cm^3).

The estimation based on ideal gas gives us some intuition on how the physical properties change with density and temperature. But for real gas more dramatic changes occur. For example, when helium approaches its critical point (pressure 2.24 atm and temperature 5.201 K), the expansion coefficient can be as large as 10, instead of 0.2 at 5 K, ν and κ can be of the order of 10^{-4} cm^2/sec. As a matter of fact, we have used gas densities ranging from 1×10^{-5} g/cm^3 to 6×10^{-2} g/cm^3 , correspondingly α changes from 0.2 to 3, ν changes from 1 cm^2/sec to 10^{-4} cm^2/sec and κ changes from 1 cm^2/sec to 4×10^{-5} cm^2/sec. We actually have 8 decades of Ra variation (table 5).

In fig.1 and fig. 2, we give the physical constants of the fluid as a function of temperature and density respectively. All the fluid properties used in this experiments are calculated from the fitting equations given by R. McCarty (1972,1973). McCarty had searched about 40,000 articles from which 634 relevant references were used. This, as far as we know, is the most complete summary of helium gas data. In each of our experimental run, the cell is closed, thus the density fixed, which is inferred from the measurement of pressure and temperature. From the temperature and density, all the physical properties can be calculated.

The errors in the physical constants come from two sources: one is from the original measurement data used in determining the equation of state and the agreement between those data and the equation of state. The second is from errors in our measurements of pressure and temperature. According to McCarty's review, in the region away from the critical point, the density has

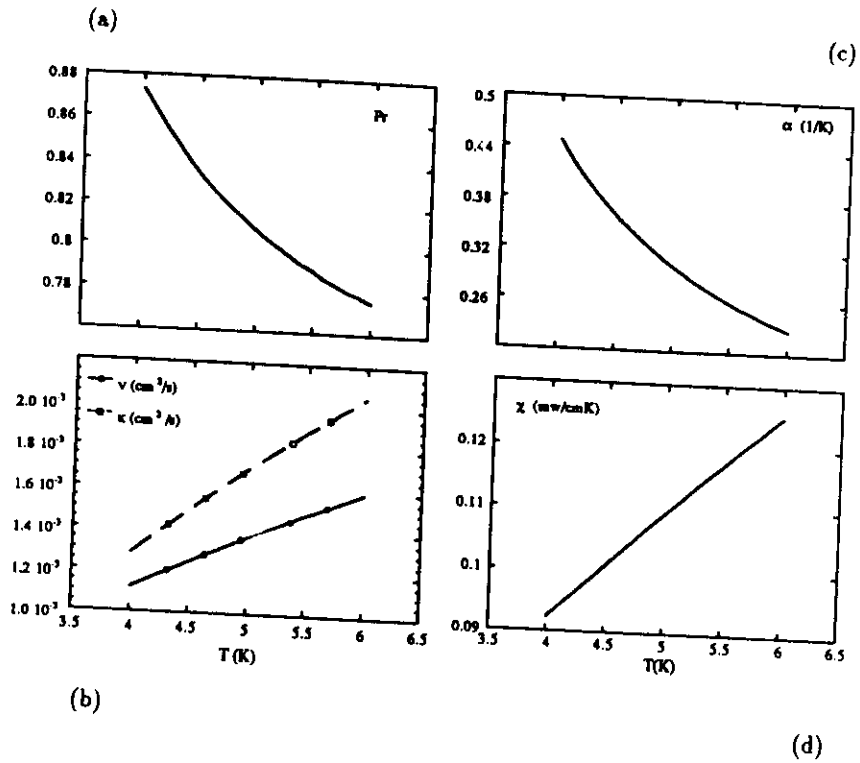

Figure 1. Fluid properties vs. temperature. For a fixed density $\rho = 0.01$ g/cm^3, (a) the Prandtl number Pr, (b) the thermal diffusivity κ and kinematic viscosity ν, (c) the thermal expansion coefficient α and (d) the thermal conductivity χ, are plotted as functions of temperature T.

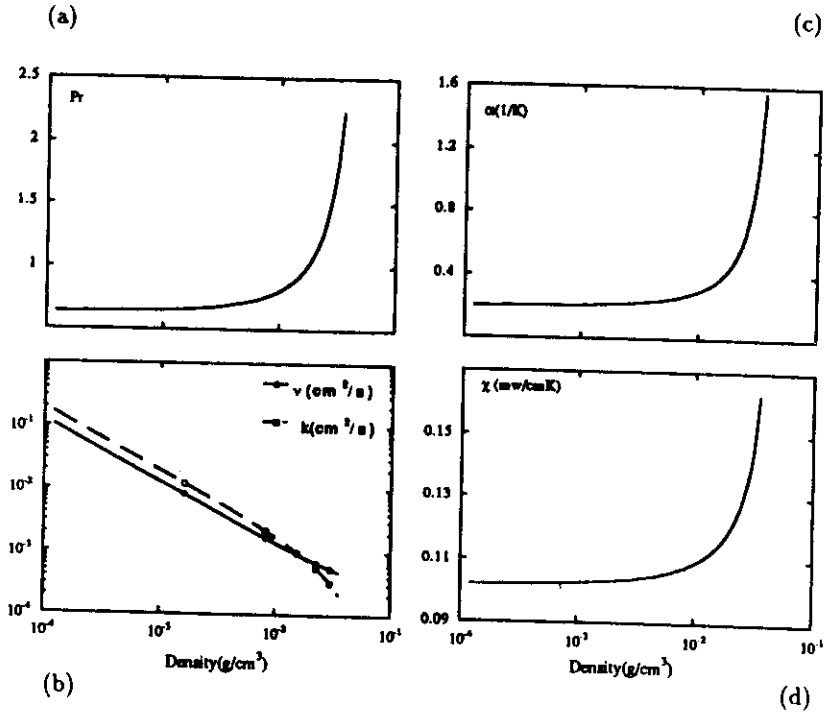

Figure 2. Fluid properties vs. density. For a fixed temperature $T = 5.0$ K, (a) the Prandtl number Pr, (b) the thermal diffusivity κ and kinematic viscosity ν, (c) the thermal expansion coefficient α and (d) the thermal conductivity χ, are plotted as functions of density.

an average uncertainty of 0.1%, the specific heat 0.1%. In the critical region, the average uncertainty of density and specific heat are about 2%, and can be as large as 10%. As we shall discuss later, the error in our temperature measurement is within a few mK, which has small effects in the fluid properties calculation. The uncertainty of the pressure measurement varies from 0.15% for $P < 1000$ torr (except for very small pressure), to 0.5% for $P > 1000$ torr. The physical constants are certainly affected by these errors, especially in the critical region, where the fluid properties change drastically. Combining the two sources of error, we give a rough estimate of the imprecisions in the physical constants for various densities at 5K in fig. 3.

For a fixed density of helium gas, Ra can be changed slightly by varying the average temperature of the cell. However experimentally, we used about ten different Δ values to cover one decade of Ra with one gas density. To cover large ranges of Ra, we have to use helium gas of different densities. We choose two successive densities in such a way that there is one or two points overlap in Ra. About ten different gas densities ranging from 10^{-5} to 6×10^{-2} g/cm^3 have been used to cover the whole Ra range. Table 3, 5 and 6 list all the densities used and the associated Ra, Nu and Pr for the three cells. In table 5, the corresponding physical constants are given as well.

2.2 Cryogenic aspects and experimental procedures

2.2.1 The cell

The first cell used was a cylinder of 8.7 cm of diameter and height (built by MTM Cryo.-Tech-Lab, Chicago, Illinois). Figure 4 is the photography of the

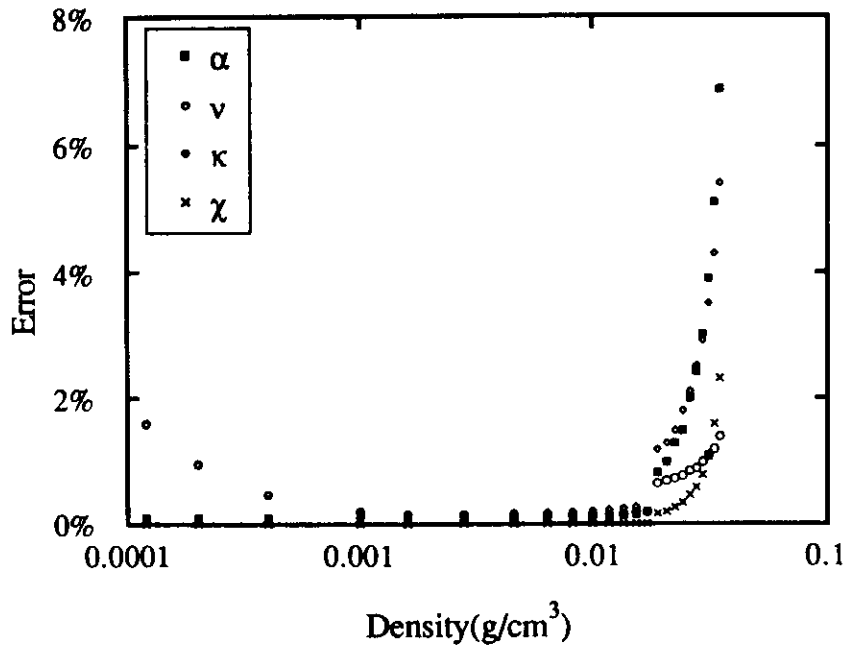

Figure 3. The errors in physical constants. For $T = 5.0$ K, the errors in physical constants for different densities.

system. For the lowest $Ra = 4 \times 10^3$, a density 1×10^{-5} g/cm^3 (pressure about 1 torr) is needed, while for the highest one, 6×10^{11} a density 3×10^{-2} g/cm^3 (pressure about 1×10^3 torr). The side wall of the cell is made from 2 mm thick stainless steel. Its thermal conductivity is small (3×10^{-3} Wcm^{-1}K^{-1}) compared with most other metals. Both the top and bottom plate are made out of OFHC (Oxygen-Free-High-Conductivity) copper to reach good temperature homogeneity. At 5 K, the thermal conductivity of OFHC copper is about 4 Wcm^{-1}K^{-1}. Figure 5 details the structure of the cell, the vacuum chamber, and all of the electrical and mechanical connections. The cell is surrounded by a cylindrical vacuum chamber of diameter 11.4 cm and height 21 cm, made of 2 mm stainless steel. The vacuum chamber is pumped through a stainless steel tube (1 cm of diameter) which is silver soldered to the copper plate.

It is essential to have a proper and well defined thermal impedance between the top plate of the cell and the top plate of the vacuum chamber (see the insert of fig. 5). The top plate of the chamber is at 4.2 K, the top plate of the cell must be regulated around 5 K, thus for a given thermal impedance, the total heat flux is fixed. The thermal impedance has to be small enough so that the total heat flux is always larger than the heat applied from the bottom of the cell in order for the regulation to function. On the other hand, the thermal impedance can not be too small since this will require excessive heating power. The thermal impedance has been made out of a 6063-T5 aluminum ring of height 1cm, O. D. 3 cm and I. D. 2.2 cm, impedance 0.7 W/K. The top plate of the cell and the vacuum chamber top plate sandwich this ring, with indium O-rings on its two ends for good contact. The aluminum ring is mechanically supported by a G-10 and a brass outer rings, which have no thermal contact with the two plates.

Electric wires come out of the sealed cell through a hole of about 5 mm at

(a)

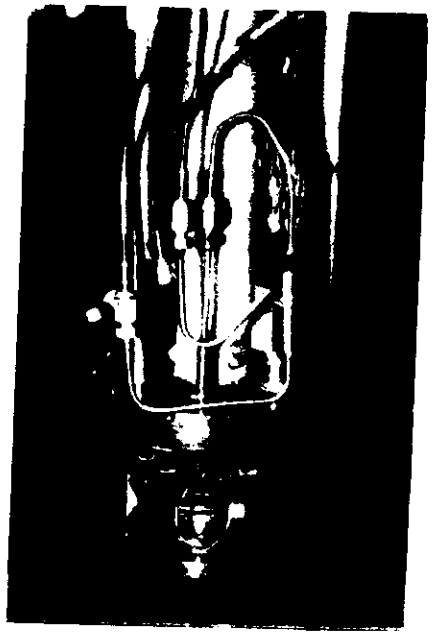

(b)

Figure 4. The photograph of the experimental system for the aspect ratio 1.0 cell. (a) shows the top plates of the vacuum chamber and the cell, with the mechanical support, cryogenic and electric connections. (b) is the covection cell.

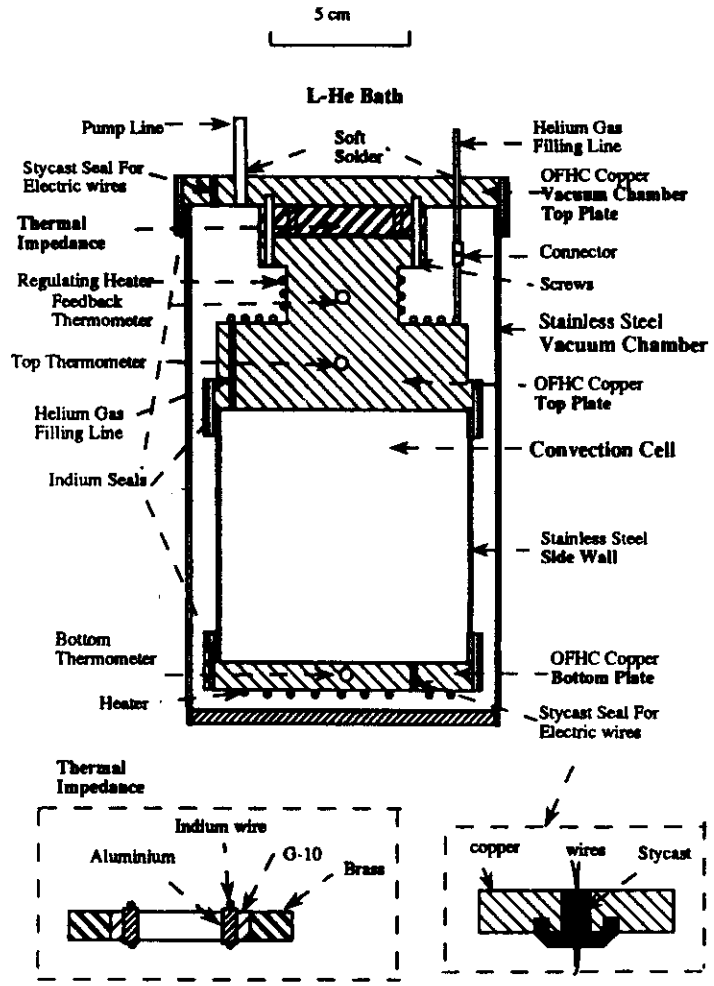

Figure 5. The sketch of the cell and the vacuum chamber. The aspect ratio is 1.0. Diagrams for the thermal link and stycast seal are inserted.

the bottom plate. The hole is later sealed with stycast 2850 FT and catalyst 24LV (Emerson & Cuming). In order to have a leak tight seal, proper care has to be taken to compensate for differential thermal expansions (see insert of fig. 5). This seal proved to be vacuum proof after many thermal cycles. It is also used for the electrical wires leaving the vacuum chamber from its top plate.

The cell at He temperature is filled with helium gas from room temperature. We thus have to build a heat exchanger to cool the gas down. We first use a thin stainless tube (1.5 mm I. D.) from room temperature down, to a control valve in helium bath (fig 6). From there a copper tube (1.5 mm I.D., 3 mm O.D.) goes through the vacuum chamber top plate (soft solder used). After getting into the vacuum chamber, a Kajon connector is used for easy dismounting. Before entering the cell, the tube wraps the top plate of the cell several turns in order to have good heat exchange and reach thermal equilibrium (fig. 5).

For the filling tube, there are two valves, one at the top of the dewar (room temperature), another in the liquid helium bath, just above the top plate of the vacuum chamber. The low temperature control valve closes when a pressure of 15 psi or higher is applied to a Teflon cone against its counterpart, opens when the pressure is released and a bellows pushes the Teflon cone back (see insert of fig. 6).

This control valve is quite helpful in eliminating acoustic oscillations, which originate from a thermal instability which sets in when a tube, closed at its top at room temperature, dips its bottom into a liquid helium bath (Taconis *et al.* 1949; Zouzoulas & Rott 1976; Yazaki *et al.* 1980). Although such oscillations are used to measure the L-He level in storage dewar, they are very harmful in a cryogenic system since it dissipates liquid helium as well as introduces extra noise into the turbulent flow. Even though the control valve could not

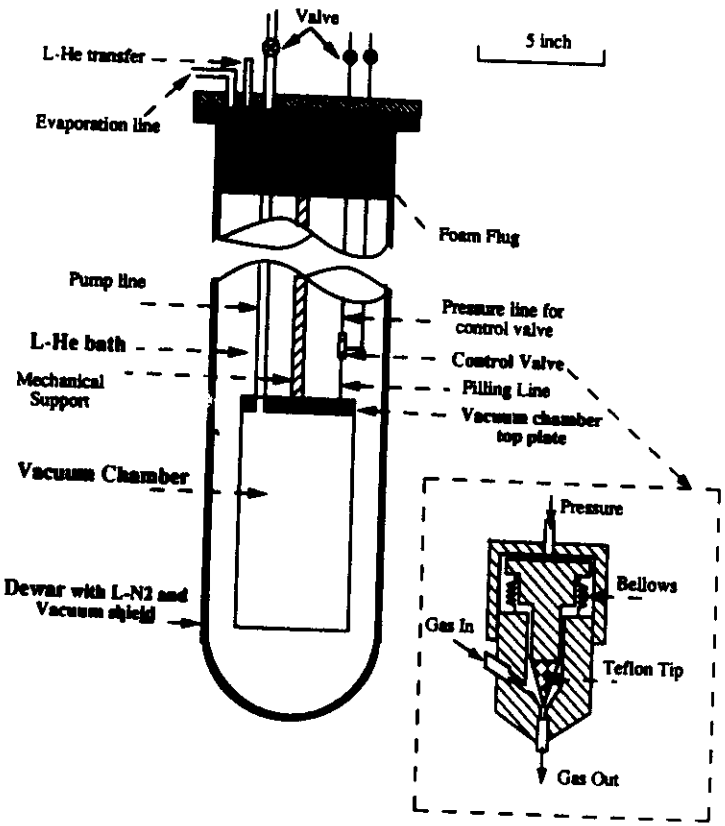

Figure 6. The experimental system in the dewar. The low temperature control valve is sketched in the insert.

be closed tightly, it increases the filling tube impedance and helps to damp out the oscillation.

The liquid nitrogen and liquid helium glass dewars are standard. The inner size of the helium dewar imposed the final size of the cell used. During operation, typical liquid consumption was about 12 liter for nitrogen and 8 liters for helium per day. The convection experiment itself needed between 10^{-4} to 0.3 watt to run (Every watt of heat evaporates about 2 liters of L-He per hour).

The vacuum pump system used during all the procedures was an Edwards 160M diffusion pump backed by a E2M12 two level mechanical pump. The pump reading was always 1×10^{-7} torr.

2.2.2 The cooling procedures

To cool the system down to He temperature, we pre-cool it down to N_2 one. The thermal capacity of metal has a T^3 dependence, thus L-N_2 reduces the thermal capacity of the system enormously. We leak check the system at both room temperature and N_2 one. Since most of the thermal shrinkage occurs in cooling down from 300 to 77 K, it is unlikely to develop a leak at He temperature if it is leak free at N_2 temperature.

Once the cell is leak tested, we close the valve and leave it in vacuum. We then put on the vacuum chamber and test it. After the test, a balloon of hydrogen gas is put into the vacuum chamber as exchange gas for cooling down. Hydrogen is used because of its low boiling point. Helium gas can not be used because it will make it impossible to leak test later at N_2 temperature.

We cool the system down by filling the N_2 dewar. The vacuum between the N_2 dewar and the He one is filled with a balloon of N_2 as exchange gas. Again helium gas can not be used since it is very hard to be pumped out and it will

stay as gas at low temperature. To monitor the temperature in the cooling down process, a cryo-controller (T.R.I research M-2000) is used to read the temperature from a diode, which is glued at the bottom of the cell.

It will take about a day to cool down the whole system to N_2 temperature. Without exchange gas, it would take days. We pump out this exchange gas when N_2 temperature is reached. Then we leak test the cell and the vacuum chamber. After the test, we fill the vacuum chamber with a balloon of helium for thermal exchange, and the system is ready to cool down to helium temperature.

We then transfer liquid He. At the beginning, the system is so warm that the liquid evaporates immediately, it can accumulate in the dewar. At this stage, we transfer slowly in order to use helium vapor to cool the system down. The temperature is again monitored by the diode. As the temperature drops, we increases the transfer speed. The helium gas in the vacuum chamber has to be pumped out at temperatures above 10 K, it would be difficult to pump out later.

The helium gas used to fill up the cell is taken from two sources: from the liquid helium main bath, or from a helium gas cylinder. The pressure of the liquid helium bath is maintained at around 770 torr, slightly higher than the atmospheric pressure to prevent air from leaking in. To reach a pressure higher than 1 atm, we usually use a pressured helium gas cylinder (99.995% purity). For both cases, we let the helium gas go through a liquid nitrogen cold trap.

We often encounter the problem that the filling tube gets stuck after running the experiment for a few months. As the helium gas used went through a nitrogen cold trap, the plug must have a melting temperature below 77 K. We have found that a big perturbation, such as He transfer, or a slight increase

of the top plate temperature (from 5 K to 7 K, for instance), helps to open the plug. Thus the plug must be close to the top plate of the cell, and quite soft, its melting temperature must be low. Checking the melting temperatures above 4 K for all kinds of solids, hydrogen has the lowest, 14 K. We therefore suspect that the plug is made of solid hydrogen, although we do not know where it comes from.

After filling the cell, we regulate its top plate, and let the whole cell relax to equilibrium. Since the diffusion time L^2/κ can be as long as many hours, we normally shorten the relaxation time by making use of convection: heat the bottom plate first, then let it relax freely. The pressure and the temperature of the bottom plate are monitored by a chart recorder. When the bottom plate temperature stabilizes, we measure the pressure of the cell and the temperatures of both plates and calculate the density. The density has to be measured at temperatures higher than the gas-liquid coexistence one so that there is only gas in the cell (or low enough so that there is only liquid).

The gas pressure in the cell is measured with an absolute pressure transducer (MKS corp.). For this cell, we have mainly used two transducers 227A and 222B of ranges 1000 torr and 5000 torr respectively. The 227A one is temperature regulated, the accuracy is 0.15% of the reading, and the temperature coefficient for the zero is 0.08 torr/K. In our measurement of small pressures, the zero is always corrected before measurement. The 222B one is labeled to have an accuracy of 0.5% of the reading, temperature coefficient for the zero 0.5 torr/K. We have calibrated it against the helium gas-liquid coexistence curve given by McCarty and find that it reads 3% less. This 3% has been corrected in our measurement.

After the helium gas density is measured, we close both the control valve

in the liquid helium, and the valve at room temperature. The density in the cell is then fixed, and ready to operate at a particular convection state.

2.2.3 Temperature regulations

To achieve good temperature stability, the top plate of the cell was built with a thickness of 6 cm. A resistance of 35 Ω (made out of manganin wire) is wrapped around it and served as the heater for the regulation. Two thermistors are embedded in the top plate. One is used for the temperature control feedback system, while the other for the temperature measurement. The resistance from the first thermistor is compared with a set resistance by a LR-110 resistance bridge (Linear Research Co.) The output of this bridge is connected to a LR-130 temperature controller. The block diagram is shown in fig. 7. Once a temperature is set, the top plate responds within half a minute to a stability of one mK. We were unable to get rid of a 2 mK amplitude, 2 hours period oscillation.

The bottom heater of the cell, the driving force for the convection experiment, is made out of 75 Ω of manganin wires, which is uniformly laid on the outer surface of the bottom plate and glued with stycast for good thermal contact. The power to the heater is provided by a current source (Keithley 220). It can provide a maximum current of 100 mA, with accuracy 0.01 mA. For a current larger than 100 mA, a Kepco power supply is used. Four leads are connected to the heater, two for the current and two for the voltage. Since the temperature coefficient of manganin is very small, the resistance reading is essentially the same from room temperature to 4 K.

The top plate temperature is normally regulated around 5 K. It can not be too low for two reasons: first, for most of the studies, we want the convection cell to satisfy the Boussinesq approximation, i.e, same fluid properties from

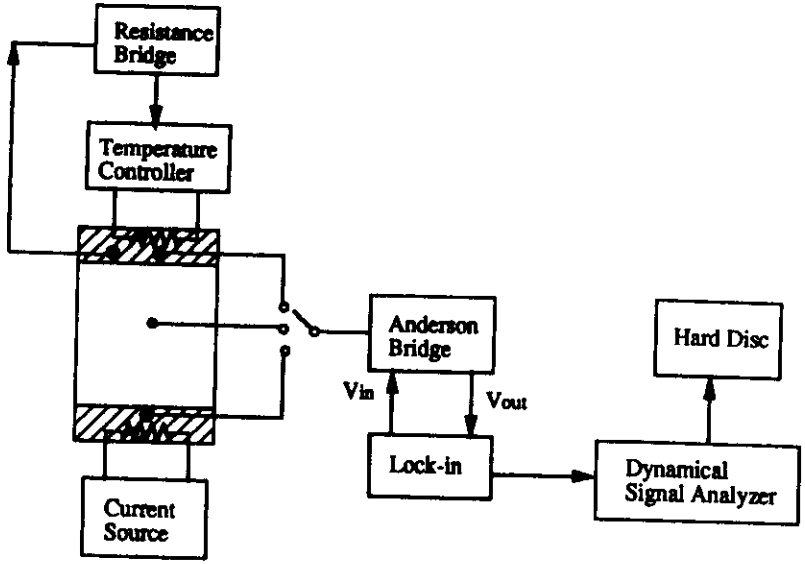

Figure 7. The block diagram. It illustrates the basic logic for temperature regulation, measurement and data acquisition.

top to bottom of the cell. Therefore the top plate has to be regulated at high enough temperature in order to be far away from the gas liquid coexistence line. Secondly, the top plate temperature has to be high enough to keep the total heat flux larger than the one applied at the bottom of the cell, in order for the regulation to work.

On the other hand, the top plate temperature can not be too high: In this experiment, it is because of the the small diffusivities and large expansion coefficient at low temperature, we can achieve a high Ra. Also, the liquid helium evaporation increases at higher top plate temperature.

The two thermistors used to measure the top and bottom plate temperatures are Germanium resistance sensors (Lake Shore 2000T). They have been calibrated by the company within 1 mK. When the cell is at equilibrium, we compare the two thermistor readings (at the same time the pressure is measured to determine the density). The top plate regulated, the bottom plate should relax to the same temperature as the top one in the ideal condition. Experimentally, an off-set Δ_0 of -0.6 ± 1.7 mK has been measured. The lower bound of the temperature difference Δ is limited by this offset. We always work with Δ larger than 50 mK to have an error smaller than 4%. There is also an upper limit for Δ. To avoid non-Boussinesq effects, Δ can not be too large compared to the average temperature (5 K). Also too large a Δ will bring up the average temperature so that there is no gain in Ra. Our values of Δ are always between 50 mK and 700 mK.

Let us give some estimates on the heating power. As we shall discuss later, Nu is approximately proportional to $Ra^{1/3}$, so the actual heat flux Q

$$Q \approx \chi \frac{\Delta}{L} \times Ra^{1/3} \quad . \tag{2.5}$$

Since the thermal conductivity χ is independent of the gas density in ideal gas

approximation,

$$Q \propto \Delta^{4/3} \rho^{2/3} \quad . \tag{2.6}$$

Experimentally, to cover a temperature range between 60-600 mK, heating power of 0.2 - 5 mW are needed for a density 5×10^{-5} g/cm^3 ($2 \times 10^5 < Ra < 1 \times 10^6$), 5 -120 mW for a density 9×10^{-3} g/cm^3 ($3 \times 10^9 < Ra < 4 \times 10^{10}$). The maximum power applied for this cell is about 300 mW (see table 3).

Once the density in the cell is fixed, a unique convection state can be reached by regulating the top plate and applying a DC heating power to the bottom one. It will take a few minutes for the cell to stabilize. The larger the Nu, the shorter time it takes. The gas density and the top and bottom plate temperatures lead to unique physical constants ν, κ and α, so they fully determine Ra and Pr, which characterize the convection state.

2.3 Measurement

Most of the measurements are temperature ones: for the top and bottom plates and local measures in the flow. The basic idea is to measure the resistance of a temperature dependant semiconductor. This resistance is measured with a bridge designed by Anderson(1973). In turbulence experiments, the signal to noise ratio is essential. However the voltage applied across the detector. thus the signal amplitude is limited by self heating at low temperature. In an ordinary bridge, the thermal noise of reference resistors at room temperature is the major source of noise. In the Anderson bridge, most of the components are low noise transformers, the only reference resistor R_s is in a feedback loop, which eliminates the thermal noise from R_s (fig. 8). The noise comes mainly from the thermal noise of the thermometer at helium temperature. Thus bridge provides a factor of 100 improvement in signal to noise ratio, compared

to the standard room temperature bridges. Experimentally, our noise level is about $10^{-9}V/\sqrt{Hz}$, close to the estimate $\sqrt{4kTR}$, provided T = 4 K and R = 1 KΩ . The maximum signal is around $10^{-5}V/\sqrt{Hz}$ provided by an excitation current of $6\mu A$. Thus the signal to noise ratio is 4 decades in amplitude, or 8 decades in power.

The bridge design (fig. 8) consists essentially of a double ac potentiometer in which the current through the reference resistor R_s (10 KΩ used) is automatically maintained at a constant value. The voltage across the thermometer R_T is ratio transformed and compared with the voltage across R_s. The voltage difference is amplified by a lock-in amplifier. The mean thermometer resistance is read directly from the null setting of the ratio transformer T_2, and the temperature fluctuations are given by the output of the Lock-in amplifier, set in the flat-band-pass filter mode. We use two bridge systems to measure two temperature sensors simultaneously. The two systems are almost identical except channel 1 uses EG&G 124A lock-in amplifier and Gertsch 1004R ratio transformer, and channel 2 EG&G 5207 and Gertsch RT-18R. Both the top and bottom plate temperatures are measured by the first one.

To find the maximum excitation current without self-heating, we have measured the bolometer resistance with various excitation current in the fluid at rest. For currents up to 6 μA we do not observe any self heating. With this current, the power dissipated by the bolometer is about 4×10^{-8} watts. The excitation voltage to the bridge is provided by the same Lock-in amplifier which does the measurement. Since the turbulent signals can be as high as several hundred Hz, the excitation source frequency has to be several KHz or higher. However, too high a frequency may cause problems such as capacitance effects. So we choose it to be around 3 KHz. The specific frequency is chosen to avoid the mixing of the excitation voltage frequency and the power supply

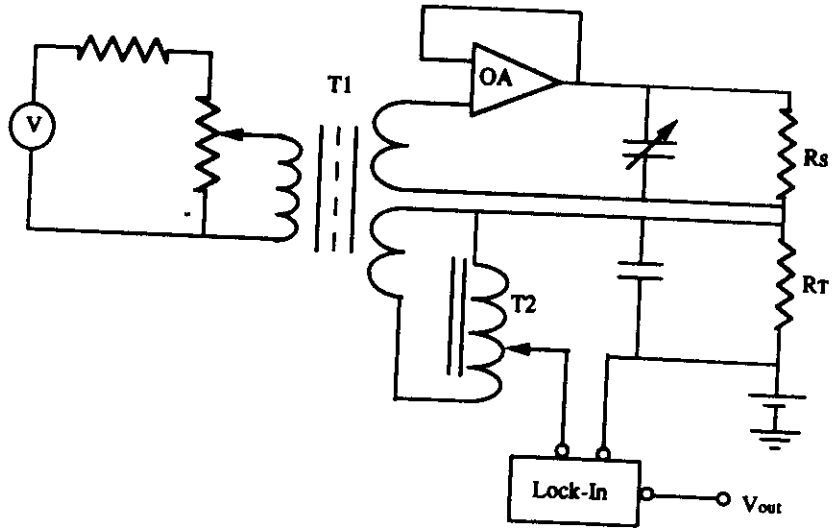

Figure 8. Anderson Bridge.

line frequency (60 Hz) and have the cleanest background in the measurement frequency range .

The thermistors for the top and bottom plate temperature measurement have typical resistance of about 2 KΩ at 4 K, sensitivity of about 1 mK/Ω. The are calibrated by the company, a fitting curve is given.

The first thing to measure in the experiment is the heat transport efficiency. For pure conduction, the heat flux Q is the thermal conductivity χ times the temperature gradient Δ/L. Once convection starts, the heat transport becomes more efficient. The Nusselt number Nu is defined as the actual heat transported normalized by that which would be conducted by the gas, i. e.

$$Nu = \frac{Q}{\chi\Delta/L} \quad . \tag{2.7}$$

The temperature drop Δ is measured from top and bottom plates. The heat we applied to the bottom plate of the cell is calculated from the current source reading and the resistance. To get the actual heat transported by the gas, one needs to subtract the part conducted by the side wall. We have measured the heat flow as a function of the temperature difference Δ for an empty cell:

$$Q_{wall} = 2.3 \times 10^{-3}\Delta \quad , \tag{2.8}$$

here Q_{wall} is in the unit of mW and Δ in mK. Q_{wall} can also be estimated as $1.9\times10^{-3}\Delta$ from the stainless steel thermal conductivity at 5 K, 3 $\mathrm{mWcm^{-1}K^{-1}}$, and the cell geometry: height and diameter 8.7 cm, wall thickness about 2 mm. Let us compare with the heat conducted by the helium gas. The helium gas conduction is about 0.1 $\mathrm{mWcm^{-1}K^{-1}}$, the cross section is $\pi D^2/4$. Therefore the gas conduction is $6.8 \times 10^{-4}\Delta$. The side wall conduction is important at low Nu regime, becomes less important as Nu increases with Ra. In the Nu calculation, the heat conducted by the side wall has been subtracted from the total heating power.

Bolometers of 0.2 mm cubes are used to measure the local temperature fluctuations, their sensitivity around 4 K is about 2 mK/Ω. They are originally made for measuring the infrared background radiation (Mather 1982; Lange *et al.* 1983). These bolometers are made from Arsenic doped Silicon. The crystals are cut and contact treated at Goddard Space Flight Center. Brass wire of 50 μm diameter are attached to the two gold coated surfaces of the 200 μm cubes by Mr. Jesewski in Prof. Hildebrand's group (Enrico Fermi Institute, the University of Chicago).

To fix a bolometer inside the cell, we suspend two parallel insulator coated manganin wires (diameter 125μm, about 1 cm apa) across the cell, and attach a small spring to each wire to maintain the ten ion at all temperatures (fig. 9 (a)). Two copper coated superconducting wire (diameter 114 μm) are wrapped and glued to the manganin wires with stycast. and bent to be parallel to the manganin wires. They serve as support for a bolometer and its brass leads. The other ends of the superconducting wires go through the stycast seal and are then connected to a classical 4 wires connection, which goes up to room temperature (manganin wires are used). Since the electric leads are very fragile, it is not easy to handle. Later we improve the technique by fixing a bolometer on a frame (about 1 cm) made of the same kind of manganin wire, and fix the frame to the two parallel wires in the cell (fig. 9 (b)). When changing a bolometer position, we usually just dismount the frame. We did not see any visible motion of the bolometer when we blow air.

The bolometers are calibrated by comparing them to the thermistors of the top and the bottom plates. Usually about 9 points are taken for a temperature range between 4.2 K and 6 K. Then a 3rd order polynomial is used to fit the $R(T)$ relation for each bolometer. The fitting precision is better than 1 mK. From the fit, the temperature T and the sensitivity dT/dR can be computed.

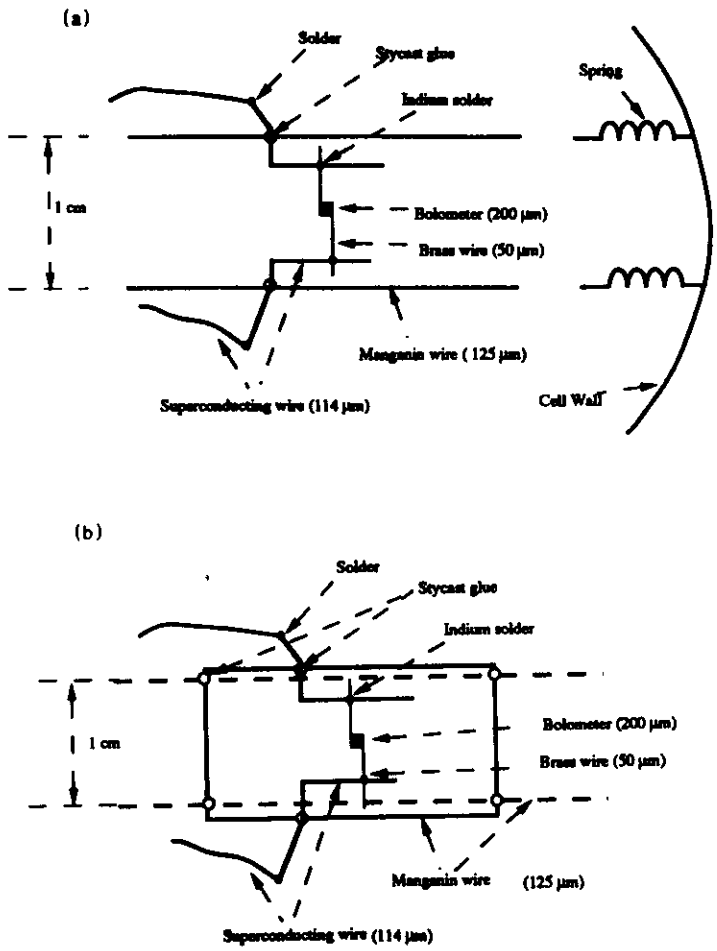

Figure 9. The bolometer mount. (a) two parallel wires across the cell, (b) The bolometer on a frame.

The resistance of the bolometer at 5 K is about 1 KΩ (around 10 Ω at room temperature), the typical sensitivity can be as large as 3 mK/Ω at 6 K, and as low as 1 mK/Ω at 4 K. The calibration curve is repeatable after thermal cycles, but we normally calibrate a few points each time.

2.4 Data acquisition

The output voltage from the bridge is proportional to the resistance variations. The sensitivity of the lock-in amplifier is chosen such that the largest signal amplitude is close to the full range: -10 V to 10 V. The ratio transformer is adjusted such that the center of the fluctuations is around zero. The output voltage is digitized by a HP 3562A Dynamical Signal Analyzer (DSA) (fig. 7). The DSA can digitize an analog data and store it into a hard disc, take Fourier transform, probability distribution function (PDF) and other statistical analysis from either on-line analog data or stored digitized data.

To include all the information in a signal, a sampling frequency has to be at least a factor of 2 of the highest frequency present in the signal. The DSA has set the factor to be 2.56 (HP 3562A Operating Manual & Programming Manual). We first sample a turbulence signal at a very high frequency and take its power spectrum. From this power spectrum, we find out the maximum frequency for which the signal to noise ratio is above one. To have all the information, a frequency slightly higher than the maximum one is entered to the DSA and it automatically samples at 2.56 times it. Experimentally, we often take another measurement at 1/10 the first frequency span to have good statistics and resolutions for low frequencies. The DSA has a anti-aliasing pre-filter to filter out any signal higher than the frequency we select. So even though there are still signals beyond the frequency span we choose, the sampled

data will not be distorted. The DSA can be set from 10.2 mHz to 100 KHz. Frequency spans in this mode are predefined; if a value other than one of these is entered for the span, the analyzer selects the next higher available value.

The resolution of the DSA is 2^{16}, that means the smallest signal it resolves is $1/2^{15}$ of the full range (with one bit for the sign). Thus the maximum dynamical range is $\log_{10}(2^{15})$, i. e. 4.5 decades in amplitude, or 9 decades in power spectrum. Coincidentally, this range is very close to the signal (with excitation current 6 μA) to thermal noise ratio (noise of the bolometers).

The DSA has two channels, which can take data simultaneously. Before digitizing, we have to decide the size of the data, and create a file (called throughput file) in the hard disc. The file sizes vary from tens to hundreds of records (here each record has 2048 points), depending on the sampling time and frequency. When the DSA is digitizing, the hard disc is connected to it to store data. The digitized data are arranged as ABABAB....., here A is a record of 2048 data points of channel 1, and B is for channel 2. From a digitized number V_N in disc, the original data V_{in} can be read out as

$$V_{in} = -4/3 * V_N * (range)/26028.55 \quad . \tag{2.9}$$

For most of the data taken, the range is set as 10 Volts to match the full range of the lock-in amplifier output.

The digitized data is temporally stored in hard disc and tranferred to an (HP 1/4-inch 16 track) cartridge tape, each of which contain about 60 Mbytes of data. The tapes are operated by a HP9144A tape driver. The tapes are rather convenient to write and read in HP system, but we had a hard time transferring the files to other computers. A computer which has access to both the general network and HP-IB cables (for instance Macintosh), may make the transfer easier.

The power spectrum measurement shows the signal in the frequency domain. It is computed by multiplying the FFT of the signal by its complex conjugate. The FFT is done for every record of 2048 points, the final power spectrum is the average of the transforms of all the records in the data file. For FFT over a finite period of time, a proper window has to be introduced to reduce the edge effects. We have selected the Hanning window. The Hanning window has the disadvantage of some amplitude inaccuracy(up to 1.5 db) and the advantage of great frequency resolution.

A power spectrum given by the DSA has 800 frequency points. In a log-log plot of a power spectrum, the zero frequency point is omitted. The DSA output directly $P_i * \Delta f$, where P_i is the digitized power spectrum $P(f)$ in units V^2/Hz. In principle, the normalization relation should be

$$\langle V^2 \rangle = \int_0^\infty P(f)df = \sum_{i=1}^{800} P_i \Delta f \quad , \tag{2.10}$$

here $\langle V^2 \rangle$ is the mean of temperature square. However because of the Hanning window, the sum should be corrected by a factor of 1.5. Experimentally, the ratio between the left hand side and the right hand side is found to be: 1.54 ± 0.08. Since the mean of a signal is arbitrary in our experiment, depending how we balance the bridge, the DC component of a power spectrum is non-intrinsic. Therefore, the power spectrum should be normalized by either the variance $\sigma^2 = \langle (V - \langle V \rangle)^2 \rangle$, or the above sum without the first point. Experimentally, the ratio between this two is 1.44 ± 0.07, and we just treat it as an empirical constant. In all the relevant discussion later, the power spectrum are normalized by the sum without the first point.

The cross spectrum is computed by multiplying the complex conjugate of the linear spectrum of channel 1 by the linear spectrum of channel 2. It shows the amplitude product of the two linear spectra and the phase difference

between them. The coherence is just the amplitude of the cross spectrum normalized by the geometric average of the two power spectra. The coherence is measured on a scale 0 to 1.

The histogram measurement shows how the amplitude of the input signal is distributed between its minimum and maximum values, which are ±12.6 Volts when the range is set as 10 Volt. Between the minimum and maximum values, 256 bins have been divided. The histogram is just the number of data points falling into each bin and its sum should be the total number of data points. The probability distribution function (PDF), computed by normalizing the histogram, is a statistical measure of the probability that a specific level occured.

$$1 = \int_{-\infty}^{+\infty} H(x)dx = \sum_{i=1}^{256} H_i \Delta x \quad , \tag{2.11}$$

where H_i is the digitized PDF $H(x)$ and Δx is $2 \times 12.6/256$

2.5 Experiment for the aspect ratio 0.5 and 6.7 cell

Both cells are cylinders of diameter 20 cm. Because of the different lateral size, a new dewar and thus a different set up was needed. The whole system, including the convection cell and the dewar, has been built by International Cryogenic Inc., Indianapolis, Indiana. Fig. 10 is the experimental system used for aspect ratio 6.7 and 0.5 cells. Compared with the previous one, it has very similar cryogenic structures, temperature regulations, measurement and data acquisition techniques. Thus we will only give brief descriptions. However, given its size, it is much harder to cool down and vacuum seal, thus I shall discuss those aspects in more detail. The sketch of the whole set up is given in fig. 11.

2.5.1 The convection system

The aspect ratio 0.5 and 6.7 cells use the same set up except for the side walls of the cells. To be specific, let us discuss the first cell of aspect ratio 0.5, thus of height 40 cm. Since *Ra* is proportional to the cube of the height of the cell L, large *Ra* can be reached with a large L. A maximum *Ra* of 1×10^{15} can be reached in this cell. A small aspect ratio cell consumes less liquid helium, simply because the heat flux is proportional to the cross section. However, the side wall must have bigger influence on the bulk turbulence flow in a small aspect ratio cell. Balancing the physics (i.e. the side wall effect) and the economy (i.e. the liquid helium consumption), the aspect ratio has been set to be 0.5, cell diameter 20 cm, height 40 cm. The maximum input power is about 2 watts (the corresponding liquid helium evaporation rate is about 4 liter/h.). The side wall of the cell is made from stainless steel of thickness about 1.5 mm. The top and bottom plates are made from OFHC copper. The top plate has a thickness of 6 cm and the bottom one 2 cm. The top and bottom plates are connected to the side wall with indium seal by 12 screws. I suggest to double the number for future experiments to enforce the seal. The vacuum chamber has a diameter of 23 cm and height 48 cm. The thermal impedance between the cell top plate and the helium bath has the same structure as in the previous system.

The bottom heater has a resistance of 127.8 Ω (Minco heater), which is glued with GE-vanish to the outer surface of the cell bottom plate. The heater is further pressed by a thin stainless plate to assure good contact. The resistance of the heater is temperature independent. It is measured with four leads. The power is provided by a Keithley 220 current source, or by a Kepco power supply. The voltage is measured with a Keithley 197 voltmeter. Let us

(a) (b)

Figure 10. The photography of the experimental system for the aspect ratio 6.7 and 0.5 cells. (a) shows the aspect ratio 6.7 cell, all the cryogenic and electric connections. (b) shows the vacuum chamber (left) and the convection cell.

give some idea about the heating power: for Δ value between 60 mK and 600 mK, 1 mW - 15 mW are needed for a pressure of 1 torr; 30 mW - 460 mW are needed for a pressure of 600 torr (see. table 5)

The top plate was regulated by a LR-130 resistance bridge and a LR-110 temperature controller. The heater for the top plate regulation is a piece of manganin wire of a resistance 35 Ω. Two germanium thermistor are embedded in the top plate, one for regulation, another for temperature measurement. A diode glued to the bottom of the cell is read by a T-2000 cryo-controller (T.R.I. Research) for monitoring the temperature when warming up or cooling down.

The two thermistors (Lake Shore 2000T Germanium) for the top and bottom plate temperature measurement are calibrated. The sensors for local temperature measurements are the same bolometers as in the previous experiment. The set-up and procedures for temperature measurement and data acquisition are the same.

The electric leads for the bolometers in the convection cell are fed through a hole on the bottom plate of the cell. The hole is sealed with stycast. For all the electric leads to come out the vacuum chamber, two thin stainless steel tube of diameter about 1 cm diameter are soldered to the top of the vacuum chamber and extended to the top of the dewar. A bellows is connected to each of the tube to absorb stress when cooling down or warming up. For a large system, a slight mismatch of thermal expansion coefficient causes large stress. In this system, the mismatch between the stainless steel and the G-10 supporting tubes have made cracks on the solder joints, until the bellows were used. Two 48 bin connectors are used at the end of the tube for the wires to come out at room temperature. One tube is sealed, another is connected to the pump system to pump the vacuum chamber.

The helium gas is taken from either the liquid helium bath or from a pure

helium gas cylinder. Before it enters the cell, the gas passes through a nitrogen cold trap. The gas is filled into the cell through a tube of inner diameter 1.5 mm. The tube of coiled shape in the liquid helium bath is then wrapped around the top plate of the cell to pre-cool the helium gas before it enters the cell. The diameter of the filling tube is chosen such that the perturbation to the cell is small, but should be large enough to fill a 13 liter cell at low temperature in a reasonable time, hours. We did not have the low temperature control valve used in the previous experiment, in order to decrease the impedance. Even though, filling is still a problem, especially when more and more "ice" accumulated in the tube. For future experiments, I suggest a safety valve being installed in the cell. The filling tube is closed and opened at the top of the dewar. Although the cell is only closed at room temperature, no acoustic oscillations are present. In fig. 11, the basic structures are sketched.

The same absolute pressure measurement transducers are used to measure the helium gas pressure (For low pressure in the aspect ratio 6.7 cell, a transducer of 10 torr range has been used to achieve better precision.)

The whole system described above, the cell and the vacuum chamber, is supported in a liquid helium dewar by three fibre-glass G-10 tubes of a diameter 0.5 inches (fig. 11). The dewar is a so called super-insulation dewar. The advantage of such dewar is that no liquid nitrogen is needed. A rigid foam fill the dewar neck to buffer the cold helium from the room temperature. The aluminum cover of the dewar is rubber O-ring sealed. When the experiment is not running, the liquid helium evaporation rate is about 5 liters per day.

The outer diameter of the dewar is about 55 cm and the overall height 140 cm. We design this dewar to contain 90 liters of L-He, in order for the systems to work continuously for one day at the largest heating power(4 liter/hour). To have such a large volume in a reasonable dimensions, the dewar has a small

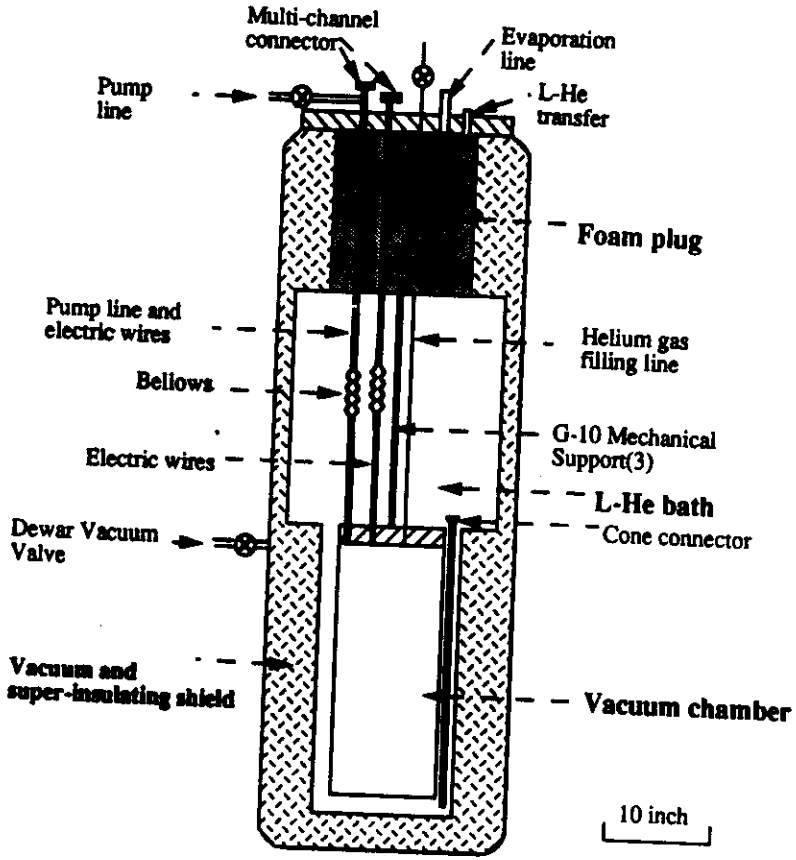

Figure 11. The sketch of the experimental system. This is for the aspect ratio 0.5 and 6.7 cell

diameter for the neck and the bottom part, a larger diameter for the interior reservoir. The neck has a diameter 27 cm, height 36 cm. The bottom part has a diameter of 27 cm and height 56 cm, so there is a 2 cm gap, or 9 liters between the vacuum chamber and the dewar. The interior reservoir has a diameter of 46 cm and height 41 cm. The helium level is measured via the resistance change of a superconducting wire. The wires starts from the top of the vacuum chamber, it is calibrated such that it reads the height of L-He above the top plate of the vacuum chamber. One centimeter corresponds to 1.6 liter, according to the geometry of the cell.

2.5.2 Leak test and cool down

After the leak test at room temperature, we put the whole system into the dewar and get ready to cool down to N_2 temperature. We fill the vacuum chamber with a balloon of H_2 for thermal exchange, then the dewar with about 70 liter of L-N_2. The temperature at the bottom of the cell is monitored with the diode. After the system reaches equilibrium, we push L-N_2 out of the dewar. It is important to push out all the L-N_2 before further cooling down to He temperature. The L-N_2 gets out via a tube, which extends down to the bottom of the dewar at one end, with a cone structure at the other end to match a G-10 tube from the top of the dewar. This tube is fixed to the outside of the vacuum chamber (fig. 11).

The system has to be leak checked again at L-N_2 temperature. Leakage is a common problem in low temperature experiment, because of the large shrinkage when a system experiences a temperature drop from room temperature to low temperature. A large system is more vulnerable to leak since the shrinkage is proportional to the system size. Most of the leakage occur when

a system is cooled down from room temperature to L-N_2 temperature. If it survives at L-N_2 temperature, it is likely to work at He temperature.

To check the seal of vacuum chamber, we first use the leak detector to pump out the N_2 gas, then fill the dewar with Helium gas and wait for the leak detector's response. If it is fine, we check the cell, by connecting the leak detector and filling the vacuum chamber with helium gas. Some helium gas is needed anyhow for thermal exchange while cooling down to He temperature. If unfortunately, there are leaks, we have to warm it up to room temperature, flush and pump the system several times until the helium level is low enough to be leak test again. In case the leak disappears at room temperature, we connect the leak detector to the cell or vacuum chamber, immerse the whole system into a L-N_2 open container (we used a garbage can) and wait for the system to reach L-N_2 temperature. Then we gradually lower the L-N_2 level and spread the helium gas at the same time. The leak should be near the L-N_2 level when the detector begins to scream. We were always able to spot and fix the leaks eventually.

If there is no leak at N_2 temperature, we cool the system down to He temperature. The first transfer of L-He is much more tricky than daily transfer. It is efficient to cool the system down by letting liquid helium or cold helium gas to start from the bottom of the dewar. The tube which was used to push L-N_2 out from the bottom, will be used to transfer helium. We insert a vacuum tube along the G-10 tube, and connect it to another vacuum tube from a L-He reservoir dewar. The L-He is transferred slowly in order to cool the system down by cold helium gas first. The transfer rate is about 2 ft^3 of gas /min (1 liter of liquid = 25 ft^3 of gas). The temperature is monitored with the diode. At about 10 K, we speed up the transfer, and starts to pump the vacuum chamber. Once the vacuum chamber is pumped, the diode at the bottom of

the cell is decoupled from the temperature of the dewar. We can not know whether there is any L-He accumulating on the bottom of the dewar, until the L-He level reaches the top of the vacuum chamber (there is about 10 liter of space around and below the chamber). It was a long anxious waiting time. We had good reason to be anxious about: sometimes after more than 1 hour elapsed and 30 liters of L-He used, the L-He level meter still gives null reading. If I had to start over again, I would measure the temperature at the bottom of the dewar or measure the L-He level from there. L-N_2 left in the dewar is one of the major problem at the final stage of accumulating L-He. Normally, the system should be in L-He temperature in 4-5 hours.

For daily L-He transfer, the tube should not extends all the way to the bottom as for the initial one. Thus, we replace the long G-10 tube by a shorter one which is slightly above the L-He level.

2.5.3 The aspect ratio 6.7 cell

Large He consumption prevents us from having both large aspect ratio and high Ra. For instance, if the cell diameter is fixed at 20 cm, an aspect ratio 0.5 cell has a height 40 cm, reach the highest Ra of 10^{15}; an aspect ratio 6.7 cell has a height of 3 cm, reach only $Ra = 10^{11}$. But if we want both the highest $Ra = 10^{15}$, and the aspect ratio 6.7, then the diameter has to be 260 cm, 13 times larger than the previous 20 cm. Consequently, the L-He consumption has to be 169 times more, which we certainly can not afford.

In order to use the experimental system of the aspect ratio 0.5 cell, the diameter of the cell is chosen to be 20 cm. To reach a Ra around 10^{11}, a reasonable high value, the cell height L is chosen to be 3 cm. For this aspect ratio 6.7 cell, only the 3 cm height side wall is new, the rest of the experimental system, like the top and bottom plates of the cell, the vacuum chamber, the

dewar, the temperature regulations and the electric c nections etc. are the same. Since the vacuum chamber is made for the cell of 40 cm height, a 37 cm high column of space is left unoccupied. The top plate has a thickness of 10 cm, which is a large thermal mass for this 3 cm high cell. Given all that, the temperature regulation achieved is the best of the three.

CHAPTER 3

MAIN EXPERIMENTAL RESULTS

The experimental results are organized chronologically.

3.1 The aspect ratio 1.0 cell

To study thermal turbulence, we have measured the heat transfer efficiency (characterized by Nu) and local temperature fluctuations signals. Nu is deduced from the measurements of heat flux, the temperature of the top and bottom plate. Local temperature signals are measured with bolometers of 200 μm size at various points in the cell. A bolometer, placed about a fraction of a millimeter above the bottom plate, scans across the thermal boundary layer when Ra is changed. Bolometers at the center of the cell measure the turbulent temperature fluctuations without direct influence from the large scale flow. Pairs of bolometers at midheight of the cell and various radial positions, give information on the large scale velocity and the effect of lateral boundaries.

The cell is of diameter 8.7 cm, Ra spans a range from 10^3 to 10^{12} (we limit our discussion on scaling relations for Ra up to 10^{11} where the Boussinesq approximation holds). The local temperature measurement indicates that there is a turbulence transition at $Ra = 4 \times 10^7$, from soft turbulence below to hard turbulence above. The PDF for the temperature fluctuations at the center is exponential for hard turbulence, while Gaussian for soft turbulence. Its rms

value scales with Ra differently in the two regimes. All the side wall bolometers show this change as well. The large scale velocity measured by the side bolometers changes differently in soft and hard turbulence. The signals detected by the side bolometers indicate that in soft turbulence, warmer fluid ascends and colder fluid descends through connected channels, while in hard turbulence, there are only individual warm and cold particles, called plumes. The frequency power spectrum shows no inertial range in soft turbulence, and an extending power law with an exponential cut-off for hard turbulence, up to $Ra \approx 10^{11}$. Nu in hard turbulence scales with Ra with an exponent 0.285, significantly different from the classical theory.

3.1.1 Heat transport and thermal boundary layers

When dealing with electrical conduction, the first thing to measure is the current I as a function of voltage V. From its $I - V$ curve, one is able to deduce some information about the material. In studying thermal turbulence, the first physical quantity to study is the heat transport through the cell. If the temperature drop Δ is an analog of the voltage drop across a resistor, the heat transport is equivalent to the electric current. We treat the convection cell as a black box, and from the relation between the heat transport and the temperature drop Δ, we get some information about the flow. As defined in equation 2.7, Nu is the heat actually transported by the gas, normalized by the heat that would be conducted. It describes the efficiency of the turbulent heat transport. The total heating power is calculated from the heater resistance and the voltage applied across it. To get the actual heat transported by the gas, one needs to subtract the part conducted by the side wall (eq. 2.8)

Figure 12 shows the experimental Nu as a function of Ra. The corresponding data are listed in table 3. For a cell of given aspect ratio, any physical

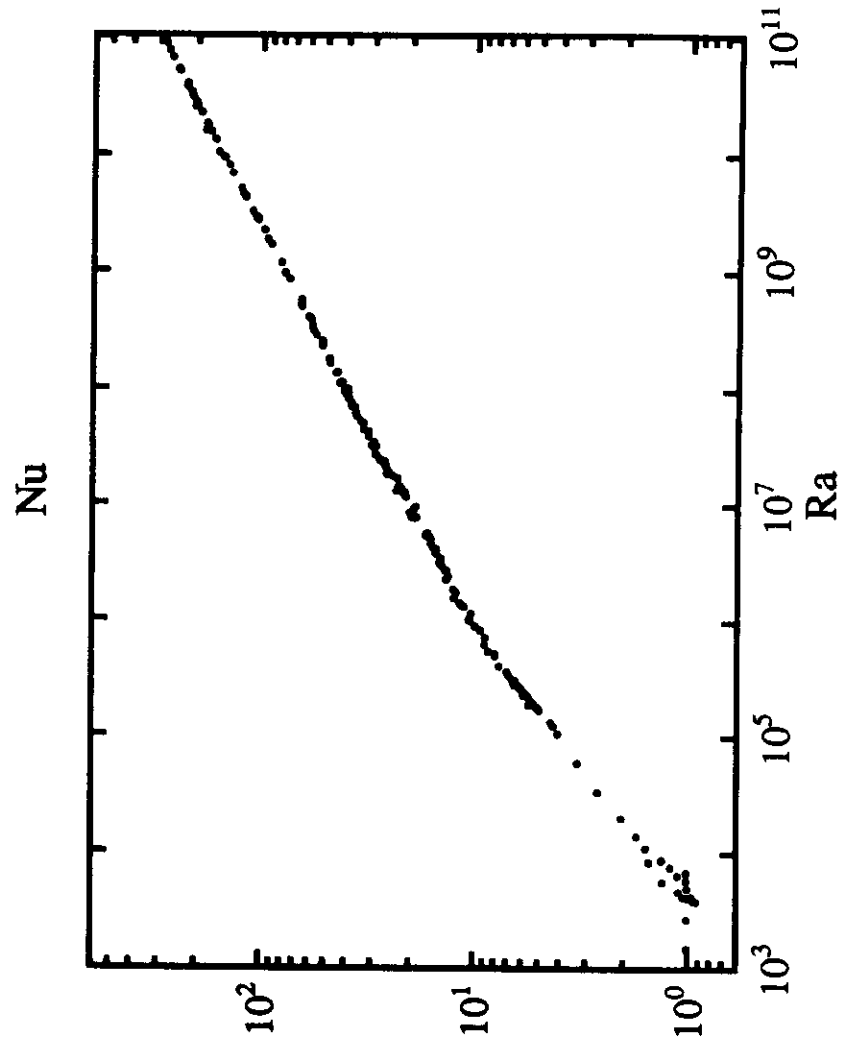

Figure 12. Nu vs. Ra for the aspect ratio 1.0 cell.

quantity will only be a function of Ra and Pr. Pr in the whole range of Ra is plotted in fig. 13. It does not change until $Ra = 10^9$. At high Ra, as shown in fig. 13, different values of Pr are possible, depending on densities. Since they do not introduce discontinuities in the Nu (fig. 12), its Pr dependence must be weak.

For Ra below 5×10^3, Nu is equal to 1. According to the definition, the heat is purely transported by conduction. The theoretical value for the onset Ra is 1700 (Chandrasekhar 1961). However, in small aspect ratio cells, the side wall plays an important roll in the onset value, as well as the Nu - Ra relation just above the onset (Behringer & Ahlers 1977; Charlson & Sani 1975).

Above $Ra = 5 \times 10^3$, Nu becomes larger than 1. This indicates that the fluid motion develops and then enhances the heat transport. To amplify possible changes, $Nu/Ra^{0.285}$ is plotted against Ra in fig. 14. From this plot, it is clear that there are changes for $Ra = 1.2 \times 10^5, 1.2 \times 10^6, 6.0 \times 10^6$ and 4×10^7. These transitions will be understood better with local flow information. The change at $Ra = 1.2 \times 10^5$ agrees with other observations (Malkus 1954; Goldstein & Chu 1969; Krishnamurti 1973; Threlfall 1974), but we observed none below this value while many more have been reported. As one can see from this plot, there is no single power law for $Ra < 4 \times 10^7$. The previous reported (Wu *et al.* 1988) scaling relation of $Nu - 1 \approx Ra^{0.333}$ for soft turbulence ($5 \times 10^5 < Ra < 4 \times 10^7$) is only an approximation.

For $Ra > 3 \times 10^7$, Nu follows a simple power law with Ra:

$$Nu = 0.22 \times Ra^{0.285 \pm 0.004} \quad . \tag{3.1}$$

This power law extends to the largest Ra reached in this cell. A simple scaling relation between Nu and Ra indicates that the flow is in a self-similar state for $Ra > 4 \times 10^7$. In other words, the flow structures are invariant, only the

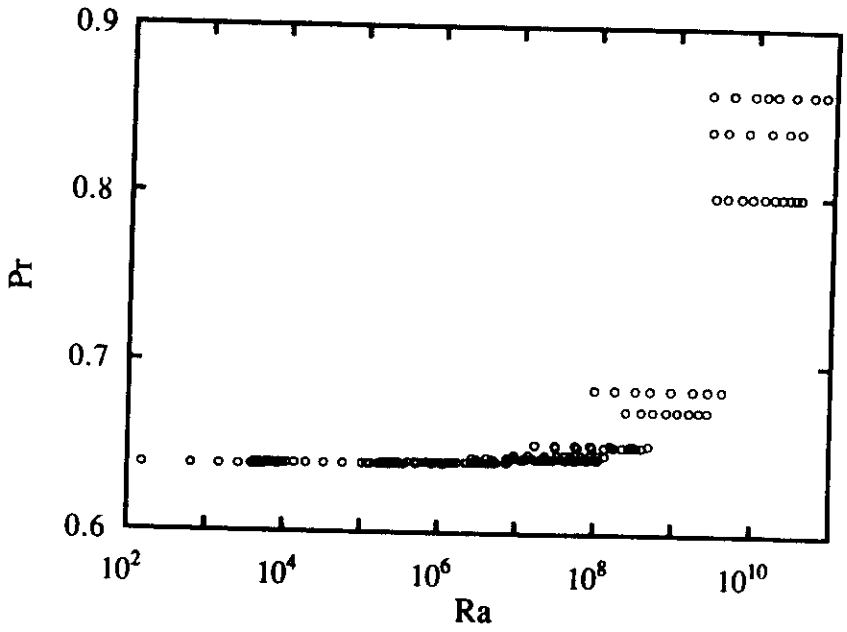

Figure 13. Pr vs. Ra. The Prandtl number Pr for various Rayleigh numbers Ra, which correspond to different densities.

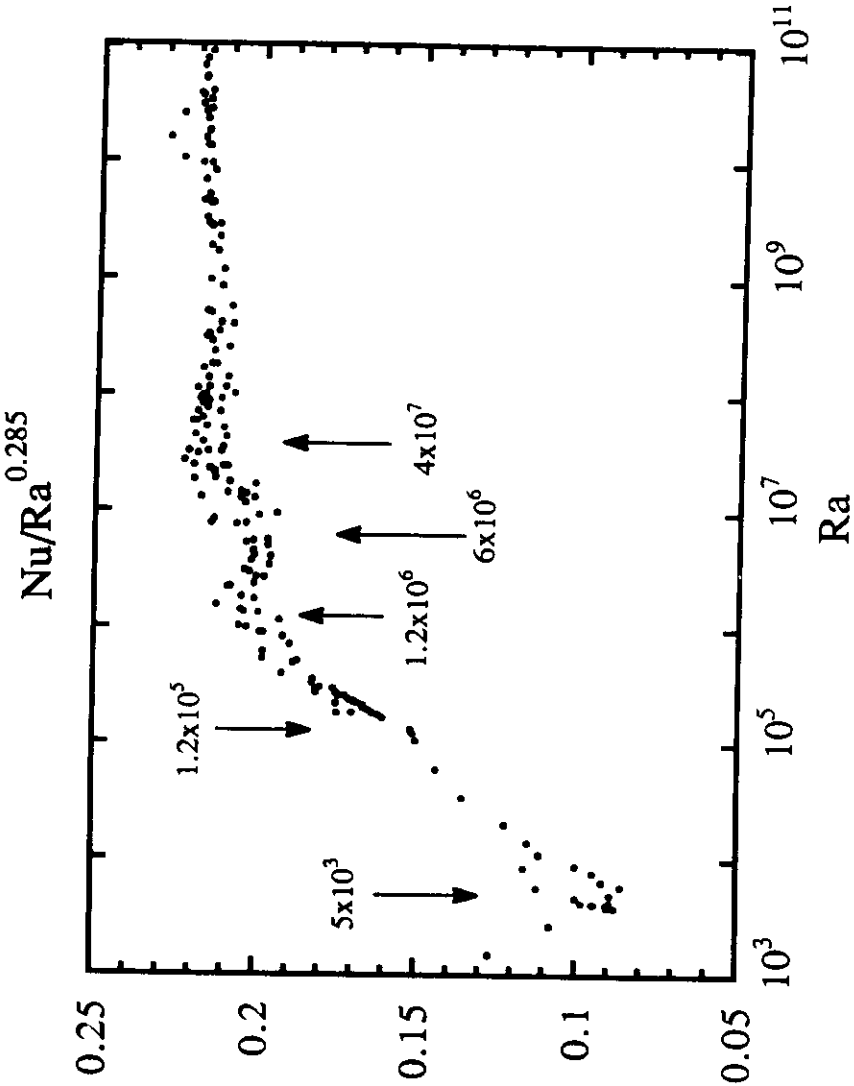

Figure 14. $Nu/Ra^{0.285}$ vs. Ra.

time scale and length scale of the flow motion change. By the flow structure, we mean the large scale structures, such as the thermal boundary layers, the side wall regions etc. The self-similarity of the large scale flow structure does not prevent the small scales from being different, since they do not influence the heat transport directly.

In the bulk of the flow, the heat is transported by convection, which is much more efficient than conduction. However there are two well defined boundary layers next to the top and bottom plates, where the velocity is small and the heat is mainly transported by conduction. Thus the bulk region is a thermal short circuit, and all the temperature drop Δ is across the two layers, $\Delta/2$ for each one (Tritton 1988). Let us call their thickness λ. Since the heat flux is transported across the two boundary layers by conduction,

$$Nu = \frac{L}{2\lambda} \ . \tag{3.2}$$

Nu is equal to 1 for $Ra < 10^4$, and 300 for $Ra = 10^{11}$. Therefore λ decreases to a minimum value 0.15 mm.

The boundary layer profile has been measured directly (Gross *et al.* 1988), but not in our experiment. Instead, a bolometer has been positioned a fraction of a millimeter above the bottom plate. It scans the boundary layer as λ changes with Ra.

Figure 15 shows the fluctuating signals, the PDF and power spectra inside ($Ra = 6 \times 10^8$, $Nu = 66$) and outside ($Ra = 4 \times 10^{10}$, $Nu = 220$) the boundary layers respectively. Inside the boundary layer, the hot temperature fluctuations come from the fluid closer to the bottom plate, which is less active than the fluid from above. Therefore the PDF is sharply cut in the hot side and extended in the cold side. Outside the boundary layer, the colder fluctuations are due to thermals from the remote top plate and the hotter ones are from

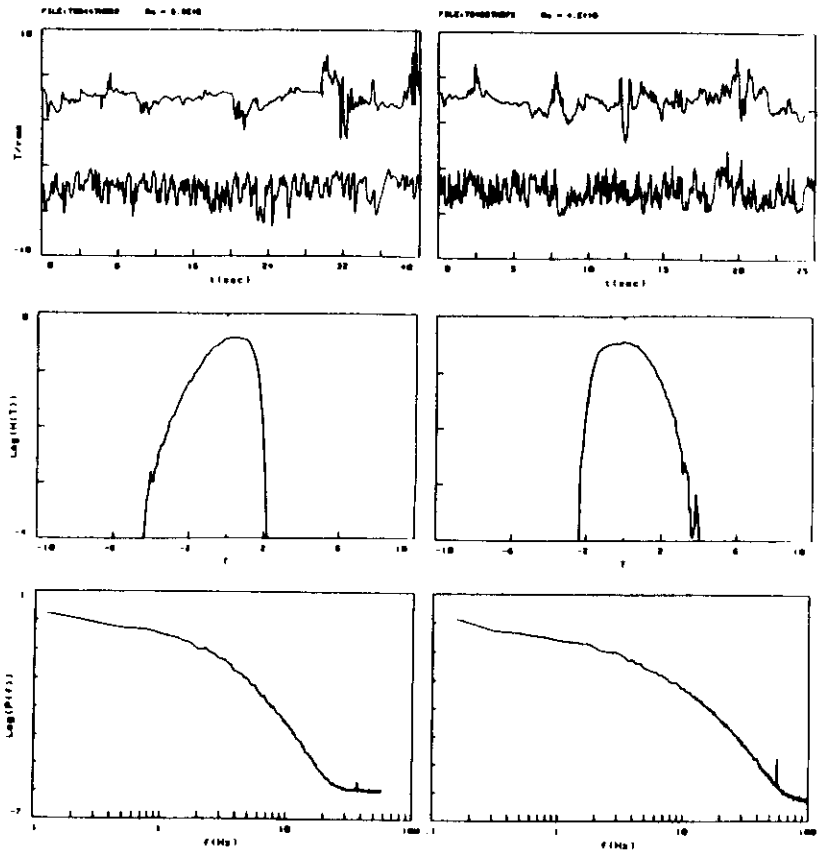

Figure 15. Time series, PDF and power spectra for the bottom bolometer inside and outside the boundary layer. (Left) for $Ra = 6 \times 10^8$, $Nu = 66$ inside, and (Right) for $Ra = 4 \times 10^{10}$, $Nu = 220$ outside the boundary layer.

the nearby bottom plate. Therefore the PDF outside the boundary layer has a more extended distribution to the hotter side. From the evolution of the PDF, we have learnt that the bolometer crosses the boundary layer when $Ra = 4 \times 10^9$, $Nu = 120$ and the corresponding λ is 0.4 mm ($L/2Nu$). Thus the height h of the bolometer above the plate must be 0.4 mm.

We have measured the rms temperature fluctuations Θ_b with the bottom bolometer. Figure 16 (a) shows Θ_b/Δ as a function of Ra. It increases with Ra for small Ra, with a discontinuity at $Ra = 4 \times 10^7$. Reaching its maximum at $Ra = 4 \times 10^9$, it then begins to decrease. The change at $Ra = 4 \times 10^9$ must reflect the bolometer crossing the boundary layer: the bolometer feels bigger temperature fluctuations as it moves out of the boundary layer since the outer part of the boundary layer is more active than the inner part; once out of the boundary layer, it detects the temperature fluctuations of the bulk flow, which decreases as Ra increases. The kink at $Ra = 4 \times 10^7$ responds to a major change of the flow structures: the soft - hard turbulence transition.

The relative depth of the bolometer in the boundary layer is $h/\lambda = 2hNu/L$. Since h and L are fixed, we can derive the boundary layer profile indirectly by plotting $2(T_{plate} - \langle T_b \rangle)/\Delta$ as a function of Nu (fig. 16 (b)), here $\langle T_b \rangle$ is the average bolometer temperature and T_{plate} is the bottom plate temperature. Qualitatively, $2(T_{plate} - \langle T_b \rangle)/\Delta$ increases linearly with Nu first, then reaches 100% asymptotically as the bolometer crosses the boundary layer into the isothermal outer region. The linear regime ends at $Nu \approx 200$, which leads to $h = \lambda = 0.2$ mm. The discrepancy between the values of h deduced from the rms (0.4 mm) and this measurement (0.2 mm), may be due to the finite size of the bolometer (0.2 mm).

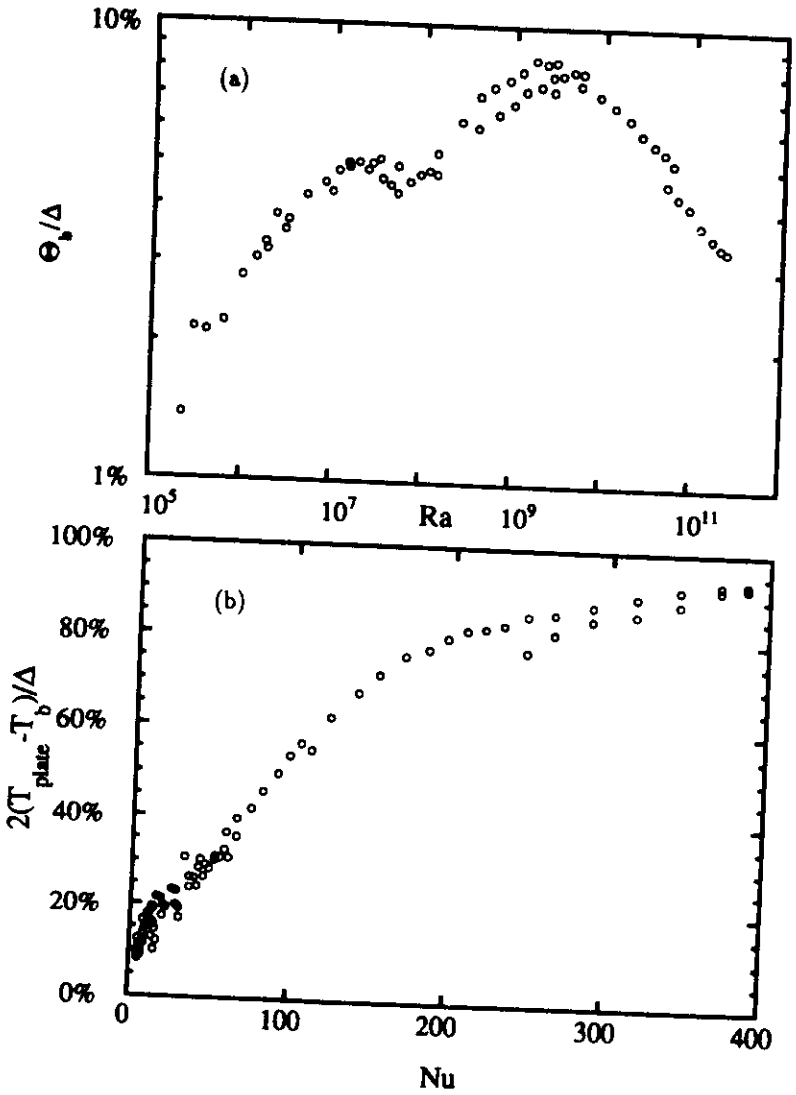

Figure 16. Bottom bolometer, (a) Θ_b/Δ vs. Ra (b) $2(T_{plate} - \langle T_b \rangle)/\Delta$ vs. Nu. Θ_b/Δ is the rms temperature fluctuation, T_{plate} and T_b are the average temperatures of the bottom plate and bolometer respectively.

3.1.2 From the onset of convection to turbulence

Studying Nu and the thermal boundary layers, we have learnt the basic structures of the convection flow. To understand the flow motion in detail, we have to study the local temperature signals measured by bolometers at various points of the cell. Local temperature measurements show that the flow motion changes from conduction to convection, then bifurcates to a limit cycle which leads to chaotic states, and further to turbulence. We shall discuss here the flow motion before it becomes turbulent. This is the range up to $Ra = 5 \times 10^5$.

For $Ra < 5 \times 10^3$, Nu is essentially 1. There is no fluid motion at all. For $Ra > 5 \times 10^3$, fluid motion appears and begins to enhance the heat transport, Nu becomes larger than one. However, no time dependent signal is measured, indicating that the motion is laminar (time independent).

At $Ra = 1.2 \times 10^5$, the first time dependent signals appear in the form of periodic oscillations (fig. 17, (a)). The change at $Ra = 1.2 \times 10^5$ in the $Nu - Ra$ relation (fig. 14) reflects the appearance of time dependent motions. This oscillatory motion was predicted by Busse (1978) as the oscillatory instability for low Pr fluids (Pr of helium gas at this pressure is 0.7). As the oscillatory motion is very pure, the spatial variation modes must be inhibited in this aspect ratio 1.0 cell.

The flow motion becomes chaotic (fig. 17, (d)) soon after the onset of the oscillatory instability. There are three universal routes to chaos (Eckmann 1982): intermittency, period doubling and quasi-periodicity. The first two have been observed in this cell, and are shown in fig. 17, (b) and (c) respectively. Unlike experiments designed to study the transition to chaos (see, Glazier & Libchaber 1988), there is no control on the way the flow motion becomes

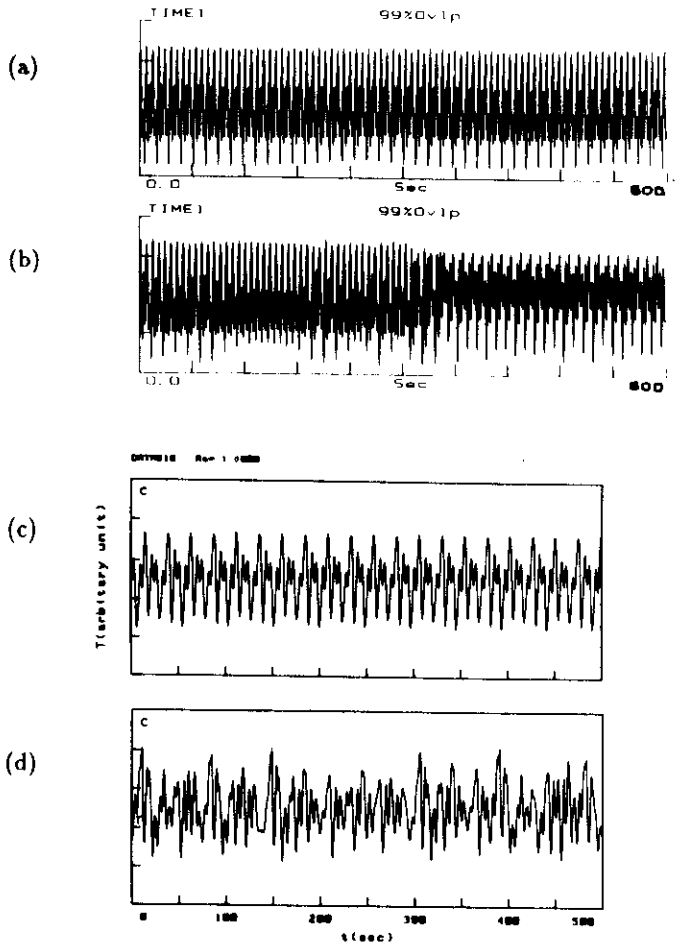

Figure 17. The center time series, the routes to chaos. (a) oscillation, (b) intermittency, (c) period four in the period doubling scenario and (d) chaos.

chaotic in this experiment. We only show their presence on the way flow develops to turbulence.

Despite the bifurcation in the time domain, the signals from the center and the bottom bolometers are strongly correlated. This is shown by their coherence in fig. 18, (a): it is 1 at the fundamental frequency and major harmonics, slightly less than 1 for higher harmonics.

For chaotic signals at $Ra = 1.5 \times 10^5$, the power spectrum is continuous (fig. 19, b), even though the oscillatory frequency is still present with its harmonics. A continuous power spectrum indicates that the flow motion has no temporal correlation and is fully chaotic. However, spatial correlation still exists, the coherence between the center and the bottom bolometers is one at low frequencies (fig. 18, (b)).

As Ra increases, the power spectra extend to higher frequencies (fig. 19 (c) and above). They show already some of the characteristics of turbulence: flat low frequencies followed by a cut-off tail. The difference with turbulence appears in the coherence function, which keeps a large value. As Ra increases, the frequency structure of the coherence function evolves (fig. 18, (c) and above), and its maximum value decrease. It is difficult to understand the changes in the structures, but this scenario is always repeatable. Typical time series of both the center and bottom bolometers are presented in fig. 20, (b)-(d). In fig. 21, we plot the maximum value of the coherence as a function of Ra. At $Ra = 5.0 \times 10^5$, it is significantly less than 1, most of the long range spatial correlations are lost. Thus a turbulent state, a state without temporal and spatial coherence, is present.

In the large Ra range which we will cover, the chaotic state is present in only a small window $1.5 \times 10^5 < Ra < 5 \times 10^5$, and the oscillatory state even a smaller one $1.2 \times 10^5 < Ra < 1.5 \times 10^5$.

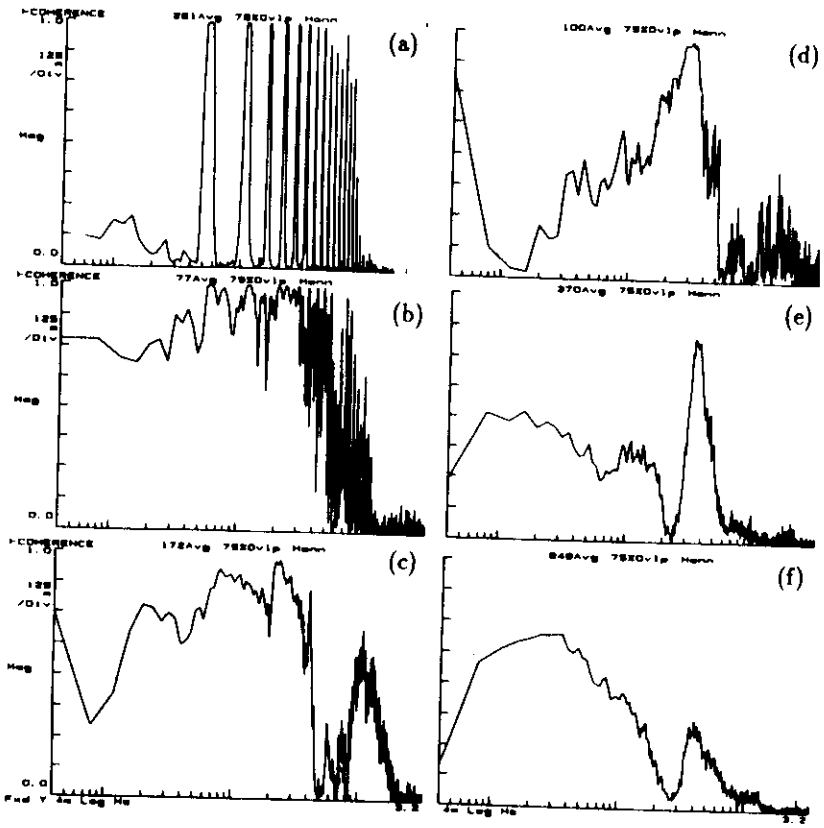

Figure 18. The coherence functions, from chaos to turbulence. Coherence between the center and bottom bolometers for (a) $Ra = 1.2 \times 10^5$, (b) 1.5×10^5, (c) 1.6×10^5, (d) 2.2×10^5, (e) 3.2×10^5 and (f) 4.0×10^5.

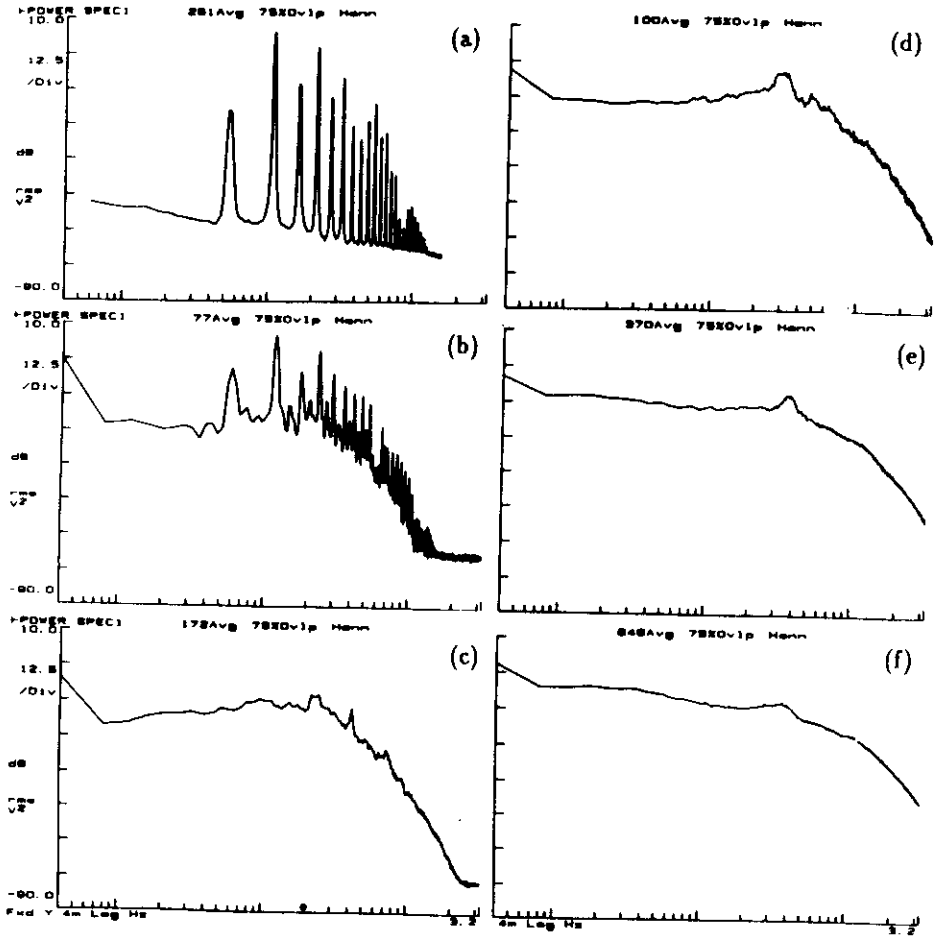

Figure 19. The power spectra, from chaos to turbulence. Power spectra of the center signals for (a) $Ra = 1.2 \times 10^5$, (b) 1.5×10^5, (c) 1.6×10^5, (d) 2.2×10^5, (e) 3.2×10^5 and (f) 4.0×10^5.

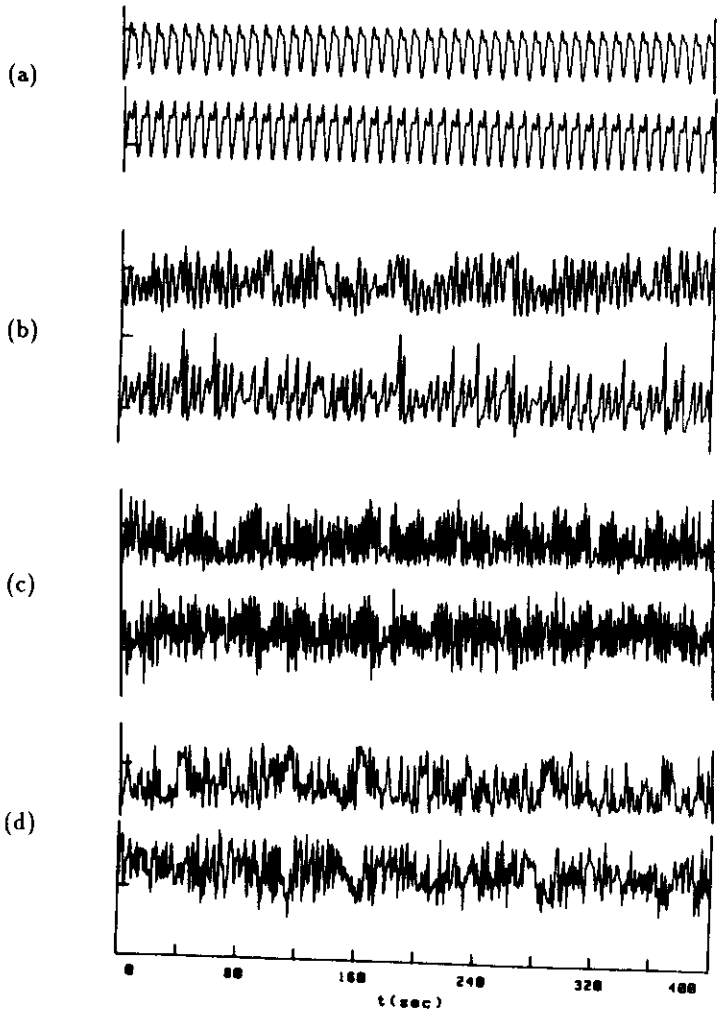

Figure 20. The time series, from chaos to turbulence. The center and bottom time series for (a) $Ra = 1.2 \times 10^5$, (b) 1.6×10^5, (c) 3.2×10^5 and (d) 4.0×10^5. In each pair, the upper one is for the center bolometer.

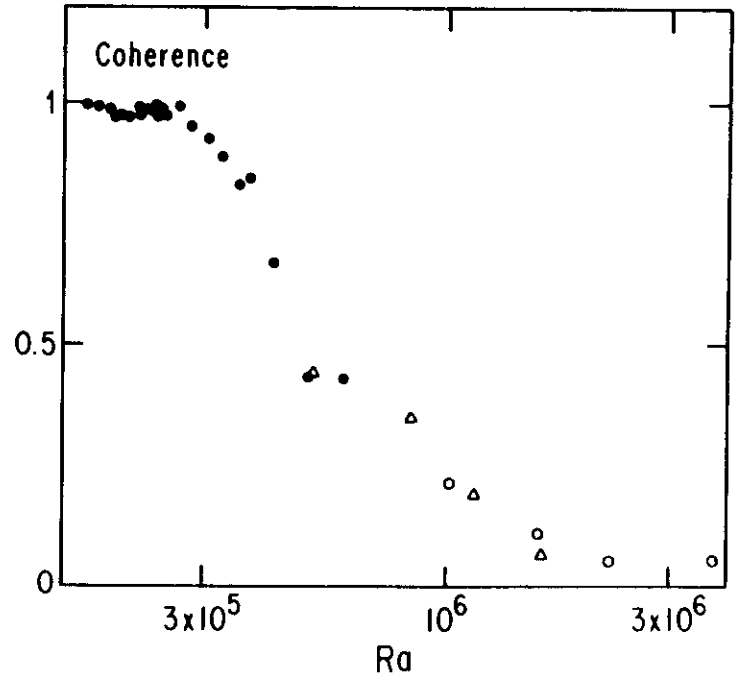

Figure 21. The maximum value of the coherence vs. Ra. It decreases when the flow becomes turbulent.

To understand the changes of the spatial coherence and the transition to turbulence, let us study the temperature signals measured by bolometers near the side wall. The bolometers have been measured to be in the cold descending flow. Figure 22 (a) and (b) are the side bolometers signals at $Ra = 2 \times 10^5$ and $Ra = 5.7 \times 10^5$, both show hot bursts. Imagine that the cold descending flow forms a connected channel, as observed by Chu & Goldstein (1973) and modeled by Lorenz (1963). As the channel becomes unstable, the bolometers inside move out and become exposed to the warmer central region from time to time. These short time exposures causes the hotter bursts, which we suspect, are responsible for the loss of spatial coherence. Figure 23 (b) plots the difference of the average temperature (normalized by Δ) of two bolometers, placed at the two opposite sides of the cell at midheight (refer to fig. 43 (a)). As Ra reaches 2×10^5, it increases up to 30%. This very large horizontal gradient is a signature of connected hot and cold channels. The temperature difference decreases as Ra further increases.

The picture we propose is: For $Ra < 2 \times 10^5$, the flow motion builds up, the horizontal temperature difference increases with Ra. As Ra gets larger than 2×10^5, more complex flow motions (turbulence motion) develop, which reduce both the temperature difference and the spatial coherence.

3.1.3 Soft and Hard turbulence, the transition

The flow is in a turbulent state when there is no more long range spatial and temporal coherence. It can then only be characterized by statistical and average measures. In this section we discuss the difference between soft and hard turbulence, in the aspects of Nu, the large scale flow velocity, the PDF, and the coherence between center and bottom signals.

Figure 22 (b) and (d) give a clear image of the difference between the two

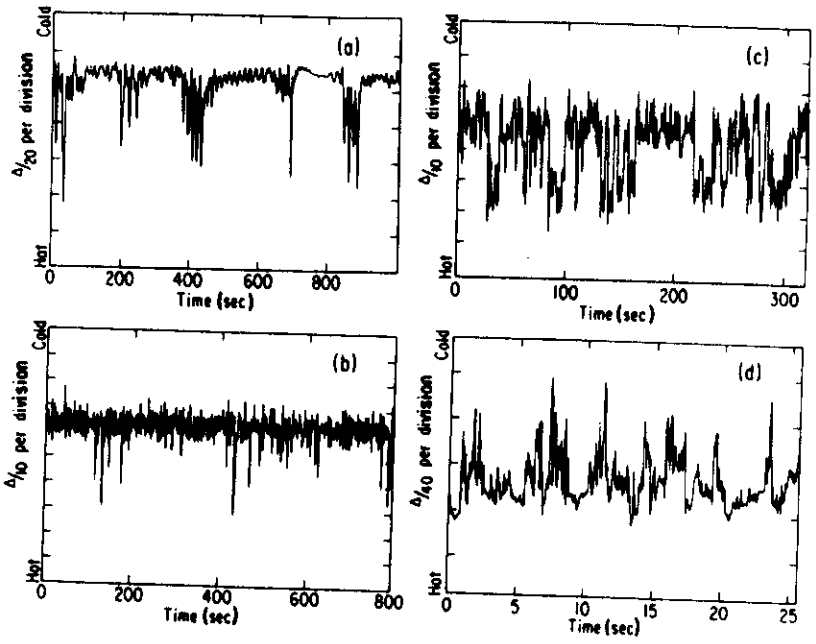

Figure 22. Time series from the side wall bolometer. It is 1.0 cm away from the side, for (a) $Ra = 2.0 \times 10^5$, (b) 5.7×10^5, (c) 5.5×10^6 and (d) 5.0×10^{10}.

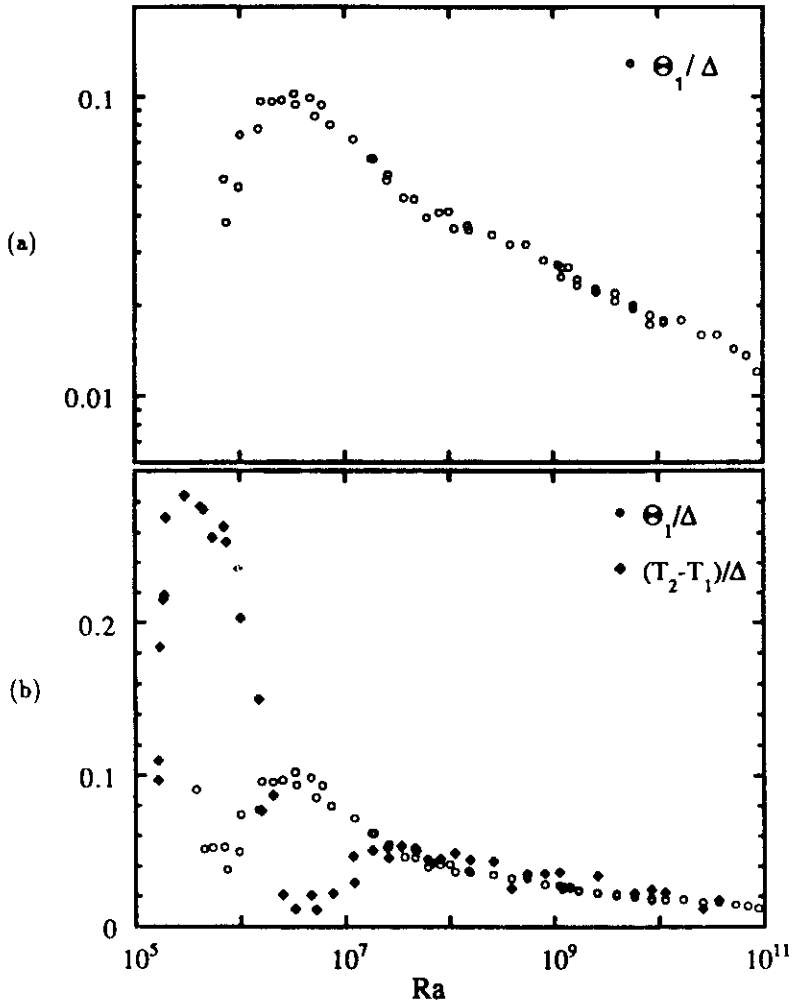

Figure 23. Side wall bolometer, Θ_1/Δ and $(T_2 - T_1)/\Delta$ vs. Ra. (a) The normalized rms temperature fluctuations Θ_1/Δ vs. Ra. (b) Θ_1/Δ (open circles) and the normalized horizontal temperature difference $(T_2 - T_1)/\Delta$ (filled diamonds) are plotted together.

states. For $Ra = 5.7 \times 10^5$, soft turbulence, the bolometer placed on the side sees hot fluctuations on a column of cold descending fluid; for $Ra = 5 \times 10^{10}$, hard turbulence, there is no connected cold flow anymore, but cold thermal plumes advected from the top boundary layer. The dramatic change in the signal at $Ra = 4 \times 10^7$ indicates a major transition in the turbulence flow.

The global measure of the turbulence states, Nu, has already been discussed in section (3.1.1). According to fig. 14, there is one regime for $Ra > 4 \times 10^7$, where Nu scales with Ra, with an exponent 0.285; the other one for $5 \times 10^5 < Ra < 4 \times 10^7$, where there is no simple scaling relation.

The mean velocity of the large scale flow is measured via the correlation of two adjacent bolometers. The velocity is normalized by a velocity scale κ/L (table 4), and plotted against Ra in fig. 24 (a). Notice that this normalized velocity VL/κ is simply $RePr$ ($Pr \approx 1$). For $Ra < 6 \times 10^6$, the normalized velocity increases sharply with Ra. It then slows down for $6 \times 10^6 < Ra < 4 \times 10^7$. For $Ra > 4 \times 10^7$, the velocity simply scales with Ra, with an exponent 0.49.

Turbulence, can be characterized by various statistical quantities. Figure 23 (a) shows the rms value of the temperature signals measured at middle height 1.0 cm away from the wall. A turbulent flow motion has two competing effects on temperature fluctuations: first, it creates the fluctuations; on the other hand, it enhances mixing, thus reducing the temperature differences. Intuitively, the large scale motion is more efficient in creating fluctuations and the small scale ones are more efficient in mixing. For $Ra < 6 \times 10^6$, the temperature fluctuations increase with Ra, this can be understood as the large scale turbulent motion is building up, as observed in the velocity measurement. For $Ra > 6 \times 10^6$, the rms value decreases with Ra, turbulent mixing is becoming dominant. The change of slope at $Ra = 4 \times 10^7$ indicates a change

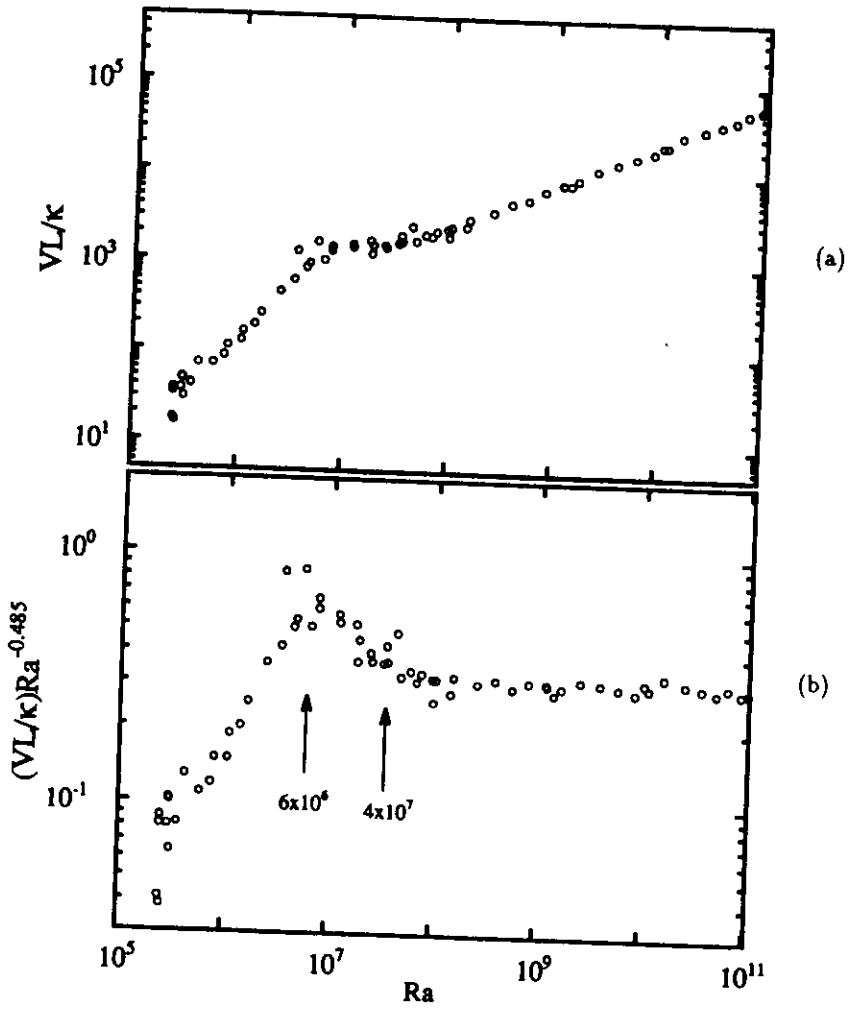

Figure 24. Velocity V, (a) VL/κ vs. Ra and (b) $(VL/\kappa)Ra^{-0.485}$ vs. Ra. VL/κ is the normalized velocity.

of turbulence structure. As already shown in fig.16 (a), the bolometer inside the boundary layer detects a change at $Ra = 4 \times 10^7$ as well.

Now let us look at the probability distribution function (PDF) which include the information of all moments. As the center region of the cell is more homogeneous and symmetric than other parts, we shall discuss the PDF for the temperature fluctuations there. Figure 25 shows six PDFs in the range $2 \times 10^5 < Ra < 2 \times 10^7$. The X-coordinate presents the temperature normalized by the rms value of each PDF, in linear scale, and the Y-coordinate the logarithm of the probability. For small Ra, the state has only a few modes, the PDF is not universal, not even symmetric (fig. 25, (a) As Ra increases, it becomes symmetric and Gaussian-like (fig. 25, (b)-(d)). The PDF becomes exponential-like (fig. 25, (e) and (f)) when Ra reaches 10^7 To visualize this change more clearly, the same PDF are plotted in fig. 26 with the square of the normalized temperature as the X-coordinate, the Y-coordinate unchanged. In this plot, a Gaussian distribution would appear as straight lines.

Contrary to $Ra < 10^7$, the PDF for $Ra > 10^7$ are invariant and exponential, as shown in fig. 27.

A Gaussian distribution can be regarded as the normal one for uncorrelated random motions; The exponential distribution for $Ra > 4 \times 10^7$ indicates that there are strong correlations among those random motions. The invariance of the PDF for $Ra > 10^7$ implies that these correlations are unchanged.

The transition from chaos to turbulence is characterized by the sharp drop of spatial coherence, now let us look at the coherence between the center and the bottom bolometers in the turbulence regime. Figure 28 shows the coherence function for six Ra values between 5.2×10^5 and 3.0×10^{10}. The coherence continues to decrease for $Ra > 5 \times 10^5$, and to zero at $Ra \approx 10^7$. However, for $Ra > 10^8$, a peak in the coherence appears. The peak frequency

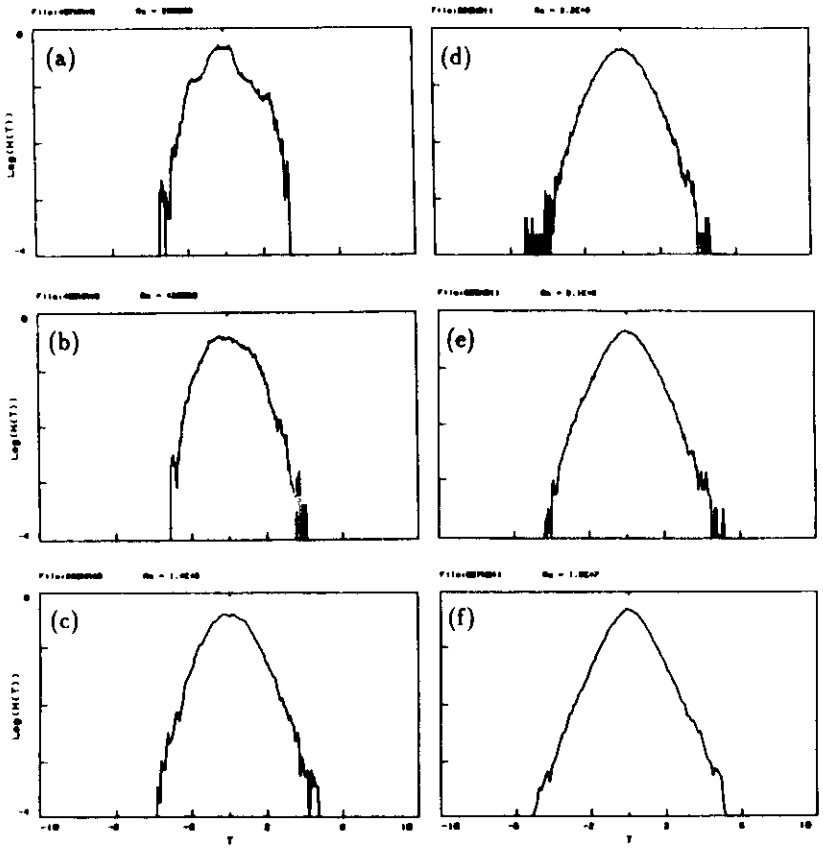

Figure 25. Soft turbulence, $\log(H(T))$ vs. T. The center PDF for (a) $Ra = 2.9 \times 10^5$, (b) 4.2×10^5, (c) 1.4×10^6, (d) 3.2×10^6, (e) 8.1×10^6 and (f) 1.5×10^7. The X-coordinate is the temperature normalized by the rms value of each PDF, in linear scale, the Y-coordinate is the logarithm of the probability.

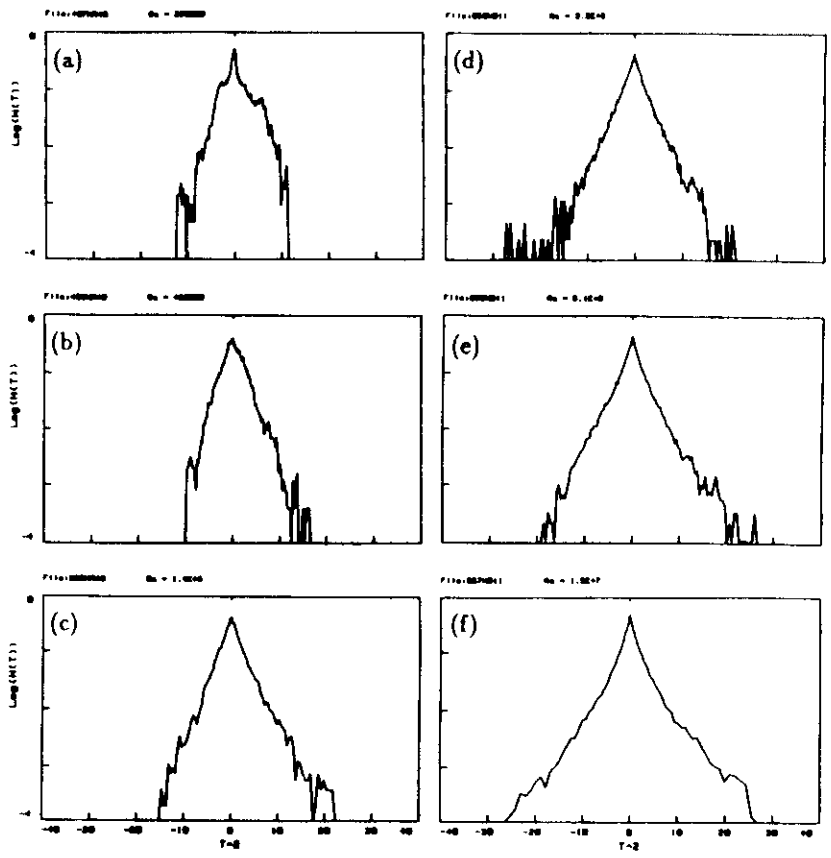

Figure 26. Soft turbulence, $\log(H(T))$ vs. $\pm T^2$. The same PDF as in the previous figure. The X-coordinate is the square of the normalized temperature, with the sign of the linear temperature.

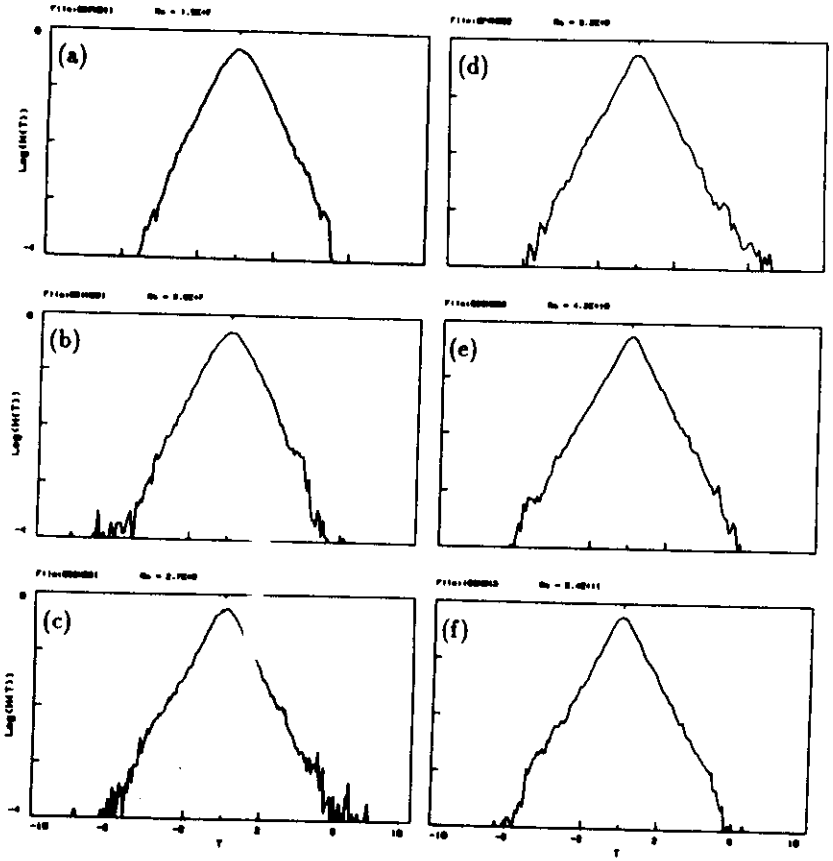

Figure 27. Hard turbulence, $\log(H(T))$ vs. T. The center PDF for (a) $Ra = 1.5 \times 10^7$, (b) 3.6×10^7, (c) 2.7×10^8, (d) 3.2×10^9, (e) 4.2×10^{10} and (f) 5.4×10^{11}. The X-coordinate is the linear temperature, normalized by the rms, the Y-coordinate is the logarithm of the probability.

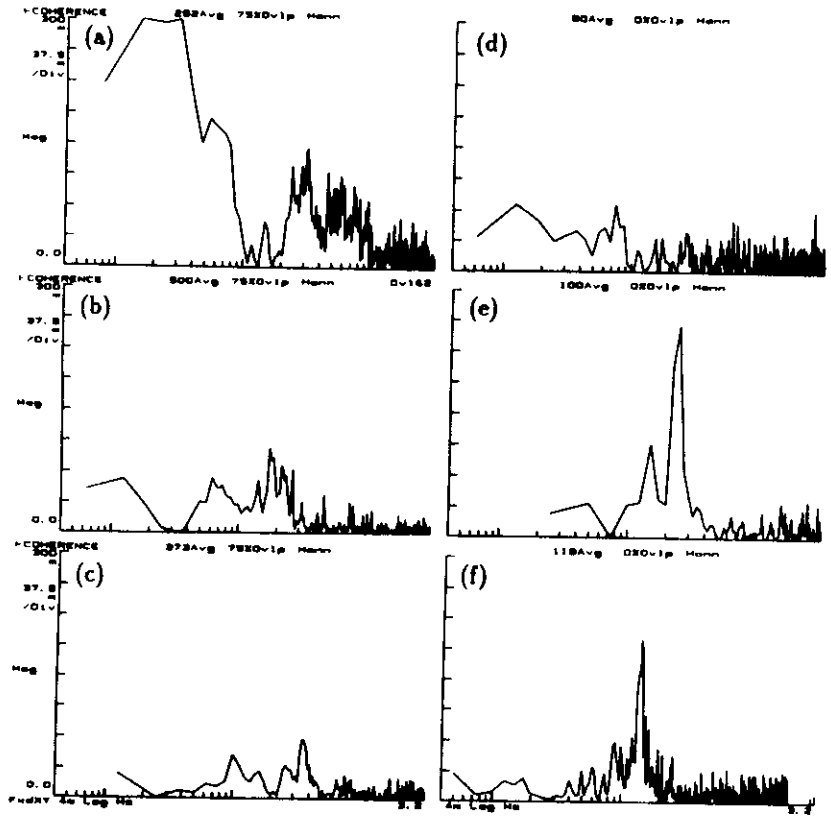

Figure 28. Coherence function: from soft to hard turbulence. Coherence between the center and bottom bolometers, for (a) $Ra = 5.2 \times 10^5$, (b) 6.8×10^5, (c) 2.7×10^6, (d) 2.5×10^7, (e) 5.0×10^8 and (f) 3.0×10^{10}.

is always at about 0.2 ± 0.1 Hz. Let us call it f_p (in some of our previous papers, ω_p is used, which is $2\pi f_p$). f_p will be shown later to be related to the size of the cell. In fig. 29, the power spectra of the center (a) and bottom (b) signals and their coherence (c) for $Ra = 1.7 \times 10^9$ are presented, they show clearly a resonance peak at f_p. The re-appearance of coherence is another signature of a new turbulence state in $Ra > 10^8$.

A final distinction between the two turbulent states is that for $Ra < 10^8$, the power spectra show no power law dependance with frequency; whereas above, a power law is present, starting at f_p as shown in fig. 29 (a).

In conclusion, the time signal from the wall region shows a dramatic turbulence transition around $Ra = 4 \times 10^7$. Nu, the large scale velocity and the rms fluctuations change behavior at this Ra. For $Ra > 4 \times 10^7$, they all have simple scaling relations with Ra; the temperature fluctuations at the center of the cell have an exponential distribution; a spatial coherence peak appears at a low frequency f_p; a power law in the power spectrum of the center bolometer signal extends from f_p. This self-similar turbulence state for $Ra > 4 \times 10^7$ is named hard turbulence. The state below it soft turbulence (Heslot *et al.* 1987).

3.1.4 Soft turbuler e

Soft turbulence, ranges from $Ra = 5 \times 10^5$ to 4×10^7, is characterized by complex large scale structures, and lack of energy cascade. We do not have a good understanding of this state. The behavior of soft turbulence and the soft-hard turbulence transition probably depend on the cell geometry.

Soft turbulence can be even divided into two substates in this cell, below and above $Ra = 6 \times 10^6$. For $5 \times 10^5 < Ra < 6 \times 10^6$, Nu (fig. 12 and fig. 14), velocity Vl/κ (fig.24 (a)) and the normalized rms temperature fluctuations Θ_1/Δ (fig. 23 (a)) increase sharply with Ra; the horizontal temperature

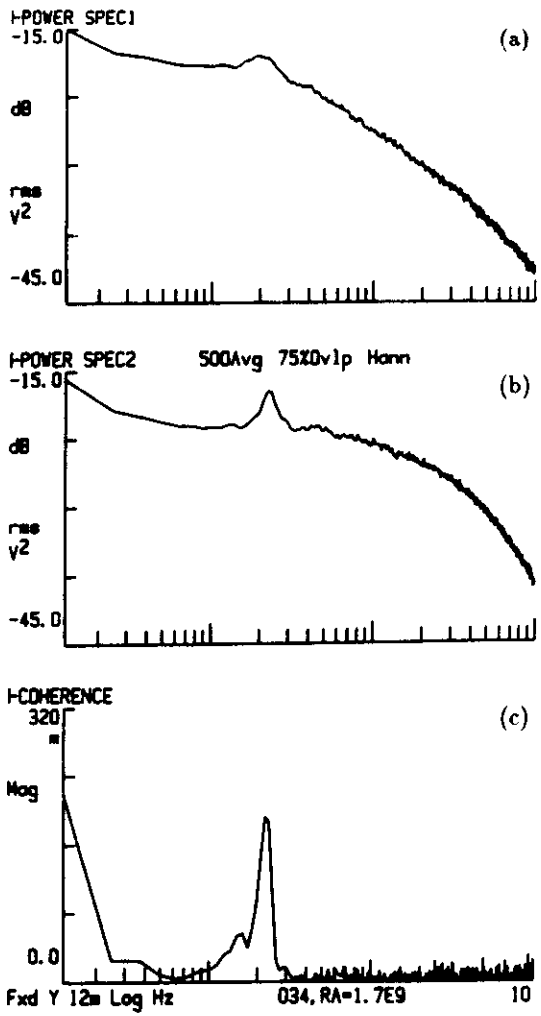

Figure 29. Hard turbulence, the center and bottom power spectra and their coherence. (a) The center power spectra, (b) the bottom one and (c) their coherence for $Ra = 1.7 \times 10^9$. Notice the resonant peak at f_p.

gradient $(T_2 - T_1)/\Delta$ (fig. 23 (b)) decreases from a large value; The coherence between the center and the bottom bolometer (fig. 28, (a) & (b)) is small but finite; the side wall bolometer in the descending flow shows hot spikes on a random background (fig. 22 b). This is a transient range from chaos to turbulence.

For $6\times10^6 < Ra < 4\times10^7$, the flow motion changes its large scale structure, and small scale ones begin to develop. This explains that for increasing Ra in this range, Vl/κ stops increasing (fig.24 (a)), Θ_1/Δ start decreasing (fig. 23 (a)). The two level switching in the time signal of the side wall (Fig. 22 (c)) can be interpreted as two flow structures of different average temperatures detected by the bolometer. $(T_2-T_1)/\Delta$ increases slowly from zero (fig. 23 (b)). The complete loss of spatial coherence (fig.28, (c) & (d)) shows the complexity of the spatial structures.

Now let us look at measurements from the more symmetric central region of the cell. The time signals at $Ra = 4.2\times10^5$ and 4.6×10^6 have no qualitative difference (fig. 30 (a), (b), (e) & (f)). They fluctuate constantly without any intermittence and characteristics. The PDFs are shown (fig. 25 and fig. 26) to be Gaussian, which indicate that turbulent flow structures are essentially independent of each other. Six power spectra for $2.9\times10^5 < Ra < 5.2\times10^7$ have been shown in fig. 31. All the power spectra in soft turbulence have a flat low frequency part with an exponential-like high frequency cut-off tail. The lack of a power law indicates that there is no energy cascade from large to small scales. The power spectra for different Ra can be superposed together with only translational transformations in log-log plot (fig. 32 (a)) Thus the cut-off tail is invariant and can be described by one characteristic frequency f_h,

$$P(f) = g(f/f_h) \ . \tag{3.3}$$

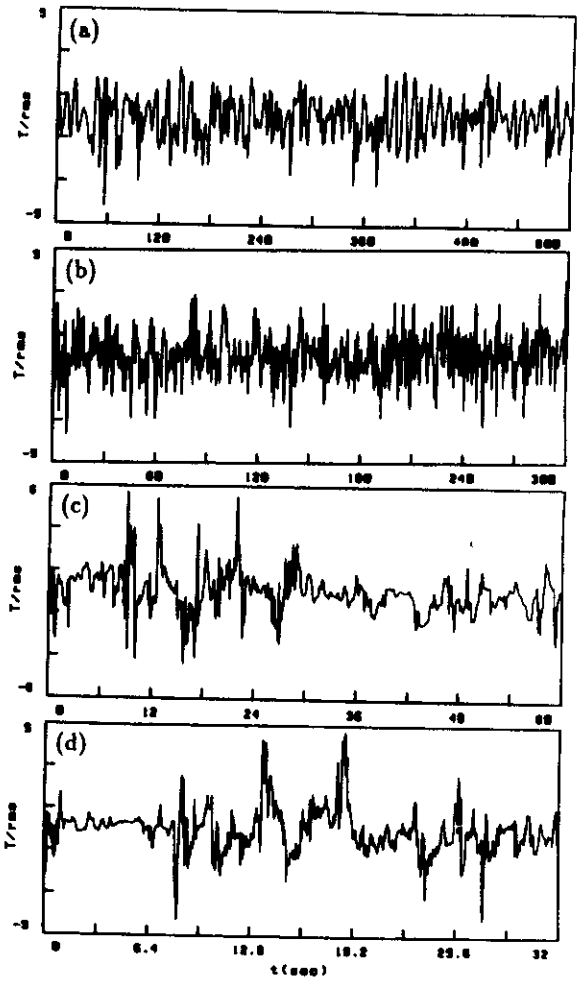

Figure 30. The center time series for $4\times10^5 < Ra < 4\times10^{10}$ (a) $Ra = 4.2\times10^5$, (b) 4.6×10^6, (c) 2.7×10^8 and (d) 4.2×10^{10}. (e), (f), (g) and (h) are the corresponding plots on a shorter time span.

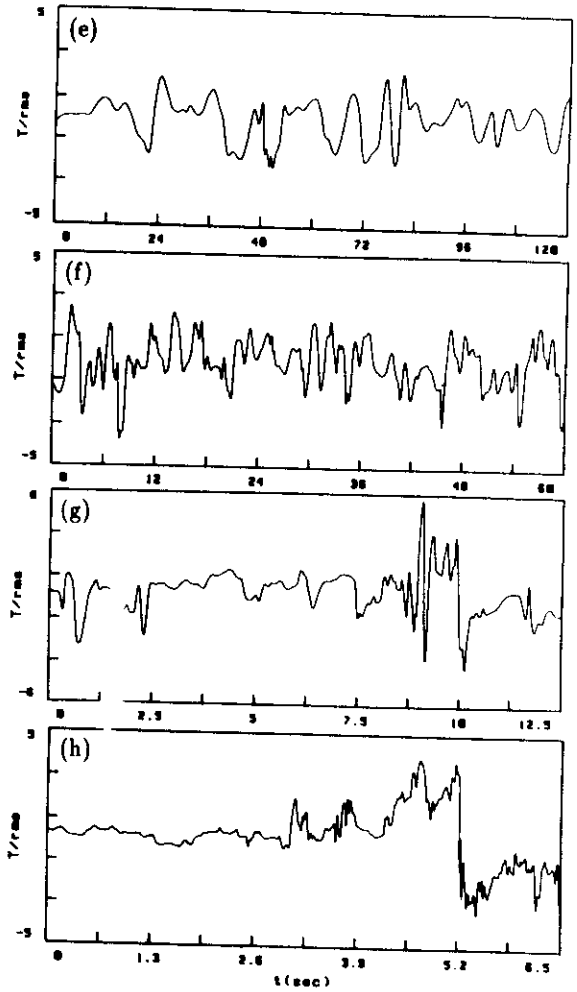

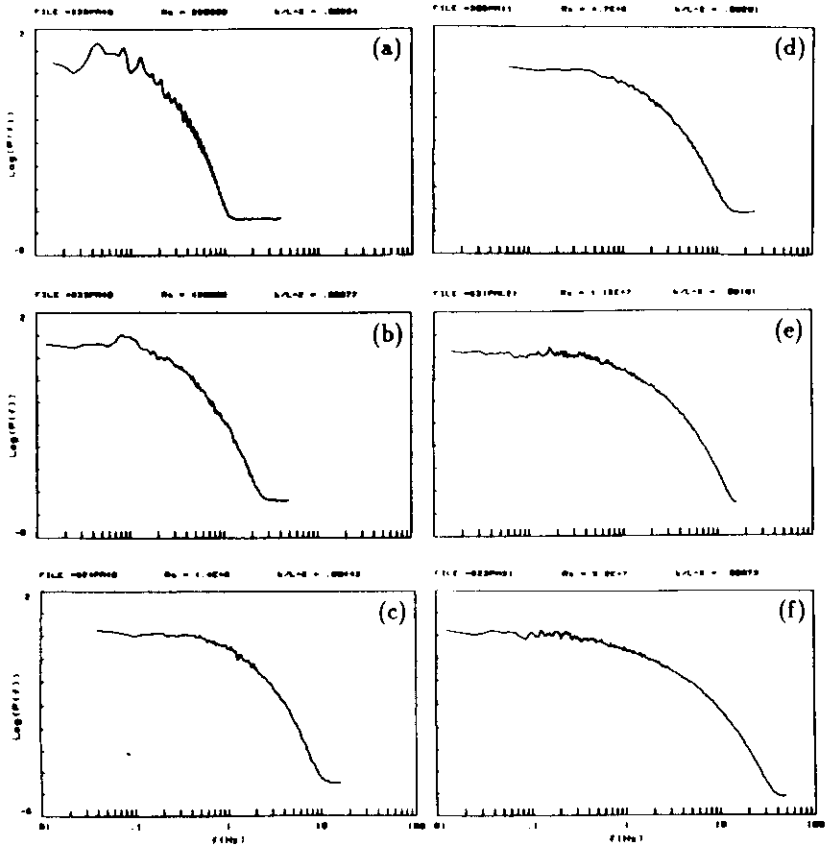

Figure 31. The center power spectra for soft turbulence. (a) $Ra = 2.9 \times 10^5$, (b) 4.2×10^5, (c) 1.4×10^6, (d) 4.7×10^6, (e) 1.2×10^7 and (f) 5.2×10^7.

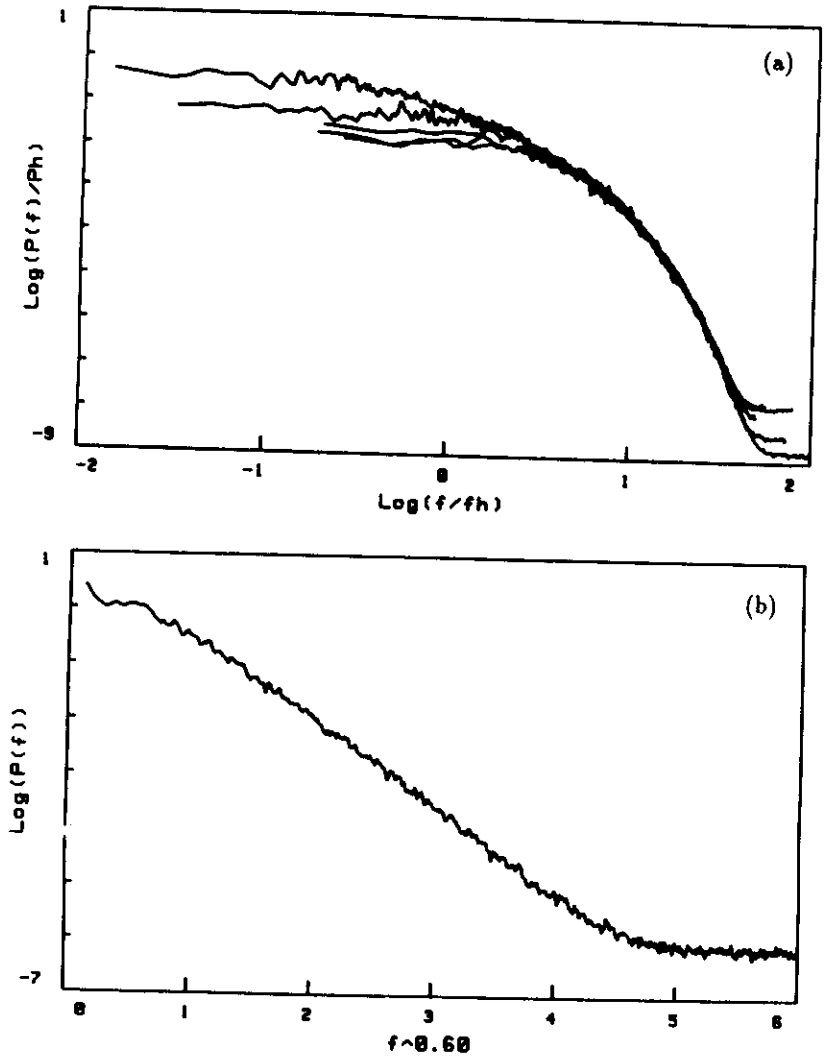

Figure 32. Soft turbulence, the power spectra are superposed according to their stretched exponential tail. (a) The superposition of power spectra for $Ra = 4.2 \times 10^5$, 1.4×10^6, 4.7×10^6, 1.2×10^7 and 5.2×10^7, (b) The power spectrum for $Ra = 4.7 \times 10^6$ in $\log(P)$ vs. $f^{0.6}$ plot to show the stretched exponential tail.

f_h, Ra dependent, determines the relative frequency shift in superposing the power spectra. The tail, or the g function can be fitted well with a stretched exponential function,

$$P(f) = P_0 \exp(-(f/f_h)^\beta) \tag{3.4}$$

with $\beta = 0.55 \pm 0.05$. Fig. 32 (b) is the power spectrum for $Ra = 4.7 \times 10^6$ in $\log(P)$ vs. $f^{0.6}$ plot to show the stretched exponential tail. The normalized frequency $f_h L^2/\kappa$ is plotted as a function of Ra in fig. 33. It shows how the characteristic frequency for the tail changes with Ra. Notice its relation with Ra is independent of the specific form of the fitting. In this soft turbulence regime, f_h increases as $Ra^{0.9}$.

3.1.5 Hard turbulence: scaling relations

Hard turbulence, unlike soft turbulence, is a self-similar state, Ra only changes the length, time and temperature scales of the flow. This self-similarity is revealed by the following facts : the PDF of the temperature fluctuations in the central region of the cell are exponential from $Ra = 4 \times 10^7$ up to the highest Ra reached; all the physical quantities measured, such as Nu, the velocity, the rms temperature fluctuations have power law dependances with Ra. Although hard turbulence is by no means simple, it may be amenable to a statistical description.

Let's first look at the time series from a bolometer in the cold descending flow, 1.0 cm away form the side wall (fig. 22 (d)). The signal shows group of colder peaks, in contrast to the hot spikes in the soft turbulence signals (fig. 22 (b) & (c)). Θ_1/Δ decreases as Ra increases (fig.23 (a)), following a power law with an exponent -0.162. $(T_2 - T_1)/2$ and Θ_1/Δ (fig. 23 (b)) are of the same order, and have the same Ra dependence. This indicates that there are

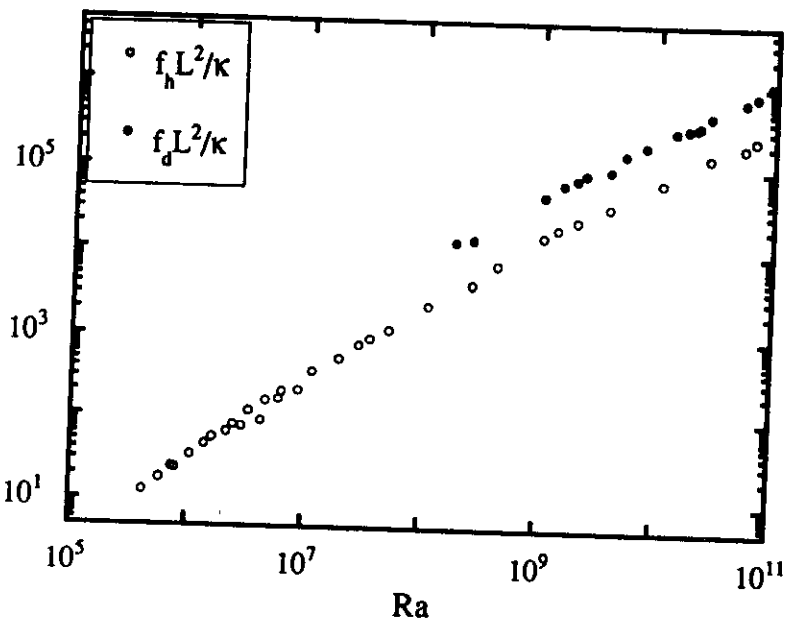

Figure 33. $f_h L^2/\kappa$ and $f_d L^2/\kappa$ vs. Ra. They are the characteristic frequencies for the cut-off tail, related to two different fitting functions.

no longer connected hot and cold channels. Rather, the thermal boundary layer nucleates separated particles, which are visualized as thermal plumes in water experiments. The cold plumes are advected by descending flow, and this leads to cold fluctuations. Those plumes are the major source of both the temperature fluctuations and the horizontal temperature gradient. These picture agrees with Solomon & Gollub's observation (1990).

Nu in hard turbulence has a scaling relation with Ra, with an exponent 0.285 (eq. 3.1). The large scale velocity increases also as a simple power law (fig. 24, fig. 36),

$$\frac{V}{\kappa/L} = 0.31 \times Ra^{0.485\pm0.005} \quad . \tag{3.5}$$

The large scale velocity can be estimated from a free-fall model, when the Re number is large. The free fall velocity V_f is:

$$V_f \approx (\alpha g \Theta L)^{1/2} \quad . \tag{3.6}$$

As the velocity V and rms temperature fluctuations Θ have been measured independently, we can compare the estimated velocity V_f with the measured one V (fig. 34 (a)). They have a slight difference in scaling, $V_f/V \approx Ra^{-0.03}$ (the prefactor is of the order 1).

Nu can also be estimated from the measurements of V and Θ. For high enough Nusselt number, heat is transported only by advection in the middle height region and thus can be approximated by ΘV. The estimated Nusselt number Nu_{adv} is

$$Nu_{adv} \approx \frac{\Theta V}{\kappa \Delta/L} = \frac{VL}{\kappa} \times \frac{\Theta}{\Delta} \quad . \tag{3.7}$$

Nu_{adv} is compared with the measured one Nu in fig. 34 (b); the scaling difference Nu_{adv}/Nu is $Ra^{0.03}$.

The signals from the side wall region are characterized by plumes advected by the large scale flow intermittently. Similar intermittence also appear in the

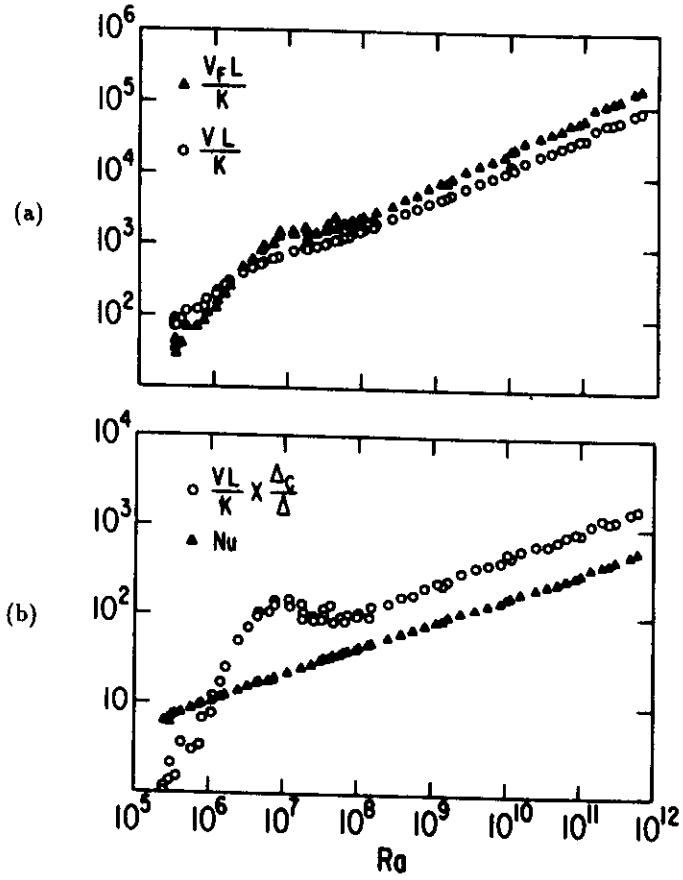

Figure 34. The estimated V and Nu compared with the measured ones. (a) The estimated free-fall velocity V_f with the measured one, (b) The estimated Nusselt number with measured one.

central region. Figure 30 (c), (d), (g) & (h) present typical hard turbulence data, they are significantly different from the soft turbulence ones in (a), (b), (e) & (f). In turbulence studies, it is often hard to describe a difference in time series although it looks obvious to the eye. However in this case, we can at least say that the large amplitude excursions in hard turbulence are well separated from the small amplitude ones. This intermittency must show up in the statistical quantities.

Figure 27 present six PDFs of the central region for $1.5 \times 10^7 < Ra < 5.4 \times 10^{11}$. They are exponential. Without actually superposing them, we know the PDF is invariant with Ra. This invariance indicates the self-similarity of hard turbulence, and the non-Gaussian shape implies correlations.

Figure 35 shows the rms value of the temperature fluctuations measured at various lateral positions, as a function of Ra. They all have scaling relations with Ra. However it seems that the scaling relations for the ones close to the exact center start at Ra higher than 4×10^7. Although the scatter in the rms value measurement is larger than for Nu and velocity measurements, we can still derive the scaling exponents from the measurements at various positions (fig. 36 (b)) and conclude that the scaling relation for the central region is:

$$\frac{\Theta_c}{\Delta} = 0.23 \times Ra^{-0.14 \pm 0.01} \quad . \tag{3.8}$$

3.1.6 Hard turbulence: power spectrum

To understand the dynamics of small scales (or small amplitudes) in turbulence, we need to study the power spectrum. Figure 37 shows six power spectra of the center bolometer for $1 \times 10^7 < Ra < 1 \times 10^{12}$. At frequencies lower than f_p, the power spectrum is flat. As we shall discuss in the next section, f_p corresponds to the largest length scale in the convection cell. There is a

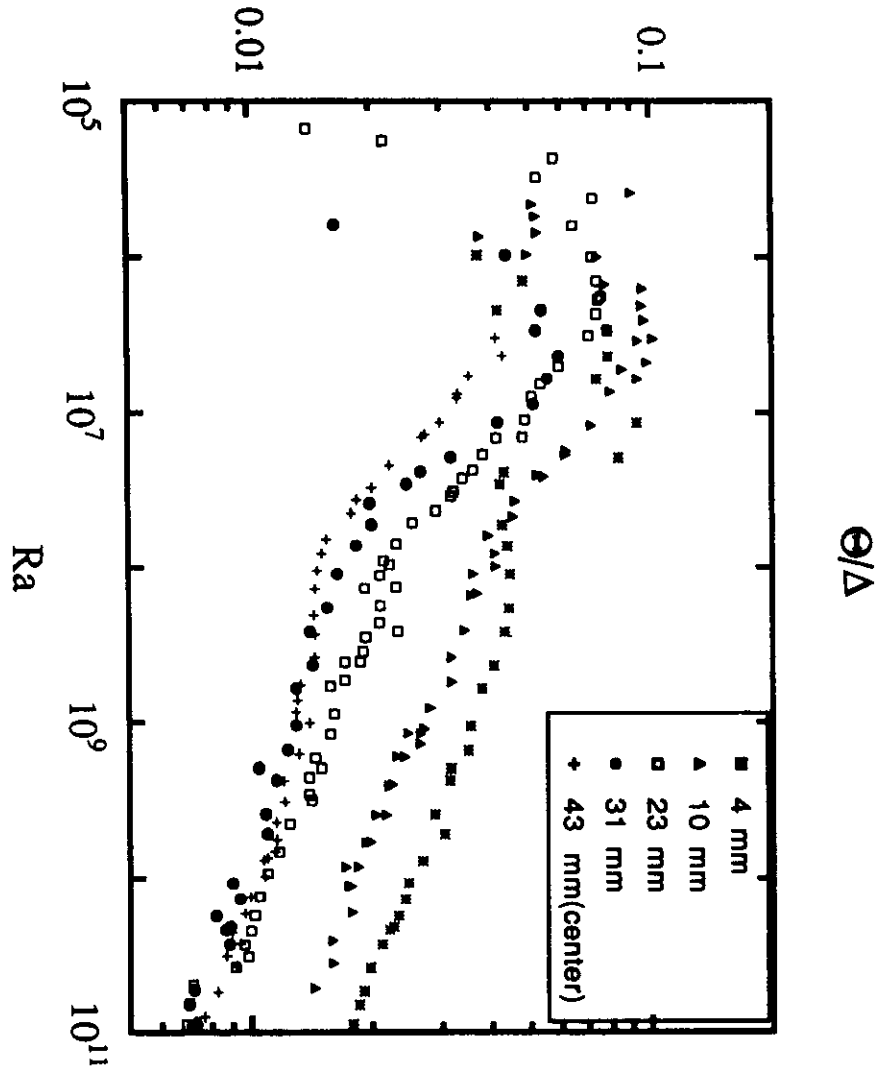

Figure 35. Θ/Δ vs. *Ra* for various radial positions. The normalized rms temperature fluctuations Θ/Δ measured at 4 mm, 10 mm, 24 mm, 31 mm and 43 mm (center) away from the side wall.

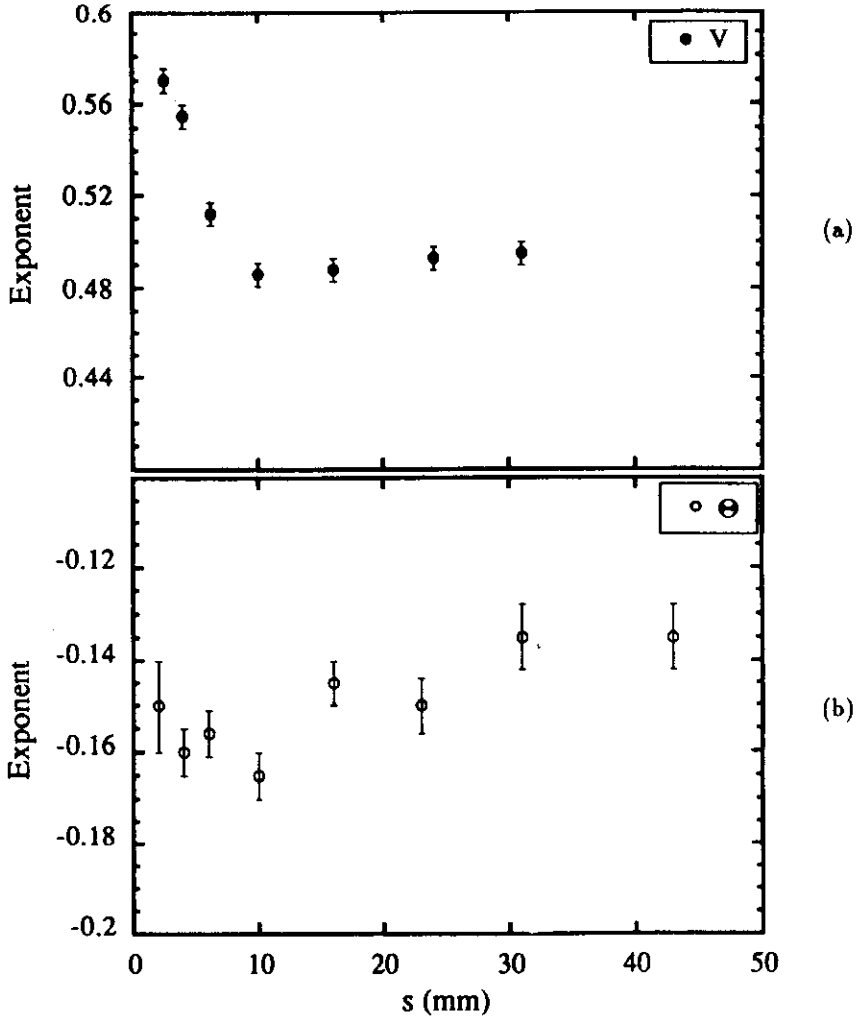

Figure 36. The scaling exponents for VL/κ and Θ/Δ as a function of the radial distance. (a) the large scale velocity VL/κ and (b) the temperature fluctuations Θ/Δ measured at s mm away from the side wall.

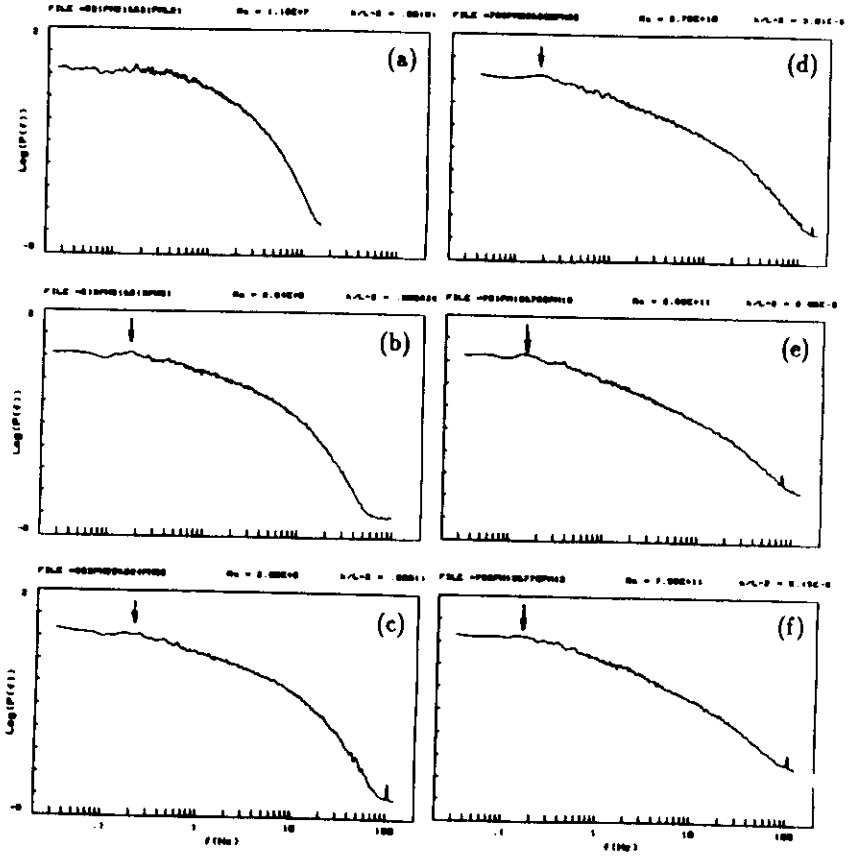

Figure 37. The center power spectra for hard turbulence. (a) $Ra = 1.2 \times 10^7$, (b) 2.8×10^8, (c) 2.1×10^9, (d) 2.8×10^{10}, (e) 2.7×10^{11} and (f) 7.6×10^{11}; the arrow indicates the position of f_p.

cut-off tail at high frequency. The part between f_p and the cut-off is a power law, whose range increases with Ra. The power law corresponds to the inertial range of the energy cascade.

We can superpose the cut-off tails for Ra up to 10^{11} (fig. 38 (a)), as was done for soft turbulence (fig. 32 (a)). Thus the high frequency part can be characterized by a function $g(f/f_h)$ with parameter f_h. The tail alone can be approximated by a stretched exponential (eq. 3.4) again, as shown in fig. 38 (b), the $\log(P(f))$ vs. $f^{0.55}$ plot for $Ra = 2.1 \times 10^9$. In this plot, a straight line indicates a stretched exponential. The parameter f_h, together with the values in soft turbulence, is plotted in fig. 33. For $10^7 < Ra < 6 \times 10^{10}$

$$\frac{f_h L^2}{\kappa} = 0.0013 \times Ra^{0.78 \pm 0.02} \quad , \tag{3.9}$$

whereas it scales as $Ra^{0.9}$ for soft turbulence.

The power spectrum has two characteristic frequencies f_p and f_h, which are the lower and higer bounds of the power law. f_p corresponds to the energy injection length scale, and f_h the dissipative one. The power law range, proportional to f_h/f_p, extends with Ra as

$$Range \propto Ra^{0.29} \quad , \tag{3.10}$$

provided f_p varies as $Ra^{0.49}$.

As we shall explain later, f_p corresponds the largest length scale in the cell. All the turbulent motions start from it. Therefore we superpose 5 center power spectra for $5 \times 10^7 < Ra < 1 \times 10^{11}$ at this frequency (fig. 39 (a)). The superposition shows that the self-similarity preserves at the low frequency part, as well as the high frequency tail. Ra only changes the range of the power law in the power spectrum.

The stretched exponential in eq. 3.4 fit the cut off tail data well. A classical

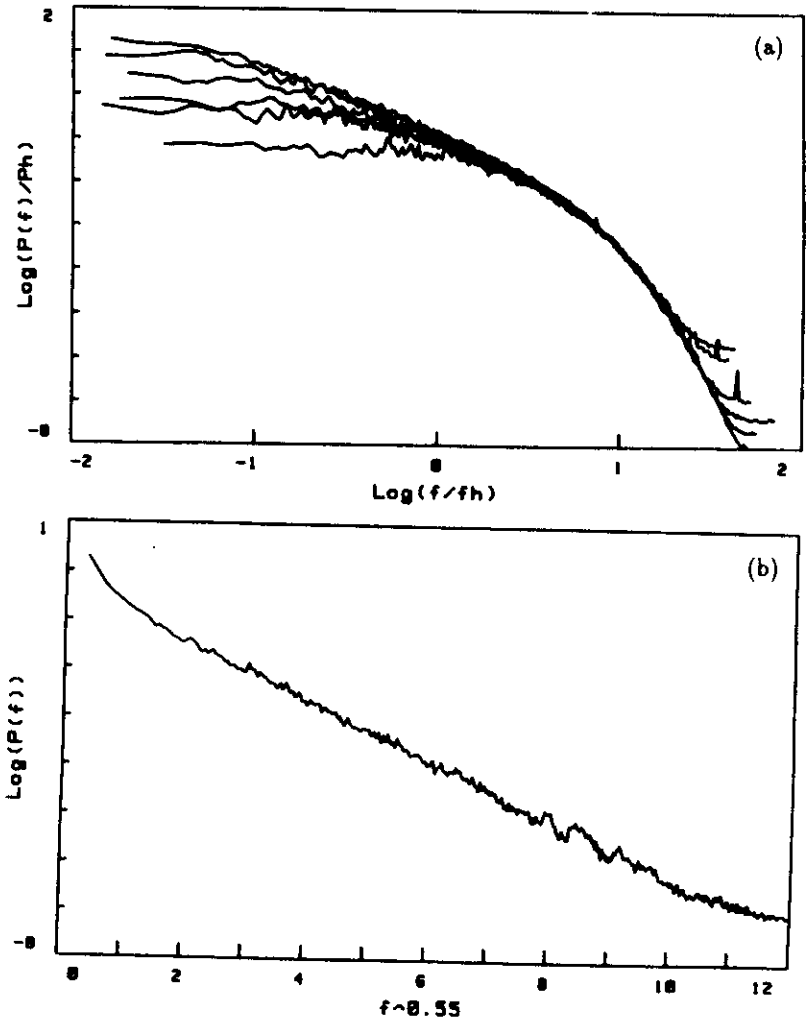

Figure 38. Hard turbulence, the power spectra are superposed according to their tails. (a) The superposition of power spectra for Ra between 1.2×10^7 and 6.7×10^{10} according to their tails, (b) the $\log(P(f))$ vs. $f^{0.55}$ for $Ra = 2.1\times10^9$. A straight line indicates a stretched exponential.

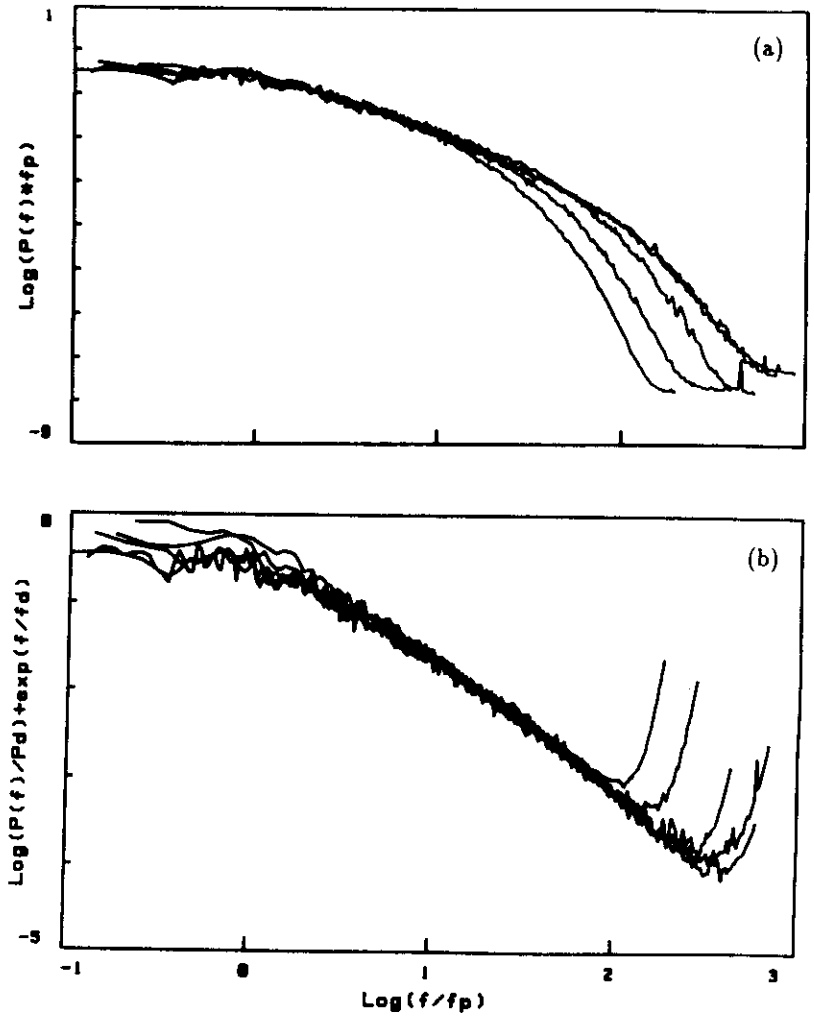

Figure 39. Hard turbulence, (a) $\log(P(f/f_p))$ vs. $\log(f)$ (b) $\log(P(f/f_p)\exp(f/f_d))$ vs. $\log(f)$. Those curves are for Ra between 1.2×10^7 and 6.7×10^{10}. The straight line in (b) shows a power law of an exponent -1.4.

form to fit the whole curve, i.e. the power law and the cut off tail, is

$$P(f) = (f/f_0)^\alpha \exp(-f/f_d) \quad . \tag{3.11}$$

Figure 40 (a) shows the fit to the center power spectrum for $Ra = 5.2 \times 10^9$ The fitting parameter f_d is plotted in fig. 33.

In fig. 39 (b), the power spectra $P(f)$ are multiplied by $\exp(f/f_d)$ to get ride of the exponential tail and to reveal in full the power law, which are straight lines in this log-log plot. The exponent for the power law is measured as

$$\alpha = -1.35 \pm 0.05 \quad . \tag{3.12}$$

In fig. 41 (b), a power spectrum $P(f)$ for $Ra = 2.8 \times 10^{10}$ is multiplied by $f^{1.4}$ to demonstrate a power law $f^{-1.4}$.

In fitting a power spectrum for low Ra with the form in eq. 3.11, one has to be careful since the power law range is so small that the fitting may have large uncertainties. The exponent of power law can only be trusted with the curves of large Ra. Since both the stretched exponential (eq. 3.4) and the power law with exponential cut-off (eq. 3.11) fit the same tail well, It is obvious that f_h and f_d in these two functions have the same Ra dependence, as shown in fig. 33. As a matter of fact, $f_d/f_h \approx 3.3$. Technically, it is more straightforward to decide f_h from the power spectrum.

The self-similarity of the power spectra is valid until Ra reaches 10^{11}. The power spectra for $Ra > 10^{11}$ can no longer be superposed with those of $Ra < 10^{11}$ at high frequencies. It seems that a second power law of larger exponent develops (fig. 41 (c)). Unfortunately, we are unable to reach higher Ra in this cell to study this change. This was one of the main reason to built a cell reaching higher Ra,the cell of aspect ratio 0.5.

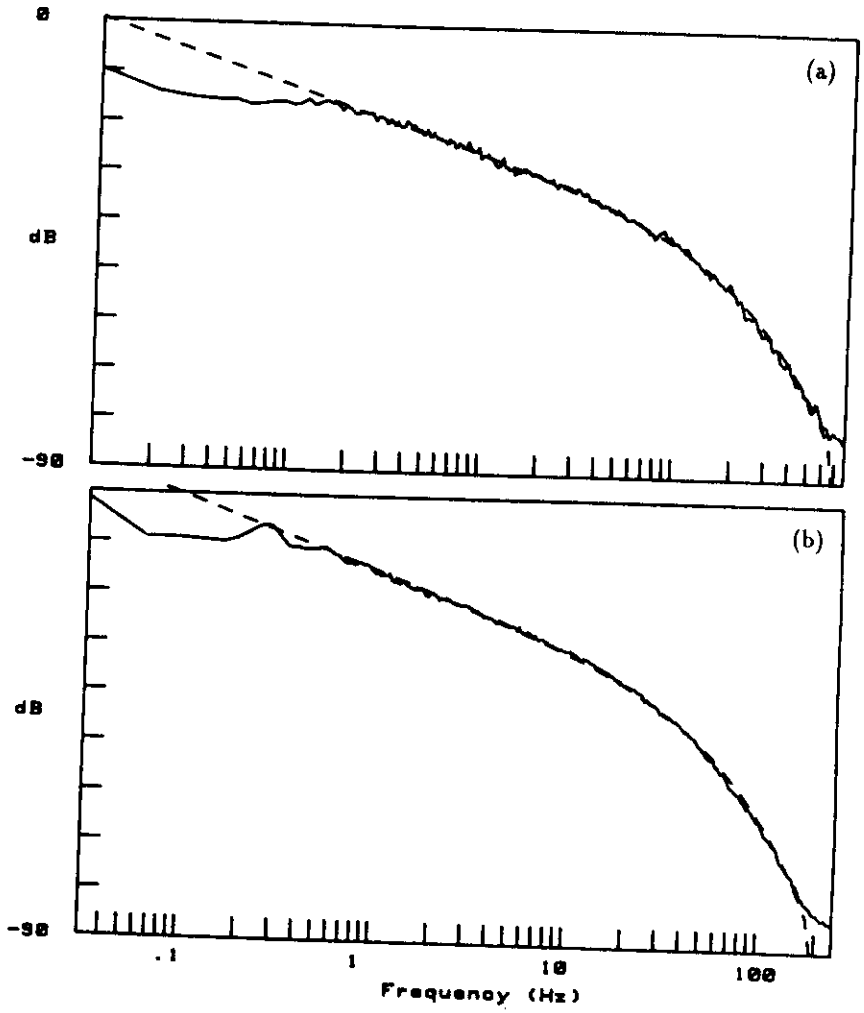

Figure 40. A power law with an exponential cut-off fit to the power spectra. (a) the center power spectrum of $Ra = 5.2 \times 10^9$ and (b) the power spectrum of 1.0 cm from the wall, for $Ra = 1.1 \times 10^{10}$.

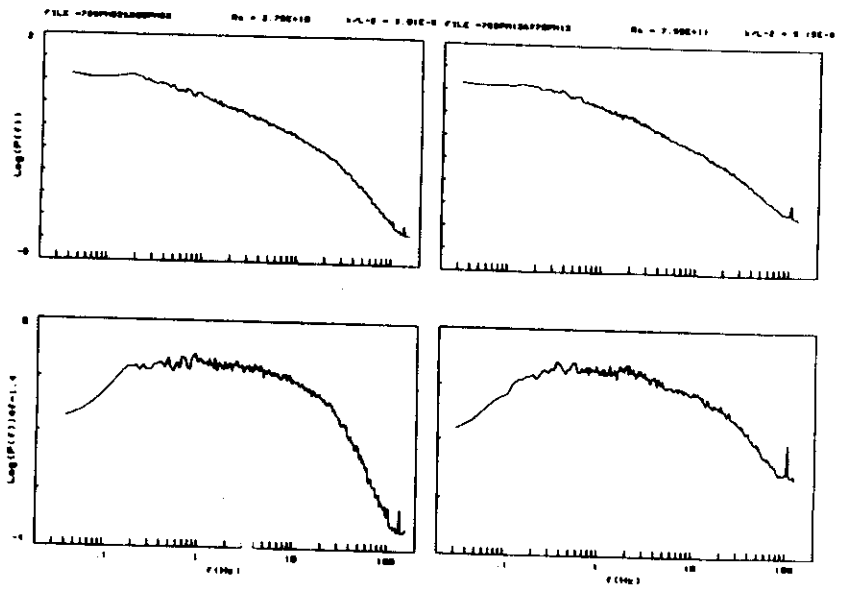

(a) (b)

Figure 41. $\log(P(f) \times f^{1.4})$ vs. $\log(f)$ for Ra below and above 10^{11}. (a) $Ra = 2.8 \times 10^{10}$ and (b) 7.6×10^{11}.

3.1.7 The large scale flow

In this section, the velocity measurement technique is discussed. The measurement shows that there is a large scale flow in this cell, whose effects on the signals and their statistical properties in various regions have been studied. The connection between the large scale flow and the coherent frequency f_p is presented.

The information on the velocity field has been extracted from the temperature correlation of two adjacent bolometers, which are supported by two parallel manganin wires (1 cm apart, suspended across the cell in the mid-height). We fixed the pairs at radial positions from 2.5 mm to 31 mm away from the side wall. Signals from the bolometers in ea h pair are measured simultaneously with the two channels of the signal ana zer.

The size of this "velocity probe" is the spacing d of he two bolometers. It has to be small enough so that the temperature signals a e correlated up to high frequencies and a reasonable fate time response can be attained. Obviously, the velocity fluctuating faster than the passage time across d can not be measured. On the other hand, the measurement error in time delay and the thermal diffusion between the two bolometer set the lower limit for d. Limited by our technique in handling small bolometer, d was set to be around 2 mm, which we feel is much above the lower limit.

If two signals detected by the bolometers are identical except for a time delay τ_0, the phase of their cross spectrum is linear with frequency with a slope $2\pi\tau_0$, and the coherence function is unity for all the frequency range. From the delay time and the spacing of the two bolometers, the velocity can be calculated as

$$V = \frac{d}{\tau_0} \quad . \tag{3.13}$$

The direction of the vertical velocity can be decided by the sign of the delay time and the relative position of the bolometers. However in real cases, the temperature signals will not be completely correlated, due to the fluctuations of the velocity and temperature fields. Fig. 42 (a) shows the coherence between the two adjacent bolometers. It is close to one in the low frequency range. The phase of the cross spectrum is linear with frequency (fig. 42 (b)).

The average time delay τ_0 in a time window Γ can also be calculated directly in the time domain by minimizing $S(\tau)$,

$$S(\tau) = \int_0^\Gamma dt[T_1(t) - T_2(t-\tau)]^2 \ , \tag{3.14}$$

where $T_1(t)$ and $T_2(t)$ are the temperatures at time t measured by the two bolometers.

For steady large scale flow (which is the case in hard turbulence), the phase of the cross spectrum is linear and the two methods lead to identical results. However, even when the large scale flow changes more slowly than the passage time (which is the case in some soft turbulence range), the phase of the cross spectrum is not a good linear function. In that case, only the second method can lead to an unambiguous mean delay time τ_0. In this cell, there are only small fluctuations around the finite mean velocity, thus τ_0 has been calculated by minimizing $S(\tau)$ based on the time window of the whole signal length. For the aspect ratio 0.5 cell, the velocity fluctuations are large, sometimes the flow even switches its direction, so we divide the signal into many blocks of size Γ, calculate the mean time delay (or mean velocity) for each block and get its distribution function. The characteristic velocity can be derived from the distribution function.

In the discussion above, it has been assumed that there is no horizontal velocity V_h. However if we are interested in the precise scaling law of the

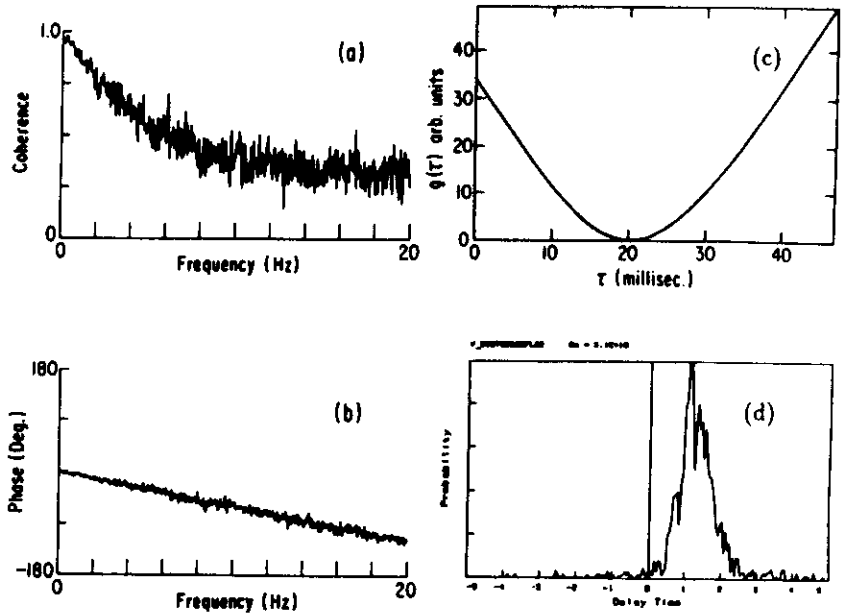

Figure 42. For two adjacent bolometers, (a) Their coherence, (b) the phase of cross spectrum, (c) the structure function $S(\tau)$ and (d) the delay time distribution.

velocity with Ra, we can not ignore the horizontal velocity V_h even though it is small in the side wall region. The modified relation between τ_0 and the velocity is

$$\tau_0 = \frac{d}{\sqrt{V_z^2 + V_h^2}} \frac{V_z}{\sqrt{V_z^2 + V_h^2}} , \qquad (3.15)$$

where $V_z/\sqrt{V_z^2 + V_h^2}$ is the correction factor due to the flow direction. However it is plausible to assume in the hard turbulence regime that V_z and V_h have the same scaling relation with Ra. Therefore eq. 3.13 will lead to the correct velocity scaling, even though the actual magnitude of the vertical velocity may not be precise. From now on, we shall calculate the velocity from eq. 3.13 and simply denote it as V.

In this cell, pairs of bolometer detect steady descending flow (fig. 42 (b) & (d)). Their time signal have group of cold peaks (lower curve in fig. 43 (b)), which are cold plumes advected by the descending flow. The velocity measurement and the temperature signals agree with each other. Another bolometer is placed in the opposite side (fig. 43 (a)). It has been measured simultaneously with one of the paired bolometers, fig. 43 (b) shows the time signals of these two bolometers (the lower data is from the descending flow). Clearly plumes of opposite signs are seen in the two sides of the cell. Therefore we conclude that the large scale motion is essentially one roll like: up in one side and down in the other side. Obviously the one roll structure is not the most symmetric configuration. What is the symmetry breaking mechanism for this steady and repeatable configuration? We do not know.

Figure 35 showed the rms temperature fluctuations Θ/Δ at various radial positions. The plumes advected in the large scale flow region are not efficiently mixed, therefore the rms value is larger than in the well mixed central region. Figure 44 shows PDF of the bolometers at various radial positions for Ra =

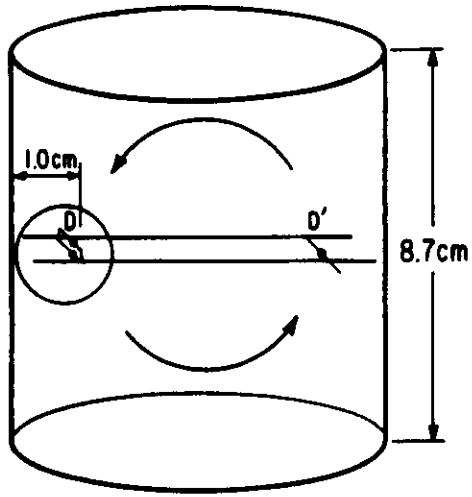

(a)

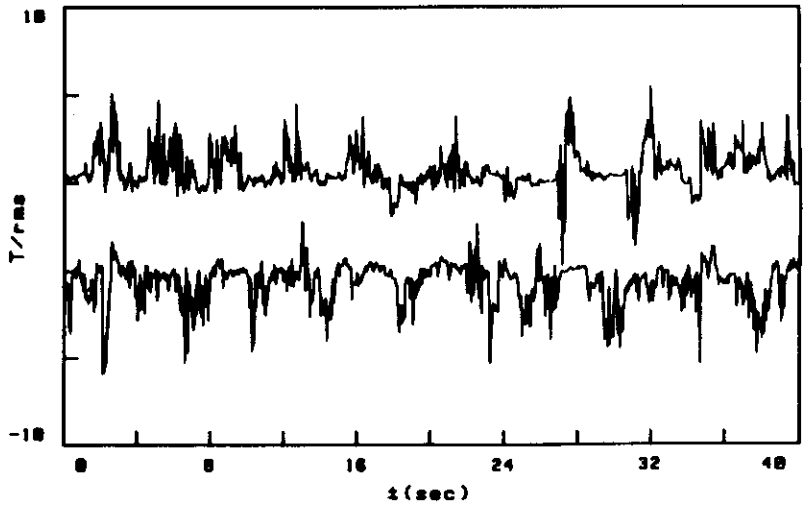

(b)

Figure 43. Two bolometers at the opposite sides of the cell, (a) their configuration and (b) their time series. In (b) the lower curve is from the descending flow for $Ra = 1 \times 10^{10}$.

5×10^{10}. The asymmetry of the PDF in the side wall region is due to the advected plumes. 2 cm further away from the side wall (or $r < 2.3$ cm), the rms temperature fluctuations becomes homogeneous and the PDF becomes symmetric and exponential.

Since the side wall region width shrinks as Ra increases, bolometers change their positions with respect to the velocity profile. Thus the measured velocity dependence on Ra is the combined effects of the velocity itself and the side wall region width. However the velocity measured outside the side wall region is free from this effect and it gives the scaling for the velocity only. The same argument can also apply to other physical measurement, such as the rms temperature fluctuations. In hard turbulence, $VL/\kappa = CRa^{\gamma}$, and we have determined the exponents γ for various radial positions. Figure 36 (a) is a plot of this exponent as a function of the distance. The exponent decreases as one goes toward the center region, and it saturates to the value 0.485, 10 mm away from the side wall. The results shown in eq. 3.5 use the data from this pair of bolometers. Similarly, the exponent for the rms temperature fluctuations saturates at the value -0.14.

The cell can be viewed as having three different sections in radial direction. The viscous boundary layer can be estimated as $\sqrt{\nu L/V}$, which is smaller than a millimeter (the typical velocity V is 10 cm/sec, ν varies from 10^{-1} to 10^{-4} cm^2/sec, and L is 8.7cm). Apparently there is an asymptotically homogeneous center region, where the mean velocity is zero. Our experiment shows the existence of another region between the viscous boundary layer and the center region, called the side wall region. In this region, the velocity has a large mean vertical component, the plumes therefore are mixed with the background flow less efficiently than in the center region. The large rms and skewness of the local temperature fluctuation are the signatures of the side

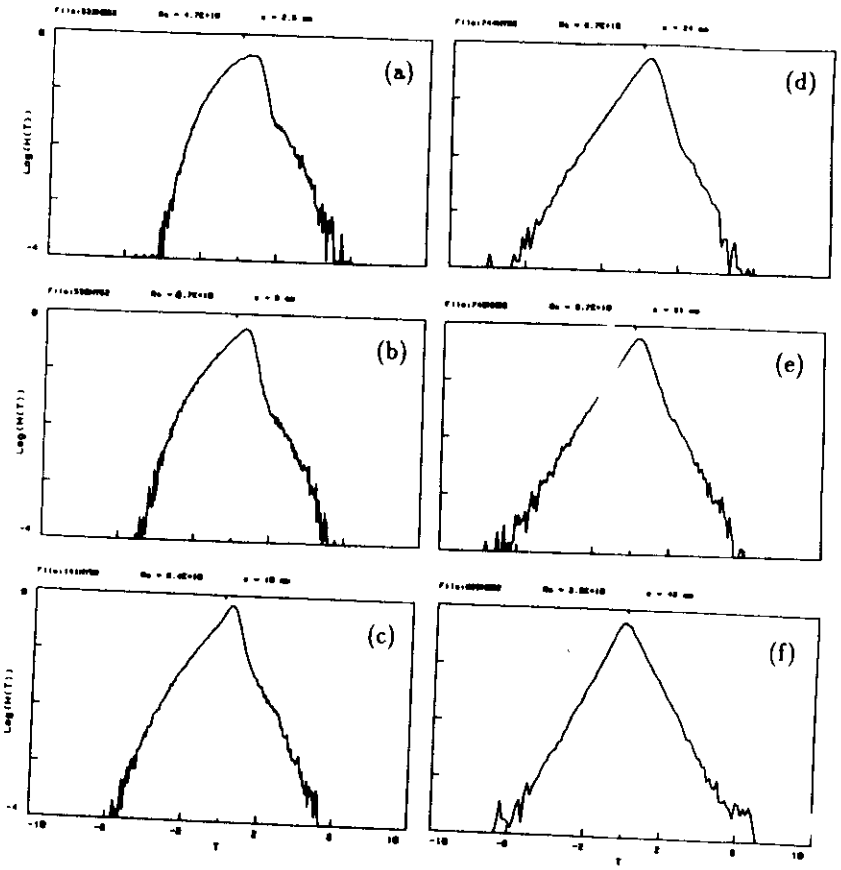

Figure 44. PDF at midheight, various radial positions for $Ra = 5 \times 10^{10}$. (a) 2.5 mm, (b) 6.0 mm, (c) 10 mm, (d) 24 mm, (e) 31 mm and (f) 43 mm away from the side wall. The cell diameter is 87 mm.

wall region. However, the side wall region shrinks as Ra increases, so the signal at any fixed point in the side wall region will asymptotically approach that of the center.

The power spectrum in the side wall region has the same shape as the one in the center region, but extends to higher frequency. Figure 45 (a) are power spectra for $Ra = 2.1 \times 10^{10}$ taken at 4.0 mm, 16 mm, 24 mm and 31 mm from the side wall. The one closer to the center has the smaller frequencies. In fig. 45 (b), all the power spectra collapse together after shifting the ones closer to the center to higher frequencies. As the region close to the center has a smaller mean velocity, we wonder whether the mean velocity is related to the frequency shift of the power spectra.

Once hard turbulence is reached, the coherent frequency f_p appears in all aspects of the flow: at this frequency, the center power spectrum starts to cascade (fig. 29 (a)), the bottom one has a peak (fig. 29 (b)) and the coherence between the center and bottom reappears (fig. 28 (e) & (f)). In fact, looking at the time series of the side wall bolometer in fig. 43 (b), clearly one can deduce f_p from the pseudo-periodic appearance of the group peaks (about every 4 seconds).

For this cell, f_p is always between 0.1 and 0.3 Hz. After normalized by κ/L^2, it has a scaling relation with Ra (fig. 46 (a)).

$$\frac{f_p L^2}{\kappa} = 0.057 \times Ra^{0.490 \pm 0.008} \tag{3.16}$$

(Notice that ω_p in the previous report (Castaing *et al.* 1989) is $2\pi f_p$).

With the measurement of the large scale velocity, a circulation frequency can be constructed and compared with f_p. The circulation frequency is $V/4L$, where L is the height of the cell and $4L$ is about the total distance for a fluid element to complete a period in this cell. The ratio between f_p and $V/4L$

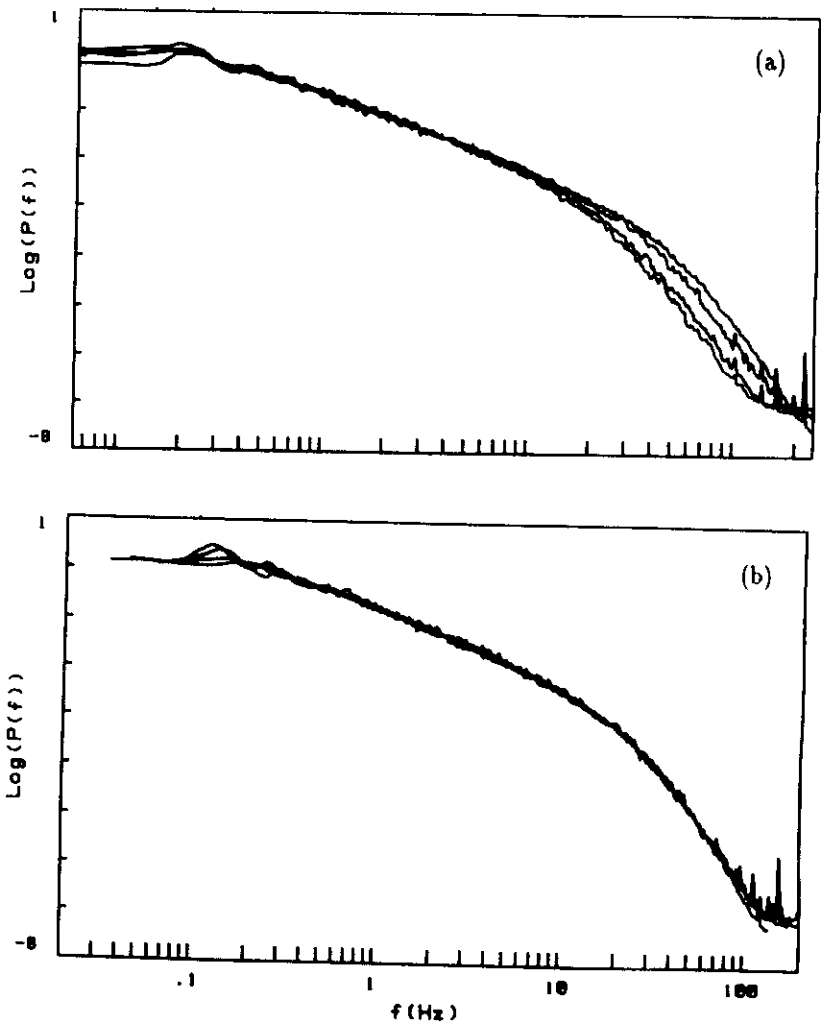

Figure 45. Power spectra at various radial positions and their superposition. (a) For $Ra = 2.1 \times 10^{10}$, 4.0 mm, 16 mm, 24 mm and 31 mm from the wall, the one closer to the side extends to higher frequencies, (b) The collapse of the power spectra in the log-log plot.

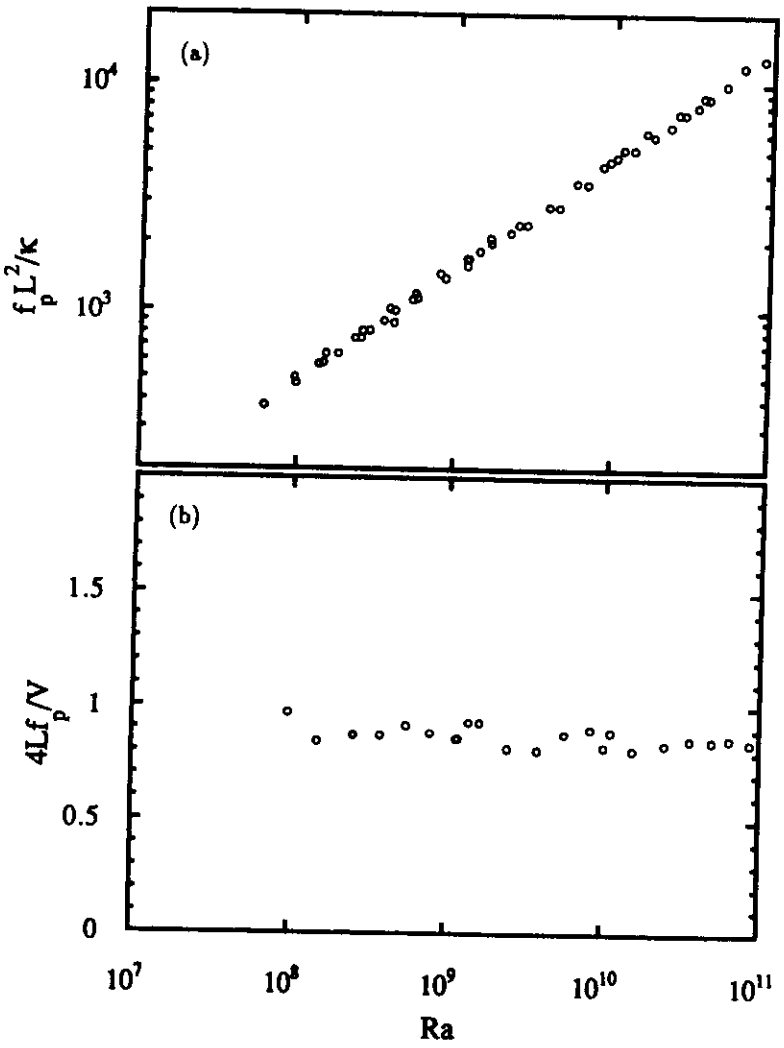

Figure 46. The resonant frequency f_p, (a) $f_p \times L^2/\kappa$ vs. *Ra* (b) $f_p \times 4L/V$ vs. *Ra*.

is plotted in fig. 46 (b). It is clear that f_p is equivalent to the circulation frequency.

Physically, it is plausible that f_p is the circulation frequency. When descending cold plumes reach the bottom plate, they perturb the bottom boundary layer. The perturbation induces waves and groups of plumes detaching from the boundary layer, as observed by Zocchi *et al.* (1990) in a water experiment and by Deluca *et al.* (1990) in a simulation. The group of hot plumes is advected up by the large scale flow and the same scenario starts again when they reach the top plate. Looking at the time series in fig. 43 (b), one sees a bursting period consisting of a train of cold bursts and a laminar period of $1/f_p$. The bursting and laminar periods from the two opposite bolometers are just 180 degree out of phase. A resonance at the circulation frequency may be due to the stability of the large scale flow.

The frequency f_p corresponds to the largest scale in a cell, $4L$. The length scales of all the flow structures are smaller than $4L$ and the frequencies of all the flow dynamics are higher than the circulation frequency f_p.

3.1.8 The difference of the signal in space and time

A classical measure in turbulence is the velocity difference taken at two different points (Kuo & Corrsin 1971; Antonia *et al.* 1982; Anselmet *et al.* 1984). The equivalent here is the temperature difference in space. However we have not modified the experimental set-up yet to move a bolometer continuously, all we have studied is the difference between signals from two fixed bolometers, as a function of *Ra*.

Two bolometers have been positioned at the center of the cell, about 0.9 mm horizontally apart. Fig. 47 (a) & (b) are the individual signals, (c) is their difference. The difference acts like a high pass filter, suppress the large

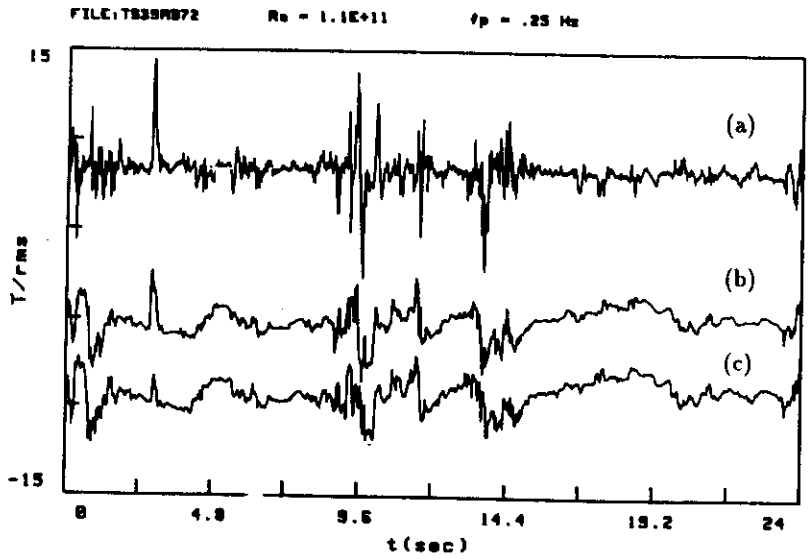

Figure 47. Individual times series from two adjacent bolometers, and their difference. (a), (b) are the individual ones and (c) is their difference, for $Ra = 1 \times 10^{11}$.

scale structures and enhance the small scale ones. The PDF of this difference in space is shown in fig. 48 (a). In fig. 48 (b), the PDF is plotted against the temperature raised to a power β. A straight line indicates a stretched exponential. The PDF for the original signal is exponential, the fact that the PDF for the difference is stretched exponential reflects that large amplitude excursions occurs more frequently.

The PDF of the difference changes with Ra. Figure 49 (a) & (b) show the rms value of the difference normalized by that of the original signal, and the exponent β for the stretched exponential fit as a function of Ra. As Ra increases, the dissipation length decreases, thus the bolometers spacing relatively increases. Turbulent structures larger than the bolometer spacing are canceled when the difference is taken. Thus the difference only reflects the effects of smaller scales. So for larger Ra, the bolometers become less correlated and the rms value of the difference increases. But inclusion of very small structures at high Ra does not contribute significantly to the amplitude, that is why the rms value saturates. A similar reasoning applies to the exponent β for the stretched exponential.

A stretched exponential fit to the PDF is only an approximation. For two uncorrelated signals with exponential distribution, the PDF of their difference T_d is

$$H(T_d) = \frac{1}{4\Theta}(1 + \frac{|T_d|}{\Theta}) \times \exp(-\frac{|T_d|}{\Theta}) \quad . \tag{3.17}$$

Thus a stretched exponential fit does not work for bolometers too far away.

Eventually, a moving frame should be built to change the spacing between bolometers continuously and conveniently. To move frame easily without low temperature leak, a bellows has to be used. It would be more tricky to achieve high precision in the spacing measurement, even though it is easy to measure

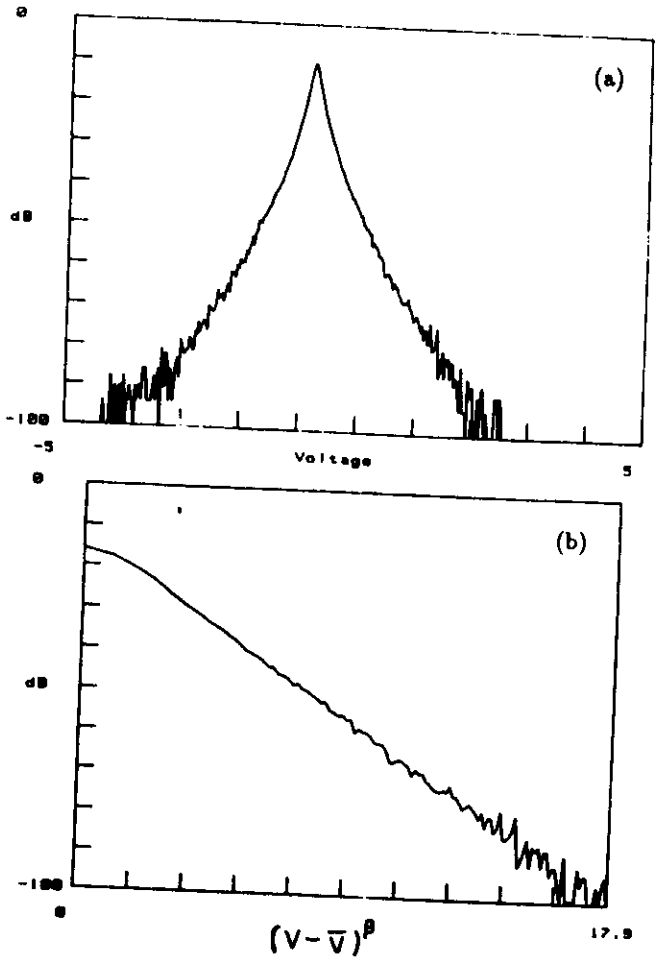

Figure 48. The PDF H_d of the differential signal. (a) $\log(H_d)$ vs. T and in (b) $\log(H_d)$ vs. T^{β}. here $\beta = 0.6$. This is for $Ra = 1 \times 10^{11}$.

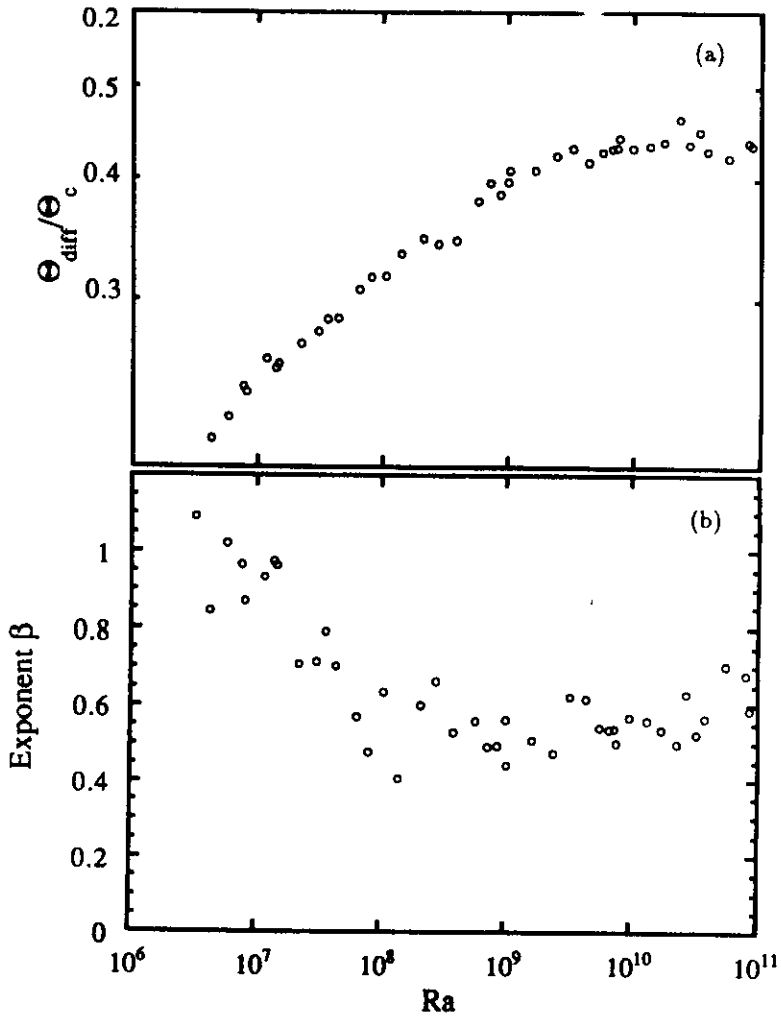

Figure 49. The rms value of the difference, and the exponent β vs. Ra. (a) The rms value of the difference, normalized by that of the original signal, and (b) the exponent β for the stretched exponential fit.

the relative change with a micrometer or a stepping-motor. However, since the rms value of the differential signal increases as the spacing increases, one could use this relation to calibrate the absolute spacing by comparing the difference measurement with the difference of a fixed pair of bolometers, whose distance is measured precisely at room temperature.

Similarly, temperature differences $T_d(t,\tau)$ could be constructed from the original signal $T(t)$, $T_d(t,\tau) = T(t) - T(t+\tau)$. The difference acts like a high pass filter, and its PDF can also be fitted by stretched exponential. This has been exhaustively studied by Ching (1990) for the signals in our aspect ratio 0.5 cell.

3.2 The aspect ratio 0.5 Cell

The study of aspect ratio 1.0 cell led to the discovery of the soft-hard turbulence transition, and th scaling relations in hard turbulence. However some questions are raised fro i those data as well: Is the hard turbulence state an asymptotic one, are po ible some of the proposed regimes, such as Nu scaling as $Ra^{1/2}$ for very l.gh Ra (Kraichnan 1962), what happens to the high frequency tail of the power spectrum at large Ra? Thus it became clear that larger Ra was desirable. The new cell we are going to discuss has a diameter 20 cm, height 40 cm. With this cell, a Ra range between 10^6 and 10^{15} is spanned. A new cryogenic system has been built for this cell. The results show some differences when compared with the aspect ratio 1.0 cell, but the soft-hard turbulence transition has been verified, all the scaling relations between the physical quantities and Ra remain and extend up to 10^{14}, the highest Ra obtained without non-Boussinesq effects. More important, the change in power spectra occurring at $Ra = 10^{11}$ has been verified and studied.

3.2.1 Heat transport and thermal boundary layers

To measure Nu, the heat conducted by the side wall has to be excluded from the total heat applied. For this cell, we did not measure the heat conduction by the side wall, since it takes too long for an empty cell to stabilize. Instead, we estimated it to be: $1 \times 10^{-3}\Delta$ (mW), here Δ is in mK. The heat conducted by the gas is $7.8 \times 10^{-4}\Delta$. In this cell, Nu varies between 20 and 2000, so small corrections to the estimate can be neglected.

We have measured the off-set for the temperature difference Δ_0 by regulating the top plate and without heating the bottom. For such a large cell, it takes a long time to reach equilibrium, it felt specially long when the liquid helium evaporates quickly with a high top plate temperature! The offset value $\Delta_0 = 0.4 \pm 2.2$ mK for $T < 5.0$ K; For $T > 5.0K$, $\Delta_0 = -6 \pm 5$ mK. The large offset for $T > 5.0$ may indicate that we did not wait long enough for the system to relax to equilibrium, but the possibility of imperfect vacuum can not be excluded. As the source of this off-set is unknown, we did not correct it in the calculations.

Figure 50 shows the Nu as a function of Ra. Table 5 lists Ra, Nu and various parameters (density, plates temperature, heating power, fluid properties, etc.). For $1 \times 10^8 < Ra < 1 \times 10^{14}$, Nu can be fitted by

$$Nu = 0.17 \times Ra^{0.290 \pm 0.005} \quad . \tag{3.18}$$

In fig. 51, Nu is divided by $Ra^{0.290}$ to amplify any misfit and show the power law more clearly. This figure shows that the power law starts at around $Ra = 1 \times 10^8$. Below, Nu has a smaller slope. The change of slope may correspond to the transition from soft to hard turbulence discovered in the aspect ratio 1.0 cell. However there (fig. 14), the slope of soft turbulence is steeper than that of hard turbulence.

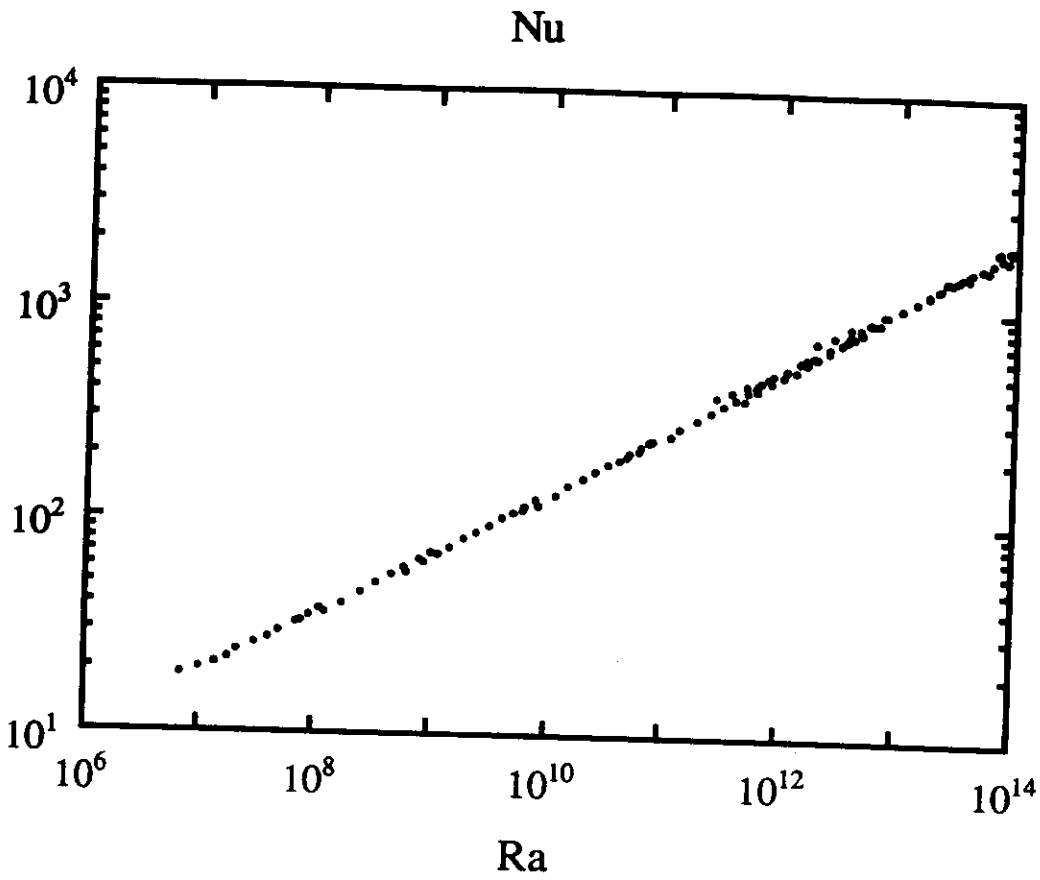

Figure 50. *Nu* vs. *Ra* for aspect ratio 0.5 cell.

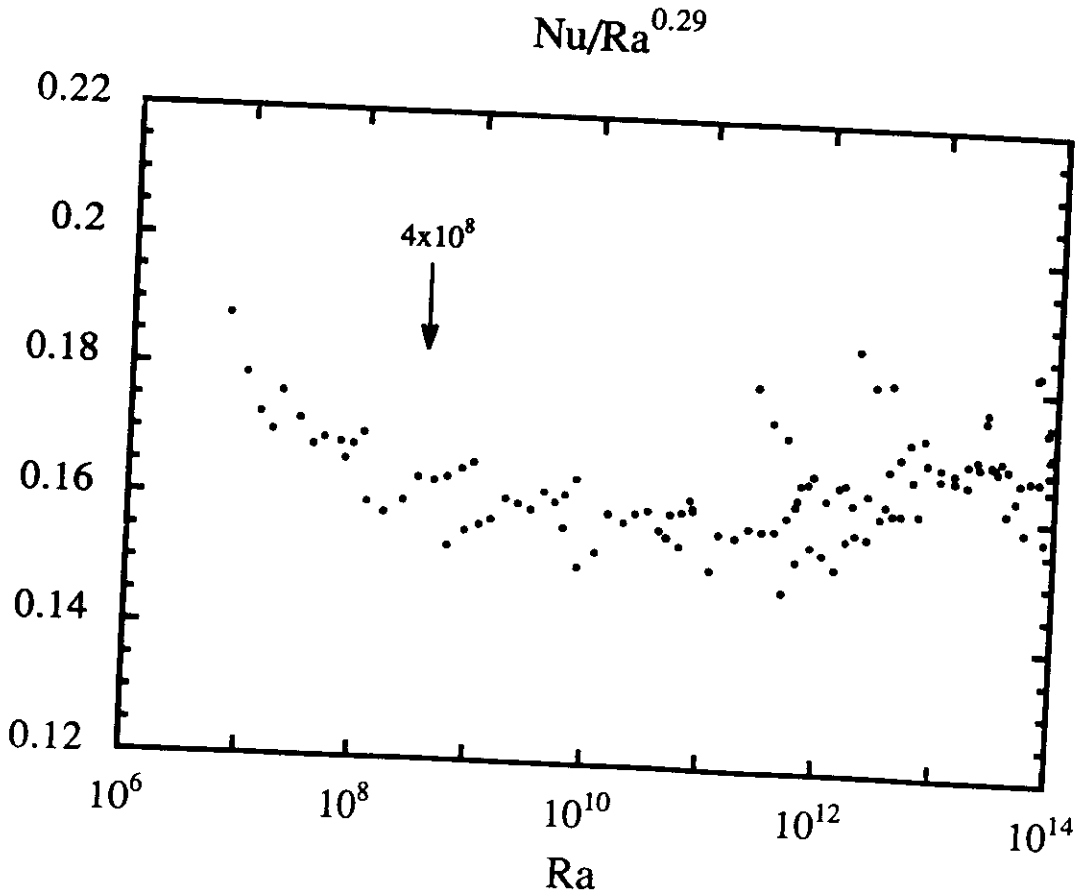

Figure 51. $Nu/Ra^{0.29}$ vs. *Ra*.

For Ra up to 10^{11}, the gas density needed is not very high, Pr is constant with value 0.7. It increases for higher densities. Figure 52 shows the variation of Pr. Using different average temperatures and gas densities, different values of Pr may correspond to the same Ra, but there is no discontinuities in the Nu vs. Ra relation (table 5 and fig. 50). The dependence of Nu on Pr is weak.

We have fixed a bolometer about 2 mm above the bottom plate. As Nu increases from 20 to 2000, the boundary layer thickness λ decreases from 1 cm to 0.1 mm. Therefore the bolometer scans across the boundary layer as Ra increases. In fig. 53 (a) the rms value measured by the bottom bolometer is plotted as a function of Ra. The change of slope at $Ra = 2 \times 10^9$ corresponds to the boundary layer crossing. The plot of $(T_c - T_b)/\Delta$ as a function of Nu in fig. 53 (b) could be interpreted as the boundary layer profile (similar to the discussion in section 3.1.1), here T_c and T_b are the average temperatures of the center and bottom bolometers. Figure 54 shows typical time series, PDF and power spectra of the bottom bolometer for (a) $Ra = 4.7 \times 10^8$ in the boundary layer and (b) $Ra = 7.7 \times 10^{10}$ outside the boundary layer. The PDF extends to the cold side for $Ra = 4.7 \times 10^8$, and to the hot side for $Ra = 7.7 \times 10^{10}$. This has been observed also in the aspect ratio 1.0 cell. In the times series outside the boundary layer, one can see hot plumes detected by the bolometer.

The power spectrum of the bottom bolometers (fig. 54) is basically a cut-off higher frequency tail with a flat low frequency region. As it is moving further out of the boundary layer with increasing Ra, its power spectrum changes (fig. 55). However for $Ra > 10^{13}$, a power law extending on a small range is present near the high frequency tail.

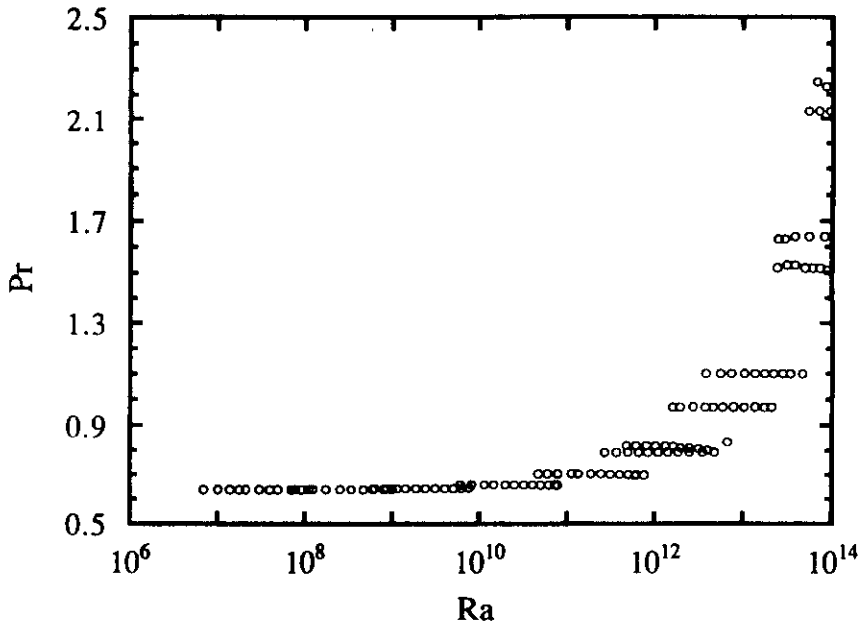

Figure 52. Pr vs. Ra.

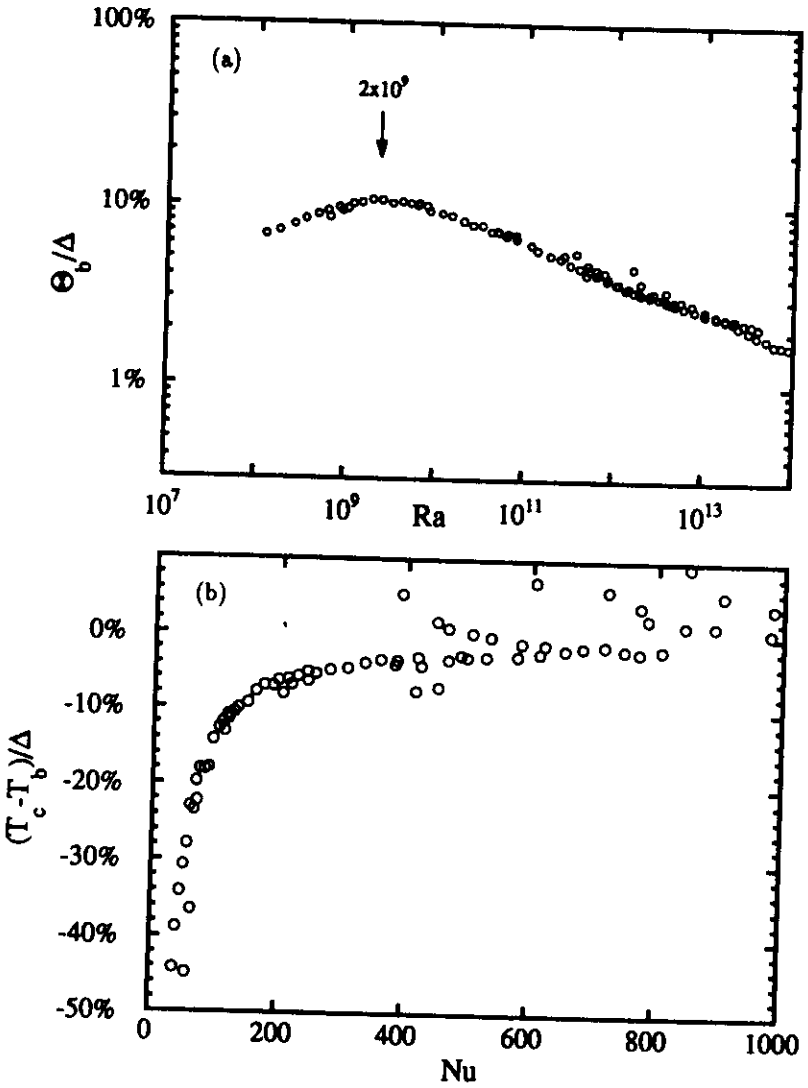

Figure 53. Bottom bolometer, (a) Θ_b/Δ vs. Ra and (b) $(T_c - T_b)/\Delta$ vs. Nu Θ_b/Δ is the rms value of the temperature fluctuations, $(T_c - T_b)/\Delta$ vs. Nu reflects the boundary layer profile, here T_c and T_b are the average temperatures of the center and the bottom bolometers.

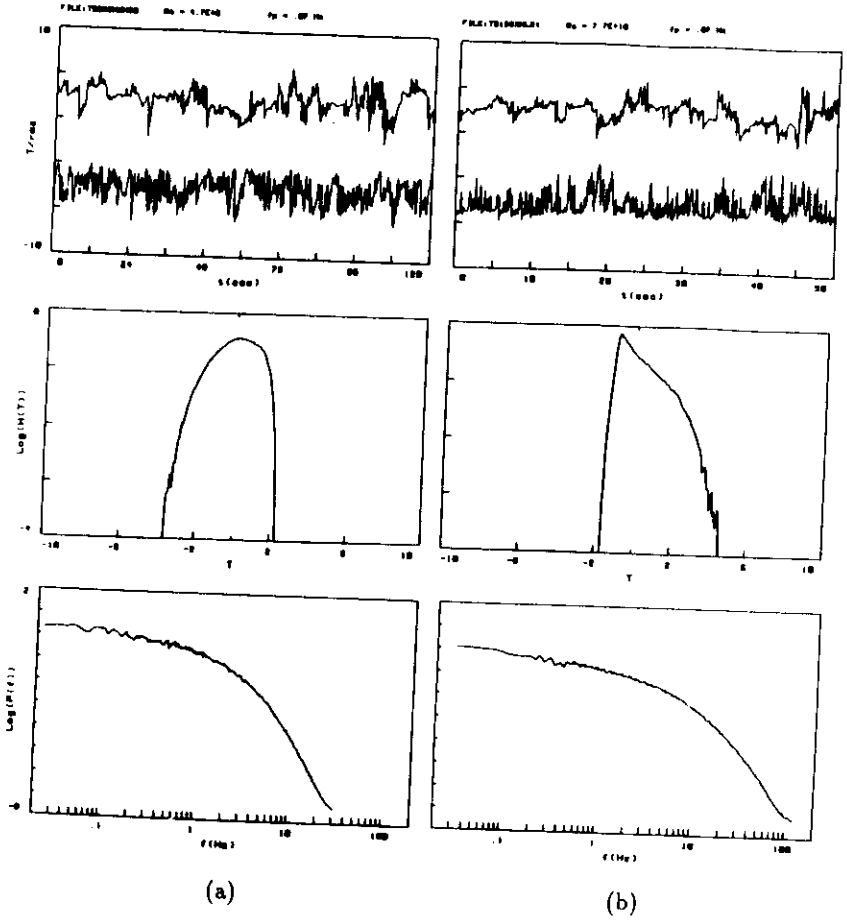

Figure 54. The time series, PDF and power spectra for th bottom bolometer inside and outside the boundary layer. (a) $Ra = 4.7 \times 10^8$ in the boundary layer and (b) $Ra = 7.7 \times 10^{10}$ outside the boundary layer. In each pair of time series, the lower one is from the bottom.

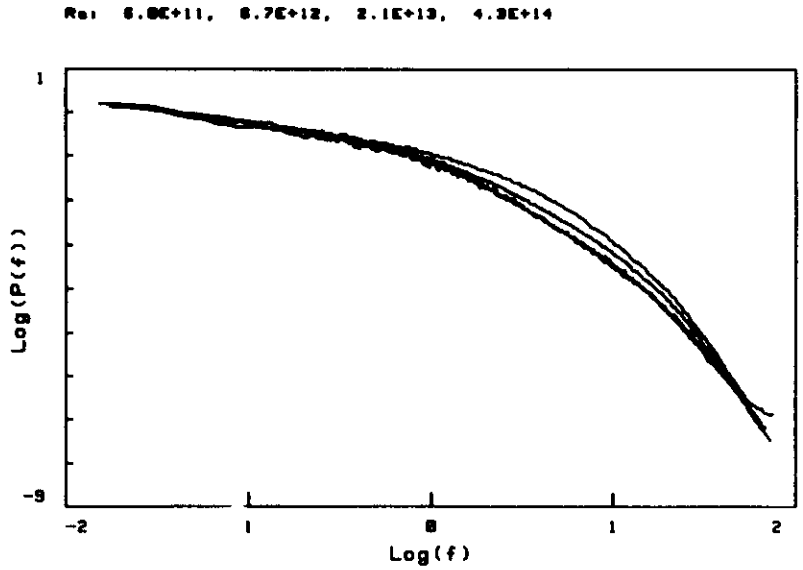

Figure 55. The superposition of the four bottom power spectra for $6 \times 10^{11} < Ra < 4 \times 10^{14}$. The Ra for the four curves are 6.0×10^{11}, 6.7×10^{11}, 2.1×10^{13} and 4.3×10^{14}, the inner one is for larger Ra.

3.2.2 The velocity measurement and the large scale flow

The large scale velocity is measured with a pair of adjacent bolometers (2 mm vertically apart), 1 cm away from the side wall. The phase of their cross spectrum is linear with frequency only for Ra between 10^9 and 10^{10}. In other ranges, its long time average is zero. This indicates that the large scale flow velocity is not steady. As discussed in detail in the previous chapter, slowly fluctuating velocities can be measured for time windows of size Γ, by minimizing the structure $S(\tau)$ function (defined in eq. 3.14) of each time window.

The size Γ has to be small enough so that the velocity is constant within each. But it cannot be too small, otherwise there is not enough temperature signal in each window for the S function to have a clear minimum. For time signals of this cell, we did calculations with three different window sizes. The distribution function for delay time has a peak at a finite value for $10^9 < Ra < 10^{10}$ (fig. 56 (a)), and becomes bimodal for other Ra range (fig. 56 (b)). The position(s) of the peak (or peaks) are the same for the three window sizes. The two peaks are symmetric with respect to the origin. Thus the large scale velocity has only one characteristic value and it switches direction from time to time.

From the peak value of the delay time, we calculate the velocity V, which is always of the order of 10 cm/sec. Compared with aspect ratio 1.0 cell, the uncertainties in the velocity measurement here are large. The normalized velocity VL/κ is plotted as a function of Ra in fig. 57 (a). For $Ra > 1 \times 10^8$, the velocity has a scaling relation with Ra,

$$\frac{V}{\kappa/L} = 0.16 Ra^{0.49 \pm 0.02} \quad . \tag{3.19}$$

The change at $Ra = 10^8$ (fig. 57 (b)), corresponds to the soft - hard turbulence transition.

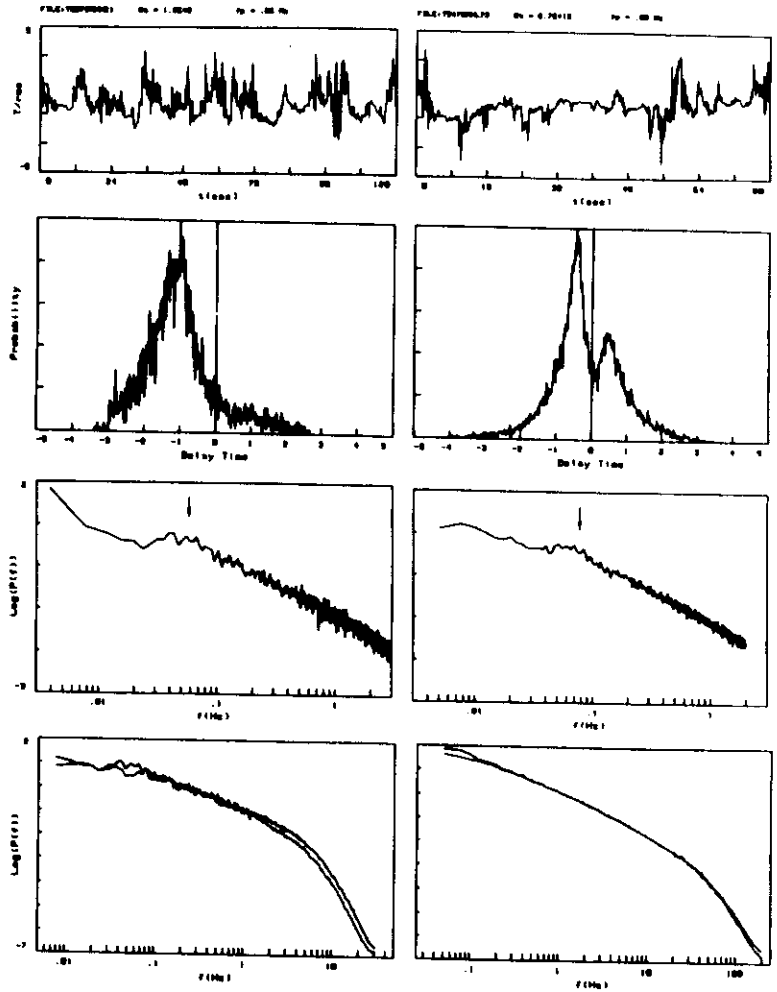

(a) (b)

Figure 56. The side wall bolometers, their time series, delay time distributions, low frequency part of the power spectra, and the comparison with the center ones. For (a) $Ra = 1.9 \times 10^9$ (left) and (b) 6.7×10^{12} (right).

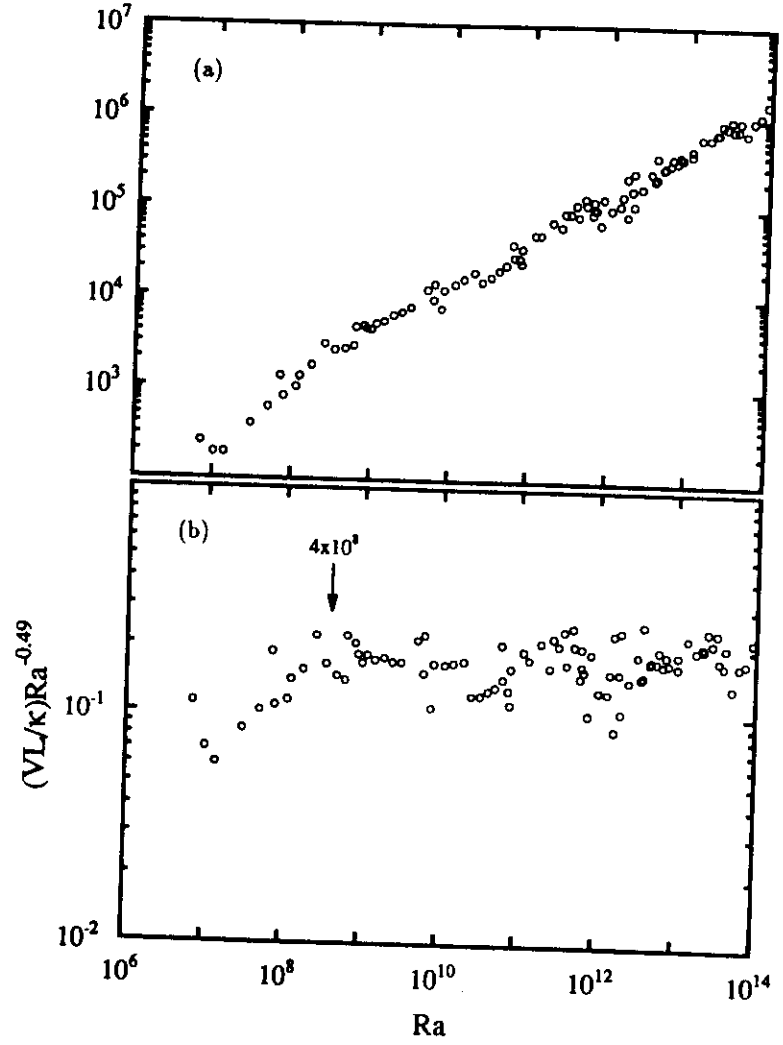

Figure 57. Velocity V, (a) VL/κ vs. Ra (b) $(VL/\kappa)Ra^{-0.49}$ vs. Ra.

The rms value of the side wall bolometer is plotted against Ra in fig. 58 (a). It has similar Ra dependence as the center one. For $Ra > 1 \times 10^8$, it scales with Ra with an exponent -0.145 ± 0.01. The relation changes at $Ra = 10^8$, another signature of the soft-hard transition.

Here again the power spectrum of the side wall bolometer has the same shape as the center one, but extends to a higher frequency (fig. 59 (a) & (b)). This frequency shift depends on the stability of the large scale flow. As shown in fig. 56, the shift is large for $Ra = 1.9 \times 10^9$ where the large scale velocity is stable, and small for (b) $Ra = 6.7 \times 10^{12}$.

The circulation frequency can be calculated from the large scale velocity V and the circumference 120 cm. In fig. 56, this frequency, marked as f_p, agrees with the starting frequency of the cascade. However, there is no resonant peak at f_p.

3.2.3 Hard turbulence

In this section, we present experimental results to show the self-similarity and scaling relations of hard turbulence. We shall concentrate on the data from the bolometers at the center of the cell. Figure 60 shows time series for about 5 and 1 circulation time for $1 \times 10^9 < Ra < 5.8 \times 10^{14}$. The time signals are intermittent, similar to the hard turbulence data in the aspect ratio 1.0 cell. For $Ra < 10^{11}$, higher frequency structures develop as Ra increases. For $Ra > 10^{11}$, the signals become more intermittent. The change of frequency range can be seen in the power spectra for $7.0 \times 10^6 < Ra < 4.3 \times 10^{14}$ (fig. 61).

The normalized rms value Θ/Δ is plotted as a function of Ra in fig. 58 (a) and $(\Theta/\Delta)Ra^{0.144}$ is plotted to amplify the change. For $Ra > 5 \times 10^8$, Θ/Δ

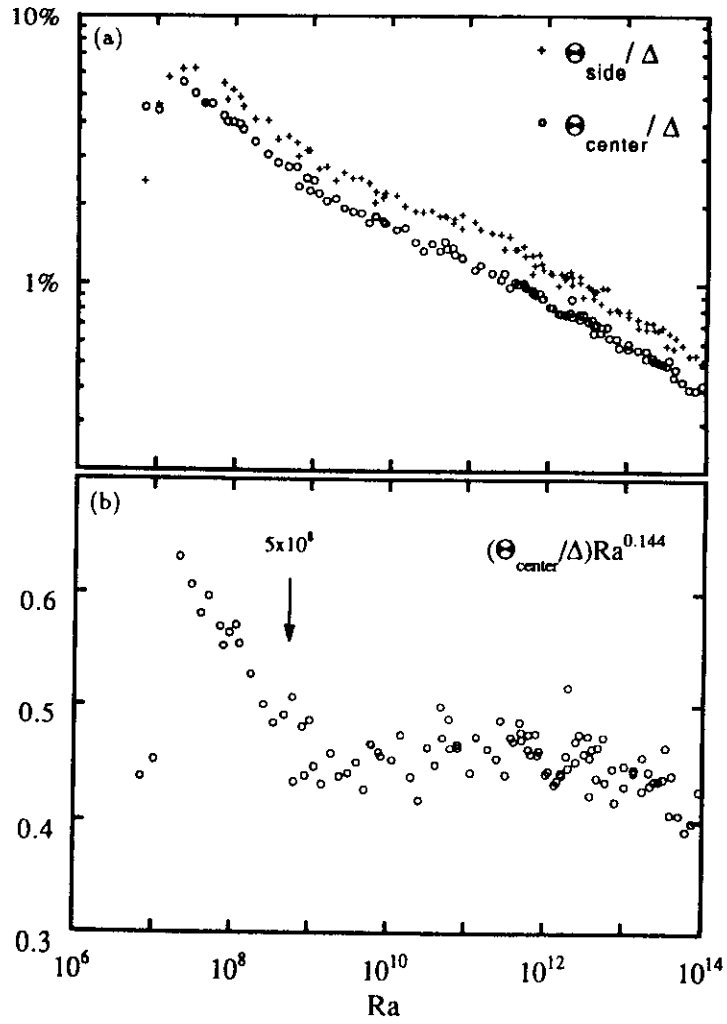

Figure 58. The rms temperature flucuations Θ, (a) Θ/Δ vs. Ra and (b) $(\Theta/\Delta)Ra^{0.144}$ vs. Ra. Θ/Δ are the normalized rms temperature fluctuations for the center (circle) and side (cross) bolometers. Only center data is plotted in (b).

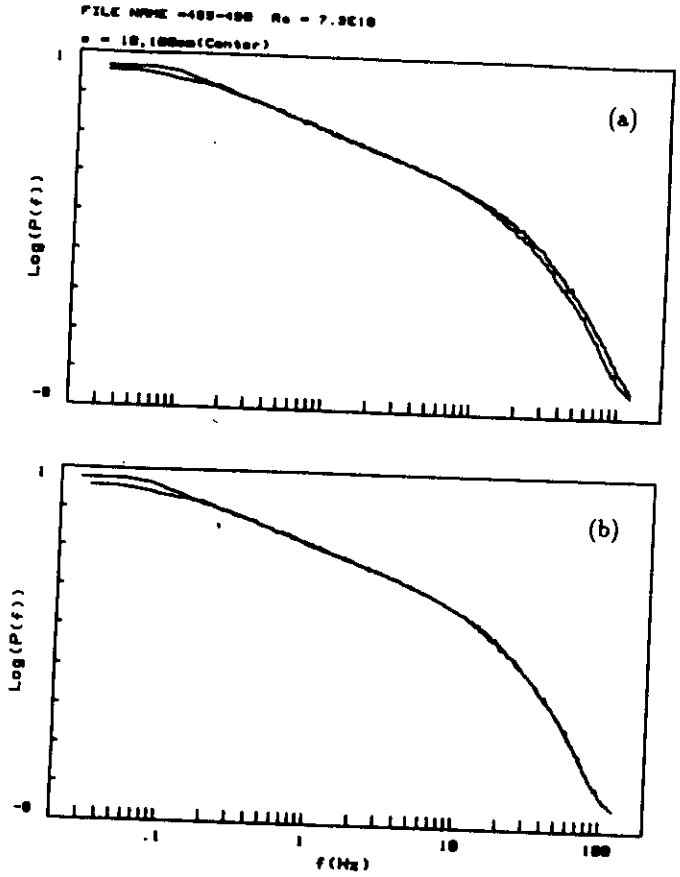

Figure 59. The power spectrum of the side bolometer compared with the center one. For $Ra = 7.3 \times 10^{10}$ (a) The side one extends to higher frequencies, (b) they have the same shape.

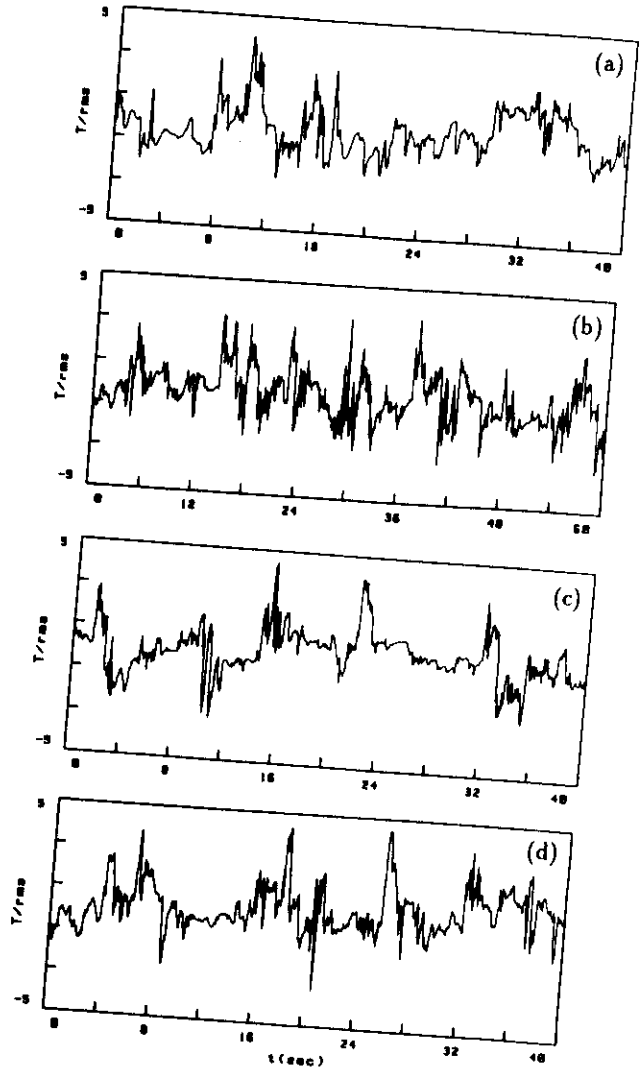

Figure 60. The center time series for $1 \times 10^9 < Ra < 6 \times 10^{14}$. (a) $Ra = 1.0 \times 10^9$, (b) 7.3×10^{10}, (c) 6.7×10^{12} and (d) 5.8×10^{14}, The Y axis unit has been normalized by the rms value of each signal, 5 circulation time has been spanned. (e), (f), (g) and (h) are the same data of 1 circulation time.

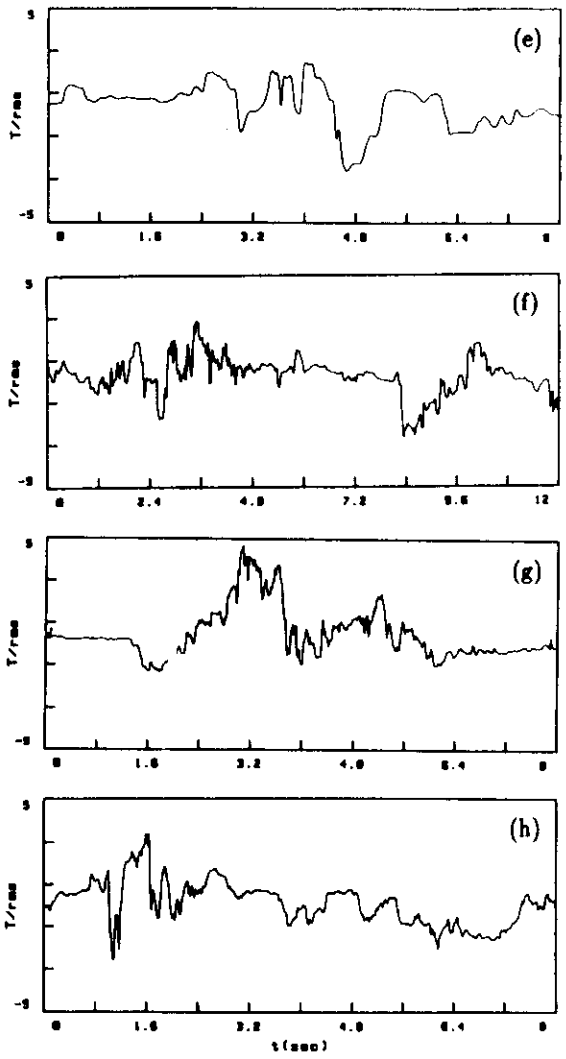

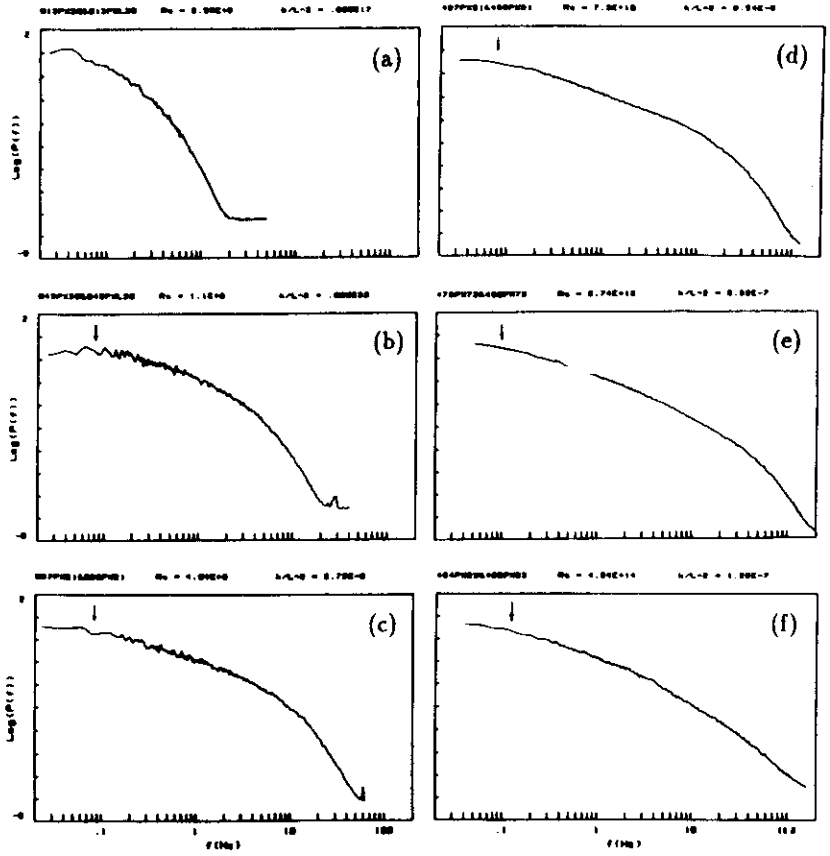

Figure 61. The center power spectra for $1 \times 10^7 < Ra < 4 \times 10^{14}$. (a) $Ra = 7.0 \times 10^8$, (b) 1.1×10^8, (c) 4.0×10^9, (d) 7.3×10^{10} (e) 6.7×10^{12} and (f) 4.3×10^{14}. The arrow indicates the position of the circulation frequency.

follows a simple power law

$$\frac{\Theta_c}{\Delta} = 0.46 \times Ra^{-0.144 \pm 0.006} \quad . \tag{3.20}$$

The change at $Ra = 5 \times 10^8$ shows the soft-hard turbulence transition.

Figure 62 shows the PDF for Ra between 7.0×10^6 and 4.0×10^9. As Ra increases in soft turbulence, the PDF changes from asymmetric to more symmetric, from non-universal to Gaussian-like. In hard turbulence, the PDF remains invariant, as shown in fig. 63. This invariance reflects the self-similarity of hard turbulence in this cell.

The PDF in hard turbulence is non-Gaussian, this can be demonstrated more clearly by plotting the logarithm of the probability against the square of the temperature fig. 64 (b). However, it is not a pure exponential either. In fig. 64 (a) plotting the logarithm of the probability vs. $T^{1.3}$, shows a "stretched" exponential with $\beta = 1.3$. Since the PDF of one point measurement is sensitive to large scale flow, the unsteadiness of the large scale flow in this cell may be responsible for the difference from the pure exponential distribution.

3.2.4 The power spectrum and a transition at $Ra = 10^{11}$

We have shown that in hard turbulence, Nu, velocity and the rms temperature fluctuations scale with Ra, and that the PDF is invariant. These facts show the self-similarity of hard turbulence. However, all these quantities are dominated by the large scale flow structure. Here we study the small scale ones via the power spectrum.

For $Ra < 10^{11}$, the high frequency tail of the power spectra is invariant and can be superposed under translational transformation in log-log plot (fig.

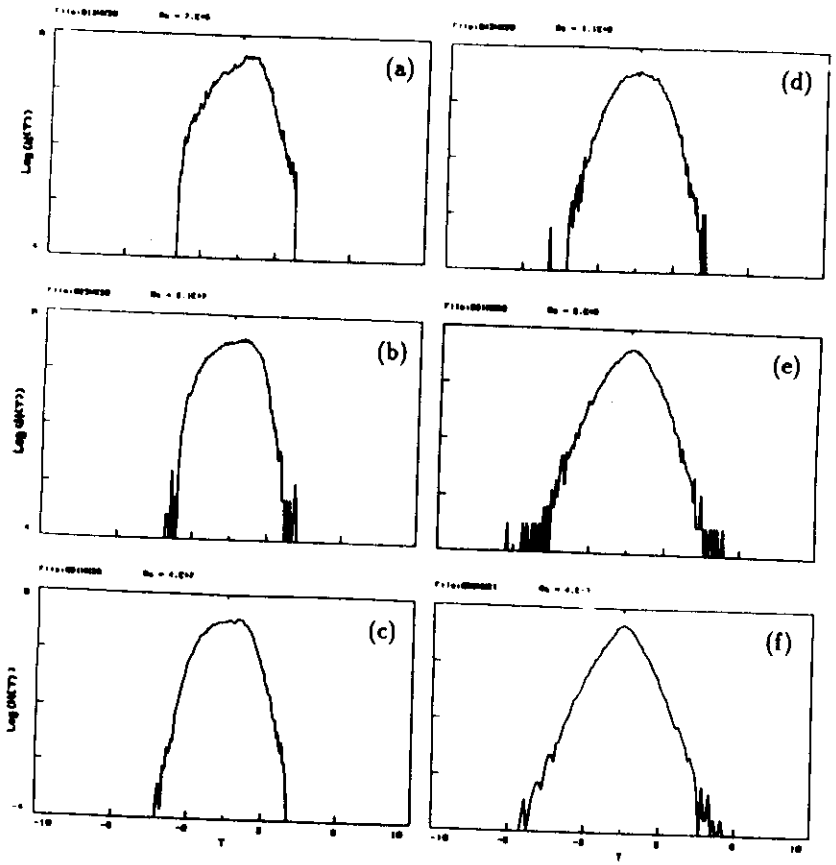

Figure 62. The center PDF, from soft to hard turbulence. (a) $Ra = 7.0 \times 10^6$, (b) 2.1×10^7, (c) 4.0×10^7, (d) 1.1×10^8 (e) 6.0×10^8 and (f) 4.0×10^9.

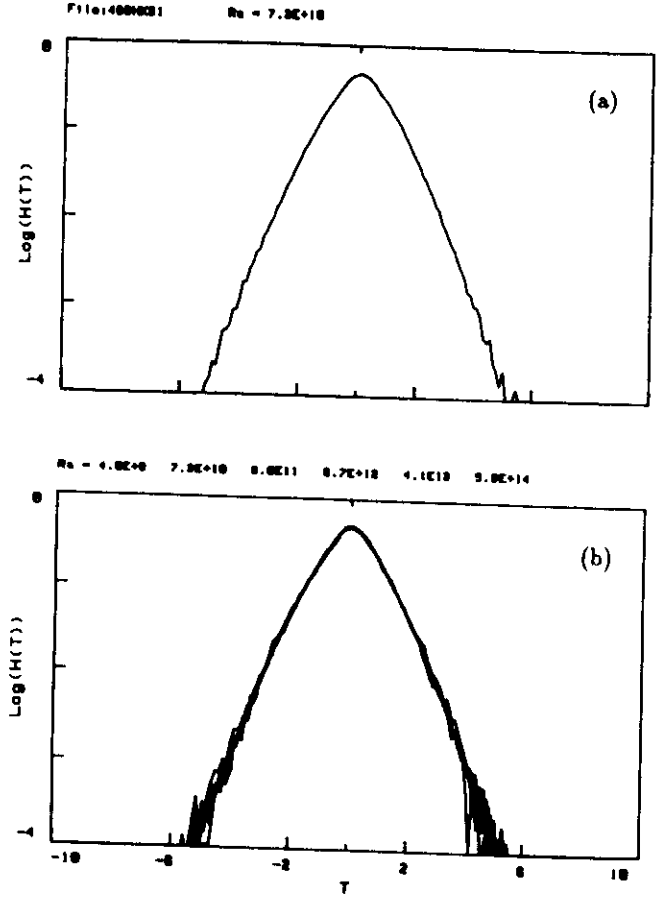

Figure 63. Hard turbulence, the superpositions of PDF. For (a) $Ra = 7.3 \times 10^{10}$ (b) rescaling of all the PDF for $Ra = 4.0 \times 10^{9}$, 7.3×10^{10}, 6.0×10^{11}, 6.7×10^{12}, 4.1×10^{13} and 5.8×10^{14}.

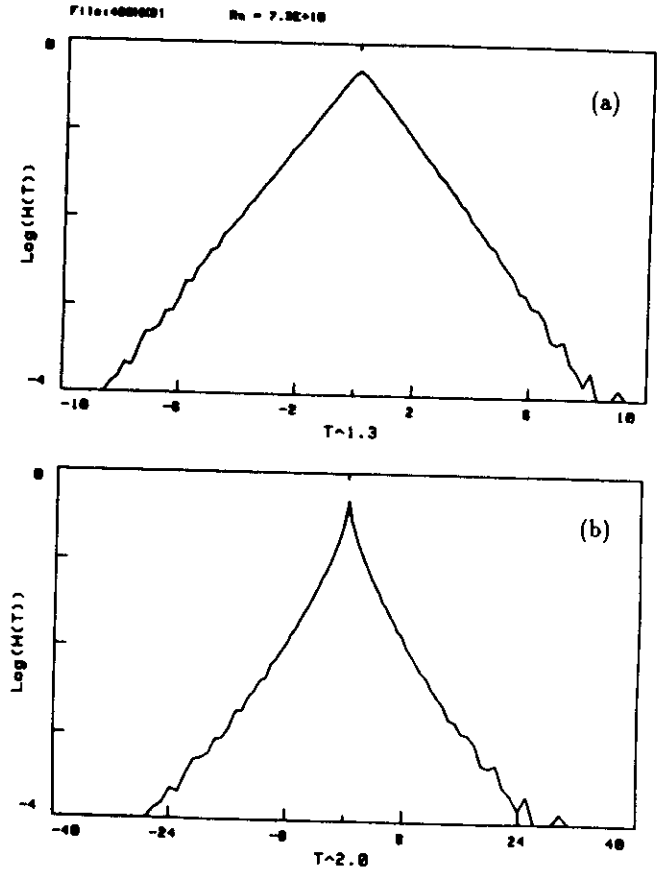

Figure 64. Hard turbulence, $\log(H(T))$ vs. $\pm T^{1.3}$ in (a) and vs. $\pm T^{2}$ in (b). This curve is for $Ra = 7.3 \times 10^{10}$.

65 (a)),

$$\log(f') = \log(f/f_h) \ , \tag{3.21}$$

$$\log(P'(f')) = \log(P(f)/P_h) \ . \tag{3.22}$$

The tail alone can be fitted by a stretched exponential (fig. 66 (b)) described in eq. 3.4 with $\beta = 0.55$. The fitted f_h is plotted in fig. 67 It has actually been used in the above translational transformation to superpose the power spectrum in fig. 65 (a). The Ra dependence of $f_h L^2/\kappa$ can be described as

$$f_h L^2/\kappa = 0.0017 \times Ra^{0.77\pm0.04} \ . \tag{3.23}$$

As shown in fig. 65 (a), a power law develops for increasing Ra. It is shown more clearly in fig. 68 (a) & (b), where the power spectra $P(f)$ is multiplied by $f^{1.4}$. The data for $Ra = 10^{11}$ has the maximum power law range, about 2 decades. A classical fit to the whole curve is a function of a power law with an exponential cut off, expressed in eq. 3.11. Figure 66 (b) shows the quality of the fit for $Ra = 7.3 \times 10^{10}$.

The exponent α for the power law is

$$\alpha = -1.35 \pm 0.05 \ . \tag{3.24}$$

The exponential cut-off frequency f_d is plotted in fig. 67 together with f_h. Since both f_h and f_d characterize the same high frequency tail, they have the same Ra dependence (f_d is about 3.3 times f_h). To study further the power law, we multiply the power spectra $P(f)$ by $\exp(f/f_d)$. The transformed power spectra $P(f) \times \exp(f/f_d)$ are shown in fig. 69 for 5 different Ra below 1×10^{11}. They are superposed together, rescaling f_p to the same value.

However for $Ra > 1 \times 10^{11}$, the data reduction with the translational transformations in eq. 3.21 and 3.22 can no longer work, simply because the

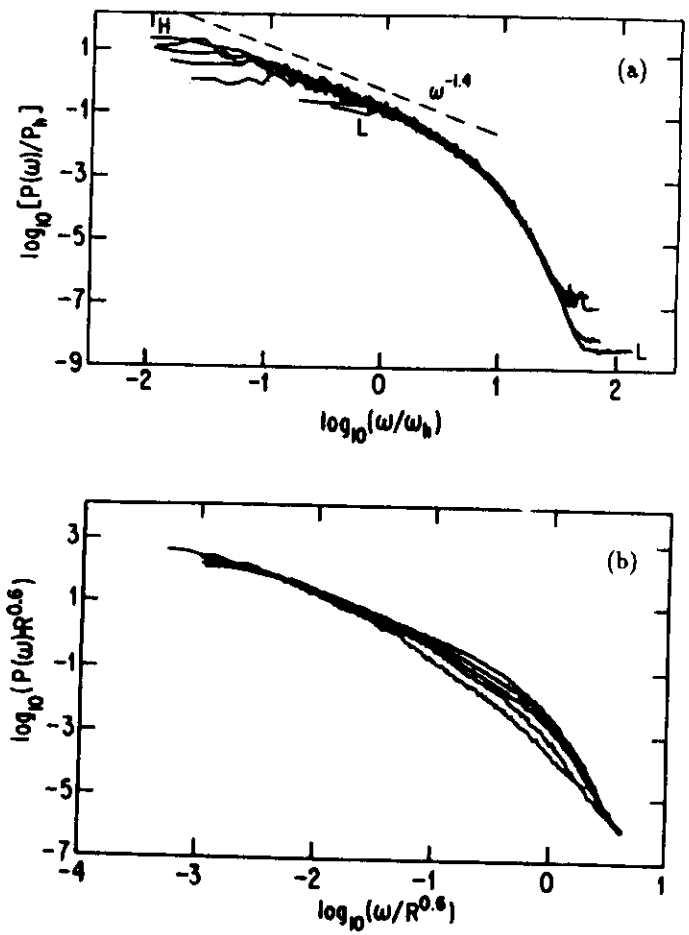

Figure 65. Superposition of the center power spectra for Ra below and above 1×10^{11}. (a) $\log(P(f)/P_h)$ vs. $\log(f/f_h)$ for $7.0 \times 10^6 < Ra < 7.3 \times 10^{10}$, the curve labeled "L" is for lower Ra. (b) $\log(P(f)Ra^{0.6})$ vs. $\log(f/Ra^{0.6})$ for $7.3 \times 10^{10} < Ra < 4.3 \times 10^{14}$, the outer curve is for lower Ra. Here, $\omega \equiv f$.

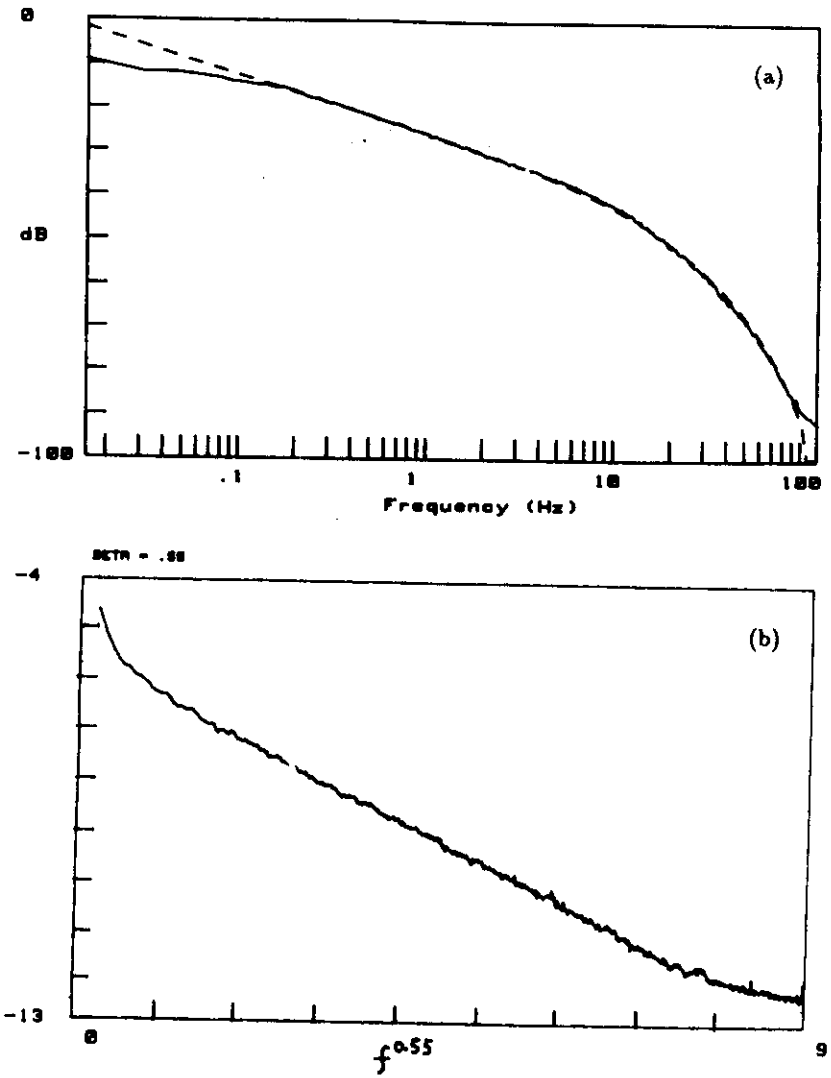

Figure 66. Two different fits to the power spectrum in hard turbulence. For $Ra = 7.3 \times 10^{10}$, (a) the power spectrum is fitted with a power law with an exponential cut off function, (b) $\log(P(f)$ is plotted against $f^{0.55}$ to show the stretched exponential tail.

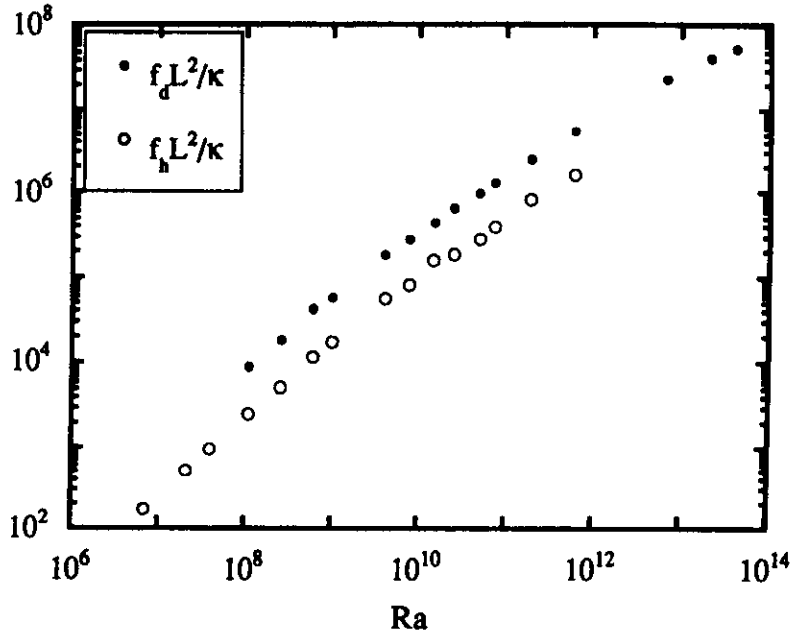

Figure 67. $f_h L^2/\kappa$ and $f_d L^2/\kappa$ vs. Ra. They are the characteristic frequencies for the cut-off tail, related to two different fitting functions.

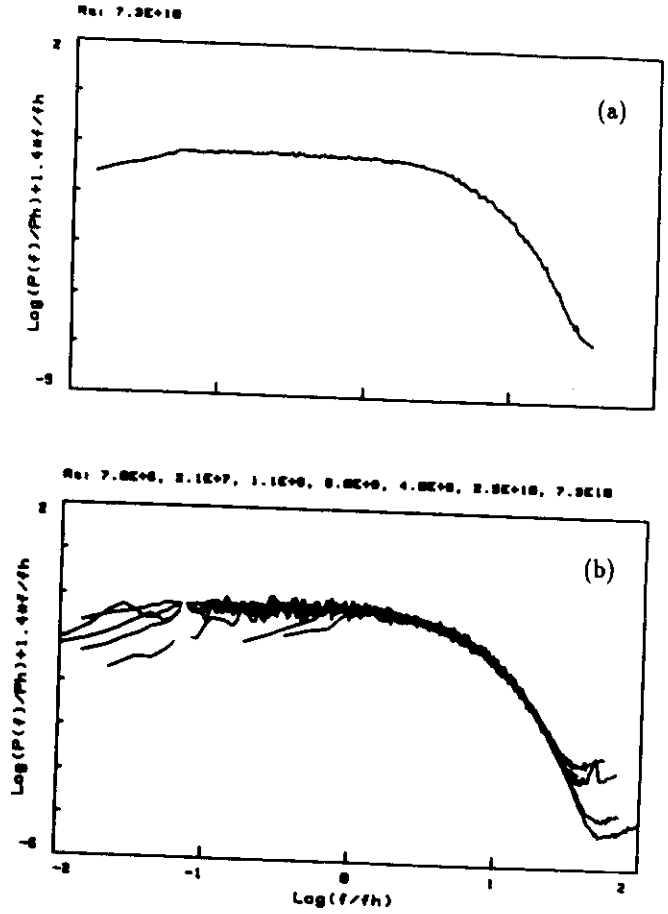

Figure 68. For $Ra < 10^{11}$, $\log(P(f)/P_h \times f^{1.4})$ vs. $\log(f/f_h)$. For (a) $Ra = 7.3 \times 10^{10}$ and (b) $Ra = 7.0 \times 10^6$, 2.1×10^7, 1.1×10^8, 6.0×10^8, 4.0×10^9, 2.5×10^{10} and 7.3×10^{10}.

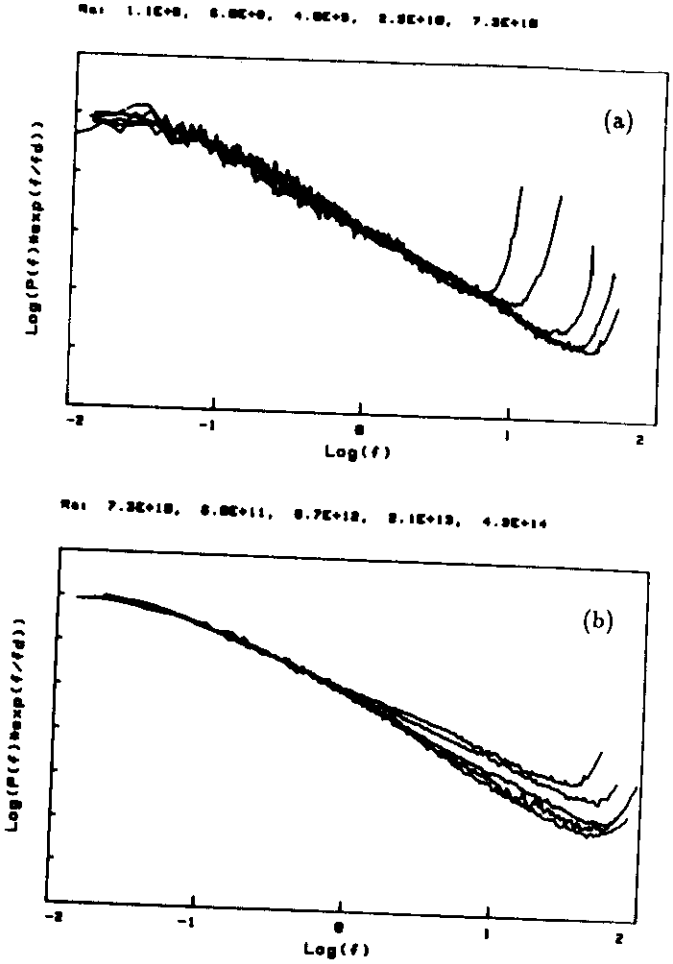

Figure 69. $\mathrm{Log}(P(f)/P_0 \times \exp(f/f_d))$ vs. $\log(f/f_p)$ for Ra below and above 10^{11}. (a) For $Ra < 10^{11}$, they collapse and a power law is revealed in full, (b) while for Ra below, they evolve with Ra.

high frequency part of the power spectra change with Ra. In fig. 65 (b), 5 power spectra for $Ra > 1 \times 10^{11}$ are displaced in a log-log plot to show their different shapes. The specific transformation in fig. 65 (b) is chosen just for the best illustration. If we try to take off the exponential tail by multiplying $P(f)$ with $\exp(f/f_d)$, as we did for Ra below 10^{11}, they do not show a simple power law (fig. 69 (b)). This change has been verified in a different, but related way in calculating the normalized temperature dissipation Q^2 from the time series (Procaccia *et al.* 1991),

$$Q^2 = \frac{\langle(\partial_t T)^2\rangle}{\Theta^2 \kappa^2 / L^4} \quad , \tag{3.25}$$

here Θ^2 is the mean square temperature fluctuations, L^2/κ the time scale and $\partial_t T$ the derivative of the signal. It is found to have different dependence with Ra, below and above 10^{11} (fig. 70).

The power spectrum for $Ra = 4 \times 10^{14}$ (fig. (71 (a)) seems to develop a second power law with an exponent -2.4. In fig. 71 (b) (c), we multiply $P(f)$ by $f^{1.4}$ and $f^{2.4}$ respectively to demonstrate the two power laws. Thus it is possible that the change of power spectra from $Ra = 7 \times 10^{10}$ to $Ra = 4 \times 10^{14}$ is simply a transient from one power law (exponent -1.35) to two power laws (exponent -1.35 and -2.4). In fig. 72 (a) & (b), the 5 power spectra for Ra between 7.3×10^{10} and 4.3×10^{14} have been multiplied with $f^{1.4}$ and $f^{2.4}$ respectively to show the change.

The power spectrum has shown a turbulence transition at $Ra = 10^{11}$. More generally, this transition appears in all the measures related to the high frequencies of the time series, such as the temperature "dissipation" Q^2. As a matter of fact, one can recognize this change from the time series directly (fig. 60 (a)-(d)). Even though it is hard to describe the difference without using statistical measures, we can at least see that the signals for $Ra > 10^{11}$ are

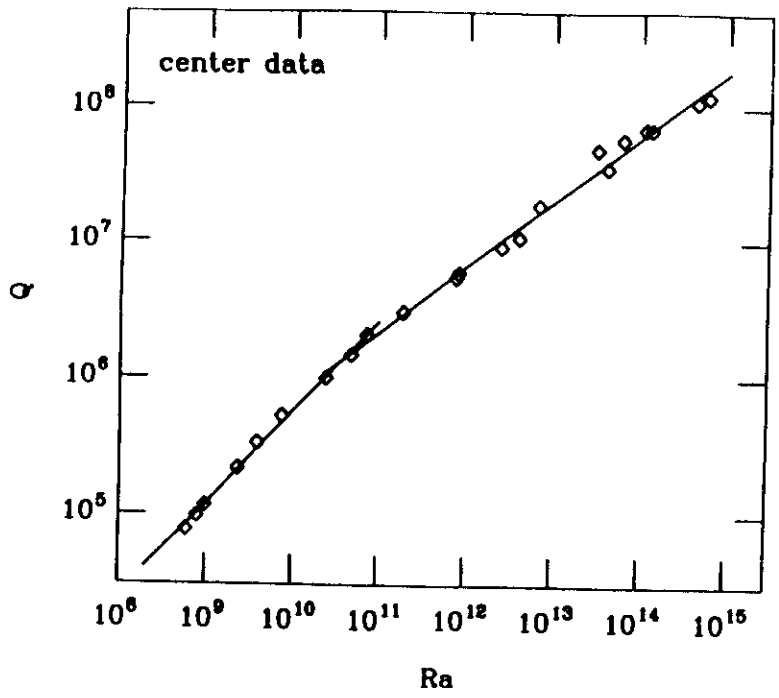

Figure 70. Q vs. Ra, here Q^2 is the normalized temperature dissipation.

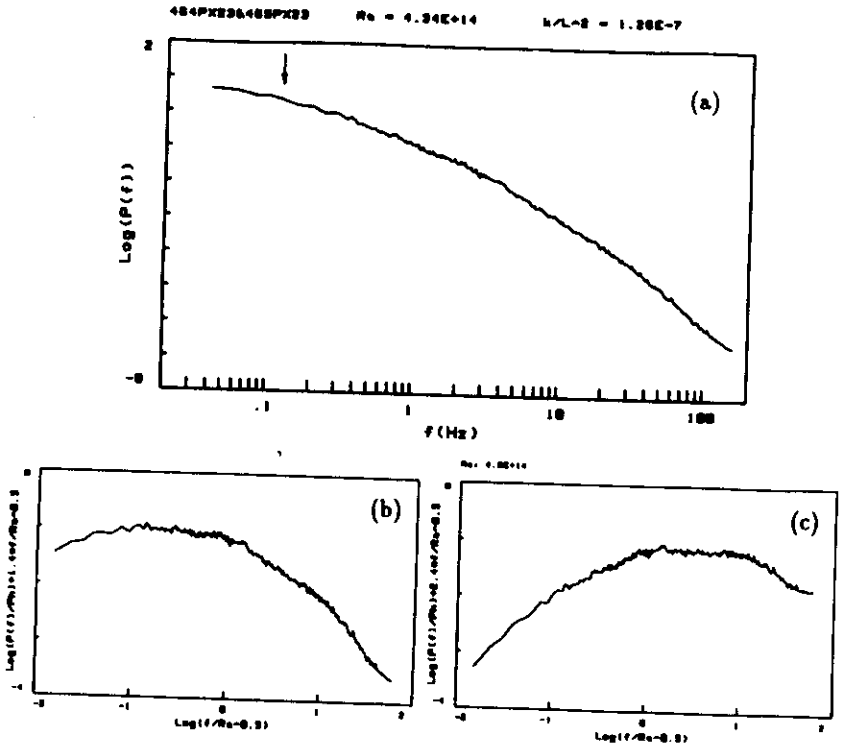

Figure 71. $Ra = 4.3 \times 10^{14}$, the power spectrum shown in different ways. (a) $\log(P(f))$ vs. $\log(f)$ in original form, (b) $\log(P(f) \times f^{1.4})$ vs. $\log(f)$ to demonstrate power law $f^{-1.4}$ and (c) $\log(P(f) \times f^{2.4})$ vs. $\log(f)$ to show the presence of $f^{-2.4}$.

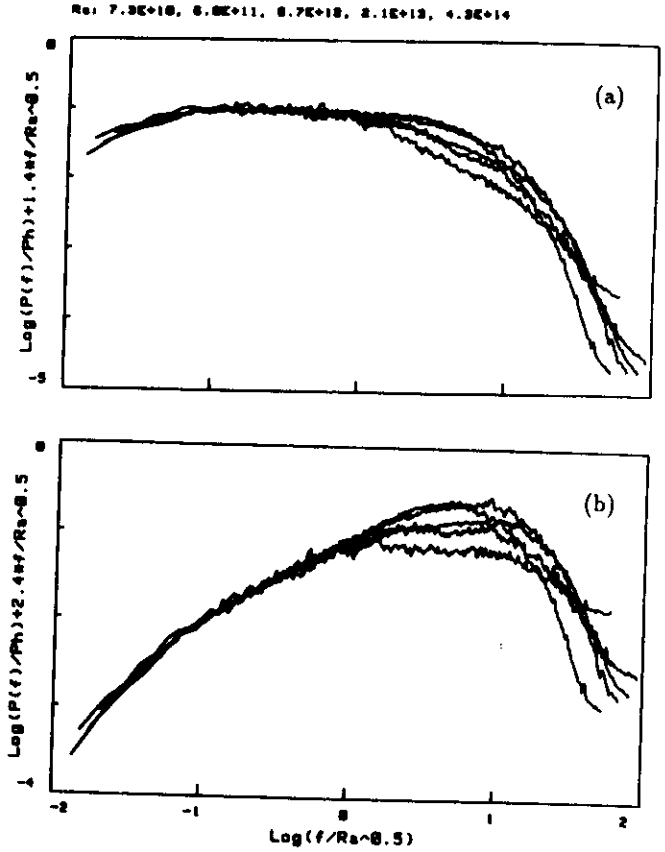

Figure 72. $Ra > 1 \times 10^{11}$, the power spectra shown in different ways. (a) $\log(P(f) \times f^{1.4})$ vs. $\log(f)$ and (b) $\log(P(f) \times f^{2.4})$ vs. $\log(f)$ for $Ra = 7.3 \times 10^{10}$, 6.0×10^{11}, 6.7×10^{12}, 2.1×10^{13} and 4.3×10^{14}.

more intermittent than those below. Since this transition is characterized by the changes at high frequencies (thus of small amplitudes), it is not surprising that it has not effects on measures dominated by large scale structures, such as Nu, PDF etc. To understand this transition, therefore it is necessary to study other quantities related to high frequencies or small structures.

3.3 The aspect ratio 6.7 cell

For small aspect ratio cells, the side wall has large effect on the flow. It is natural to extend the study to a large aspect ratio one, to see how robust are the results obtained.

In this cell, a better temperature regulation led to the most precise measurements of Nu. It starts to scale at $Ra = 10^4$. The scaling exponent is 0.286, consistent with the results in the previous two cells. Bolometers were placed at center of the cell. for $Ra > 10^8$, the PDF are self-similar, non-Gaussian, but not purely exponent al; the power spectrum asymptotically approaches the form of a power law with exponential cut off; the rms temperature fluctuations scales with Ra, w ith an exponent -0.20, smaller than -0.14 in previous cells.

3.3.1 The Nusselt number

The heat conducted by the side wall is estimated as $1 \times 10^{-4}\Delta$ (mW), here Δ is in mK, and the gas conduction $7.5 \times 10^{-5}\Delta$. We have slightly corrected the estimate for wall conduction to have $Nu = 1$ before the onset. The temperature difference off-set Δ_0 for zero heating has an approximate relation with the average temperature T

$$\Delta_0 = 41.5 - 9.3 \times T \ , \tag{3.26}$$

T is in K and Δ is in mK. Most of the measurements are taken with $T < 4.8K$ thus $|\Delta_0| < 3$ mK. The Ra, Nu, and heating power, average temperature etc. are listed in table 6. Nu is plotted as a function of Ra in fig. 73.

For low enough Ra, Nu should be 1. This has been used to calibrate the side wall thermal conduction. Our experimental data shows the onset of convection at $Ra_c = 1700 \pm 100$, quite close to the theoretical value 1708 for infinite aspect ratio. According to Landau's argument (see Landau & Lifshiz, 1985), the velocity and temperature at the onset should scales as $\sqrt{Ra - Ra_c}$, thus $Nu - 1$ increases linearly with $Ra - Ra_c$. The slope may depends on the cell aspect ratio (Behringer & Ahlers 1977; Charlson & Sani 1975). In the insert of fig. 73, Nu is plotted against Ra around the onset region in lin-lin scale.

For all the range of $Ra > 10^4$, Nu scales with Ra. The relation is fitted as

$$Nu = 0.146 \times Ra^{0.286 \pm 0.003} \ . \tag{3.27}$$

In fig 74, we plot $NuRa^{-0.286}$ vs. Ra to demonstrate the scaling relation. The scaling starts at $Ra = 10^4$, much before the soft-hard turbulence transition Ra (10^8) in this cell. Wheres in small aspect ratio cells, the scaling starts at the same Ra (10^8) as the transition.

3.3.2 Local temperature measurements

As is already known (see, Normand *et al.* 1977; Behringer 1985; Manneville1989), in large aspect ratio cells, temporal motions always coupled with the spatial ones (called weak turbulence). In this cell, as soon as the time dependant signals appear at $Ra = 4800$, they are random.

The time series for $Ra = 1.1 \times 10^4$, 9.2×10^5, 2.1×10^8, 8.1×10^9 are shown in fig. 75 for illustration. Similar to soft turbulence signal in small cells, the time

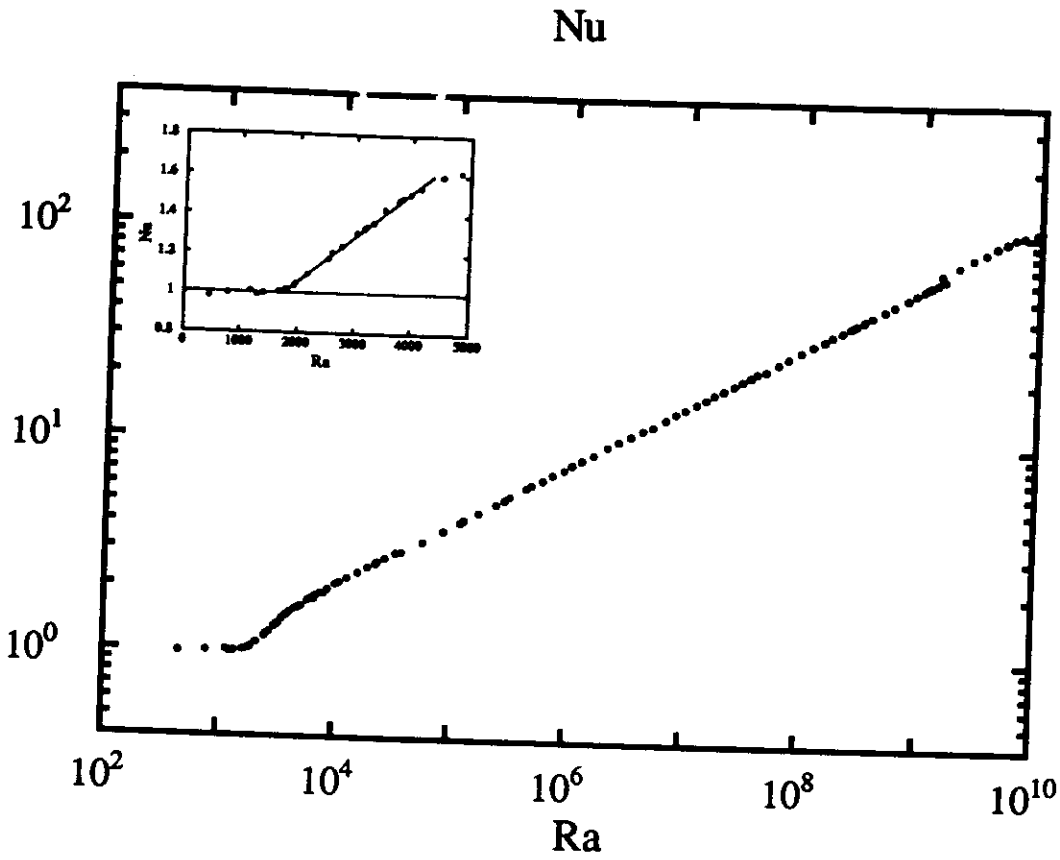

Figure 73. *Nu* vs. *Ra* for aspect ratio 6.7 cell. In the insert, *Nu* is plotted against *Ra* around the onset region in lin-lin scale.

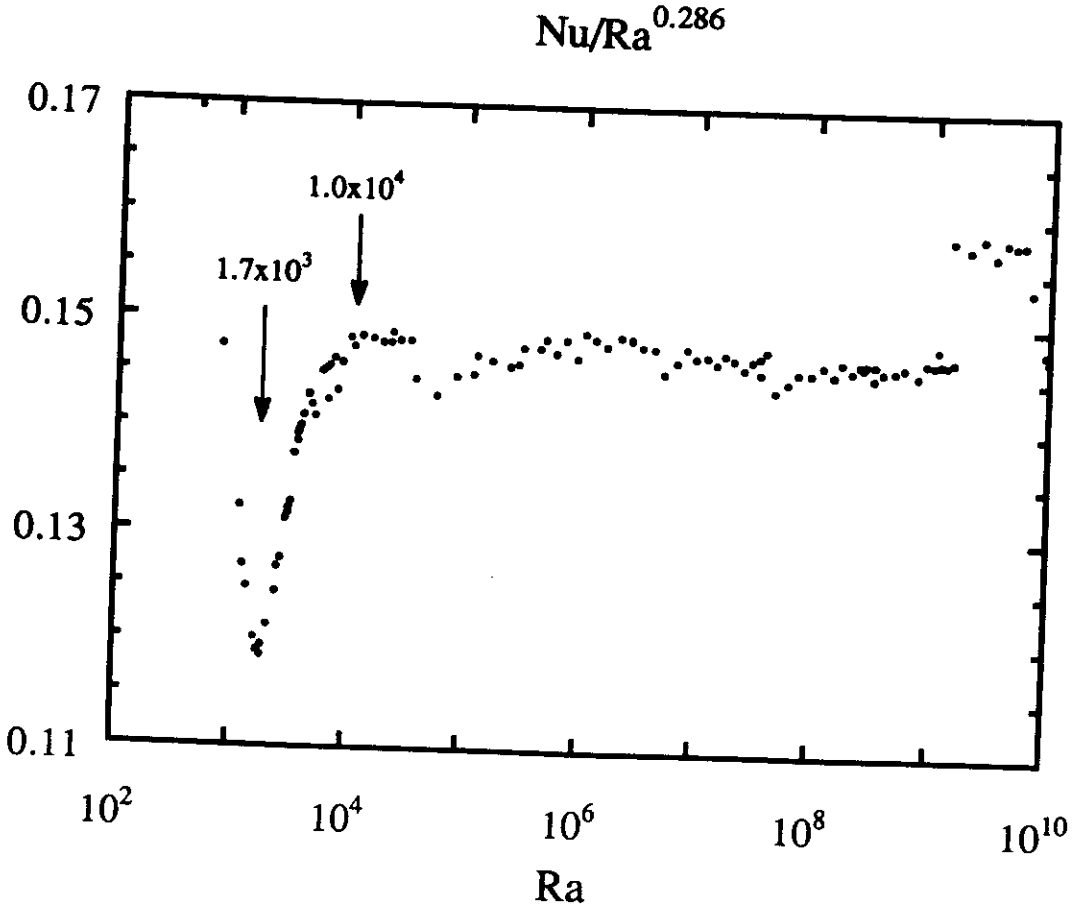

Figure 74. $Nu/Ra^{0.286}$ vs. *Ra*.

series for $Ra < 10^6$ fluctuates constantly without any characteristic features; for Ra above it becomes intermittent, similar to hard turbulence signals in small aspect ratio cells.

We have done standard statistics to characterize the time series. Let us first look at the PDF of the center signal (fig. 76). For $Ra < 10^6$, They are neither invariant with Ra, nor symmetric. The asymmetry of the PDF indicates that the large scale flow structures are complex. As Ra increases, the PDF becomes more symmetric. This implies that the flow structure becomes simpler as Ra increases. As Ra reaches 10^6, the PDF becomes symmetric. We speculate that while small scale flow structures are developing, the complex large scale ones are gradually replaced by a simple one roll circulation, which has been visualized by Krishnamurti and Howard (1981). For $Ra > 10^6$, the PDFs can be superposed, after normalization by their rms value. Therefore the flow motion is self-similar in this Ra regime. The PDF is non-Gaussian, but it is not exponential as the one in hard turbulence of the aspect ratio 1.0 cell.

In fig. 78, the normalized rms temperature fluctuations Θ_c/Δ is plotted as a function of Ra. It decreases for $Ra < 10^5$. After a plateau, it decreases again with a scaling relation with Ra for $Ra > 2 \times 10^7$

$$\frac{\Theta_c}{\Delta} = 1.9 \times Ra^{-0.20 \pm 0.01} \quad . \tag{3.28}$$

The exponent -0.2 is different from the exponents -0.14 of small aspect ratio cells.

From the time series, its PDF and rms temperature fluctuations, we conclude that the soft-hard turbulence transition occurs at this cell as well. As in the small aspect ratio cells, hard turbulence is characterized by the intermittent temperature signals. its PDF is invariant and the rms value scales with Ra. The transition Ra is between 10^7 and 10^8.

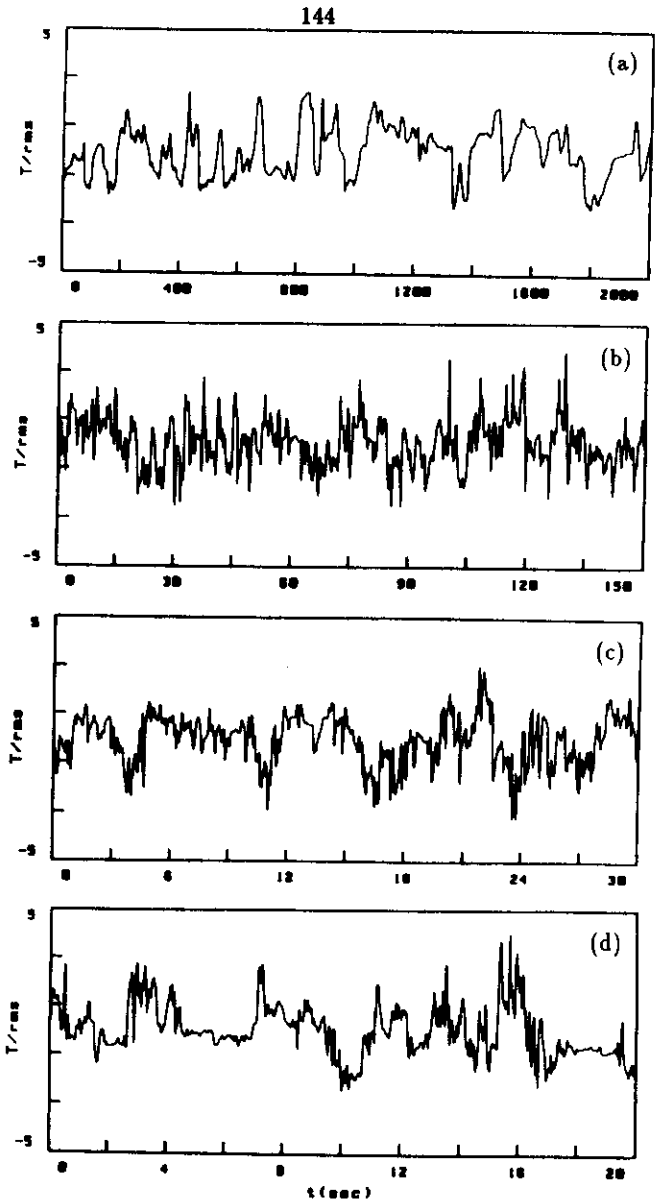

Figure 75. The times series for $1 \times 10^4 < Ra < 8 \times 10^9$. (a) $Ra = 1.1 \times 10^4$, (b) 9.2×10^5, (c) 2.1×10^8, (d) 8.1×10^9.

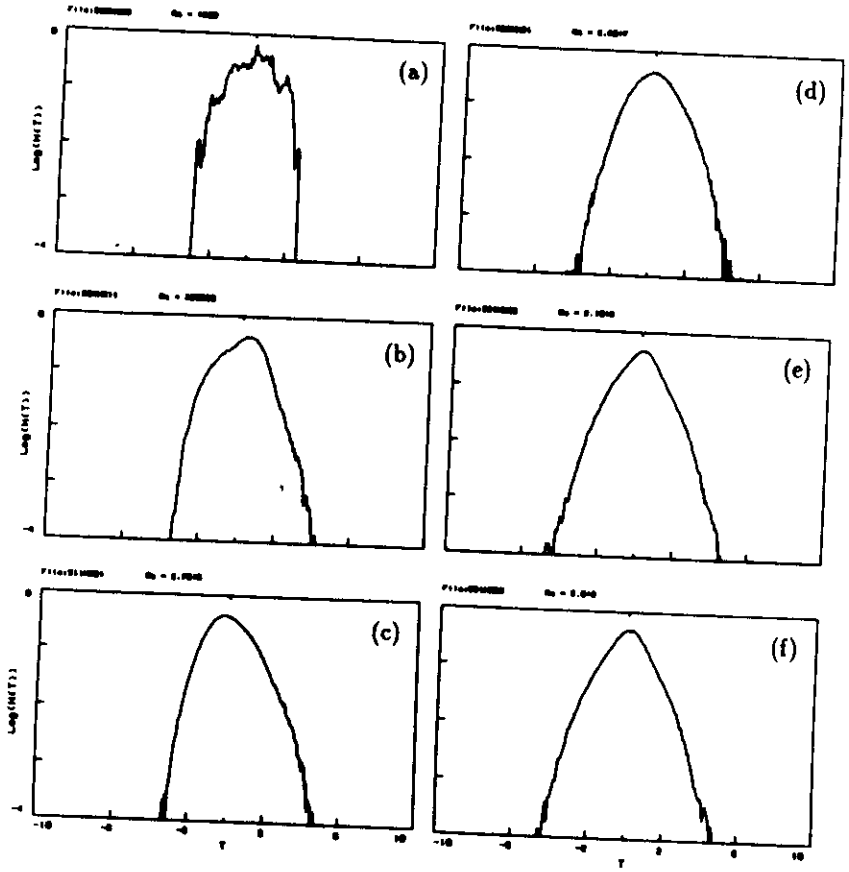

Figure 76. The center PDF, from soft to hard turbulence. For (a) $Ra = 4.8 \times 10^3$, (b) 3.2×10^5, (c) 2.7×10^6, (d) 2.6×10^7, (e) 2.1×10^8 and (f) 5.0×10^9.

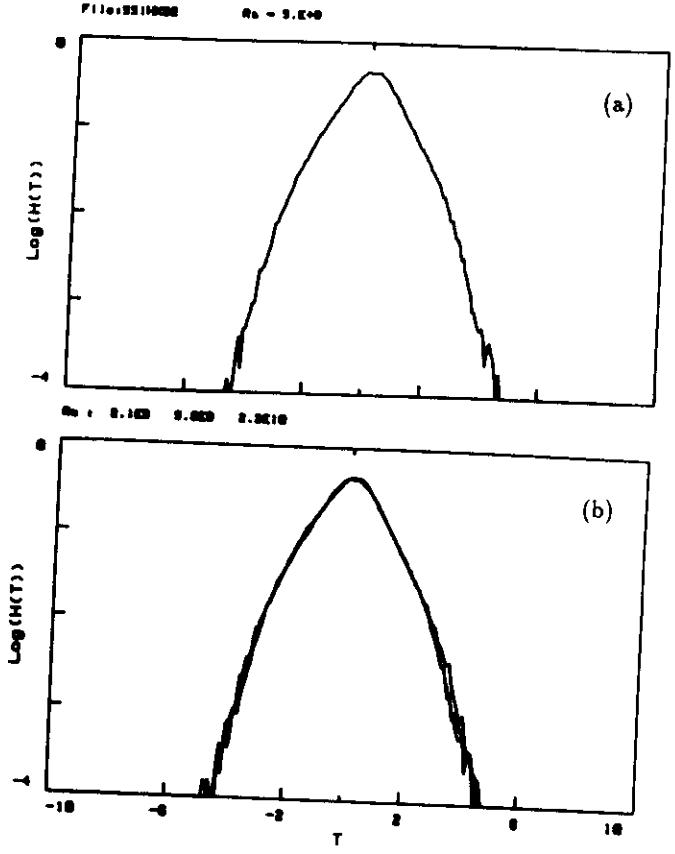

Figure 77. The superposition of PDF for $Ra > 1 \times 10^8$. (a) the PDF for $Ra = 5 \times 10^9$ and (b) the PDF for $Ra = 2.1 \times 10^8$, 5.0×10^9, 2.3×10^{10}.

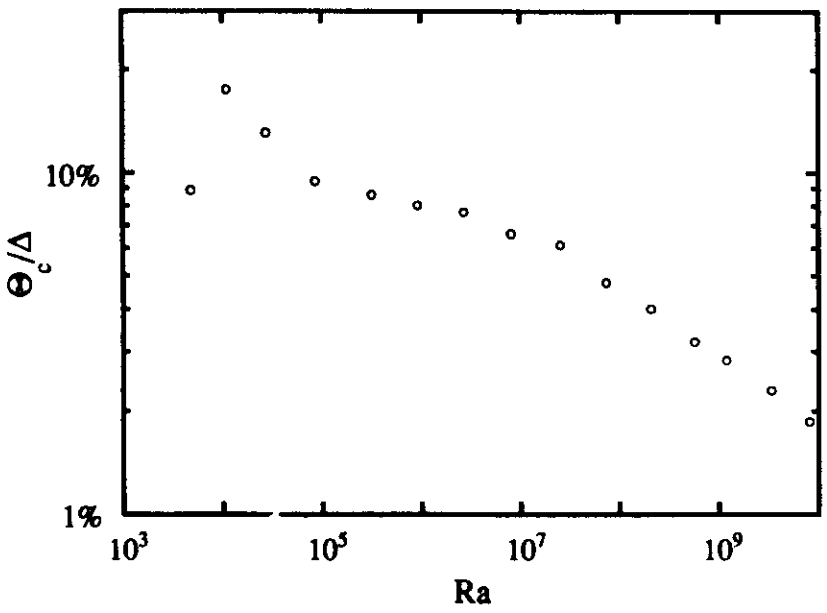

Figure 78. Θ_c/Δ vs. *Ra*. Θ_c/Δ is the normalized rms temperature fluctuations.

The evolution of the center power spectra are sh. wn in fig. 79. They have the same high frequency tail, thus can be superposed (fig. 80 (a)) The power law in the power spectrum changes its exponent with *Ra*, behaves differently from the ones in small aspect ratio cells. However as *Ra* increases, the exponent does asymptotically approaches a constant value of -1.4, the same exponent as in the previous cells. To demonstrate this evolving process, $\log(P(f) \times f^{1.4}$ has been plotted against $\log(f)$ in fig. 80 (b).

In large aspect ratio cells, the interaction among rolls creates wide range of structures and dynamics, which are different from the general turbulence we try to study. As *Ra* increases, these structures are replaced by simpler ones, as indicating by the more symmetric PDF. For $Ra > 10^8$, the PDF has become symmetric and the rms values begin to scale. But this only indicates that the complex large structures has disappears, since they play dominating roles in PDF and rms value, while the smaller structures from the roll interactions have not vanished completely yet. This explains the asymptotic behaviors of the power spectrum.

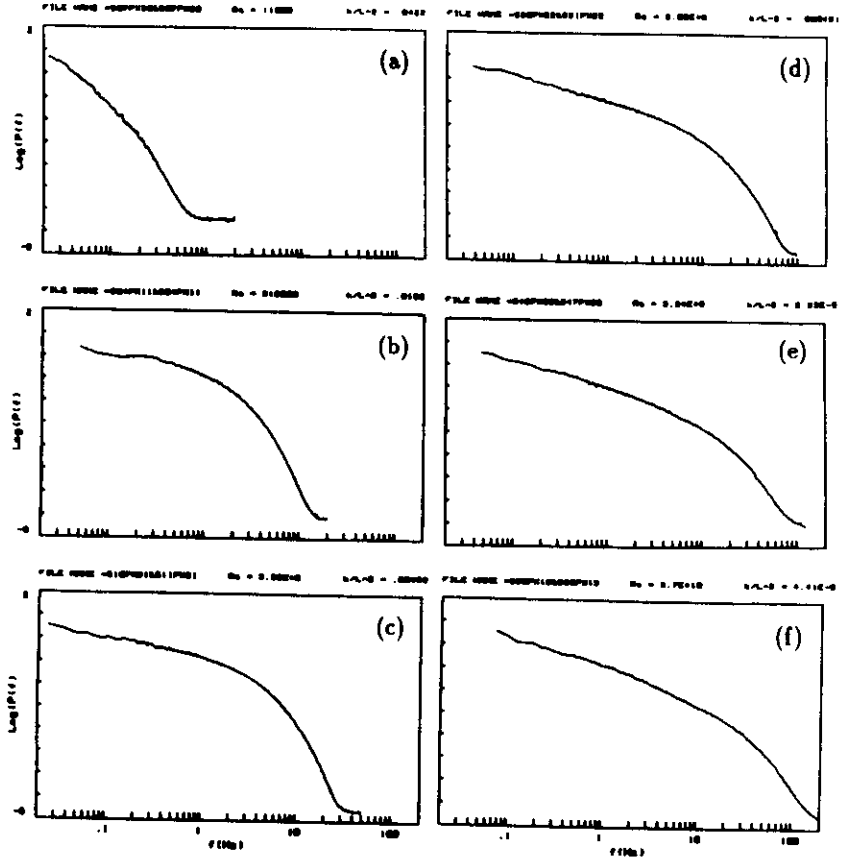

Figure 79. The power spectra for $1 \times 10^4 < Ra < 4 \times 10^{10}$. (a) $Ra = 1.1 \times 10^4$, (b) 3.2×10^5, (c) 2.7×10^6, (d) 2.1×10^8, (e) 3.3×10^9 and (f) 3.7×10^{10}.

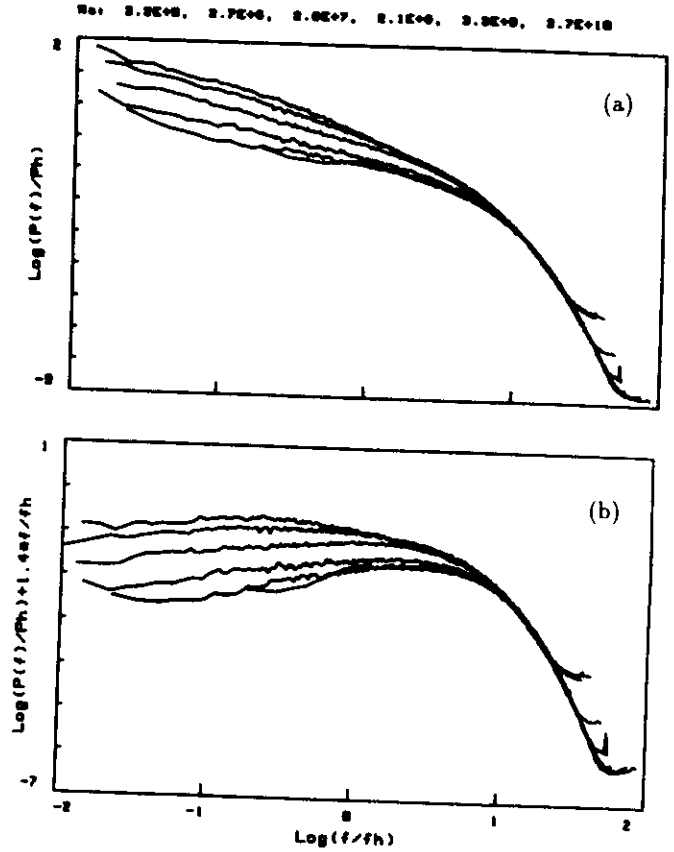

Figure 80. The superposition and transformation of the power spectra. (a) The superposition of the center power spectra according to their tail f_h for $Ra = 3.2 \times 10^5$, 2.7×10^6, 2.6×10^7, 2.1×10^8, 3.3×10^9 and 3.7×10^{10}, (b) $\log(P(f/f_h) \times (f/f_h)^{1.4})$ vs. $\log(f/f_h)$.

3.4 Summary

In the three cells of aspect ratio 1.0, 0.5 and 6.7, two distinct turbulence states, soft and hard turbulence have been discovered. The transition occurs at around $Ra = 10^8$. Soft turbulence is basically due to the dynamics of large scale structures, while hard turbulence is characterized by intermittent dynamics of thermal plumes.

In hard turbulence, all quantities change with Ra as power laws, the scaling relations are summarized in table 1. The Nu value for each decade of Ra and its scaling relations, from different experiments of various aspect ratios are listed in table 2. The PDF in hard turbulence is invariant and non-Gaussian. For $Ra < 10^{11}$, the power spectrum is essentially a flat low frequency part followed by a power law of exponent -1.4, and a cut off tail. The power law range f_d/f_p increases as $Ra^{0.3}$ (Note $f_d \approx 3.2 f_h$ and $f_p \propto V$).

For $Ra > 10^{11}$, a new transition has been observed in the power spectrum, which seems to develop another power law of exponent -2.4. At this Ra, changes are also present in measures related to high frequency signals, such as the temperature dissipation Q^2 and the PDF of differential signals. No change in scaling relations for Nu, Θ/Δ and VL/κ have been observed.

Table 1. The scaling relations in the three cells: $A \times Ra^{\gamma}$.

Aspect Ratio		Nu	Θ_c/Δ	VL/κ	$f_p L^2/\kappa$	$f_h L^2/\kappa\ (Ra < 10^{11})$
0.5	A	0.17	0.46	0.16		0.0017
	γ	0.290	-0.144	0.49		0.77
		±0.005	±0.005	±0.02		±0.04
1.0	A	0.22	0.23	0.31	0.057	0.0013
	γ	0.285	-0.14	0.485	0.490	0.78
		±0.004	±0.01	±0.005	±0.005	±0.02
6.7	A	0.146	1.9			
	γ	0.286	-0.20			
		±0.003	±0.01			

Table 2. Comparison of Nu of different aspect ratios cells. Nu, its value for each decade of Ra and its scaling relations, from different experiments of various aspect ratios.

Pr	Ra 10^6	10^6	10^7	10^8	10^9	10^{10}	Aspect Ratio	Source $Nu = Nu(Ra)$
0.7 Air		7.14	14.1	27.7			1.5 - 4.4	Goldstein & Chu(1969) $0.123Ra^{0.294}$
0.7 Helium			28.5	52.7	96.6	178	0.14	Threlfall(1974) $0.398Ra^{0.265}$
		10.6	20.7	37.3	67.4	122	0.33	Threlfall(1974) $0.328Ra^{0.257}$
			19.7	35.7	68.4	134	0.5	Present work $0.165Ra^{0.291}$
	3.99	10.3	20.4	41.9	79.8	154	1.0	Present work $0.217Ra^{0.285}$
	4.35	8.28	15.8	30.1	57.3		2.5	Threlfall(1975) $0.173Ra^{0.280}$
	4.00	7.83	15:0	28.9	56.0	109	6.7	Present work $0.147Ra^{0.287}$
6.8 Water	4.14	8.27					6.4 - 44	Rossby(1969) $0.131Ra^{0.300}$
			14.6	28.7	56.4		2.5- 4.5	Garon & Goldstein(1973) $0.130Ra^{0.293}$
	4.49	8.52	16.2	30.7			1.5 - 6.0	Chu & Goldstein(1973) $0.183Ra^{0.278}$
				30.3	59.1		3.5 - 14	Tanaka & Miyata(1980) $Nu = 0.145Ra^{0.29}$

Table 3. The aspect ratio 1.0 cell, Ra-Nu, and the experimental conditions. The density ρ (g/cm^3), and the pressure P (torr) and temperature T (K) from which ρ is deduced, are in the 1st. column; The heating power Q, temperature difference Δ and the average temperature T for a convection state are in the last three columns.

P,T, ρ	Ra	Nu	Pr	Q(mW)	Δ(mK)	T(K)
1.830t	1.680e+05	4.950	0.6380	1.672	377.0	4.669
4.479K	1.730e+05	5.010	0.6380	1.743	389.0	4.675
2.620e-05	1.780e+05	5.080	0.6380	1.817	401.0	4.681
	1.870e+05	5.210	0.6380	1.968	425.0	4.692
	1.970e+05	5.330	0.6380	2.126	450.0	4.705
	2.060e+05	5.450	0.6380	2.289	475.0	4.718
	2.170e+05	5.530	0.6380	2.459	504.0	4.732
	2.260e+05	5.650	0.6380	2.634	529.0	4.745
	2.310e+05	5.720	0.6380	2.724	542.0	4.751
	2.360e+05	5.760	0.6380	2.816	557.0	4.758
	2.400e+05	5.830	0.6380	2.909	569.0	4.764
	2.450e+05	5.880	0.6380	3.003	583.0	4.772
	2.630e+05	6.040	0.6380	3.346	632.5	4.797
	2.790e+05	6.240	0.6380	3.708	681.0	4.821
	3.040e+05	6.430	0.6380	4.256	757.0	4.859
2.100t	6480	1.120	0.6370	0.01892	10.90	4.491
4.485K	7630	1.210	0.6370	0.02289	12.70	4.491
3.010e-05	8750	1.330	0.6370	0.02724	14.40	4.492
	1.100e+04	1.580	0.6370	0.03708	17.90	4.494
	1.380e+04	1.740	0.6370	0.04843	22.20	4.496
	1.960e+04	2.050	0.6370	0.07567	31.40	4.501
	3.350e+04	2.640	0.6370	0.1483	52.70	4.512
	5.890e+04	3.290	0.6370	0.3027	93.10	4.532
	1.050e+05	4.050	0.6370	0.6364	168.0	4.569
	1.220e+05	4.260	0.6370	0.7749	197.0	4.584
	1.330e+05	4.380	0.6370	0.8747	217.0	4.594
3.580t	1.860e+05	5.550	0.6370	0.4729	102.0	4.531
4.480K	2.620e+05	6.100	0.6410	0.7272	145.0	4.553
5.130e-05	3.110e+05	6.620	0.6370	0.9270	173.0	4.567
	3.360e+05	6.860	0.6370	1.036	187.0	4.574
	3.640e+05	7.010	0.6370	1.151	204.0	4.582
	5.200e+05	7.970	0.6380	1.892	298.0	4.631
	8.280e+05	9.320	0.6380	3.708	502.0	4.732
	1.150e+06	10.30	0.6370	6.129	743.0	4.853
6.120t	2.250e+05	5.870	0.6390	0.3027	55.90	4.846
4.828K	2.960e+05	6.570	0.6390	0.4359	74.30	4.855
8.150e-05	4.070e+05	7.620	0.6390	0.6810	104.0	4.870
	6.250e+05	8.880	0.6390	1.211	163.0	4.899

Table 3, *Continued*

P,T, ρ	*Ra*	*Nu*	*Pr*	*Q*(mW)	Δ(mK)	*T*(K)
	9.930e+05	10.40	0.6390	2.289	267.0	4.952
	1.410e+06	11.60	0.6390	3.708	392.0	5.014
	1.840e+06	12.50	0.6400	5.467	534.0	5.085
	2.270e+06	13.50	0.6400	7.567	685.0	5.160
9.090t	5.440e+05	8.540	0.6380	0.3027	46.50	4.505
4.483K	1.020e+06	10.60	0.6380	0.6810	86.40	4.525
1.300e-04	1.570e+06	12.40	0.6380	1.211	133.0	4.548
	2.240e+06	13.50	0.6390	1.892	193.0	4.577
	2.990e+06	14.20	0.6390	2.724	262.0	4.612
	3.750e+06	15.10	0.6390	3.708	335.0	4.650
	4.540e+06	15.90	0.6390	4.843	414.0	4.689
	5.300e+06	16.80	0.6390	6.129	496.0	4.730
	7.700e+06	18.70	0.6390	10.90	780.0	4.873
21.95t	3.130e+06	14.50	0.6420	0.6810	59.60	4.847
4.814K	5.030e+06	16.00	0.6420	1.211	97.70	4.867
2.940e-04	7.730e+06	19.70	0.6420	2.289	153.0	4.894
	1.150e+07	21.00	0.6420	3.708	233.0	4.934
	1.860e+07	25.20	0.6420	7.567	396.0	5.016
	2.070e+07	26.00	0.6420	8.826	447.0	5.041
	2.240e+07	26.80	0.6420	10.01	492.0	5.063
	2.640e+07	29.10	0.6430	12.79	597.0	5.117
33.80t	8.41[illegible]+06	20.10	0.6430	0.6810	49.30	4.506
4.536K	1.30 [illegible]+07	23.20	0.6430	1.211	76.20	4.520
4.830e-04	1.82[illegible] e+07	25.80	0.6440	1.892	107.0	4.536
	2.39 e+07	27.90	0.6440	2.724	143.0	4.553
	3.0[illegible] [illegible]+07	29.70	0.6430	3.708	183.0	4.573
	4.3[illegible] e+07	33.10	0.6430	6.129	300.0	4.617
	5.7[illegible]0e+07	36.00	0.6440	9.156	369.0	4.667
	8.100e+07	39.10	0.6440	14.83	542.0	4.754
	1.110e+08	43.10	0.6440	24.52	797.0	4.881
47.40t	9.470e+06	18.90	0.6460	0.6810	44.90	5.018
5.007K	1.430e+07	22.50	0.6460	1.211	68.80	5.022
6.140e-04	2.330e+07	26.40	0.6460	2.289	113.0	5.027
	3.390e+07	29.60	0.6460	3.708	165.0	5.027
	4.200e+07	31.30	0.6460	4.843	205.0	5.026
	5.030e+07	33.10	0.6460	6.129	247.0	5.030
	6.890e+07	36.40	0.6460	9.156	338.0	5.026
	8.970e+07	39.20	0.6460	12.79	440.0	5.025
	1.130e+08	41.60	0.6460	17.03	554.0	5.024
	1.380e+08	43.90	0.6460	21.87	677.0	5.030
79.00t	3.180e+07	30.50	0.6520	1.211	55.20	4.902
5.125K	6.130e+07	36.10	0.6520	2.724	105.0	4.896
1.010e-03	9.530e+07	41.00	0.6520	4.843	164.0	4.914
	1.360e+08	45.00	0.6520	7.567	234.0	4.913
	1.800e+08	48.50	0.6520	10.90	312.0	4.929
	2.310e+08	51.90	0.6520	14.83	398.0	4.926
	2.850e+08	55.30	0.6520	19.37	490.0	4.918

Table 3, *Continued*

P,T, ρ	*Ra*	*Nu*	*Pr*	*Q*(mW)	Δ(mK)	*T*(K)
	3.480e+08	58.00	0.6520	24.52	593.0	4.904
	4.080e+08	60.50	0.6520	30.27	701.0	4.918
196.0t	2.520e+08	52.10	0.6730	2.724	68.00	5.100
5.102K	3.980e+08	59.00	0.6730	4.843	108.0	5.101
2.570e-03	5.630e+08	65.30	0.6730	7.567	153.0	5.102
	8.410e+08	74.30	0.6730	12.79	229.0	5.099
	1.160e+09	81.30	0.6730	19.37	319.0	5.104
	1.640e+09	90.60	0.6730	30.27	449.0	5.102
	2.180e+09	98.00	0.6730	43.59	599.0	5.102
	2.780e+09	105.0	0.6730	59.33	763.0	5.100
604.0t	3.160e+09	111.0	0.7780	4.843	57.80	5.101
5.097K	4.450e+09	123.0	0.7780	7.567	81.70	5.109
8.770e-03	6.720e+09	138.0	0.7780	12.79	123.0	5.105
	9.290e+09	152.0	0.7780	19.37	170.0	5.103
	1.320e+10	167.0	0.7780	30.27	240.0	5.107
	1.760e+10	181.0	0.7780	43.59	321.0	5.103
	2.230e+10	194.0	0.7780	59.33	407.0	5.104
	2.750e+10	205.0	0.7780	77.49	502.0	5.106
	3.290e+10	216.0	0.7780	98.07	603.0	5.110
	3.890e+10	226.0	0.7780	121.1	712.0	5.109
614.0t	1.310e+10	166.0	0.8560	10.01	84.80	4.526
4.490K	2.950e+10	209.0	0.8510	30.27	202.0	4.598
1.090e-02	5.150e+10	247.0	0.8450	68.10	381.0	4.691
	7.430e+10	274.0	0.8380	121.1	600.0	4.805
	1.120e+11	317.0	0.8220	272.4	1127	5.090
619.0t	2.670e+09	105.0	0.8620	1.211	16.10	4.492
4.490K	4.980e+09	126.0	0.8620	2.724	30.40	4.498
1.100e-02	9.260e+09	150.0	0.8610	6.129	57.30	4.512
	1.800e+10	182.0	0.8590	14.83	114.0	4.540
	3.020e+10	213.0	0.8550	30.27	199.0	4.583
	4.370e+10	237.0	0.8520	51.15	300.0	4.635
856.0t	1.024e+10	160.5	0.9080	6.129	48.60	5.029
5.028K	1.570e+10	184.7	0.9060	10.90	75.30	5.028
1.380e-02	2.510e+10	207.4	0.9060	19.37	119.0	5.028
	3.610e+10	224.2	0.9080	30.27	172.0	5.028
	5.000e+10	245.1	0.9020	47.29	247.0	5.029
	6.440e+10	264.0	0.8970	68.10	330.0	5.028
	8.660e+10	284.1	0.9050	92.70	417.0	5.028
	1.010e+11	300.8	0.8970	121.1	516.0	5.028
1394t	1.400e+11	356.0	1.410	24.52	73.80	5.195
5.197K	1.970e+11	382.0	1.420	36.62	102.9	5.192
2.760e-02	2.500e+11	394.0	1.400	51.15	141.9	5.198
	3.000e+11	437.0	1.340	77.49	193.5	5.197
	4.800e+11	500.0	1.410	121.1	260.4	5.199
	6.000e+11	548.0	1.390	174.3	344.6	5.197

Table 4. The aspect ratio 1.0 cell, Ra, Nu, VL/κ, $f_y L^2/\kappa$, Θ/Δ, κ/L^2 and Pr.

Ra	Nu	VL/κ	$f_y L^2/\kappa$	Θ/Δ(%)	$\kappa/L^2(10^3)$	Pr
2.4700e+05	6.2900	33.800		3.1100	296.00	0.63700
3.0200e+05	6.8600	46.700		4.7100	319.00	0.63700
4.2100e+05	7.9100	69.700		5.2900	378.00	0.63800
5.8600e+05	8.9100	69.700		4.4600	390.00	0.63800
7.4100e+05	9.5600	85.000		4.1100	423.00	0.63800
1.1100e+06	10.800	161.00		7.5500	172.00	0.63800
1.4100e+06	11.900	195.00		8.8100	440.00	0.63800
1.6400e+06	12.500	264.00		9.6900	181.00	0.63800
2.4600e+06	14.200	459.00		11.000	191.00	0.63800
3.3400e+06	15.800	620.00		11.500	196.00	0.63800
4.6500e+06	17.300	935.00		11.400	194.00	0.63800
5.4900e+06	17.400	1610.0		10.900	85.800	0.64000
7.5300e+06	19.700	1440.0		10.000	86.700	0.64000
1.2000e+07	22.900	1440.0		8.6300	86.700	0.64000
1.8500e+07	25.800	1530.0		6.9900	88.700	0.64000
2.3700e+07	28.200	1530.0		6.4300	40.800	0.64400
2.4800e+07	28.400	1440.0		6.0100	93.900	0.64000
3.4800e+07	32.300	1700.0		5.8500	40.900	0.64400
5.8100e+07	36.300	2010.0		4.7100	41.500	0.64400
7.3700e+07	39.200	2210.0		4.6200	42.900	0.64500
9.7200e+07	40.800	1950.0	473.0	4.8800	14.600	0.66100
1.5000e+08	46.800	3050.0	641.5	4.1100	14.600	0.66100
2.5500e+08	55.000	3730.0	810.2	3.7100	14.600	0.66100
3.7900e+08	61.200	4700.0	1020	3.4800	14.700	0.66100
5.5100e+08	67.900	5240.0	1191	3.3000	14.700	0.66100
7.8700e+08	75.400	6600.0	1450	3.1600	14.800	0.66000
1.1600e+09	84.000	7900.0	1687	3.0000	14.900	0.66000
1.1900e+09	83.900	7880.0	1687	3.0600	5.0400	0.70900
1.3900e+09	88.300	7840.0	1815	2.8500	15.200	0.66100
1.6300e+09	96.900	9010.0	2085	2.7900	5.0400	0.70900
2.4700e+09	108.00	11700	2388	2.6200	5.0200	0.70900
3.8300e+09	119.00	14200	2865	2.5000	5.0400	0.70900
5.7200e+09	133.00	16700	3661	2.2900	5.0600	0.70900
8.3900e+09	146.00	19300	4346	2.1200	5.0600	0.70900
1.0200e+10	160.00	23100	4760	2.2200	1.4700	0.90800
1.1300e+10	161.00	23200	5158	2.0700	5.0400	0.70800
1.5700e+10	185.00	30300	6129	1.8600	1.4700	0.90600
2.5100e+10	207.00	35800	7482	1.7800	1.4700	0.90600
3.6100e+10	224.00	41300	8835	1.5500	1.4700	0.90800
5.0000e+10	245.00	46600	9933	1.5300	1.4700	0.90200
6.4400e+10	264.00	55400	11910	1.4800	1.4700	0.89700
8.6600e+10	284.00	60700	12800	1.4700	1.4700	0.90500
1.0100e+11	301.00	66500	13800	1.3300	1.4700	0.89700
1.4000e+11	356.00	94300		1.1600	0.54400	1.4100
1.9700e+11	382.00	1.0600e+05		1.2000	0.54100	1.4200
2.5000e+11	394.00	1.1600e+05		1.0400	0.55000	1.4000
3.0000e+11	437.00	1.2300e+05		1.0200	0.59200	1.3400
4.8000e+11	500.00	1.5600e+05		0.97200	0.55000	1.4100
6.0000e+11	548.00	1.7300e+05		0.95500	0.56300	1.3900

Table 5. The aspect ratio 0.5 cell, Ra, Nu, Θ/Δ, the experimetnal conditions and the fluid properties. The density ρ (g/cm^3), and the pressure P (torr) and temperature T (K) from which ρ is deduced, are in the 1st. column; The heating power Q, temperature difference Δ and the average temperature T for a convection state are in the 5-7th columns; The last four columns are the fluid properties for density ρ at average temperature T. κ in cm^2/sec, χ in mW/cmK.

P,T,ρ	Ra	Nu	Θ/Δ(%)	Q(mW)	Δ (mK)	T (K)	α (1/K)	Pr	$\kappa(10^4)$	$\chi(10^2)$
3.310t	6.960e+06	18.70	4.520	0.5111	36.70	4.316	0.2320	0.6370	3480	8.960
4.294K	1.020e+07	19.90	4.420	0.7986	54.12	4.325	0.2320	0.6370	3490	8.970
4.950e-5	1.380e+07	21.00		1.150	74.00	4.334	0.2310	0.6370	3490	8.990
	1.760e+07	22.20		1.565	95.00	4.345	0.2310	0.6370	3500	9.010
	2.100e+07	24.20	5.570	2.044	114.0	4.354	0.2300	0.6370	3510	9.030
	2.990e+07	26.20	5.090	3.194	165.0	4.379	0.2290	0.6370	3520	9.070
	3.970e+07	27.80	4.680	4.600	223.0	4.405	0.2280	0.6370	3540	9.120
	4.920e+07	29.80	4.660	6.261	281.0	4.437	0.2260	0.6370	3570	9.180
	6.990e+07	32.90	4.230	10.35	417.0	4.504	0.2220	0.6370	3610	9.300
	9.120e+07	35.50	4.030	15.46	570.0	4.582	0.2190	0.6370	3670	9.440
	1.120e+08	38.10	3.960	21.59	732.0	4.662	0.2150	0.6380	3720	9.590
9.720t	7.760e+07	33.40	4.040	1.150	47.40	4.320	0.2330	0.6380	1180	8.970
4.298K	1.240e+08	36.80	3.790	2.044	76.50	4.334	0.2320	0.6380	1190	9.000
1.460e-4	1.750e+08	40.30	3.430	3.194	109.0	4.350	0.2310	0.6380	1190	9.020
	2.560e+08	45.60	3.080	5.398	159.0	4.376	0.2300	0.6380	1200	9.080
	3.410e+08	50.70	2.860	8.177	220.0	4.407	0.2280	0.6380	1200	9.130
	4.690e+08	55.50	2.770	12.78	312.0	4.453	0.2260	0.6380	1220	9.210
	6.010e+08	59.90	2.760	18.40	413.0	4.503	0.2230	0.6390	1230	9.310
	8.020e+08	65.70	2.510	28.75	579.0	4.586	0.2190	0.6390	1250	9.460
	1.000e+09	70.50	2.460	41.40	765.0	4.680	0.2150	0.6390	1270	9.620
26.70t	6.300e+08	56.80	2.340	2.044	50.00	4.3[illegible]	0.2350	0.6420	428.0	8.990
4.301K	8.750e+08	63.50	2.260	3.194	69.90	4.335	0.2380	0.6420	429.0	9.010
4.020e-4	1.150e+09	69.20	2.210	4.600	91.60	4.341	0.2340	0.6420	429.0	9.020
	1.440e+09	74.30	2.070	6.261	117.0	4.359	0.2330	0.6420	431.0	9.060
	1.890e+09	82.10	2.110	9.231	155.0	4.379	0.2320	0.6420	433.0	9.090
	2.420e+09	87.90	1.950	12.78	200.0	4.401	0.2310	0.6420	435.0	9.140
	3.140e+09	94.30	1.890	18.40	267.2	4.435	0.2290	0.6420	438.0	9.200
	4.040e+09	103.3	1.860	26.86	353.0	4.478	0.2270	0.6420	441.0	9.280
	5.040e+09	109.2	1.710	36.93	455.0	4.529	0.2250	0.6420	446.0	9.370
	6.190e+09	116.8	1.810	51.11	582.0	4.594	0.2210	0.6420	451.0	9.490
	7.680e+09	126.3	1.730	73.60	763.0	4.684	0.2170	0.6430	459.0	9.650
1.330e-3	7.300e+10	240.0	1.380	115.0	628.0	4.660	0.2260	0.6560	137.0	9.670
88.80t	6.030e+09	112.2	1.820	3.194	39.70	4.321	0.2460	0.6570	124.0	9.050
4.302K	8.200e+09	118.1	1.700	4.600	54.20	4.328	0.2450	0.6570	125.0	9.060
1.360e-3	1.140e+10	132.1	1.610	7.187	75.70	4.339	0.2450	0.6570	125.0	9.080
	1.450e+10	147.3	1.630	10.35	97.60	4.350	0.2440	0.6570	125.0	9.100
	1.970e+10	159.8	1.440	15.46	134.0	4.368	0.2430	0.6570	126.0	9.140
	2.500e+10	172.9	1.330	21.59	172.0	4.387	0.2420	0.6570	126.0	9.170
	3.220e+10	186.8	1.420	30.70	226.0	4.415	0.2400	0.6570	127.0	9.220
	4.030e+10	195.7	1.330	41.40	289.0	4.446	0.2390	0.6570	128.0	9.280
	4.940e+10	211.1	1.360	56.35	362.0	4.483	0.2360	0.6560	129.0	9.350
	6.220e+10	226.2	1.290	79.86	473.0	4.541	0.2330	0.6560	130.0	9.450
	7.710e+10	241.9	1.260	115.0	625.0	4.645	0.2280	0.6560	133.0	9.640
3.740e-3	5.970e+11	442.0	1.020	204.4	593.0	4.699	0.2490	0.6940	47.20	9.900
246.9t	4.700e+10	203.3	1.450	4.600	31.10	4.317	0.2790	0.7030	40.60	9.230
4.302K	5.980e+10	216.3	1.370	6.261	39.70	4.321	0.2790	0.7030	40.60	9.230
3.990e-3	7.820e+10	242.4	1.250	9.231	52.20	4.328	0.2780	0.7030	40.70	9.250

Table 5, *Continued*

P,T,ρ	Ra	Nu	Θ/Δ(%)	Q(mW)	Δ (mK)	T (K)	α (1/K)	Pr	$\kappa(10^4)$	$\chi(10^8)$
	1.130e+11	264.6	1.130	14.09	75.70	4.339	0.2770	0.7030	40.80	9.270
	1.340e+11	277.4	1.180	18.40	90.60	4.347	0.2760	0.7020	40.90	9.290
	1.870e+11	304.8	1.100	28.75	128.0	4.365	0.2750	0.7020	41.00	9.320
	2.430e+11	332.4	1.040	41.40	169.0	4.387	0.2730	0.7020	41.30	9.360
	3.140e+11	357.4	0.9710	59.06	223.0	4.415	0.2710	0.7010	41.50	9.410
	3.990e+11	383.6	1.000	83.08	290.0	4.448	0.2690	0.7010	41.80	9.470
	5.070e+11	417.0	0.9690	122.8	389.0	4.526	0.2630	0.7000	42.50	9.610
	6.200e+11	450.1	0.9510	174.9	505.0	4.615	0.2570	0.6990	43.40	9.770
	7.600e+11	485.3	0.9250	258.7	676.0	4.747	0.2480	0.6980	44.50	10.00
504.0t	4.780e+11	380.3	1.010	12.78	44.00	4.323	0.3650	0.8200	16.00	9.690
4.302K	6.150e+11	422.6	0.9260	18.40	57.00	4.330	0.3640	0.8190	16.10	9.700
9.080e-3	8.090e+11	465.0	0.8810	26.86	75.50	4.340	0.3330	0.8190	16.10	9.720
	1.030e+12	495.3	0.8200	36.93	97.30	4.351	0.3610	0.8180	16.20	9.740
	1.320e+12	525.3	0.7760	51.11	127.0	4.366	0.3590	0.8170	16.20	9.760
	1.640e+12	575.9	0.7650	70.56	159.0	4.384	0.3570	0.8160	16.30	9.790
	1.970e+12	611.5	0.7560	100.2	209.0	4.489	0.3430	0.8100	16.80	9.970
	2.480e+12	651.6	0.7400	139.1	271.0	4.520	0.3390	0.8090	16.90	10.00
	3.170e+12	714.8	0.7250	204.4	360.0	4.569	0.3330	0.8060	17.10	10.10
	4.040e+12	770.1	0.7070	319.4	510.0	4.704	0.3180	0.8000	17.70	10.30
	4.730e+12	806.5	0.6930	460.0	682.0	4.879	0.3000	0.8000	18.50	10.60
1.080e-2	6.740e+12	894.9	0.6780	460.0	607.0	4.859	0.3220	0.6330	15.10	10.90
939.3t	1.600e+12	603.6	0.7710	28.75	51.80	5.069	0.3990	0.9690	9.160	11.70
4.909K	1.940e+12	719.2	0.8780	41.40	62.70	5.063	0.4000	0.9690	9.150	11.70
1.640e-2	2.720e+12	770.6	0.7690	61.84	87.40	5.060	0.4000	0.9700	9.140	11.70
	3.720e+12	783.5	0.6540	86.37	120.0	5.063	0.4000	0.9690	9.150	11.70
	4.590e+12	842.9	0.6560	115.0	149.0	5.065	0.4000	0.9690	9.150	11.70
	5.910e+12	889.5	0.6280	156.5	192.0	5.067	0.4000	0.9690	9.160	11.70
	7.780e+12	979.4	0.5800	225.4	251.0	5.061	0.4000	0.9700	9.140	11.70
	1.030e+13	1048	0.5750	319.4	332.0	5.063	0.4000	0.9690	9.150	11.70
	1.370e+13	1140	0.5700	460.0	440.0	5.062	0.4000	0.9700	9.140	11.70
	1.740e+13	1216	0.5290	626.1	561.0	5.064	0.4000	0.9690	9.150	11.70
	2.090e+13	1314	0.5340	817.7	678.0	5.069	0.3990	0.9690	9.160	11.70
982.0t	3.760e+12	848.8	0.7020	51.11	61.80	5.176	0.4570	1.070	7.120	12.30
4.661K	5.540e+12	902.8	0.6900	79.86	90.80	5.173	0.4580	1.070	7.120	12.30
2.000e-2	7.310e+12	983.3	0.6250	115.0	120.0	5.174	0.4570	1.070	7.120	12.30
	1.030e+13	1059	0.5980	174.9	169.0	5.178	0.4560	1.070	7.120	12.30
	1.350e+13	1141	0.5680	247.4	222.0	5.176	0.4570	1.070	7.120	12.30
	1.740e+13	1240	0.5640	345.5	286.0	5.176	0.4570	1.070	7.120	12.30
	2.190e+13	1323	0.5170	460.0	357.0	5.169	0.4590	1.070	7.120	12.30
	2.770e+13	1421	0.5040	626.1	453.0	5.168	0.4590	1.070	7.120	12.30
	3.390e+13	1513	0.5220	817.7	555.0	5.172	0.4580	1.070	7.120	12.30
	4.060e+13	1595	0.4820	1035	656.0	5.174	0.4570	1.070	7.120	12.30
1424t	2.440e+13	1424	0.5130	156.5	99.90	5.207	0.7890	1.520	3.650	14.00
5.148K	3.140e+13	1465	0.4970	204.4	126.9	5.199	0.7940	1.530	3.630	14.00
2.960e-2	3.870e+13	1562	0.4490	270.4	157.0	5.202	0.7920	1.530	3.640	14.00
	5.000e+13	1662	0.4320	372.6	204.0	5.205	0.7900	1.520	3.640	14.00
	6.100e+13	1766	0.4050	491.1	253.0	5.215	0.7830	1.520	3.660	14.00
	7.340e+13	1863	0.4020	626.1	306.0	5.217	0.7820	1.520	3.670	14.00
	8.880e+13	1983	0.4180	817.7	375.0	5.227	0.7750	1.510	3.690	14.00
	1.080e+14	2096	0.3860	1035	449.0	5.229	0.7740	1.510	3.690	14.00
	1.260e+14	2199	0.3700	1278	528.0	5.223	0.7780	1.510	3.680	14.00
1553t	1.140e+14	2105	0.3660	539.8	205.0	5.419	1.060	1.910	2.480	16.00
5.148K	1.360e+14	2280	0.3300	817.7	287.0	5.432	1.050	1.900	2.510	16.00
3.750e-2	2.120e+14	2467	0.3110	1278	415.0	5.466	1.010	1.870	2.570	15.90
	2.670e+14	2629	0.2810	1840	562.0	5.504	0.9670	1.830	2.630	15.90

Table 6. The aspect ratio 6.7 cell, Ra, Nu, Θ/Δ, and the experimental conditions. The density ρ (g/cm^3), and the pressure P (torr) and temperature T (K) from which ρ is deduced, are in the 1st. column; The heating power Q, temperature difference Δ and the average temperature T for a convection state are in the last three columns.

P,T, ρ	Ra	Nu	Θ/Δ(%)	Pr	Q(mW)	Δ(mK)	T (K)
1.050t	456.0	0.9820		0.6360	1.150	61.90	4.394
4.363K	788.0	0.9990		0.6360	2.044	108.5	4.417
1.545e-05	1190	1.010		0.6360	3.194	167.6	4.447
	1410	1.000		0.6360	3.865	202.1	4.476
	1670	1.010		0.6360	4.600	239.0	4.483
	1790	1.020		0.6360	5.071	260.5	4.505
	1950	1.050		0.6360	5.398	276.0	4.466
	2170	1.100		0.6360	6.261	311.0	4.483
	2330	1.140		0.6360	7.187	345.8	4.537
	2600	1.210		0.6360	8.177	382.7	4.525
	2770	1.240		0.6360	9.231	420.0	4.574
	3040	1.310		0.6360	10.30	458.0	4.562
	3200	1.340		0.6360	11.53	498.0	4.614
	3520	1.430		0.6360	12.78	535.7	4.578
	3840	1.490		0.6360	15.46	618.5	4.674
1.350t	1300	0.9930		0.6360	2.044	108.8	4.418
4.364K	1940	1.040		0.6360	3.194	165.0	4.447
1.986e-05	2540	1.180		0.6360	4.600	220.0	4.475
	3160	1.330		0.6360	6.261	279.2	4.504
	3780	1.480		0.6360	8.177	339.5	4.535
	6640	1.780		0.6360	18.40	657.4	4.694
3.090t	3320	1.360		0.6370	1.150	51.90	4.393
4.364K	3760	1.470		0.6370	1.308	56.40	4.397
4.549e-05	3980	1.510		0.6370	1.477	62.80	4.399
	4160	1.540		0.6370	1.565	65.40	4.401
	4530	1.600		0.6370	1.749	71.30	4.404
	4540	1.600		0.6370	1.749	71.50	4.403
	4840	1.620	8.870	0.6370	1.845	75.10	4.382
	5190	1.640		0.6370	2.044	81.90	4.407
	5870	1.750		0.6370	2.362	91.40	4.388
	6310	1.790		0.6370	2.587	98.60	4.394
	6770	1.830		0.6370	2.822	105.9	4.395
	7450	1.890		0.6370	3.194	117.0	4.402

Table 6, *Continued*

P,T, ρ	Ra	Nu	Θ/Δ(%)	Pr	Q(mW)	Δ(mK)	T (K)
	8010	1.890		0.6370	3.455	126.3	4.407
	8690	1.970		0.6370	3.865	137.9	4.411
	1.010e+04	2.090		0.6370	4.600	157.7	4.398
	1.100e+04	2.130	17.40	0.6370	5.233	175.5	4.432
	1.280e+04	2.240		0.6370	6.261	203.4	4.421
	1.590e+04	2.380		0.6370	8.177	254.0	4.426
	1.930e+04	2.510		0.6370	10.35	309.5	4.431
	2.270e+04	2.630		0.6370	14.09	395.0	4.567
	2.740e+04	2.780	13.00	0.6370	18.40	491.0	4.616
	3.370e+04	2.950		0.6370	25.04	630.5	4.686
10.60t	2.340e+04	2.670		0.6390	1.150	32.50	4.482
4.362K	3.800e+04	2.960		0.6390	2.044	53.10	4.492
1.564e-04	5.810e+04	3.330		0.6390	3.194	76.50	4.479
	8.570e+04	3.770	9.410	0.6390	5.398	118.0	4.464
	1.190e+05	4.150		0.6390	8.177	165.0	4.473
	1.690e+05	4.630		0.6390	12.78	235.0	4.485
	2.410e+05	5.110		0.6390	19.96	337.0	4.488
	3.140e+05	5.580	8.580	0.6390	28.75	448.0	4.523
	4.360e+05	6.130		0.6390	46.12	653.0	4.604
29.10t	1.260e+05	4.270		0.6430	1.150	22.60	4.475
4.365K	2.850e+05	5.370		0.6430	3.194	51.70	4.490
4.315e-04	4.860e+05	6.360		0.6430	6.261	87.80	4.483
	6.010e+05	6.700		0.6430	8.177	109.0	4.494
	7.280e+05	7.140		0.6430	10.35	131.0	4.480
	9.160e+05	7.540	7.990	0.6430	13.56	164.0	4.471
	1.070e+06	8.010		0.6430	16.90	193.2	4.487
	1.300e+06	8.440		0.6430	21.59	235.7	4.484
	1.630e+06	8.970		0.6430	28.75	296.7	4.492
	2.150e+06	9.770		0.6430	41.40	394.2	4.507
	2.690e+06	10.40	7.620	0.6430	56.35	503.9	4.541
	3.370e+06	11.05		0.6430	79.86	663.8	4.623
95.70t	2.680e+06	10.40		0.6580	4.600	41.20	4.489
4.368K	4.250e+06	11.80		0.6580	8.177	65.30	4.488
1.446e-03	5.190e+06	12.30		0.6580	10.35	79.60	4.483
	6.640e+06	13.30		0.6580	14.09	100.9	4.469
	8.090e+06	14.20	6.580	0.6580	18.40	123.8	4.481
	9.760e+06	14.90		0.6580	23.29	149.5	4.481
	1.220e+07	15.90		0.6580	30.70	185.7	4.475
	1.470e+07	16.70		0.6580	39.13	226.0	4.484
	1.730e+07	17.60		0.6580	48.58	267.0	4.493
	2.080e+07	18.50		0.6580	61.84	323.1	4.500
	2.550e+07	19.50	6.110	0.6580	79.86	396.1	4.503

Table 6, *Continued*

P,T, ρ	Ra	Nu	Θ/Δ(%)	Pr	Q(mW)	Δ(mK)	T (K)
	2.980e+07	20.50		0.6580	100.2	471.0	4.530
	3.490e+07	21.50		0.6580	130.8	580.1	4.610
	3.970e+07	22.40		0.6580	165.6	695.0	4.693
254.8t	3.560e+07	21.40		0.6990	12.78	57.90	4.417
4.365K	4.760e+07	23.00		0.6990	18.40	77.80	4.427
4.059e-03	6.070e+07	24.80		0.7030	25.04	98.60	4.417
	7.380e+07	26.40	4.760	0.7030	32.71	120.9	4.429
	9.530e+07	28.40		0.7030	46.12	158.2	4.448
	1.200e+08	30.50		0.7020	61.84	198.5	4.445
	1.480e+08	32.20		0.7020	79.86	243.4	4.434
	1.720e+08	33.90		0.7010	100.2	288.8	4.460
	2.080e+08	35.60	4.000	0.7010	130.8	357.3	4.497
	2.430e+08	37.40		0.7000	165.	428.0	4.536
	2.710e+08	38.60		0.7000	204	504.6	4.612
	3.180e+08	40.40		0.6990	270	627.8	4.704
495.6t	2.560e+08	37.90		0.8010	28.[illegible]5	71.30	4.477
4.363K	3.140e+08	39.90		0.8010	36.[illegible]	87.30	4.475
8.698e-03	3.730e+08	42.10		0.8020	46.[illegible]	103.3	4.471
	4.730e+08	45.10		0.8020	61.84	129.9	4.461
	5.700e+08	47.70	3.200	0.8010	79.86	158.4	4.474
	7.480e+08	51.30		0.8020	115.0	211.3	4.495
	8.860e+08	54.30		0.8010	147.7	255.6	4.521
	1.040e+09	56.80		0.8010	184.5	304.0	4.536
	1.120e+09	58.60		0.8010	270.4	411.5	4.836
	1.190e+09	59.10	2.830	0.7970	225.4	356.4	4.564
	1.340e+09	61.10		0.7960	270.4	411.0	4.597
	1.530e+09	63.60		0.7960	345.5	498.9	4.672
900.0t	1.440e+09	67.30		1.060	51.11	63.10	4.729
4.631K	2.010e+09	73.70		1.060	79.86	89.90	4.744
1.760e-02	2.650e+09	80.30		1.060	115.0	119.0	4.748
	3.380e+09	85.20	2.300	1.060	156.5	152.6	4.754
	4.170e+09	91.30		1.060	204.4	186.3	4.745
	5.040e+09	96.20		1.060	258.7	224.0	4.740
	5.960e+09	101.0		1.060	319.4	263.7	4.736
	7.040e+09	103.0		1.060	386.5	313.6	4.742
	8.120e+09	104.7	1.860	1.060	460.0	366.0	4.746
	9.170e+09	107.0		1.050	539.8	420.8	4.769
	9.950e+09	109.0		1.190	662.4	499.3	4.853

CHAPTER 4

SPECULATIONS, MODELS AND THEORIES

First of all, I have to declare that this is an experimentalist's view on theories. So the reader should not expect too much rigour in the discussion. Often, I give only speculations and hand waving arguments, which I do not expect to convince anyone but myself.

Let me start by writing the basic equations for convection:

$$\partial_t \mathbf{v} + (\mathbf{v}\cdot\nabla)\mathbf{v} - \nabla p = Pr(\nabla^2\mathbf{v} + Ra\theta\mathbf{e_z}) \ , \tag{4.1}$$

$$\partial_t \theta + \mathbf{v}\cdot\nabla\theta = \nabla^2\theta \ , \tag{4.2}$$

$$\nabla\cdot\mathbf{v} = 0 \ . \tag{4.3}$$

The boundary conditions are $\mathbf{v} = 0$ at $z = \pm 1/2$ and at the side walls, and $\theta = \pm 1/2$ at $z = \pm 1/2$. In these equations, the temperature θ is normalized by Δ, length $\mathbf{x}$ by L, time t by L^2/κ and consequently velocity $\mathbf{v}$ by κ/L.

4.1 Scaling relations

The word *hard turbulence* was first introduced by Libchaber to distinguish it from fully developed turbulence (Heslot *et al.* 1987). Kadanoff and coworkers (Castaing *et al.* 1989) developed the first theoretical model of it. They proposed a model for the flow structures, from which the scaling relations between

Ra and Nu, Θ_c/Δ, VL/κ were derived and compared with the experimental results. Explanations for the shape of the PDF, the resonant frequency f_r were also proposed.

The root of the problem is that in the experiment Nu scales as $Ra^{0.286}$, definitely different from the classical $Ra^{1/3}$. As we discussed earlier (section 3.1.1), there are two well defined thermal boundary layers (thickness λ) which support all the temperature drop Δ, and where heat Q is transported by conduction:

$$Q = \chi \frac{\Delta/2}{\lambda} \quad . \tag{4.4}$$

Ra based upon λ is Ra_λ,

$$Ra_\lambda = \frac{g\alpha\lambda^3\Delta/2}{\nu\kappa} \quad . \tag{4.5}$$

Obviously it has to be small enough so that the boundary layer is stable. But what is its lower limit? A marginal stability theory has been proposed by Malkus (1954a, b; 1963) and further developed by Howard (1966). The main idea is that the layer is stable but will tend to grow by diffusion, thus Ra_λ is set at the critical value Ra_c

$$Ra_\lambda = Ra_c \ , \ \text{constant} \quad . \tag{4.6}$$

The value of Ra_c can be extrapolated (Chandrasekhar 1961) from known results for simple layers (Pellew & Southwell 1940; Reid & Harris 1958) and a reasonable value is $Ra_c \approx 10^3$. From the above relations (eq. 4.4, 4.5 & 4.6), then

$$Nu = (\frac{Ra}{16Ra_c})^{1/3} \quad . \tag{4.7}$$

This 1/3 relation has been supported by Townsend (1959), Goldstein & Tokuda (1980). But the Ra ranges in Townsend's experiment was too small

($3 \times 10^6 < Ra < 7 \times 10^8$) to critically check the power law; the power law in Goldstein & Tokuda's experiment was deduced from cells of aspect ratio ranging from 0.57 to 4.5. Deardorff & Willis (1965) have observed that Nu changes non-monotonically with the aspect ratios, and reach an asymptotic value for large aspect ratio. In table 2, Threlfall's data compiled with ours show similar aspect ratio dependence. On the other hand, most of the experiments show that Nu has a scaling relation with Ra smaller than 1/3 (table 2). Our Nu measurements in three different cells show unambiguously that the exponents are smaller than 1/3. So the marginal stability theory is not valid.

A convection cell is a integrated system, all parts are coupled together. Therefore it is unlikely that the boundary layer is marginally stable by itself. The very idea of the scaling theory proposed by Kadanoff *et al.* is to consider the interaction and matching of the boundary layer with the central region.

Since the boundary layer temperature drop Δ is orders of magnitude different from the temperature fluctuation Θ_c in the central region, a mixing layer of thickness d_m has to be introduced between as a buffer. In this mixing layer, the pieces of the detached boundary layer accelerate, break to smaller ones, and match their velocity and temperature with those of the central region. Let the final velocity of a detached boundary layer of temperature Δ be w_b, which can be derived from the balance between the buoyancy force and the viscous force:

$$g\alpha\Delta \ = \ \nu\frac{w_b}{\lambda^2} \quad , \tag{4.8}$$

then

$$w_b \ = \ \frac{g\alpha\lambda^2\Delta}{\nu} \quad . \tag{4.9}$$

The time scale associated with the boundary layer is λ^2/κ, and the mixing

layer thickness d_m is just the product of the velocity w_b by this times scale

$$d_m = \frac{g\alpha\lambda^4\Delta}{\nu\kappa} \ . \tag{4.10}$$

Suppose the pieces of the detached boundary layer of temperature Δ breaks to smaller ones of temperature Θ_m, the conservation of the heat flux through the boundary layer, the mixing layer and the central region leads to :

$$c_p\kappa\Delta/\lambda = c_p w_b\Theta_m = c_p u_c\Theta_c \ , \tag{4.11}$$

w_b has already been expressed in terms of λ in eq. 4.9, therefore Θ_m can be expressed as

$$\Theta_m = \frac{\nu\kappa}{g\alpha\lambda^3} \ . \tag{4.12}$$

The right hand side can be regarded as the temperature scale of the boundary layer. So far there are only three independent equations (one in eq. 4.9 and two in eq. 4.11), but five unknowns: λ, w_b, u_c, Θ_m and Θ_c, so further assumption have to be made. The mixing layer temperature fluctuation Θ_m is then assumed to match the central region one Θ_c (or equivalently w_b matches with u_c):

$$\Theta_m = \Theta_c \ . \tag{4.13}$$

Since the central region is turbulent enough to neglect viscosity at large scales, it is natural to assume that the velocity there is the free fall velocity:

$$u_c = \sqrt{g\alpha\Theta_c L} \ . \tag{4.14}$$

Now the number of equations matches the number of unknowns, leading to :

$$Nu \propto Pr^{-1/7}Ra^{2/7} \ ; \tag{4.15}$$

$$\Theta_c/\Delta \propto Pr^{-3/7}Ra^{-1/7} \ ; \tag{4.16}$$

$$u_c L/\kappa \propto Pr^{2/7}Ra^{3/7} \ . \tag{4.17}$$

The scaling index 2/7 (0.286) for Nu respect to Ra is extremely close to the experimental value 0.285, and -1/7 (0.143) for temperature fluctuation is close to the experimental value -0.14. We are unable to measure the velocity fluctuations to compare with the theory. However, it has been measured by Tanaka and Miyata (1980) in a water experiment to scale as $Ra^{0.43}$. This scaling theory corroborates the scaling relations of the experimental data well.

After this theory was proposed, we have discovered the presence of a large scale flow in the convection cell, which has been reported before by Krishnamurti and Howard(1981). Our measurement shows that the large scale velocity scales with Ra with an exponent 0.49, different from 3/7 proposed for the fluctuation velocity. In fig. 81 (a), we plot the $(VL/\kappa)Pr^{-2/7}Ra^{-3/7}$ as a function of Ra to show the difference. However, it is against my intuition that the two velocities scale differently in the self-similar hard turbulence regime. A more serious question is whether the large scale flow can be contained in the scaling theory, and if so, what is the relation between the thermal boundary layer and the viscous boundary layer.

Shraiman and Siggia (1990) answered this very question. In their model, besides the thermal boundary layers, which bear all the temperature drop Δ, a viscous sublayer layer and a turbulent boundary layer have been introduced. It has been assumed that the thermal boundary layer lies completely in the viscous sublayer of the turbulent boundary layer.

They first derive from the basic equations (eq. 4.1 & 4.3) the exact relation between the Nu and the average velocity dissipation.

$$\langle(\nabla v)^2\rangle(L^2/\kappa)^2 = (Nu-1)Ra \ . \tag{4.18}$$

Then from eq. 4.2, they relate the heat flux to the rate of shear in the viscous

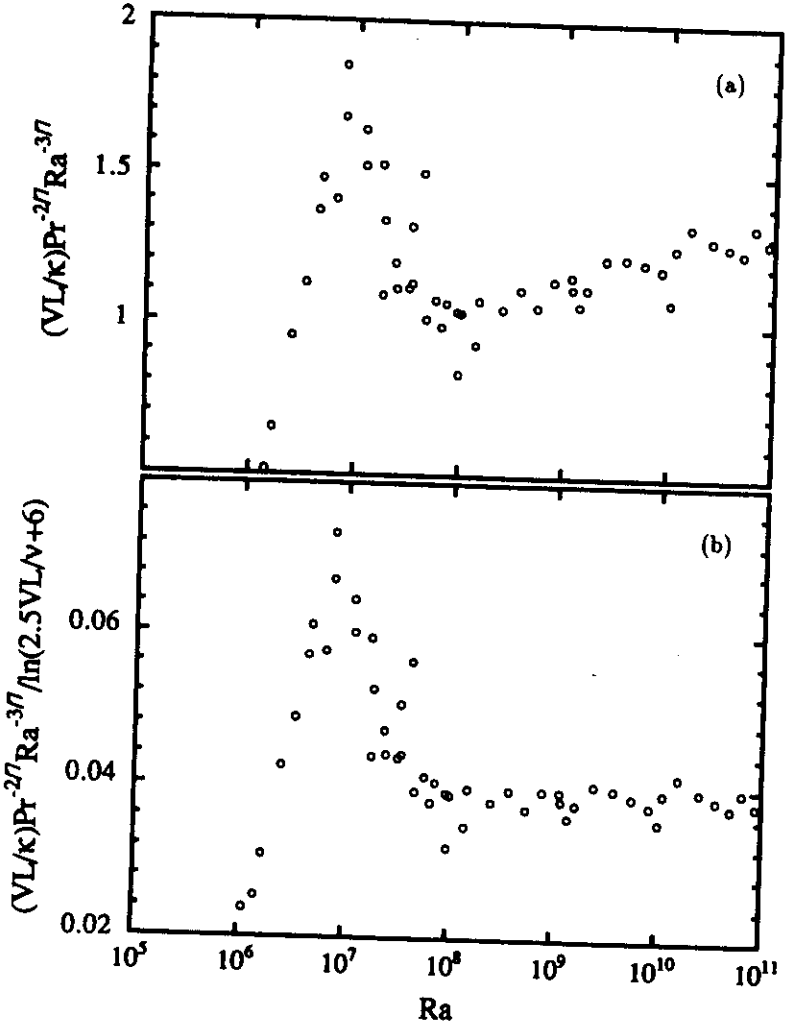

Figure 81. Compare the scaling of VL/κ with theories. (a) $(VL/\kappa)Pr^{-2/7}Ra^{-3/7}$ is plotted against Ra to show VL/κ behave differently with $Ra^{3/7}$. (b) $(VL/\kappa)Pr^{-2/7}Ra^{-3/7}/(2.5\ln(VL/\nu)+6)$ is plotted to show that the logarithmic cor ction fit data well

boundary layer, i.e., $Nu(Re)$ and use standard turbule ' boundary layer theory in conjunction with eq. 4.2 to yield $Re(Ra)$ and $Nu(Ra)$. The final results are

$$Nu = 0.27Pr^{-1/7}Ra^{2/7} , \tag{4.19}$$

$$\frac{V}{\kappa/L} = 0.14Pr^{2/7}Ra^{3/7}(2.5\ln(Re)+6) . \tag{4.20}$$

The first relation is identical to the corresponding one in the scaling theory, which describes the experimental data well. The second one differs only by a logarithmic term. The 3/7 (0.429) exponent for the velocity is smaller than the experimental value 0.49, the extra logarithmic term brings the theory and experiment closer, as shown in fig. 81 (b). This theory has also deduced analytically that the temperature fluctuations scale with Nu with an exponent 1/2, that is again identical to the former theory.

In my opinion, the two theory complement each other. The first one lies upon general scaling argument and dimensional analysis, it must be close to the truth. However, it does not give a detailed physical mechanism for the existence of the mixing layer and the matching of the temperature and velocity. It is not strange that some logarithmic factors are left out in such a simple analysis. The second one starts from basic equations and a specific model, and derive rigorously the scaling relations. But it is hard to get the general vision as that from the first one. Naively speaking, fractions with denominator 7 are uncommon, it must be more than coincidence that the two theories give essentially the same scaling exponents. It seems that the turbulent boundary layer in the second theory is playing the same role as the mixing layer proposed in the first one. It would be nice to unify the two theories.

Shraiman and Siggia's theory is valid when the thermal boundary layer is thinner than the viscous one. Since the thermal boundary layer changes as

$Ra^{-2/7}$ and the viscous one as $Ra^{-3/7}$, there must be a cross over between the two at a large enough Ra (estimated as $(10^{13} \sim 5\times10^{14})Pr^4$). When this cross over occurs, not only the scaling relations should be different, the local temperature and velocity signals may also change their characters. We do observe a change of frequency power spectrum of temperature fluctuations around 10^{11}, but the scaling relation of the Nu, Θ_c/Δ and velocity are invariant.

She (1989) has proposed a theory with only a thermal boundary layer and central isothermal region. The basic assumptions is that the thermal boundary thickness λ is equal to the dissipation length scale of the central turbulence. He starts from a scaling relation of the velocity fluctuations v_l of length l,

$$v_l = \varepsilon^{1/3} l^{1/3} (l/\lambda)^{-\mu/6} \quad , \tag{4.21}$$

here ε is the energy transfer rate and μ is interpreted as a measure of the deviation from the Kolmogorov turbulence. Equating the heat flux in different regions, he is able to express the scaling exponents of Nu, v_c and Θ_c/Δ in terms of μ only, which is further determined as -1 by balancing the buoyancy force θv_l with the kinetic energy v_l^3/l. The exponents derived are exactly the same as the ones given by Castaing *et al.* (1989). In my opinion, it is hard to justify the basic assumption in this theory, but it is worthwhile to check more carefully the connection with the other two, and the k^{-2} kinetic energy spectrum predicted by this theory.

The validity of all above theories lay upon the stability of the boundary layer. One can derive from eq. 4.5 & 4.15 that Ra_M increases as $Ra^{1/7}$. To save the stable boundary layer, it has been proposed that the shear in the convection cell has increased the critical Ra (Castaing *et al.* 1989). Zaleski (1991) further develops this idea by employing the Richardson number into the instability analysis.

However, even though Ra_M is less than 1000 for $Ra \leq 10^{14}$ (fig. 50 and table 5), our bottom bolometer detects plumes as soon as it gets out the boundary layer at $Ra = 10^9$ (fig. 54). In visualizing the convections in water, Chu & Goldstein (1973), Solomon & Gollub (1990) and Zocchi (1990) found that the boundary layer is not stable: they release thermal plumes. Shelley & Vinson (1991), Deluca *et al.* (1990), Balachandar *et al.* (1989) have also shown the releasing of plumes in numerical simulations. Even the very scaling theory assumes the detachment of the boundary layer. So I think that the thermal boundary layer is unstable in a static sense, but stable dynamically: once the boundary layer thickness λ exceeds a critical value, it injects plumes, then relax back and accumulates heat for the next eruption. The relevant question should be how the boundary layer becomes stable against convection by releasing thermal plumes.

4.2 Power spectrum

First of all, let us introduce the two fundamental concepts of turbulence: cascade and scaling. Only with these two concepts, we can have a proper language for later discussion (see Frisch & Orszag 1990).

Richardson (1922) was the first to propose a hierarchical model of turbulence. In his model, the motion of the largest length scale is driven by external force. It becomes unstable and thus produces ones of smaller length scales, which then become unstable and produces even smaller ones. This process continues until the viscosity becomes important. This qualitative picture is the dominating one in turbulence study since then.

Based on this picture, Kolmogorov (1941, 1962) (see Monin & Yaglom 1975; Tennekes & Lumley 1972) developed a scaling theory. He first assumed

that there exists a range of length scales, where the flow is homogeneous and isotropic. In other words, the inhomogeneity and anisotropy of the large scale forcing has no effect on the subsequent smaller scale motions. Therefore the only relevant physical quantities are the energy transfer rate ε, and the viscosity ν. Then an inertial range was assumed, where the energy transfers from larger scales to smaller ones without dissipation. The lower limit η of this inertial range is when the viscosity becomes important, i. e., $Re_\eta \approx 1$. He then expressed the energy transfer rate ε_l of length l in quantities only local to l, specifically $\varepsilon_l = (v_l)^3/l$.

In the inertial range, ε_l is the constant ε, thus

$$v_l = (\varepsilon)^{1/3} l^{1/3} \ . \tag{4.22}$$

Consequently, the power spectrum $P(k)$, which is Fourier transform of the correlation function, satisfies the famous $-5/3$ power law:

$$P(k) \propto (\varepsilon)^{2/3} k^{-5/3} \ . \tag{4.23}$$

The dissipation cut-off length η is decided from $Re_\eta = 1$ as

$$\eta = (\nu^3/\varepsilon)^{1/4} \ . \tag{4.24}$$

The inertial range thus increase as $\varepsilon^{1/4}$, or $Re^{3/4}$.

In problems involved temperature as well as velocity, the basic cascade and scaling concepts are still valid. Bolgiano(1959) and Obukhov(1959, 1962) (see Monin & Yaglom 1975) have used these concepts in studying turbulence in stably stratified medium. In the range where the flow motions are independent of the detail boundary condition and external forcing, the only relevant physical quantities are ν and κ, the kinetic energy transfer rate ε_v and the temperature "energy" transfer rate ε_θ, here ε_v is v_l^3/l as defined before, and

$\varepsilon_\theta = \theta_l^2/t_l = v_l\theta_l^2/l$. In this system, there exist exchanges between the kinetic v_l^2 and the potential energy $g\alpha\theta_l v$. Considering this exchange:

$$v_l^3/l = \theta_l v_l \ , \tag{4.25}$$

$$v_l\theta_l^2/l = \varepsilon_\theta \ , \tag{4.26}$$

here ε_θ is constant (derived from eq. 4.2). These two equations lead to the new scaling relations,

$$v_l = \varepsilon_\theta^{1/5} l^{3/5} \ , \tag{4.27}$$

$$\theta_l = \varepsilon_\theta^{2/5} l^{1/5} \ . \tag{4.28}$$

However for small enough length scales, the buoyancy force becomes unimportant, θ acts just like passive scalar. Then the right hand side of eq. 4.25 is replaced by constant ε_v and the Kolmogorov scaling relations are recovered,

$$v_l = \varepsilon_v^{1/3} l^{1/3} \ , \tag{4.29}$$

$$\theta_l = \varepsilon_\theta^{1/2} \varepsilon_v^{-1/6} l^{1/3} \ , \tag{4.30}$$

here ε_v and ε_θ are constant. The cross-over length l_* between the two different scaling regimes (called the buoyancy subrange and the inertial subrange respectively) can be constructed from a dimension analysis as

$$l_* \propto (\varepsilon_{v_l})^{5/4}/(\varepsilon_{\theta_l})^{3/4} \ . \tag{4.31}$$

For length scales larger than l_*, buoyancy effects dominate the dynamics, and for smaller length scales Kolmogorov behavior prevails. Summarize the above results for wave-number power spectrum, for $k \ll 1/l_*$

$$P_v(k) \propto k^{-11/5} \ , \tag{4.32}$$

$$P_\theta(k) \propto k^{-7/5} \ ; \tag{4.33}$$

and for $k \gg 1/l_*$

$$P_v(k) \propto k^{-5/3} \quad , \tag{4.34}$$

$$P_\theta(k) \propto k^{-5/3} \quad . \tag{4.35}$$

Although the above scaling analysis was originally for stable thermal stratification, it can be equally applied to free thermal convection (the unstable stratification). Thomae (1989) has carefully checked each step of the scaling arguments, Proccacia *et al.* (1990) and L'vov & Falkovich (1991) have derived in a different approach from the basic equations, they all end up in exactly the same scaling relations. However the estimation of l_* as a function of Ra seems non-trivial, Thomae gives $l_* \propto Ra^{-5/16}$ and Proccacia *et al.* $Ra^{-3/28}$.

Shraiman and Siggia (1990) have a different point of view. They checked the Ra dependence of the prefactors in Obukhov-Bolgiano's scaling relations (eq. 4.27 & 4.28), and concluded that they will lead to an inefficient kinetic energy dissipation required by the basic convection equations (eq. 4.1 - 4.2). Although their view is illuminating, I am not convinced by all of their arguments, particularly the ones deducing the kinematic energy dissipation from the thermal diffusion cut-off length, instead of l_* (eq. 4.31), and treating the correlation $\langle v_z(r)T(0)\rangle$ as constant for large r in the Karman-Howarth analysis. Recently Grossmann and Lohse (1991) have solved the basic equations for thermal convection using a Fourier decomposition with a geometrically scaling selection of wave numbers. They did not find the buoyancy subrange. Since I have not understood this work, I will not comment on it.

Most of the theories (including all above) and simulations are about the wave-number power spectrum. But we measure the turbulent signal at one fixed point which only yields a frequency power spectrum. The generally accepted bridge between the two is the Taylor "frozen flow" hypothesis (1938),

which states that in the presence of fast steady flow, the smaller flow structures can be regarded "frozen". Thus the flow structures along the sweeping direction are simply mapped onto the time series measured by a fixed probe. Then the wave-number k and the frequency f are related as

$$f = kv_0 \quad , \tag{4.36}$$

here v_0 is the sweeping velocity. This hypothesis works well in wind tunnel turbulence experiment. For this thermal convection, the condition for Taylor "frozen flow" hypothesis obviously does not hold.

However I suspect that even without a fast steady sweeping flow, a linear relation between f and k still exists statistically in lower frequency range. Since the velocity of large scale is large but change slowly, we can regard it as the steady sweeping velocity in a short time interval. Thus within this time interval, the "frozen flow" hypothesis holds and the wave-numbers are proportional to the frequency. For an other time interval, the large scale flow has changed of course, the coefficient of the linear relation will be different from the one in the previous time interval. But statistically, a linear relation between f and k may be valid, with the coefficient being some kind of statistics of the large scale flow (for example $\sqrt{\langle V^2\rangle}$) (Tennekes (1975) has given similar arguments). This speculation is supported by the fact that, the power spectrum in the side wall region, where there is a steady large scale flow, is essentially the central one shifted to higher frequency. Of course, it would be nice to measure the wave number power spectrum directly and find a relation between $\langle (T(t,r+x)-T(t,x))^p\rangle_{t,x}$ and $\langle (T(t+\tau,x)-T(t,x))^p\rangle_{t,x}$.

There are a few theoretical effort directly on the frequency power spectrum. Following the arguments for wave number power spectrum (Monin & Yaglom 1975), the frequency power spectrum in the reference frame of moving fluid

elements, called Lagrangian spectrum has a power law f^{-2}. Using renormalization approach, Yakhot *et al.* (1984) pointed out that the power spectrum measured at one fixed point in lab frame, i. e. the Eulerian spectrum is essentially the same as the Lagrangian one. Thus it has a power law f^{-2}, different from the model given by Tennekes and our above speculation. Nelkin & Tabor (1990) have discussed the possibilities to resolve the controversy.

Experimentally, the frequency power spectrum of temperature fluctuations has an invariant shape for $Ra < 10^{11}$: a power law with an exponential cut-off. The exponent of the power law is -1.35 ± 0.05, the range increases as $Ra^{0.3}$

For $Ra > 10^{11}$, the high frequency part of the power spectrum changes with Ra, and seems to reach asymptotically another power law of exponent -2.4. We have phenomenologically used a multi-fractal like transformation (Wu *et al.* 1990) to bring all the power spectra together (fig. 82)

$$F = \log(P/P_0)/S \ , \tag{4.37}$$

$$\alpha = \log(f/f_0)/S \ , \tag{4.38}$$

where S is a constant $\log(10^{11}/R_0)$ for $Ra < 10^{11}$, and changes as $\log(Ra/R_0)$ for $Ra > 10^{11}$, R_0, P_0 and f_0 are Ra independent parameters:

$$R_0 = 1 \times 10^8, \ P_0 = (5.8 \pm 0.7) \times 10^{-7}, \ f_0 = (1.1 \pm 0.2) \times 10^5 \ . \tag{4.39}$$

The most important parameter among the three is R_0, which decides how much the curve, at a given Ra, should be bent under this transformation. P_0 and f_0 merely determine the relative positions of each curve. Since the transformation depends on $\log(R_0)$, R_0 being any value between 8×10^7 and 8×10^8 leads to good superposition, but $R_0 = 1 \times 10^8$ is slightly better. It is interesting that R_0 is about the same Ra of the soft-hard turbulence transition.

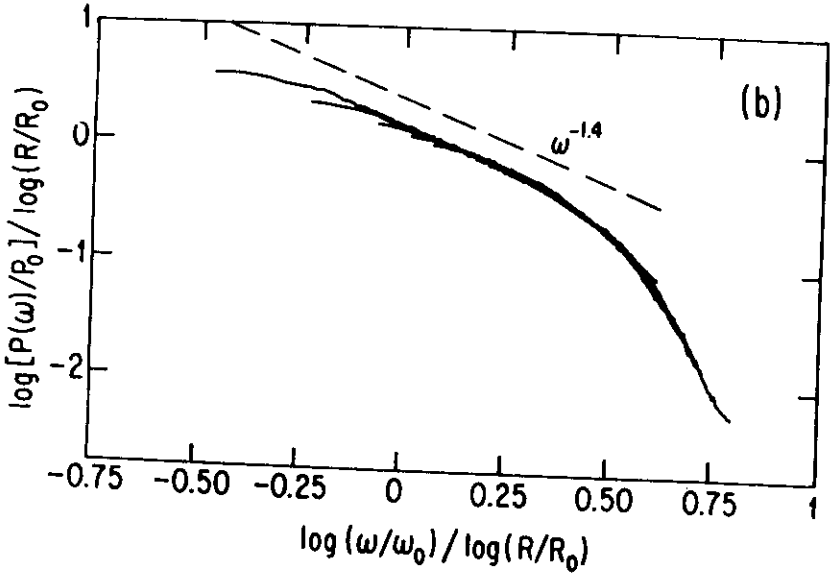

Figure 82. $F - \alpha$ plot of the power spectra for $1 \times 10^{11} < Ra < 4 \times 10^{14}$. $F = \log(P/P_0)/S$, $\alpha = \log(f/f_0)/S$ and $S = \log(Ra/R_0)$. The curves are for $Ra = 7.3 \times 10^{10}$, 6.0×10^{11}, 6.7×10^{12}, 4.1×10^{13} and 4.3×10^{14}. In this plot, the shorter piece is for larger Ra. ω is f.

I have to point out, first, due to the limitation of both the Ra range and the frequency range (there is always not enough experimental range, of course), we are not sure that this transformation is correct asymptotically. We are a little bothered by the fact that the larger Ra, the smaller the range it covers. Secondly we have no idea about the physics underlying it at the time we did this transformation.

Two different theories by Castaing (1989; 1990) and Frisch *et al.* (1983 1991) have lead to power spectra $P(k)$ which are Re invariant under the transformation $F = \log(P(k)/P_0)/\log(Re/R_0)$ and $\alpha = log(k/k_0)//\log(Re/R_0)$. This transformation is essentially the same as what we suggested in eq. 4.37 & 4.38.

Castaing and coworkers (Castaing 1989; 1990; Castaing *et al.* 1991) started from an extremum principle for the energy transfer rate ϵ as a function of k. ϵ is then found to satisfy a log-normal distribution

$$\Pi(\epsilon) = \frac{1}{\Gamma\sqrt{2\pi}} \exp(-\ln^2(\epsilon/\epsilon_m)/2\Gamma^2) \quad , \tag{4.40}$$

with $\Gamma \propto k^\beta$. The most probable value ϵ_m has to be $\epsilon_0 \exp(-\Gamma^2/3)$ in order to keep the average ϵ_0 constant. β has been interpreted as the co-dimension of the dissipative structures, which is $\beta_0/\ln(Re/R_0)$ for large Re and constant for smaller one. They then followed the Kolmogorov's scaling relation $P(k) = C\epsilon_m^{2/3}k^{-5/3}$ which led to

$$\frac{P(k)}{P_0} = \left(\frac{k}{k_0}\right)^{-5/3} \exp\left(-\frac{1}{\beta}(\frac{k}{k_0})^\beta\right) \quad , \tag{4.41}$$

which has a Re independent form $F(\alpha) = -5/3\alpha - \exp(\alpha)$ under the $F - \alpha$ transformation similar to eq. 4.37 & 4.38. By changing the -5/3 to 1.3 and adding a prefactor in front of the last term, this form actually fits our experimental data well (Castaing 1990).

Developing a multifractal model proposed by Parisi & Frisch (1985), Frisch & Vergassola (1991) have shown that the the viscous cut-off length $l_d \propto Re^{-1/(1+h)}$, here h is the scaling exponent in a continuous range (1/3 for Kolmogorov's scaling relation). In a range much larger than the Kolmogorov cut-off, the power spectrum still obeys the ordinary -5/3 power law with a small mutifractal correction. However in a range much smaller, the power spectrum changes it shape with Re, which again can be brought together by the above $F - \alpha$ transformation.

Although both models are similar in leading to $F - \alpha$ type power spectra, Frisch's model has this $F - \alpha$ behavior only in the dissipative range of the power spectra, while Castaing's model exhibit it in the whole range. It seems to me that the power spectrum form in Castaing's model is more similar to ours. However one has to remember that both theories are about the wave-number power spectrum, the connection to frequency one is not clear, unless one applies the equivalent "frozen flow" hypothesis discussed before. In that case, the Bolgiano-Obukhov's scaling exponent $-7/5$, instead of Kolmogorov's $-5/3$, has to be used to explain the power law of -1.35 ± 0.05. Also, both theories have to face the theoretical challenge (Foias & Temam 1989; Foias *et al.* 1990) that the power spectrum has to decay as fast as $\exp(-k/\eta)$ to prevent the velocity field from diverging.

In a recent work by Procaccia *et al.* (1991), an unified mechanism is suggested for the soft-hard turbulence transition and the change of power spectrum at $Ra = 10^{11}$. The main ingredient of the analysis is a calculation that suggests that isothermal surfaces wrinkle, or appear fractal, above an inner scale λ_*, which diminishes upon increasing Rayleigh number. It is estimated that λ_* goes through $L/2$ at $Ra = 10^8$, where soft-hard turbulence transition occurs, and the mixing layer thickness at $Ra = 10^{11}$, where the second tran-

sition occurs. Thus it is speculated that the crossing of each relevant length scale create a turbulence transition. This theory tries to explain why there are transitions, but it does not give any explanation to the actual behavior of the power spectra. It seems to me that there is no concrete correlation to the experimental results.

After the discussion on the above three theories, I want to remind the reader of the possibility that the power spectrum behaviors may simply fall into the prediction of Bolgiano and Obukhov. First, No one has any faintest clue on how to connect a power law exponent -1.35 ± 0.05 in frequency power spectrum to the Kolmogorov -5/3 in wave-number one. it seems to me more than a coincidence that the power law exponent -1.35 is so close to $-7/5$ suggested by Bolgiano and Obukhov for wave number one, it may well be that the equivalent "frozen flow" hypothesis does work in the buoyancy sub-range. Then suppose the length l_* (eq. 4.31) becomes larger than the diffusive cut-off at $Ra = 10^{11}$, then Kolmogorov inertial range will emerge, and the power spectrum begins to change at high frequencies. In this case, $F - \alpha$ transformation just describe this changing process. To answer why the second power is -2.4, different from $-5/3$, I have to argue that the equivalent "frozen flow" hypothesis no longer works in high frequency range since the corresponding motions may change faster than the sweeping time. For this frequency range, frequency power spectrum has to be studied directly.

Conclusion: there is no theory to explain directly the change of the frequency power spectrum at $Ra = 10^{11}$, and the behavior below and above. The main problem is the disconnection between the frequency and wave vector power spectrum. Clearly experimental effort are needed to measure the spatial behavior, as well as to increase the Ra range and signal to noise ratio. On the other hand, it is challenging to develop theoretical models for the frequency power spectrum.

4.3 Probability distribution function

In most of the turbulence studies, velocity and other passive scalar fluctuations obey a Gaussian distribution (Monin & Yaglom 1971), although their derivatives may have an exponential tail (Van Atta & Chen 1970; Kuo & Corrsion 1971;). Therefore it came to be a surprise that the temperature fluctuations measured at one point in the aspect ratio 1 cell has a very clean exponential distribution. The fluctuations in the other two cells also exhibit exponential tails.

It is well known that a large number of stochastic uncorrelated variables will lead to a Gaussian distribution; the presence of an exponential distribution implies that the flow motions are strongly correlated. With PDF unchanged after low pass filtering, we are convinced that a PDF is mainly determined by the low frequency, large amplitude fluctuations. In a general turbulence system, the large scale structures are influenced by external forcing, and no general correlation and scaling relations are expected in this range, therefore a Gaussian distribution is a natural outcome. On the contrary, in free thermal convection system, the only external influence is the temperatures of the two plate temperatures, the velocity and temperature fields are self-generated, therefore correlations may appear even in the large length scales. In hard turbulence regime, the velocity of the largest scale (the cell size) is measured to be stable in the aspect ratio 1 cell, therefore the correlation may extend to wide range of length scales. A pure exponential distribution may reflect the intrinsic correlations of the large scale structures. However an exponential

distribution can be easily contaminated by the flow of the largest size. In the aspect ratio 0.5 and 6.7 cell, the flow of the largest scale is less stable, and the PDFs are less stretched than an exponential. The extreme case is soft turbulence, where the flow of the largest scale are unstable. Dominated by these instabilities, the PDF behaves as Gaussian.

In the paper by Castaing *et al.* , a simple model is given to explain the exponential distribution. It describes that thermals in the mixing zone are injected intermittently into the central region. Between these aspiration events the mixing zone is heated at a constant rate H and its temperature grows as

$$T_m(t) \propto (t - t_a) \ , \tag{4.42}$$

where t_a is the time of the last emission. It is further assumed that the time interval between two aspirations satisfies a Poisson distribution. From the exponential distribution of waiting time, an exponential distribution of temperature T_m follows. However, from the time series of the temperature fluctuations, it is hard to classify an "aspiration" event, thus the basic assumptions of these model: well defined aspiration and Poisson distribution of the time interval, can not be justified.

Sinai and Yakhot (Sinai & Yakhot 1989; Yakhot 1989) have proposed a theory to explain the exponential distribution. Starting from the basic equations, they have derived analytically the recursion equations for all moments of the temperature fluctuations. Then they express the PDF in terms of the conditional averages of $\langle v_z \theta \rangle$ and $\langle v^2 \rangle$, which have to be assumed according to physical pictures before a specific PDF can be predicted. To get an exponential distribution, they assume that there is a characteristic velocity in the cell. This assumption, the essence of this theory, comes from the observation of a large scale velocity in the helium cell, and visualization of plumes emitting

with a well defined velocity from the boundary layer in water cell (Gross *et al.* 1988; Solomon & Gollub 1990). With the velocity measurement technique introduced early (section 3.1.7), we are unable to see any characteristic velocity at the center of the cell, although more direct measurement technique is desired to draw a conclusion. In any case, the idea is illuminating that plumes, which are coherent objects in thermal turbulence, are responsible for the exponential distribution.

Pumir, Shraiman and Siggia (1990) have proposed a passive scalar model. With local mixing, transport by random advection and an imposed, an exponential distribution can come out of this model. However, the model is just a one dimensional model equation and can only be compared with the experiment only in spirit. There is a need to develop a more realistic model.

CHAPTER 5

CONCLUSION

We have studied the development of thermal turbulence in closed cells. Two distinct turbulence states, soft turbulence below $Ra = 10^8$ and hard turbulence above have been discovered. At $Ra = 10^{11}$, change appears in local temperature signals, especially in its power spectrum.

Soft turbulence motion is essentially due to the dynamics of large scale structures, which are shown by our experiment to be complex and non-universal. Lorenz (1963) has demonstrated that complexity can be attained with only three modes. Despite of the progress in understanding temporal chaos and spatial-temporal dynamics of one dimension systems in the last ten years (see, Hao, 1984; Manneville, 1990), the dynamics of three dimensional systems seems still formidable. The difficulties come from the fact that the number of modes involved is not small enough to be solved analytically, nor large enough to be treated statistically. However, our experiment did show some encouraging results. In small aspect ratio cells where turbulence starts after temporal chaos has fully developed, the spatial coherence diminishes in a unique and repeatable scenario. Unlike chaos, all statistical measures in soft turbulence only depend on Ra (possibly Pr) and show no sign of hysteresis. More noticeably, in the center region of the cell, the probability distribution function is Gaussian and the power spectrum can be characterized by an invariant cut-off tail and a low frequency plateau. Our impression is that soft turbulence can

be attacked statistically, but detail boundary conditions have to be taken into account.

As Ra increases, soft turbulence always simplifies its large scale structures and turns to hard turbulence. The dynamics in hard turbulence is dominated by individual plumes released from the thermal boundary layers, and not by connected channels between the top and bottom. One of its most important characteristics is the intermittence in the local temperature signals: large amplitude fluctuations well separated from the small amplitude ones. Hard turbulence is a self-similar, strongly correlated state, where the probability distribution function is invariant and exponential-like. Up to $Ra = 10^{11}$, the power spectrum is characterised by a power law of exponent -1.4, whose range depends on Ra, and an exponential cut-off tail. Note that in large aspect ratio cells, this shape of power spectra is reached only asymptotically with Ra, as the effects of the large scale flows decrease gradually. The Nusselt number, velocity and rms temperature fluctuations have simple scaling relations. The scaling exponent for Nusselt number is certainly smaller than 1/3, and its asymptotic value is 0.286 (table 2). The theories for the scaling relations are satisfactory, but there is no unified model to explain all aspects of hard turbulence.

At $Ra = 10^{11}$, a transition has been discovered in the high frequency part of the power spectrum. It has been confirmed in other measures related to local temperature signals, such as the temperature dissipation Q^2 (eq. 3.25), the probability distribution function of the temporal difference (Ching, 1991). Except for these, we have not observe any changes in the other measurements at this Ra, such as the Nusselt number, the rms temperature fluctuations. This is not surprising since the change at high frequencies, which correspond to small scale structures, has small impact on the average quantities. This

new transition has been suggested to be due to the fractalization of dissipation structures or isothermal surfaces (Castaing 1990; Procaccia *et al.* 1991). But the understanding is only in its early stage both experimentally and theoretically.

Our experiment has shown both the richness and the simplicity of thermal turbulence. But thermal turbulence is by no means fully understood nor the search exhausted. New experimental techniques are needed to understand hard turbulence better, to verify the changes at $Ra = 10^{11}$ and to search for the asymptotic developed turbulence.

First, moving frame for bolometers should be built to study spatial correlations along various directions. This is necessary not only for connecting theories and experiments, but for better understanding of the flow structures as well.

The bolometers for local temperature measurements should be improved. For large Ra, the danger that a bolometer would perturb significantly the flow has always been our great concern. Thus small bolometers are certainly desired. The size of the present ones is 200 μm, certainly larger than the limit of modern micro-mechanics and semiconductor technology. Also, a large signal to noise ratio in turbulence studies is always helpful.

Measuring physical quantities other than temperature, such as velocity and pressure are necessary and interesting. Piezoelectric transducers for pressure measurement are currently under test in our laboratory. Optical methods (such as laser Doppler velocimeter) may be employed to study the velocity field. With improved bolometer size and spacing, the bolometer pair we used to measure slowly varying velocities could be feasible for fast ones. The visualization of the flow structures may be another helpful avenue.

One of the most important aspects in turbulence studies is data analysis.

So far, we are limited to the conventional analysis, such as power spectrum and probability distribution function. They are often inefficient in characterizing the time series. There is a need for new statistical measures for turbulence signal analysis, the recent application of the wavelet transformation is one of these efforts (Grossman & Morlet 1987; Argoul *et al.* 1989).

It is certainly interesting to reach larger *Ra* to study the turbulence states beyond hard turbulence, and simulate the convection of the earth atmosphere in the laboratory. Thermal turbulence, a general natural phenomena, deserves to be studied in a 10 meter high cell some day, may be in the liquid-helium storage tank in Fermi Lab.

APPENDIX

THE NON-BOUSSINESQ EFFECTS

In this appendix, we provide our paper on the non-Boussinesq effects.

PHYSICAL REVIEW A VOLUME 43, NUMBER 6 15 MARCH 1991

Non-Boussinesq effects in free thermal convection

Xiao-Zhong Wu and Albert Libchaber
The Department of Physics and the Research Institutes, The University of Chicago, 5640 South Ellis Avenue, Chicago, Illinois 60637
(Received 17 July 1990)

Non-Boussinesq effects in a Rayleigh-Benard convection system lead to a symmetry breaking between the top and the bottom boundary layers. We have found that the two layers adjust their temperature drops and the thicknesses λ such that their temperature scales $\nu\kappa/g\alpha\lambda^3$ are equal, where α is the thermal expansion coefficient, g is the gravitational acceleration, and ν and κ are the kinematic viscosity and thermal diffusivity, respectively.

I. INTRODUCTION

In most of the studies of thermal convection, the Oberbeck-Boussinesq[1,2] (OB) approximation has been assumed; i.e., the temperature dependence of all the fluid properties other than the fluid density are considered constant. This approximation simplifies the convection problem greatly. However, there are cases where this approximation is no longer valid, hence it is natural to study how it influences the experimental results. Furthermore, since the symmetry between the top (colder) and bottom (hotter) boundary layers is broken, some relations, which are hidden in the OB case, may be revealed. This in turn may shed some light on the OB case.

When the Rayleigh number R is less than 10^3, the heat is transported by conduction. In this case, the temperature profile, heat flux, etc., can be calculated analytically from the diffusion equation. When the convection starts, the situation becomes nontrivial. A few researchers[3-10] have studied the non-OB effects near the onset of convection. However, as the flow in the convection cell reaches a different turbulence state, non-OB effects may have different behaviors. In this paper we shall discuss the non-OB effects in hard turbulence[11] ($R > 10^7$), far above the onset of convection.

In Sec. II of this paper, we shall briefly describe the experimental setup and procedures. The situation where the non-OB effects appear is explained. In Sec. III, we present the experimental results, such as the asymmetry of the two boundary layers, the strange behavior of the Nusselt number, and the rms temperature fluctuations. Finally, in Sec. IV, we discuss three different models. Since the equations available are not enough to determine uniquely the temperature drops and the thicknesses of the two boundary layers, one more relation has to be proposed. We discuss the equality of the Rayleigh numbers, the equality of the velocity scales, and the equality of the temperature scales, for the two boundary layers. The last one is proved to be the best experimentally. The consequences of the last model are discussed and compared with the experimental results.

II. EXPERIMENT

We have performed the low-temperature helium-gas convection experiment in three different vertical cylindrical cells, with diameters 8.7, 20, and 20 cm, heights 8.7, 40, and 3 cm, thus aspect ratio 1, 0.5, and 6.7, respectively. Of these three cells, the one of the largest aspect ratio, diameter 20 cm and height 3 cm, has the best temperature regulation. Thus we shall focus on this cell in this paper. The cell sidewall is 2-mm-thick stainless steel. The sidewall heat transport is of the same order of magnitude as the heat conducted by the gas, thus much smaller than the heat transported by convecting gas. Both the top and bottom plates are made from oxygen-free high-conductivity copper. The bottom plate has a thickness of 2.0 cm and the top plate of 6.4 cm. GR-200A germanium resistance temperature sensors from the Lake Shore Cryotronics, Inc., are used to measure the temperatures of the plates. At 5 K, their typical resistance is around 1.5 kΩ, and the sensitivity is about 1 mK/Ω. They are embedded in both plates, several millimeters away from the inner surfaces. The method of measuring the thermometers, as well as the local temperature bolometers in the fluid, has been described in Ref. 12. The entire cell is in a vacuum jacket with its top plate in thermal contact with a liquid-helium bath. The top plate is regulated at a given temperature around 5 K. The top-plate temperature fluctuation is a fraction of 1 mK for low Rayleigh numbers and can reach a few mK for the highest Rayleigh numbers. When not heating the bottom plate, the temperature difference of the two plates is not zero and increases slightly with the top-plate temperature, but the maximum difference is less than 5 mK. We think that this difference is due to the imperfect vacuum. By applying a constant dc heat to the bottom plate, a temperature drop Δ is imposed. The cell is filled with helium gas of various densities. The density of the gas is computed by measuring the equilibrium pressure with an absolute pressure transductor of MKS Instruments, Inc., and the temperature of both plates. The fluid properties and the relations are based on the equations and tables given by McCarty,[13,14] who has reviewed most of the works on helium-gas properties.

The control parameter of this experiment is the Rayleigh number

$$R = \frac{\alpha g L^3 \Delta}{\nu\kappa}, \tag{1}$$

where α is the thermal expansion coefficient, g is the

TABLE I. Experimental values of the Rayleigh number R; Nusselt number N; temperature difference Δ; the ratio of the temperature drops across the top and bottom boundary layers x; and the fluid properties in central region c, top t, and bottom b boundary layers.

R	N	Δ (mK)	x	ρ (10^{-2} g/cm^3)	Region	T (K)	α (1/K)	ν (10^{-4} cm^2/s)	κ (10^{-4} cm^2/s)	χ (mW/cmK)
2.10×10^{9}	35.7	357	0.89	0.406	*c*	4.486	0.267	29.1	41.4	0.0954
					t	4.402	0.274	28.0	39.7	0.0939
					b	4.581	0.259	30.3	43.4	0.0970
5.75×10^{8}	47.7	158	0.87	0.870	*c*	4.469	0.339	14.1	17.6	0.0990
					t	4.432	0.345	13.8	17.1	0.0985
					b	4.511	0.331	14.4	18.1	0.0996
1.21×10^{9}	59.2	356	0.87	0.870	*c*	4.553	0.329	14.3	17.9	0.100
					t	4.469	0.343	13.7	17.0	0.0993
					b	4.648	0.314	15.0	19.1	0.102
5.13×10^{8}	92.7	358	0.85	1.53	*c*	4.723	0.440	8.90	9.13	0.110
					t	4.633	0.479	8.44	8.35	0.110
					b	4.812	0.409	9.35	9.90	0.111
3.35×10^{8}	86.5	150	0.89	1.76	*c*	4.747	0.499	7.92	7.49	0.114
					t	4.712	0.519	7.75	7.21	0.114
					b	4.787	0.478	8.12	7.84	0.114
8.42×10^{8}	105	366	0.79	1.76	*c*	4.725	0.507	7.87	7.41	0.113
					t	4.644	0.559	7.48	6.72	0.114
					b	4.827	0.456	8.37	8.27	0.114
1.27×10^{10}	119	287	0.77	2.38	*c*	5.139	0.579	6.55	5.30	0.128
					t	5.077	0.637	6.29	4.85	0.129
					b	5.221	0.518	6.89	5.91	0.127
2.44×10^{10}	135	509	0.65	2.38	*c*	5.073	0.605	6.48	5.15	0.127
					t	4.973	0.723	6.04	4.37	0.130
					b	5.227	0.492	7.13	6.30	0.126
3.07×10^{10}	132	715	0.58	2.38	*c*	5.164	0.571	6.57	5.35	0.128
					t	5.033	0.711	6.02	4.35	0.131
					b	5.392	0.439	7.48	6.95	0.127
2.75×10^{10}	156	280	0.77	2.84	*c*	5.106	0.793	5.66	3.77	0.137
					t	5.045	0.934	5.38	3.27	0.141
					b	5.126	0.753	5.76	3.95	0.136
3.18×10^{10}	153	325	0.70	2.84	*c*	5.113	0.789	5.66	3.78	0.137
					t	5.046	0.948	5.36	3.22	0.141
					b	5.208	0.646	6.08	4.53	0.133
4.00×10^{10}	148	433	0.58	2.84	*c*	5.141	0.767	5.70	3.86	0.137
					t	5.062	0.949	5.34	3.20	0.142
					b	5.278	0.592	6.27	4.89	0.133
5.30×10^{10}	147	601	0.53	2.84	*c*	5.179	0.746	5.72	3.91	0.137
					t	5.075	0.987	5.25	3.06	0.144
					b	5.376	0.535	6.52	5.35	0.132
6.97×10^{10}	164	313	0.52	3.36	*c*	5.149	1.12	4.99	2.66	0.152
					t	5.096	1.45	4.71	2.16	0.163
					b	5.252	0.800	5.47	3.53	0.142
9.56×10^{10}	157	515	0.43	3.36	*c*	5.241	1.00	5.06	2.83	0.150
					t	5.163	1.41	4.67	2.14	0.164
					b	5.420	0.646	5.82	4.19	0.140
1.10×10^{11}	159	504	0.42	3.36	*c*	5.159	1.10	4.99	2.68	0.151
					t	5.085	1.64	4.59	1.95	0.169
					b	5.337	0.677	5.78	4.10	0.139

gravitational acceleration, L is the height of the cell, Δ is the temperature drop across the cell, and ν and κ are the kinematic viscosity and thermal diffusivity, respectively. In the OB case, the fluid properties throughout the cell are the same, thus there is no ambiguity in the definition of Rayleigh number. However, as the fluid properties vary with the temperature across the cell, we shall redefine the Rayleigh number based on the fluid properties of the central region of the cell. Although this choice is arbitrary, it seems most reasonable since the central region occupies the majority of the cell volume. The Rayleigh number can be increased by adjusting the temperature difference Δ, or by changing the fluid properties. As the gas approaches its critical point by either increasing the gas density or decreasing the average temperature, α increases, ν and κ decrease, consequently the Rayleigh number increases. In this experiment, we vary Δ between 50 and 700 mK, but the Rayleigh number spans eight decades, from 10^3 to 10^{12}. However, for too large a gas density or too low a temperature where the gas is close to its critical point, the fluid properties become so sensitive to the temperature variations that their values differ from the top to the bottom plate. Thus the OB approximation breaks down.

Table I gives the fluid properties for various densities and temperatures. The Rayleigh number R and the Nusselt number N are calculated based on the fluid properties in the central region (the Nusselt number is defined as the actual heat flux normalized by the one which would be transported by gas conduction). x is the ratio of the temperature drop of the top boundary layer to that of the bottom boundary layer; it will be the center topic of this paper. The fifth column is the gas density ρ, which is calculated from the equilibrium pressure and temperature. The cell is isolated after the pressure has been measured. The cell, with a given gas density, may be operated at different average temperatures. Since the central region occupies most of the cell volume, the density there should be very close to the density measured at equilibrium. The fluid properties α, ν, κ, and γ (the thermal conductivity) are computed correspondingly from the density ρ and T_c, where T_c is the central region temperature. The pressure is calculated only from the central region temperature and density, but should be the same throughout the cell. From the average temperature T_t of the top boundary layer and the pressure, the corresponding physical constants α_t, ν_t, κ_t, and γ_t can be calculated. The same calculation can be done for the bottom boundary layer. Note that the subscripts t and b are for top and bottom boundary layer, respectively, while those variables with the subscript c or without any subscript are for the central region.

In the central region, the heat is dominantly transported by convection, while in the top and bottom boundary layers where the velocity tends to zero, the heat is transported by conduction. Since conduction is much more resistive than convection, the total temperature drop across the cell Δ is applied only across the two boundary layers, the central region is isothermal (essentially a thermal short circuit):

$$\Delta = \Delta_t + \Delta_b \,. \tag{2}$$

where Δ_t and Δ_b are the temperature drop across the top and bottom boundary layers, respectively. Δ_c is calculated from the difference of the top-plate and the central region temperatures, while T_t is from the average of the two. Δ_b and T_b are calculated similarly. In the aspect-ratio-1 cell, the temperature profile of the boundary layer has been measured[12] indirectly by varying the Rayleigh number to change the relative position of a fixed bolometer near the bottom plate. In a convection experiment with water, Zocchi, Moses, and Libchaber have measured[15] directly the temperature profile of the convection cell at $R = 10^9$ with a moving bolometer. Both results indicate that there are two well-defined boundary layers, which bear all the temperature drop across the cell with a constant gradient.

The temperatures of the top and bottom plates are measured with the thermometers which are fixed in the plates. To measure the central region temperature, a bolometer is positioned at the center of the cell. The bolometer is an arsenic-doped silicon cube of 0.2 mm, which was originally made by NASA for astrophysics observation.[16,17] At 5 K, its typical resistance is around 1 kΩ, and the sensitivity is about 2 mK/Ω. Principally, the central region temperature has to be computed as the average over the whole cross section of the cell, but this is impractical experimentally. In soft turbulence,[11] since there are many independent large-scale structures, our previous study in an aspect-ratio-1 cell shows[18] that the time-average temperature at different points of the same height can be as large as 30% of Δ. Therefore one point measurement at the center cannot be taken as the central region temperature for soft turbulence. In contrast, for hard turbulence,[14] the central region becomes more homogeneous. The maximum temperature difference of the two points is 5% Δ at the onset of hard turbulence, and the difference decreases with the Rayleigh number monotonically. Thus it is a good approximation to use the center temperature measurement as the central region temperature, especially for large Rayleigh numbers. In this paper, we shall only discuss the hard-turbulence regime.

III. EXPERIMENTAL RESULTS

When the OB approximation is valid, x, the ratio between Δ_t and Δ_b, is 1. However, as the OB approximation breaks down, x departs from 1. Thus x is a quantitative measure of the non-OB effects.

Figure 1 is a plot showing x for different Rayleigh numbers. By changing the density, one can coarsely adjust the Rayleigh number. As shown both in Table I and Fig. 1, the density needed to reach $R = 10^{10}$ is not large enough for the fluid properties of the two boundary layers to differ dramatically, consequently x is not very different from 1. The fact that the x value is 0.89 for $R = 2\times10^9$, smaller than 1, may come from approximating the central region temperature with one point measurement. This approximation improves as the Rayleigh number increases. However, for $R > 10^{10}$, x becomes significantly smaller than 1. Since a specific Rayleigh

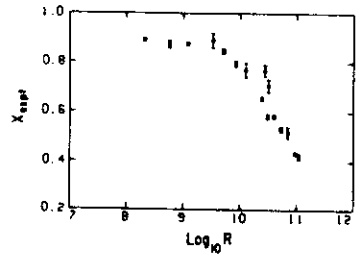

FIG. 1. x_{exp}, the ratio between the measured temperature drops of the top and the bottom boundary layers, is plotted against the Rayleigh number R.

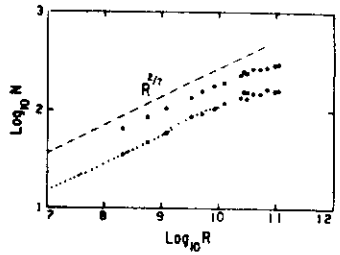

FIG. 3. The log-log plot of the Nusselt number N vs Rayleigh number R. The small dots and the solid circles are the experimental data, but only the solid circles have been analyzed in this paper. The open circles are the theoretical points. The theoretical value has an arbitrary prefactor.

number can be realized with different densities, although they must be close to each other, there is not a one-to-one relation between x and a given Rayleigh number.

As shown in Fig. 1, x can be as small as 0.4, so the two boundary layers are significantly different. Then how does the turbulent temperature fluctuation in the central region feel this difference? Figure 2 shows the histograms of the temperature fluctuation in the central region for $R = 1.2\times10^9$, $x = 0.87$ and $R = 9.6\times10^{10}$, $x = 0.43$. They are normalized by their rms temperature fluctuation Δ_c. The normalized histogram for $x = 0.43$ has the same shape as that of $x = 0.87$, it is symmetric around its mean temperature, despite the big difference between the two boundary layers. These boundary layers adjust themselves somehow so that the fluctuation in the central region is still symmetric around its mean. By the way, the histogram of this large aspect ratio cell is exponential only in certain range, rather than in the full range for the aspect ratio 1 cell.[11] This difference shall be discussed in a future work.

However, non-OB effects may alter the Rayleigh number dependences of the Nusselt number N and rms temperature fluctuation Δ_c normalized by Δ. The solid circles and triangles in Fig. 3 reveal the R dependence of N, whereas the solid circles in Fig. 4 reveal the R dependence of Δ_c/Δ. For $R < 10^{10}$, both N and Δ_c/Δ have simple power-law relations with R, N with an exponent 0.29, close to $\frac{1}{3}$, and Δ_c/Δ with an exponent -0.14, close to $-\frac{1}{7}$. These relations have been proposed[12] in a scaling model for hard turbulence, which fits the experimental results for the aspect-ratio-1 cell. However, N and Δ_c/Δ deviate away from the simple power laws for $R > 10^{10}$. N seems to saturate with R and Δ_c/Δ decreases faster than with the $-\frac{1}{7}$ power law. The deviation cannot be put into the framework of hard turbulence, unless non-OB effects play a role.

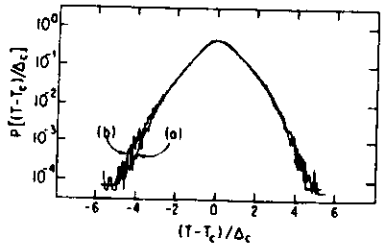

FIG. 2. Comparison of histograms of the temperature fluctuation for (a) $R = 1.2\times10^9$, $x = 0.87$ and (b) $R = 9.6\times10^{10}$, $x = 0.43$. The probability for a given temperature is plotted against this temperature. The histograms are all rescaled so that the rms temperature fluctuations coincide

IV. PROPOSED MODELS

Now we try to answer the question of how the cell, with a given density and given top- and bottom-plate temperature, chooses the central region temperature, in

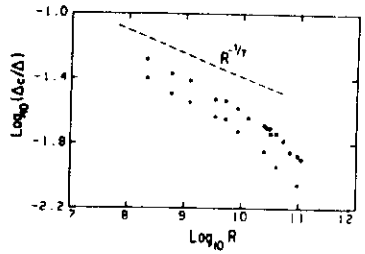

FIG. 4. The log-log plot of Δ_c/Δ vs R. The solid circles are the experimental data, and the open circles are the theoretical points. The theoretical value has an arbitrary prefactor.

other words, how it selects the asymmetry of the two boundary layers, namely x. Furthermore, we try to understand whether non-OB effects have anything to do with the strange Rayleigh number dependences of N and Δ_c/Δ.

Let us consider how many equations we have. We already have Eq. (2), which states that the total temperature drop is across the two boundary layers only. Furthermore, there is the conservation of heat flux. Since the heat is transported purely by conduction in the two boundary layers, then

$$Q = \gamma_t \frac{\Delta_t}{\lambda_t} , \tag{3a}$$

$$Q = \gamma_b \frac{\Delta_b}{\lambda_b} , \tag{3b}$$

where Q is the heat flux, γ_t and γ_b are the thermal conductivities for the two boundary layers, and λ_t and λ_b are the two boundary layer thicknesses. From the three equations (2), (3a), and (3b), we are unable to solve for the four unknowns Δ_t, Δ_b, λ_t, and λ_b. One more equation is needed to connect the two boundary layers.

Classically[19,20] the boundary layers are assumed to be marginally stable, therefore their Rayleigh numbers are constant. This implies the equality of the Rayleigh numbers R_t and R_b for the two boundary layers, i.e.,

$$\frac{g\alpha_t\lambda_t^3\Delta_t}{\nu_t\kappa_t} = \frac{g\alpha_b\lambda_b^3\Delta_b}{\nu_b\kappa_b} , \tag{4}$$

where the left-hand side is R_t and the right-hand side is R_b. This assumption can be checked from the experimental data. If one substitutes the measured Q, Δ_t, and Δ_b into Eqs. (3a) and (3b), the boundary layer thicknesses λ_t and λ_b can be determined; they are listed in Table II. Thus R_t and R_b can be calculated independently. R_t and R_b have been listed in Table II, and their ratio R_b/R_t is plotted against x in Fig. 5 as open triangles. As x decreases, the ratio diverges away from 1. Therefore this assumption is not corroborated by the experimental results.

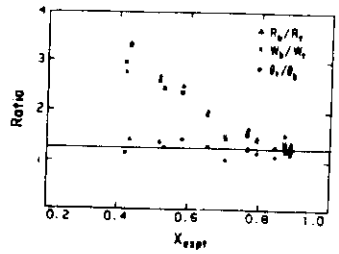

FIG. 5. Ratios between R_b and R_t (open triangles), w_b and w_t (crosses), and Θ_t and Θ_b (solid circles) vs the measured x.

It has been observed that there are many thermals in the central region, which are released from the boundary layers.[15,21,22] Therefore the temperature fluctuations in the central region must be directly related to the properties of the boundary layers. In the scaling model introduced in Ref. 12 (where the OB approximation is assumed), the thermals, with their initial temperature $\Delta/2$, merge into the central region with a velocity w,

$$w = \frac{g\alpha\Delta\lambda^2}{\nu} , \tag{5}$$

where this velocity w comes from the balance between the buoyancy force $g\alpha\Delta$ and the viscous force $\nu w/\lambda^2$. Further the temperature fluctuation Δ_c in the central region is the temperature scale Θ of the boundary layers,

$$\Delta_c = \frac{\kappa\nu}{g\alpha\lambda^3} , \tag{6}$$

where the right-hand side is Θ. In the OB case, these two

TABLE II. Calculated values of the thickness $\lambda_{t,b}$, the Rayleigh numbers $R_{t,b}$, velocity scales $w_{t,b}$, and temperature scales $\Theta_{t,b}$ of the two boundary layers for different Rayleigh number R.

R	λ_t (μm)	λ_b (μm)	R_t	R_b	w_t (cm/s)	w_b (cm/s)	Θ_t (mK)	Θ_b (mK)	$2S/(S_t+S_b)$
2.10×10^{8}	390	452	241	337	24.5	32.3	0.698	0.561	0.998
5.75×10^{8}	291	338	261	406	15.3	21.7	0.282	0.208	0.999
1.21×10^{9}	235	276	310	428	22.4	29.6	0.536	0.444	1.00
5.13×10^{9}	148	177	356	466	20.0	26.1	0.461	0.416	1.01
3.35×10^{9}	163	184	279	362	12.3	15.5	0.253	0.219	0.997
8.42×10^{9}	128	161	368	548	19.3	28.2	0.441	0.372	1.00
1.27×10^{10}	110	141	343	573	15.1	23.9	0.364	0.283	0.983
2.44×10^{10}	89.8	133	391	783	19.0	37.0	0.515	0.394	0.979
3.07×10^{10}	85.5	143	437	1086	22.2	52.9	0.602	0.416	0.963
2.75×10^{10}	86.1	108	404	656	15.3	23.9	0.301	0.242	1.05
3.18×10^{10}	83.4	112	419	611	16.2	24.8	0.321	0.312	0.976
4.00×10^{10}	77.3	124	400	995	16.6	39.1	0.399	0.275	1.01
5.30×10^{10}	74.1	128	510	1243	21.1	51.9	0.408	0.316	0.943
6.97×10^{10}	70.0	113	447	1202	14.4	37.6	0.239	0.172	0.935
9.56×10^{10}	63.1	124	541	1801	18.3	60.7	0.287	0.199	0.909
1.10×10^{11}	62.5	122	654	1809	20.4	60.8	0.228	0.196	0.897

equations are equivalent. Starting from either, one is able to draw a series of predictions which fit the experimental data of the OB case well.[12] In the non-OB case, although it is not obvious that w_t is the same as w_b, and Θ_t is the same as Θ_b, it is revealing to compare their values in an effort to generalize either Eq. (5) or (6) to the non-OB case. Thus we calculate w_t and w_b, Θ_t and Θ_b, from the fluid properties in Table I and from the boundary layer thickness in Table II. Their values are listed in Table II.

The ratio between w_b and w_t is plotted as crosses in Fig. 5. It diverges away from 1 as x decreases, therefore w_t and w_b do not match. On the other hand, the ratio between Θ_t and Θ_b is plotted as solid circles in Fig. 5. For all the experimental values of x, the ratio remains constant at 1.27 ± 0.13. Compared with the previous two cases (the equality of R and the equality of w), the equality of the two boundary layer temperature scales

$$\Delta_t = \frac{\kappa_t\nu_t}{g\alpha_t\lambda_t^3} = \frac{\kappa_b\nu_b}{g\alpha_b\lambda_b^3} \tag{7}$$

appears to be the best assumption. This assumption is also consistent with the experimental fact that the histogram of the central temperature fluctuations is symmetric even in the strongly non-OB case, i.e., the colder temperature fluctuations is the same as that from the hotter ones. Generalizing Eq. (6), the rms temperature fluctuations in the central region is the same as the two boundary layer temperature scales.

Now that we have Eq. (7), we can write out the expression for x in terms of only the fluid properties. From Eqs. (2), (3a), (3b), and (7), Δ_t and Δ_b can be calculated. Their ratio x is

$$x = \left|\frac{\alpha_b^3\nu_b^2\kappa_b}{\alpha_t^3\nu_t^2\kappa_t}\right|^{1/3}\frac{\gamma_b}{\gamma_t} = \frac{S_t}{S_b} , \tag{8}$$

where S_t and S_b are defined as $(\nu\kappa/\alpha)^{1/3}(1/\gamma)$ for the top and bottom boundary layers. Note that the fluid properties in the two boundary layers are related to x, thus the right-hand side of Eq. (8) is also a function of x. This allows one to uniquely solve for x. Here we use the measured temperature to compute the fluid properties, from which we calculate the theoretical x value from Eq. (8). Figure 6 shows the ratio between the theoretical x value and the experimental x value. The ratio is constant with a value 1.08 ± 0.04, indicating a good agreement between experiment and theory.

Let us point out the uncertainties in the measurement and analysis. First, there are errors in the temperature measurement and the consequence in the fluid properties. The second factor comes from assuming the fluid properties in the boundary layer to be the mean temperature value. Third, there are uncertainties in the McCarty tables and equation, especially close to the critical point. In the error bars of Fig. 6, only the first error is plotted, although the scatter may be due to the second and the third factors as well.

The rms temperature fluctuation Δ_c in the central region has been assumed to be the same as the boundary

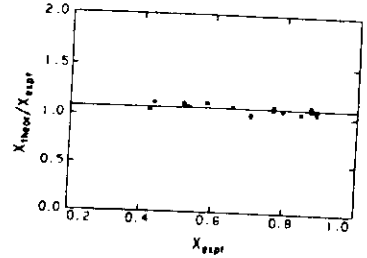

FIG. 6. Ratio between the theoretical and the measured x vs the measured x.

layer temperature scales in Eq. (7). However, in order to express the heat flux Q only in terms of Δ and the fluid properties, a further assumption has to be made about the velocity in the central region. As in Ref. 12, we assume that the thermals in the central region are only driven by the buoyancy force, then

$$V_c = (\alpha g L\Delta_c)^{1/2} . \tag{9}$$

The heat flux is

$$Q = C_p\rho\Delta_c V_c , \tag{10}$$

Combining Eqs. (8) and (9), one finds

$$Q = C_p\rho(\alpha g L)^{1/2}\Delta_c^{3/2} . \tag{11}$$

Here the fluid properties are those of the central region of the cell. From Eqs. (2), (3a), (3b), and (7), λ_t and λ_b can be expressed in terms of Q, Δ, and the fluid properties. Then combining Eq. (7) with (11), the heat flux Q is expressed as

$$Q = \gamma\frac{\Delta}{L}\left|\frac{g\alpha L^3\Delta}{\nu\kappa}\right|^{3/7}\left|\frac{\kappa}{\nu}\right|^{1/7}\left|\frac{S}{S_t+S_b}\right|^{9/7} , \tag{12}$$

or

$$N = R^{3/7}P^{-1/7}\left|\frac{S}{S_t+S_b}\right|^{9/7} , \tag{13}$$

and the temperature fluctuation is

$$\frac{\Delta_c}{\Delta} = R^{-1/7}P^{-3/7}\left|\frac{S}{S_t+S_b}\right|^{6/7} , \tag{14}$$

where R and P are the Rayleigh number and Prandtl number ($P=\nu/\kappa$) based on the fluid properties of the central region. For small non-OB effects, $(S_t+S_b)/2$ is close to S, thus the relations between N and R, and between Δ_c/Δ and R are the same as those of the ideal OB case. However, when the non-OB effects are so strong that $(S_t+S_b)/2$ becomes different from S, then both N and Δ_c/Δ depart from the simple power laws. The ratio $2S/(S_t+S_b)$ is listed in Table II. The theoretical Nusselt number is plotted in Fig. 3 as open circles to compare

with the experimental data. One can see that besides the power-law region for $R < 10^{10}$, the theoretical Nusselt numbers change in the same way as the experimental data for $R > 10^{10}$. The theoretical Δ_c/Δ is compared to the experimental one in Fig. 4, with good agreement.

V. CONCLUSION

The assumption that the temperature scales of the two boundary layers are the same is verified experimentally. It is consistent with the observation that the histogram of the central region fluctuation is symmetric even in the strongly non-OB case. This assumption allows us to calculate the ratio of the temperature drops across the two boundaries, and compare it with the measurement. If the velocity in the central region is assumed to be a free-fall velocity, the heat flux and the rms of the temperature fluctuation can be further computed. The agreement is good between the experiments and theory. The scatter of the results may come from the errors in the temperature measurements, the apparent crude approximation about the fluid properties of the boundary layers, and the uncertainties in the fluid properties themselves. All of the above discussion is about hard turbulence, where the large-scale flow is not important in the central region.

ACKNOWLEDGMENTS

We thank M. Sano for helping in all aspects of the experiment, S. Thomae for stimulating discussions, Professor Hilderbrand of the Astrophysics Department for providing us with the bolometers, and A. Simon for revising the manuscript. Special thanks should go to Professor Kadanoff for his guidance in all phases of the work. This research has been supported by the National Science Foundation under Contract No. DMR 8722714.

---

[1]A. Oberbeck, Ann. Phys. Chem. 7, 271 (1879).
[2]J. Boussineq, *Theorie Analytique de la Chaleur* (Gauthier-Villars, Paris, 1903), Vol. 2.
[3]E. L. Koschmieder, Beitr. Phys. Atmos. 39, 1 (1966).
[4]F. H. Busse, J. Fluid Mech. 30, 625 (1967).
[5]C. Q. Hoard, C. R. Robertson, and A. Acrivos, Int. J. Heat Mass Transfer 13, 849 (1970).
[6]E. F. C. Somerscales and T. S. Dougherty, J. Fluid Mech. 42, 755 (1970).
[7]F. M. Richter, J. Fluid Mech. 89, 553 (1978).
[8]M. Dubois, P. Berge, and J. Wesfreid, J. Phy· (Paris) 39, 1253 (1978).
[9]G. Ahlers, J. Fluid Mech. 98, 137 (1980).
[10]R. W. Walden and G. Ahlers, J. Fluid Mech 09, 89 (1981).
[11]F. Heslot, B. Castaing, and A. Libchaber, hys. Rev. A 36, 5870 (1987).
[12]B. Castaing, G. Gunaratne, F. Heslot, L. danoff, A. Libchaber, S. Thomae, X. Z. Wu, S. Zaleski, d G. Zanetti, J. Fluid Mech. 204, 1 (1989).
[13]R. D. McCarty, Natl. Bur. Stand. (U.S.) Tech. Note 631, (1972).
[14]R. D. McCarty, J. Phys. Chem. Ref. Data 2, 923 (1973).
[15]G. Zocchi, E. Moses, and A. Libchaber, Physica A 166, 387 (1990).
[16]A. E. Lange, E. Kreysa, S. E. McBride, and P. L. Richards, Int. J. Infrared Millimeter Waves 4, 689 (1983).
[17]J. C. Mather, Appl. Opt. 21, 1125 (1982).
[18]M. Sano, X. Z. Wu, and A. Libchaber, Phys. Rev. A 40, 6421 (1989).
[19]W. V. R. Malkus, Proc. R. Soc. London Ser. A 225, 196 (1954).
[20]L. N. Howard, in *Proceedings of 11th International Congress of Applied Mechanics, Munich, 1966*, edited by Henry Goertler (Springer, Berlin, 1966), p. 1109.
[21]T. Y. Chu and R. J. Goldstein, J. Fluid Mech. 60, 141 (1973).
[22]H. Tanaka and H. Miyata, Int. J. Heat Mass Transfer 23, 738 (1980).

REFERENCES

ANDERSON, A. C. 1973 Low-noise ac bridge for resistance thermometry at low temperatures. *Rev. Sci. Instrum.*, **44**, 1475.

ANSELMET, F. A., GAGNE, Y., HOPFINGER, E. J. & ANTONIA, R. A. 1984 High-order velocity structure functions in turbulent shear flows. *J. Fluid Mech.* **140**, 63.

ANTONIA, R. A, SATYAPRAKASH, B. R. & CHAMBERS, A. J. 1982 Reynolds number dependence of velocity structure functions in turbulent shear flows. *Phys. Fluids* **25**, 29.

ARGOUL, F., ARNEODO, A., GRASSEAU, G., GAGNE, Y., HOPFINGER, E. J. & FRISCH, U. 1989 Wavelet analysis of turbulence data reveals the multifractal nature of the Richardson Cascade. *Nature* **338**, 51.

BALACHANDAR, S., MAXEY, M. & SIROVICH, L. 1989 Numerical Simulations of high Rayleigh number convection, *J. Sci. Comput.* **4**, 219.

BEHRINGER, R. P & AHLERS, G. 1977 Heat transport and critical slowing down near the Rayleigh-Benard instability in cylindrical container. *Phys. Lett.* **62** A, 329.

BEHRINGER, R. P. 1985 Rayleigh-Benard Convection and turbulence in liquid helium. *Rev. of Mod. Phys.* **57**, 657.

BENARD, M. 1901 Les tourbillons cellulaires dans une nappe liquide transportant de la chaleur par convection en régime permanent *Ann. de Chimie et de Physique* **23**, 62.

BOLGIANO, R. JR. 1959 Turbulent spectra in a stably stratified atmosphere. *J. Geophys. Res.* **64**, 2226.

BRUNT, D. 1927 The period of simple vertical oscillation in the atmosphere. *Q. J. R. Met. Soc* **53**, 30.

BUSSE, F. H. 1978 Non-linear properties of thermal convection. *Rep. Prog. Phys.* **41**, 1929.

CASTAING, B., GUNARATNE, G. HESLOT, F., KADANOFF, L., LIBCHABER, A., THOMAE, S., WU, X. Z., ZALESKI, S. & ZANETTI, G. 1989 Scaling of hard thermal turbulence in Rayleigh-Benard convection. *J. Fluid Mech.* **204**, 1.

CASTAING, B. 1989 *J. Phys. (Paris)* Consequences d'un principe d'extremum en turbulence. **50**, 147.

CASTAING, B. 1990 Scaling of turbulence Spectra. *Phys. Rev. Lett.* **65**, 3209.

CASTAING, B., GAGNE, Y. & HOPFINGER, E. 1990 Velocity probability density functions of high Reynolds number turbulence *Physica D* **46**, 177.

CHAMPAGNE, F. H. 1978 The fine-structure of the turbulent velocity field. *J. Fluid Mech.* **86**, 67.

CHANDRASEKHAR S. 1961 *Hydrodynamic and Hydromagnetic Stability*, Clarendon Press, Oxford.

CHARLSON, G. S. & SANI, R. L. 1975 Finite amplitude axisymmetric thermoconvective flows in a bounded cylindrical layer of fluid. *J. Fluid Mech.* **71**, 9175.

CHU, T. Y. & GOLDSTEIN, R. J. 1973 Turbulent convection in a horizontal layer of wate , *J. Fluid Mech.* **60**, 141.

CVITANOVIC, P. 1984 *Universality in Chaos*, Adam Hilger Ltd., Bristol, England.

DEARDORFF, J. W. & WILLIS, G. E. 1965 The effect of two dimensionality upon the supression of thermal turbulence. *J. Fluid Mech.* **23**, 337.

DELUCA, E. E., WERNE, J., ROSNER, R. & CATTANEO, F. 1990 Numerical simulations of soft and hard turbulence: preliminary results for two-dimensional convection. *Phys. Rev. Lett.* **64**, 2370.

ECKMANN, J. -P. 1981 Roads to turbulence in dissipative dynamical systems. *Rev. Mod. Phys.* **53**, 643.

ECKMANN, J. -P. & RUELLE, D. 1985 Ergodic theory of chaos and strange attractors. *Rev. Mod. Phys.* **57**, 617.

FITZJARRALD, D. E. 1976 An experimental study of turbulent convection in air. *J. Fluid Mech.* **73**, 693.

FOIAS, C. & TEMAM R. 1989 *J. Funct. Anal.* **87**, 359.

FOIAS, C., MANLEY, O. & SIROVICH, L. 1990 *Phys. Fluid* **A2**, 464.

FRISCH, U., SULEM, P. & NELKIN, M. 1978 A simple dynamical model of intermittent fully developed turbulence. *J. Fluid Mech.* **87**, 719.

FRISCH, U. & ORSZAG, S. A. 1990 Turbulence: Challenges for theory and experiment, *Physics Today* **43(1)**, 24.

FRISCH, U. & VERGASSOLA, M. 1991 A prediction of the multifractal model: the intermediate dissipation range. *Europhys. Lett.* **14(5)**, 439.

GLAZIER J. A. & LIBCHABER, A. 1988 Quasi-periodicity and dynamical systems: an experimentalist's view. *IEEE Transactions on Circuits and Systems* **35**, 790.

GOLDSTEIN, R. J. & CHU, T. Y. 1969 Turbulent convection in a horizontal layer of air. *Prog. in Heat and Mass Transfer* **2**, 55.

GARON, A. M. & GOLDSTEIN, R. J. 1973 Velocity and heat transfer measurement in thermal convection. *Phys. fluids* **16**, 1818.

GOLDSTEIN, R. J. & TOKUDA, S. 1980 Heat transfer by thermal convection at high Rayleigh numbers. *Int. J. Heat Mass Transfer* **23**, 738.

GLOBE, S. & DROPKIN, D. 1959 Natural convection heat transfer in liquids confined by two horizontal plates and heated from below. *Trans. Am. Soc. Mech. Eng. Pap.* **81**, 24.

GROSS, S., ZOCCHI, G. & LIBCHABER, A. 1988 Waves and plumes of thermal boundary layer. *C. R. Acad. Sci. (Paris)* **307**, 447.

GROSSMANN, A. & MORLET, J. 1987 in *Mathematics and Physics, Lecture on Recent Results*. ed. Streit L., World Scientific, Singapore.

GROSSMANN, S. & LOHSE, D. 1991 Fourier-Weierstrass mode analysis for thermally driven turbulence. Submitted to *Phys. Rev. Lett.*

HAO B. L. 1984 *Chaos*, World Scientific, Singapore

HESLOT, F., CASTAING, B. & LIBCHABER, A. 1987 Transition to turbulence in helium gas. *Phys. Rev. A* **36**, 5870.

HOWARD, L. N. 1966 Convection at high Rayleigh number. *Applied Mechanics, Proc. of the 11 the Int. Congr of Appl. Mech. Munich (Germany)*, ed. Gortler H., Springer, Berlin.

KOLMOGOROV, A. N. 1941 The local structure of turbulence in incompressible viscous fluid for very large Reynolds numbers. *C. R. Acad. Sci. URSS* **30**, 301.

KOLMOGOROV, A. N. 1941 Dissipation of energy in locally isotropic turbulence. *C. R. Acad. Sci. URSS* **32**, 16.

KOLMOGOROV, A. N. 1962 A refinement of previous hypothesis concerning the local structure of turbulence in a viscous incompressible fluid at high Reynolds number. *J. Fluid Mech.* **13**, 82.

KRAICHNAN, R. H. 1962 Turbulent thermal convection at arbitrary Prandtl number. *Phys. Fluids* **5**, 1374.

KRISHNAMURTI, R. 1973 Some further studies to turbulent convection *J. Fluid Mech.* **60**, 285.

KRISHNAMURTI, R. & HOWARD, L. 1981 Large-scale flow generation in turbulent convection. *Proc. Nat. Acad. Sci.* **78**, No. 4,1981.

KUO, A.& CORRSIN, S. 1971 Experiments on internal intermittency and fine-structure distribution functions in fully turbulent fluid. *J. Fluid Mech.* **50**, 285.

LANDAU, L. D. & LIFSHITZ, E. M. 1980 *Statistical Physics*, Pergamon, Oxford, England

LANDAU, L. D. & LIFSHITZ, E. M. 1986 *Fluid Mechanics*, Pergamon, Oxford, England.

LANGE, A. E., KREYSA, E., MCBRIDE, S. E. & RICHARDS, P. L. 1983 *Int. J. Infrared Millimeter Waves* **4**, 689.

LIBCHABER, A. & MAURER, J. 1982 A Rayleigh Benard experiment: Helium in a small box. *Nonlinear Phenomena at Phase Trasitions and Instabilities*, Proceedings NATO ASI, Geilo Mar., ed. Riste T, Plenum Press, New York.

LORENZ, E. 1963 Deterministic nonperiodic flow, *J. Atmos. Sci.* **200**, 130.

L'VOV, V. S. 1991 submitted to *Phys. Rev. Lett.* (Weizmann Institute, WIS-913Feb.-PH)

L'VOV, V. S. & FALKOVICH, C. E. 1991 Conservation law and two-flux spectra of hydrodynamic convective turbulence. Preprint (Weizmann Institute, WIS-917March-PH)

MCCARTY, R. D. 1972 Thermophysical properties of helium-4 from 2 to 1500 K with pressures to 1000 atmospheres. *NBS Technical Note* **631**

MCCARTY, R. D. 1973 Thermodynamic Properties of Helium 4 from 2 to 1500K at Pressures to 10^8 Pa. *J. Phys. Chem. Ref. Data* **2**, 923.

MALKUS, W. V. R. 1954 Discrete transitions in turbulent convection. *Proc. Roy. Soc. (London)* **A225**, 185.

MALKUS, W. V. R. 1954 Heat transport and spectrum of thermal turbulence *Proc. Roy. Soc. (London)* **A225**, 196.

MALKUS, W. V. R. 1963 Outline of a theory of turbulent convection, In *Theory and Fundamental Research in Heat Transfer*. Pergamon, Oxford, England.

MANNEVILLE, P. 1990 *Dissipative Structures and Weak Turbulence*, Acad. Press, US.

MATHER, J. C. 1982 Bolometer noise: nonequilibrium theory *Appl. Opt.* **21**, 1125.

MONIN, A. S. & YAGLOM, A. M. 1971 *Statistical Fluid Mechanics* **1** MIT Press, Cambridge, MA, USA.

MONIN, A. S. & YAGLOM, A. M. 1975 *Statistical Fluid Mechanics* **2** MIT Press, Cambridge, MA, USA.

NELKIN, M. & TABOR, M. 1989 Time correlations and random sweeping in isotropic turbulence. *Phys. Fluids* A **2(1)**, 81.

NORMAND, C., POMEAU, Y. & VELARDE, M. 1977 Convective instability: A physicist's approach. *Rev. Mod. Phys.* **49**, 581.

OBUKHOV, A. M. 1959 *Dokl. Akad. Nauk. SSSR* **125**, 1246.

OBUKHOV, A. M. 1962 Some specific features of atmospheric turbulence. *J. Fluid Mech.* **13**, 77.

PARISI, G. & FRISCH, U. 1985 in *Turbulence and Predictability in Geophysical Fluid Dynamics and Climate Dynamics, Proceedings of the International E. Fermi School of Physics, Varenna, Italy*, ed. M. Ghil, R. Benzi & G. Parisi North-Holland, Amsterdam.

PELLEW, A. & SOUTHWELL, R. V. 1940 On maintained convective motion in a fluid heated from below. *Proc. R. Soc. Lond.* A **176**, 312.

PROCACCIA, I. & ZEITAK, R. 1989 Scaling exponents in nonisotropic convective turbulence. *Phys. Rev. Lett.* **62**, 2128.

PROCACCIA, I., CHING, E. S. C., CONSTANTIN, P., KADANOFF, L., LIBCHABER, A. & WU, X. Z. 1991 Transitions in convective turbulence: the role of thermal plumes. preprint.

PUMIR, A., SHRAIMAN, B. & SIGGIA, E. 1990 Exponential tails and random advection. preprint.

RAYLEIGH LORD 1916 On convection currents in a horixontal layer of fluid, when the higher temperature is on the underside. *Phil. Mag.* **32**, 529.

REID, W. H. & HARRIS, D. L. 1958 Some further results on the Benard problem. *Phys. Fluids* **1**, 102.

RICHARDSON, L. F. 1922 *Weather Prediction by Numerical Process*, Cambridge Univ. Press, Cambridge.

ROSSBY, H. T. 1969 A study of Benard convection with and without rotation. *J. Fluid Mech.* **36**, 309.

SANO, M., WU, X. Z. & LIBCHABER, A. 1989 Turbulence in helium-gas free convection. *Phys. Rev. A* **40**, 6421.

SHE, Z. S. 1989 On the scaling laws of thermal turbulence convection. *Phys. Fluids* A **1(6)**, 911.

SHELLEY, M. & VINSON M. 1991 Coherent structures on a boundary layer in Rayleigh-Benard turbulence, submitted to *Nonlinearity*.

SINAI, Y. G. & YAKHOT, V. 1989 Limiting probability distributions of a passive scalar in a random velocity field. *Phys. Rev. Lett.* **63**, 1962.

SOMERSCALES, E. F. C. & GAZDA, I. W. 1969 Thermal convection in high Prandtl number liquids at high Rayleigh number. *Int. J. Heat Mass Transfer* **12**, 1491.

SOLOMON, T. H. & GOLLUB, J. P. 1990 Sheared boundary layers in turbulent Rayleigh-Benard convection *Phys. Rev. Lett.* **64**, 2382.

SPIEGEL, E. D. 1971 Convection in stars. *Annual review of astronomy and astrophysics* **9**, 324.

SHRAIMAN, B. I. & SIGGIA, E. D. 1990 Heat transport in high-Rayleigh number convection. *Phys. Rev. A* **42**, 3650.

TACONIS, K. W., BEENAKKER, J. J. M., NIER, A. O. C. & ALDRICH, L. T. 1949 Measurements concerning the vapour-liquid equilibrium of solutions of He^3 in He^4 below 2.19 K. *Physica* **15**, 733.

TANAKA, H. & MIYATA, H. 1980 Turbulent Natural convection in a horizontal water layer heated from below. *Int. J. Heat Mass Transfer* **23**, 1273.

TAYLOR, G. I. 1938 *Proc. Roy. Soc.* **A164**, No. 919, 476.

TENNEKES, H. & LUMLEY, J. L. 1972 *A First Course in Turbulence.* MIT Press, Cambridge, MA.

TENNEKES, H. 1975 Eulerian and Lagrangian time microscales in isotropic turbulence. *J. Fluid Mech.* **67**, 561

THOMAE, S. 1990 Private Communication.

THRELFALL, D. C. 1974 *Natural Convection in helium gas*, Ph. D thesis, University of Cambridge.

THRELFALL, D. C. 1975 Free convection in low temperature gaseous helium. *J. Fluid Mech.* **67**, 17.

TOWNSEND, A. A. 1959 Temperature fluctuations over an heated surface. *J. Fluid. Mech.* **5**, 209.

TRITTON, D. J. 1988 *Physical Fluid Dynamics.* 2nd. ed. Clarendon Press, Oxford, England.

VAISALA 1925 *Soc. Fennica, Commun. Phys. Maths* **2**, 38.

VAN ATTA C. W. & CHEN W. Y. 1970 Structure functions of turbulence in the atmospheric boundary layer over the ocean. *J. Fluid Mech.* **44**, 145.

WU, X. Z., CASTAING, B., HESLOT, F. & LIBCHABER, A. 1988 Springer Proceeding in Physics **32**, *Universalities in Condensed Matter*, ed. Jullien R., Peliti L., Rammal R. & Boccara N, Springer-Verlag, Berlin, Germany.

WU, X. Z., KADANOFF, L., LIBCHABER, A. & SANO, M. 1990 Frequency power spectrum of temperature fluctuation in free convection. *Phys. Rev. Lett.* **64**, 2140.

YAKHOT, V., SHE, Z. S. & ORSZAG, V. 1984 *Phys. Fluids* A 1, 184.

YAKHOT, V. 1989 Probability distribution in high-Rayleigh-number Benard Convection. *Phys. Rev. Lett.* **63**,1965.

YAZAKI, T., TOMINAGA, A. & NARAHARA, Y. 1980 Experiments on thermally driven acoustic oscillation of gaseous helium. *J. Low Temp. Phys.* **41**, 45.

ZALESKI, S. 1991 Thermal convection in sheared layers. Preprint.

ZALESKI, S. 1991 The transition to hard thermal turbulence in Rayleigh Benard Convection. Preprint.

ZOCCHI, G., MOSES, E. & LIBCHABER, A. 1990 Coherent structures in turbulent convection, an experimental study. *Physica A* **166**, 387.

ZOCCHI, G. 1990 *Flow structures in turbulent convection*, Ph.D thesis, University of Chicago.

ZOUZOULAS, G. & ROTT, N. 1976 Thermally driven acoustic oscillations, Part V: Gas-Liquid oscillations. *J. App. Math. Phys.* **27**, 325.